Thorium-229 nuclear clock using a VUV frequency comb

by

Chuankun Zhang

B.S., Tsinghua University, 2017

M.S., University of Colorado, 2020

A thesis submitted to the

Faculty of the Graduate School of the

University of Colorado in partial fulfillment

of the requirements for the degree of

Doctor of Philosophy

Department of Physics

2025

Committee Members:

Jun Ye, Chair

Eric A. Cornell

James K. Thompson

Shuo Sun

Kelvin H. Wagner

Zhang, Chuankun (Ph.D., Physics)

Thorium-229 nuclear clock using a VUV frequency comb

Thesis directed by Prof. Jun Ye

Laser-based measurement and control of atomic and molecular states form the foundation of modern quantum technology and provide deep insights into fundamental physics. Today's most precise clocks are based on measurements of optical transitions in atoms. To this end, transitions with high quality factors, low sensitivities to external perturbations, and good signal-to-noise ratios are desired.

In this thesis, we achieve frequency-based laser spectroscopy of the ^{229}Th nuclear clock transition using a vacuum ultraviolet (VUV) frequency comb. The high transition frequency of 2,020,407,384,335(2) kHz (in 150 K CaF_2 crystals) and a long excited state lifetime of 641(4) s show the high intrinsic quality factor of this nuclear transition. This transition frequency is predicted to be insensitive to external perturbations due to 1) the small electromagnetic moment of the atomic nucleus and 2) the shielding effect of the outer electronic shell. Further, the large number density of quantum emitters in a solid-state crystalline host promises a high signal-to-noise ratio. Moreover, based on the different fundamental interactions involved in nuclear versus electronic transitions, precise comparisons between nuclear and atomic clocks offer dramatically enhanced sensitivity to new physics. Resolving individual nuclear quantum states in its host crystal enables us to perform the first steps in characterizing the nuclear clock performance.

Probing the ^{229}Th nuclear transition required new tools. Building upon previous generations of extreme-ultraviolet (XUV) comb projects in our lab, we construct a VUV comb to perform direct frequency comb spectroscopy of the ^{229}Th nuclear clock transition. We calibrate the absolute frequency by linking this comb to the JILA ^{87}Sr atomic clock. We also present our effort in making ^{229}Th thin-film samples for reducing the cost and radioactivity of future nuclear clocks.

Dedication

To my mother, whose love I will forever cherish but am unable to repay.

Acknowledgements

I once walked back from lunch with my thesis advisor, Prof. Jun Ye. Jun opened the door to JILA for me. As he is a renowned scientist and I was a young student, I hesitated and told Jun that I should hold the door for him instead. "Go ahead," Jun said, "At JILA, there are two criteria for what we should do: we do things that serve science and serve the people." This principle guided me through graduate school and will continue to shape my future career decisions.

Words cannot express my sincere gratitude to Jun, not only for all the guidance he provided for my studying, creative scientific ideas that made this thesis project possible, but also for the endless support when I make mistakes in the lab. Jun genuinely cared about the growth of students as much as he cared about the scientific outcome. Whenever we have fun and exciting moments, he is there to share the joy and to propose new ideas. There have also been difficult times, such as in the global COVID-19 pandemic. But I'm lucky to be a student at JILA, where Jun and the entire JILA community have created a well-protected environment for pure science.

Much of the fun I had in graduate school came from working with fantastic colleagues. All the work presented here was accomplished as a team effort. I would like to give my special thanks to Lars von der Wense. During the 3 years we shared in the lab, one can always hear us laughing, whether things worked as planned or not. Besides all the nuclear physics knowledge he taught me, I hope I've learned some of his optimism toward science and instinct for lab work. "Don't break the symmetry unless you need to!" I can hear him saying. I would like to thank Stephen Schoun and Gil Porat for getting me on track when I first join the lab. They would definitely have had more scientific progress without me constantly bugging them for explanations of things. Yet, they chose

to spend time teaching me every detail of the experiment. I was also lucky to work with Jacob Higgins, who offered a unique perspective to the experiment using his chemistry and spectroscopy instinct. I was fortunate to have the joy of working with extremely bright young students, Tian Ooi and Jack Doyle. Their paces of learning always amazes me. A significant part of the work in this thesis were made possible thanks to their intellectual contributions. I look forward to seeing their future achievements at JILA. While I did not have the chance to overlap with some of the previous lab members on the project, including Dylan Yost, Craig Benko and Christoph Heyl, I would like to also thank them for their support whenever I needed their advice. I had lots of fun discussions in the frequency comb group meeting, with Thinh Bui, Ya-Chu Chan, Bryan Changala, Kana Iwakuni, Qizhong Liang, Lee Liu, Prof. David Nesbitt, Dina Rosenberg, Jutta Toscano, Marissa Weichman. Specially, I wish the young students on mid-IR combs, Apoorva Bisht and Jonas Boettner, continued success in the future.

Our work also relies on the Sr clock and stable laser system built in the Ye group. I would like to sincerely thank Alexander Appeli, Zoey Hu, Dhruv Kedar, Dahyeon Lee, Ben Lewis, Kyuntae Kim, Will Milner, Will Warfield, Lingfeng Yan and everyone else in the Sr clock/stable laser team for their heroic work maintaining an absolute optical frequency reference.

This work couldn't be done without also the support from the amazing research community at JILA and CU Boulder. I would like to thank Kim Hagen, Cavin Schwadron, Hans Green, Kyle Thatcher, James Uhrich, and Dani Warren at the JILA instrument shop, Terry Brown, Ivan Rýger, James Fung-a-Fat, Felix Vietmeyer at the JILA electronics shop, Curtis Beimborn, Amy Ekiriwang, Dave Alchenberger, Scot Bohnenstiehl, Alan Copley at the JILA Keck metrology lab/clean room, Margaret Ashton, Bradley Denton, Mckenzie Statham and Logan Deison at the CU Radiation Safety Office for their help and technical assistance. I would like to also thank Andrew Cavanagh in the CU Department of Chemistry for XPS measurements, Joe MacLennan, Vicky Martinez in the CU Department of Physics for XRD measurements, Tomoko Borsa for teaching me the capabilities of the CU COSINC facility.

It was a privilege for me to work and/or discuss scientific questions with many scientists

worldwide. I would like to thank Thorsten Schumm, Kjeld Beeks and Georgy Kazakov in Vienna for growing, characterizing the beautiful ^{229}Th-doped CaF_2 crystals and providing suggestions on the spectroscopy signal detection setup, Eric Hudson, Richard Elwell, James Terhune for measuring the nuclear transition signal in $^{229}ThF_4$ thin films almost as soon as we sent the targets over, as well as driving their precious ^{229}Th:$LiSrAlF_6$ samples to JILA, Peng Li, Jie Jiang, and Martin Fermann for building and teaching us about the powerful Yb-fiber comb used in the experiment, Peter Thirolf for providing stimulating discussions and lending us useful lab optics, Uli Frible for his insight and help in building the physical vapor deposition setup for thin films, Christoph Düllmann, Dennis Renisch for offering test ^{229}Th material and advice on ^{229}Th target fabrication. I would also like to thank Mette Gaarde, Andrei Derevianko, and Marianna Safronova for their theory support, Ioachim Pupeza and Maximilian Hogner for discussions on the time-domain applications of XUV combs. Some of our discussions with external collaborators unfortunately haven't turned to concrete scientific results yet. I would like to thank Alexander Gaeta, Yoshitomo Okawachi, Francesco Tani, Philip Russell, John Travers for teaching me about dispersive wave and four-wave mixing in hollow-core fibers for VUV generation, Sae Woo Nam, Galen O'Neil, Dileep Reddy for discussions and preliminary tests on Th-coated superconducting nanowire single photon detectors, Xinxin Zhao for discussions about recoil-implanted targets, Johannes Weitenberg, Akira Ozawa, Oleg Pronin for useful discussions on XUV comb generation and outcoupling, Thomas Allison and Jason Jones for sharing optics coating runs. I also had fun discussions with professors in my Comps III exam and thesis committee besides my advisor, they are: Eric Cornell, Scott Diddams, Henry Kapteyn, Thomas Schibli, Shuo Sun, James Thompson, Kelvin Wagner.

I would also like to thank all the Ye lab members, past and present, for the friendship, the scientific discussions, and the support I had from them.

Lastly, I own many thanks to my family. My parents' love shaped my character. I'm sure my mother would be so proud of what I learned in graduate school. Special thanks to Ziru for bravely marrying me, for her endless support and love, and for the inspiring persistence she has in chasing her own dream career. I'm grateful for always having her by my side.

Contents

Chapter

Tables

Table

Figures

Figure

Chapter 1

Introduction and review: A nuclear clock transition in ^{229}Th

In this chapter, we provide a brief introduction to optical clocks and go through the history of the ^{229}Th nuclear clock development.

1.1 Optical atomic clocks

1.1.1 Using oscillators to keep track of time

Clocks often use periodic events in nature to keep track of time. From grandfather clocks using mechanical pendulums oscillating about once per second to tiny quartz crystals in watches oscillating typically at 32,768 Hz, we see that smaller oscillators offer a couple of advantages: they are typically less prone to systematic shifts, their higher oscillation frequency allows us to measure smaller intervals, and their smaller physical package makes them more portable for practical use.

A parameter typically used to characterize oscillators is the "quality factor", Q, defined as the ratio between the loss of energy per cycle and the total energy stored in the oscillator.[1] Naturally, a higher Q oscillator allows us to measure its free oscillating period more precisely by counting more cycles. Treating an oscillator with resonance frequency ω_0 and quality factor Q as a linear system, we see that its impulse response can be written as:[2]

$$x(t) = \mathrm{e}^{i\omega_0 t}\mathrm{e}^{-\omega_0 t/(2Q)} \times u(t) \tag{1.1}$$

[1] i.e., if we give the oscillator a kick, how many cycles will it oscillate before damped out?

[2] The idea of treating physical systems as linear systems and analyzing their behavior in the frequency domain (transfer functions) is used repeatedly in this thesis work. Ref. [1] serves as a good reference for this topic. Note the factor of 2 comes from the difference between amplitude and energy of the system

where u(t) is the unit step function. Through a simple Fourier transform, this corresponds to a frequency response of

$$H(i\omega) = \frac{1}{i(\omega - \omega_0) + \omega_0/(2Q)}, \tag{1.2}$$

which has a full width at half maximum (FWHM) of

$$\delta/\omega_0 = 1/Q. \tag{1.3}$$

It is thus obvious that a higher quality factor also corresponds to a narrower relative linewidth, and hence a more precise center frequency can be determined.

1.1.2 Atomic clocks as modern frequency standards

As discussed in Ref. [2], the stability of an atomic clock limited by quantum projection noise can be written as

$$\sigma = \frac{1}{2\pi f_0 \sqrt{N T_{\mathrm{m}} \tau}}, \tag{1.4}$$

where f_0 is the clock oscillator frequency, T_{m} is the measurement time of each measurement cycle, which is ultimately limited by the coherence time T, τ is the averaging time used to average out statistical noise, and N is the number of clock atoms used. Clearly, a higher clock frequency, longer coherence times, and a larger number of atoms are desirable for more stable atomic clocks. The quality factor mentioned above $Q \propto f_0 T$ serves as a helpful guide for choosing suitable clock transitions.

Mechanical oscillators have quality factors up to 10^6, while electronic orbits in atoms [3] can reach quality factors higher than $\sim 10^{16}$, making them much better oscillators for precision timekeeping. This extremely high quality factor comes from the combination of long coherence times and the high oscillation frequency of atomic clocks. The best frequency standards [4] today are optical clocks [2] that use atomic electronic transitions ticking at frequencies on the order of ~ 500 THz with linewidth approaching $\sim$ mHz [3, 5].

Besides the much higher precision coming from the high quality factor, the fact that atoms are identical to each other means that we have an absolute frequency reference independent of

manufacturing errors. Today's optical lattice clocks can trap a large number ($\sim 10^5$) of atoms in ultra-high vacuum using laser beams. With careful characterization and understanding of the systematic shifts, optical clocks can reach an accuracy of 8×10^{-19} [5]. This precision enables people to explore the boundaries of our understanding of fundamental physics [6, 3]. The measurement tools developed in optical clocks also enable observation of minuscule quantum many-body effects such as the collective Lamb shift in a quantum gas [7]. Novel quantum technologies [8, 9] are explored to improve clock precision even beyond classical limits.

1.2 Preparation for a nuclear clock based on ^{229}Th

Naturally, one may ask if there are even smaller objects that are less sensitive to environmental perturbations, with a higher transition frequency and a better quality factor, and thus can be used as a more precise clock. Ideally, due to the insensitivity to environmental perturbations, we can also pack a large number of oscillators in a small volume, therefore averaging down the statistical noise quickly according to Eqn. 1.4.

In fact, transitions in atomic nuclei that involve the configuration of nucleons may satisfy these criteria [10, 11, 12, 13, 14]. For building a nuclear-based optical clock, ^{229}Th stands out as a unique candidate due to its low transition energy, accessible with coherent lasers [15, 16, 17]. Comprehensive reviews of the ^{229}Th nuclear clock concept and recent progress can be found in Refs. [18, 19, 20, 21]. Readers interested in the nuclear structure can refer to Ref. [22] for the description of ^{229}Th nucleus with the Nilsson mode [23].

For the scope of this thesis, we may consider the nuclear transition as a simple two-level system, with properties shown in Fig. 1.1 and listed in Table 1.1. Briefly, the nuclear ground state $^{229\mathrm{g}}$Th and the isomeric excited state $^{229\mathrm{m}}$Th form a two-level system with a radiative decay lifetime ~ 2000 s. In addition, $^{229\mathrm{m}}$Th can be quenched by the hyperfine interaction between the nucleus and the electrons. This internal conversion (IC) process leads to a much shorter $^{229\mathrm{m}}$Th lifetime of $\tau_{\mathrm{ic}} \sim 10\,\mu\mathrm{s}$ if energetically allowed (i.e., electronic transitions matching the transition energy exist, such as in a solid with a bandgap smaller than the transition energy).

Figure 1.1: Properties of the ^{229}Th nuclear clock transition. The ground (^{229g}Th) and excited isomeric (^{229m}Th) state are labeled with their Nilsson quantum numbers [23, 22], magnetic dipole moment and electric quadrupole moment. Direct radiative excitation and decay has been experimentally observed, with the transition frequency and ^{229m}Th lifetime (converted to lifetime in vacuum) listed in purple color. Dashed blue lines corresponds to an internal conversion (IC) process, where the ^{229}Th nucleus couples to the electrons via hyperfine interactions V_{HFI}. As ^{229m}Th decays to ^{229g}Th, an electron is brought up from ground state $|g\rangle_e$ to the excited state $|e\rangle_e$, possibly in a continuum. Values and references of quoted parameters are listed in Table 1.1.

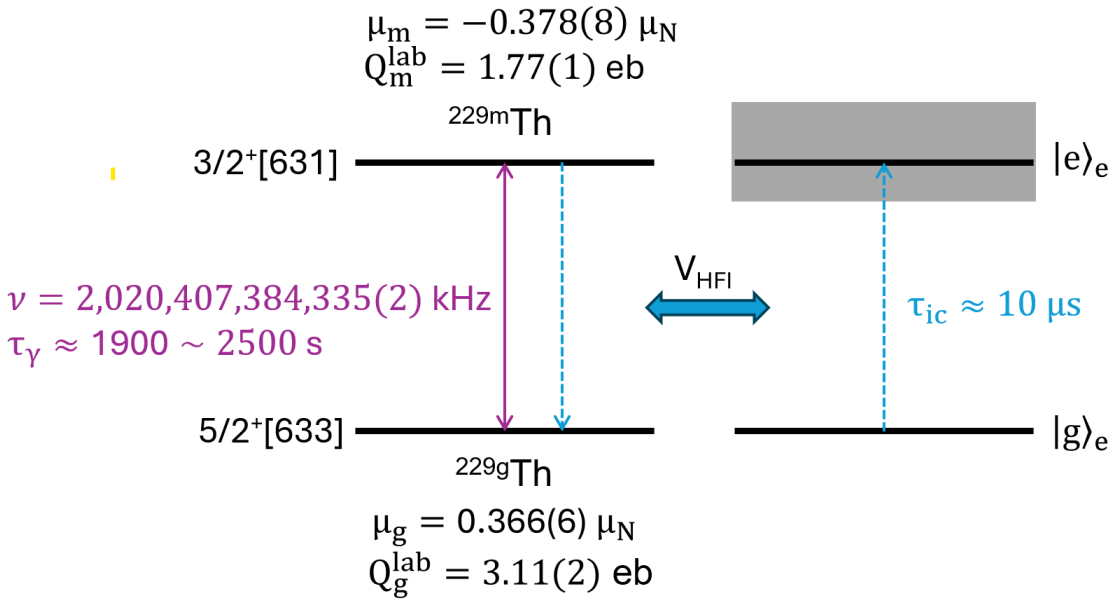

Parameter	Variable	Value	Reference
Transition frequency	ν	$2,020,407,384,335(2)$ kHz	Ref. [24]
Radiative Lifetime	τ_γ	$1900 \sim 2500$ s	Refs. [25, 26, 27, 28]
Internal conversion lifetime	τ_{ic}	$10(2)$ μs	Ref. [29]
^{229m}Th Magnetic Dipole	μ_e	$-0.378(8)\,\mu_N$	Ref. [26]
^{229m}Th Electric Quadrupole	Q_e	$1.77(1)$ eb	Refs. [24, 30]
^{229g}Th Magnetic Dipole	μ_g	$0.366(6)\,\mu_N$	Ref. [31]
^{229g}Th Electric Quadrupole	Q_g	$3.11(2)$ eb	Ref. [31]

Table 1.1: Parameters of the ^{229}Th nuclear clock transition shown in Fig. 1.1. Transition frequency ν is measured with the experimental conditions detailed in Ref. [24]. Internal conversion lifetime is listed for neutral ^{229m}Th on a conductive surface, as reported in Ref. [29].

1.2.1 ^{229}Th γ-ray spectroscopy revealing a transition for nuclear clocks

Typical nuclear transitions are in the γ-ray range, outside today's technological reach for phase-coherent quantum state manipulation and laser frequency counting. However, a significant amount of nuclear spectroscopy work has been performed by resolving the energy of the γ-ray fluorescence photons emitted after radioactive decay decay events. Due to the tight confinement of the crystal lattice in solids, recoil-free γ-ray photon emission and absorption are observed.[3] Using a relative motion between the radioactive source and the resonant absorber material, the nuclear γ-ray fluorescence is Doppler-shifted to characterize nuclear transitions and energy splittings in different materials. This process is typically termed Mössbauer spectroscopy [33].

High relative precision can be achieved in Mössbauer spectroscopy setups. In 1960, Pound and Rebka demonstrated the first observation of the apparent frequency shift of light in the Earth gravitational field [34] using a Mössbauer transition in ^{57}Fe [35]. An even narrower Mössbauer line in ^{67}Zn was proposed to serve as a "clock" with high precision [10], although without discussing techniques for absolute frequency readout.

To obtain absolute energy resolution, the energy of single γ photons can be measured using detectors such as thallium-activated NaI crystals [36] by counting scintillation photons or in Li-drifted germanium detectors [37] by counting electron-hole pairs created. Using these absolute energy sensors, Kroger and Reich measured the γ spectrum of ^{229}Th created by the α-decay of ^{233}U. After careful analysis of the γ spectrum, they concluded that there is a low energy nuclear excited state in ^{229}Th, whose excitation energy was originally determined to be < 0.1 keV, limited by their detector energy resolution [38]. This low-energy metastable isomeric state is referred to as $^{229\mathrm{m}}$Th in this thesis. With improved detector resolution and more careful analysis of the spectroscopy data, the $^{229\mathrm{m}}$Th energy was measured to be 4.5 ± 1 eV in 1993 [39], 3.5 ± 1.0 eV in 1994 [40] and was further refined to 5.5 ± 1.0 eV using the existing data [41] in 2005. Unfortunately, experiments looking for direct observation of the nuclear transition guided by these early reports

[3] Qualitatively, the confinement needs to be strong enough such that the momentum uncertainty of the nucleus is much larger than the recoil momentum change. Equivalently, the photon wavelength needs to be much larger than the confinement dimensions. Chap. 2 in Ref. [32] gives a great explanation.

were not successful, as these reported energy values were still significantly different from the true value.

In 2007, a new type of detector, the microcalorimeter spectrometer, was used to perform high-resolution spectroscopy on ^{229}Th nuclear fluorescence and reported a new value of 7.6 ± 0.5 eV [42], which was then corrected to 7.8 ± 0.5 eV in 2009 [43]. The large energy difference from previous reports explains the failure of a lot of previous experiments and re-ignited the interest in the community for this nuclear transition. This increased transition energy corresponds to light in the vacuum-ultraviolet (VUV), which poses additional technological challenges for direct spectroscopy of ^{229m}Th. More recently, the ^{229m}Th energy deduced from γ spectroscopy was further improved to 8.30 ± 0.92 eV using more precise γ ray energy and branching ratio measurements [44] and 8.10 ± 0.17 eV [45] with high-resolution magnetic microcalorimeters.

The existence of a low-energy nuclear transition, possibly within the reach of table-top laser technologies, attracted a lot of attention not only from nuclear physicists but also from spectroscopists for precision metrology applications [11]. With the radiative lifetime of the ^{229m}Th predicted to be on the order of hours [46, 47], it was proposed that precision spectroscopy of the ^{229m}Th state can be used to build an optical clock [12]. However, because of the large energy uncertainty known to the authors of these early proposals, the assumptions in the original proposals need to be reexamined.

1.2.2 Characterization of ^{229m}Th in trapped-ion platforms

Individual ions can be trapped inside the vacuum using properly designed electromagnetic fields [48], with the quantum states of individual ions precisely controlled [49]. This ion trapping technology enabled many exciting works in quantum information processing [50] as well as precision metrology [51]. A significant amount of knowledge of the ^{229m}Th state has been learned using trapped ^{229}Th ions, with the prospect of building a nuclear clock based on $^{229}Th^{3+}$ ions [52].

In Ref. [12], it was proposed that a nuclear-electron double resonance technique can be used to operate a nuclear clock based on $^{229}Th^{3+}$ in an ion trap. In this scheme, the nuclear

state is excited by a laser, while the population of the excited state can be read out via hyperfine spectroscopy of the nuclear excited state which depends on the nuclear magnetic moment. Trapping and cooling of first the naturally abundant ^{232}Th [53] then the radioactive ^{229}Th isotope [54] has been demonstrated. In addition to direct laser cooling, sympathetic cooling of $^{229}Th^{3+}$ is also possible using $^{88}Sr^{+}$ ions [55, 56]. With proper selection of the electronic states, the clock stability using a single $^{229}Th^{3+}$ ion is estimated to be $1 \times 10^{-15}/\sqrt{\tau}$ with τ being the measurement time in seconds, approaching a systematic uncertainty (inaccuracy) of 1.5×10^{-19} with an averaging time of around 2 years [52].[4]

Although direct laser excitation of ^{229m}Th has not yet been achieved in ion traps, the decay of ^{233}U has been used to populate the ^{229m}Th state with a branching ratio of $\sim 2\%$ [58]. Using a buffer gas stopper cell to collect recoil ^{229}Th ions ejected from a thin film ^{233}U target, and a quadrupole mass separator to select ion species according to the charge-to-mass ratio, doubly or triply charged ions of excited state ^{229m}Th have been extracted and characterized [22]. The ^{229m}Th gives a unique delayed electron emission signal due to the internal conversion (IC) decay of the excited nuclear state when implanted in a microchannel plate (MCP) detector, constituting the first direct observation of the ^{229m}Th state [59].

By neutralizing the excited-state ^{229m}Th ions obtained from the buffer gas stopping cell [22], the isomer property in neutral ^{229}Th atoms can also be studied. Since the energy of ^{229m}Th is higher than the ionization potential of neutral Th, the IC decay channel of ^{229m}Th is predicted [60, 61] and observed [59, 29] to dominate the nuclear decay. In the IC process, ^{229m}Th directly transfers its energy to an electron, causing autoionization (see Fig. 1.1). The half-life of the IC decay channel is measured to be 7 ± 1 µs in Ref. [29]. Further, the IC decay channel is used to measure the ^{229m}Th energy by performing kinetic energy spectroscopy of conversion electrons using a magnetic bottle spectrometer [62], yielding a value of 8.28 ± 0.17 eV.

With the ^{229m}Th generated by ^{233}U decay and trapped in ion traps, the double resonance

[4] This estimation assumes 1 Hz clock cycle. It would be possible to increase the stability using a clock laser with coherence times > 1 s [57] to further improve the clock stability.

technique [12] was tested. By performing electronic hyperfine spectroscopy on $^{229m}Th^{2+}$ ions [63], fundamental properties of the nuclear excited state were determined, including its magnetic dipole moment, electric quadrupole moment and nuclear charge radius. Recently, another hyperfine spectroscopy work on $^{229m}Th^{3+}$ [26] also reported that the ^{229m}Th lifetime in vacuum is 1400^{+600}_{-300} s.

1.2.3 X-ray pumping for ^{229m}Th excitation

The second excited state of ^{229}Th at 29 keV can be excited and measured with a synchrotron light source [64], enabling X-ray pumping to populate the clock isomer state ^{229m}Th. This X-ray pumping technique was recently extended to optically transparent ^{229}Th-doped crystals, where fluorescence from the ^{229m}Th decay was observed [65, 66]. A quenching effect from X-ray irradiation is reported, which is theorized as a way to control the ^{229m}Th population [66].

1.2.4 Optical spectroscopy of the nuclear transition in crystals

While the IC channel dominates the decay of ^{229m}Th in neutral atoms, it has been proposed that the IC decay channel would be suppressed if ^{229}Th was doped in a crystal with a sufficiently high band gap [47]. Crystal materials of high bandgap, such as $LiSrAlF_6$ [67] and CaF_2 [68], are therefore proposed and grown, with high transparency at the VUV wavelength corresponding to the predicted ^{229m}Th nuclear transition energy. However, with the weak transition signal and large energy uncertainty, many pilot spectroscopy studies yielded null results [69, 70, 71], raising questions in the community whether the IC channel is sufficiently suppressed for the observation of radiative decay photons.

A different approach is to populate the ^{229m}Th state via nuclear decay and search for fluorescent photons. Using ^{233}U decay and buffer gas stopping cell, the implantation of ^{229m}Th into a MgF_2 coated metal plate was performed and the search for nuclear radiative decay was attempted at the Ludwig Maximilian University of Munich (LMU). However, no signal was observed despite the high estimated signal-to-noise ratio [22]. Therefore, it was suspected that unknown quenching mechanisms may possibly occur even in large bandgap materials, possibly due to surface effects

caused by insufficient ion-implantation depth or defect states caused by the ^{229m}Th doping or implantation process.

^{229}Ac has a short half-life of 62.7 min and a high branching ratio $\geq 14\%$ [72] to the ^{229m}Th state. Thus, it was also proposed to use ^{229}Ac to populate ^{229m}Th [72]. The production of ^{229}Ac, the ion implantation into CaF_2 and MgF_2 crystals, and the subsequent direct observation of fluorescent photons were achieved at the Isotope mass Separator On-Line facility (ISOLDE) at the European Organization for Nuclear Research (CERN). The fluorescence photon wavelength was measured using a grating-based VUV spectrometer to be $148.71 \pm 0.06(\text{stat.}) \pm 0.41(\text{syst.})$ nm, corresponding to a measured energy of $8.338 \pm 0.003(\text{stat.}) \pm 0.023(\text{syst.})$ eV [25]. This measurement also reported that the half-life of ^{229m}Th in MgF_2 crystals to be 670(102) s, and proved for the first time that the IC decay channel of ^{229m}Th can be largely suppressed for radiative photon detection in suitable crystals. Recently, a follow-up experiment reported a similar radiative decay fraction in $LiSrAlF_6$ using the ISOLDE beamline, but no signal was observed in a-SiO_2 or AlN substrates due to their smaller band gaps [73].

This observation of the radiative decay signal at ISOLDE [25] in contrast to the failed attempt using the ^{233}U decay [22] may come from several differences in the experimental conditions. The implantation is performed at a 30 keV kinetic energy of the ions [25] instead of a few keV [22], leading to a deeper implantation depth. The crystalline substrates used create a better controlled environment for the ^{229m}Th compared to the likely amorphous coating layers [22]. It is unclear whether directly implanting the ^{229m}Th isomer [22] versus implanting the mother isotope and waiting for the β decay may also make a difference in quenching the nuclear radiative decay.

The observation of the radiative decay signal from ^{229m}Th convinced us to focus our search effort on photon-based detection and provided important parameters for other crystal-based ^{229m}Th experiments. Meanwhile, a four-wave mixing nanosecond pulsed laser built at the University of California, Los Angeles (UCLA), using a two-photon transition in Xe for enhanced nonlinearity [70], was used for the ^{229}Th nuclear transition search [70, 74]. A similar laser system was built in the Physikalisch-Technische Bundesanstalt (PTB) [75]. Using these broadband laser systems,

direct laser excitation was reported first in ^{229}Th-doped CaF_2 crystals [27] at PTB and then in ^{229}Th-doped $LiSrAlF_6$ crystals [28] at UCLA. These measurements further pinned down the ^{229m}Th transition wavelength to be 148.3821(5) nm and $148.38219(4)_{\text{stat.}}(20)_{\text{syst.}}$ nm, respectively. The reported excitation rates and the ^{229m}Th lifetime served as useful guides for our experiments reported in this thesis. Soon after these studies, the observation of the ^{229}Th nuclear transition in a $^{229}ThF_4$ thin film fabricated in this thesis work was achieved in our collaborator's lab in UCLA [76], with a wavelength consistent with that reported in Refs. [27, 28].

In our lab at JILA, we focused on the frequency metrology of the nuclear clock and excited the nuclear isomer using a narrow linewidth frequency comb. The transition frequency is read out directly using our VUV frequency comb stabilized to the JILA ^{87}Sr optical clock [24]. This measurement reduces the uncertainty of the nuclear clock transition frequency by six orders of magnitude and represents the first direct frequency connection between a nuclear and an atomic clock. With the quantum states of ^{229}Th resolved in the crystal environment, the systematic uncertainties of the nuclear clock can finally be experimentally characterized in a state-dependent way [77]. In Fig. 1.2, we summarize the historical measurements of the ^{229m}Th nuclear transition energy.

1.3 ^{229}Th material availability

Due to the relatively short half-life of 7917 years [80], ^{229}Th is not a naturally abundant isotope and must be created by nuclear reactions. In addition to the aforementioned α-decay of ^{233}U and β-decay of ^{229}Ac, other processes such as the electron capture decay of ^{229}Pa and the neutron capture of ^{228}Th also produce ^{229}Th. However, most of the existing ^{229}Th stock was produced by ^{233}U α-decay. During the Cold War, about 1 metric tonne ^{233}U was produced in nuclear reactors for its potential use as a weapon material [81]. Using the nuclear decay rate of ^{233}U that produces ^{229}Th, it is estimated that there are about 40 grams of ^{229}Th with sufficiently high isotope purity for building nuclear clocks [81, 20]. Most of them are still mixed with the ^{233}U stock, and need to be chemically extracted.

Figure 1.2: Measurements of the ^{229m}Th energy and the corresponding uncertainty. Differences between energies of previous measurements from the result reported in this thesis work [24] are plotted in logarithmic scale for clarity. Values taken from Kroger 1976 [38], Akovali 1989 [78], Reich 1990 [79], Reich 1993[39], Helmer 1994 [40], Guimaraes 2005 [41], Beck 2007 [42], Beck 2009 [43], vdWense 2016 [59], Seifele 2019 [62], Masuda 2019 [64], Yamaguchi 2019 [44], Sikosky 2020 [45], Kraemer 2023 [25], Tiedau 2024 [27], Elwell 2024 [28], and Zhang 2024 [24]. See Ref. [18] for a summary before the recent optical spectroscopy experiments.

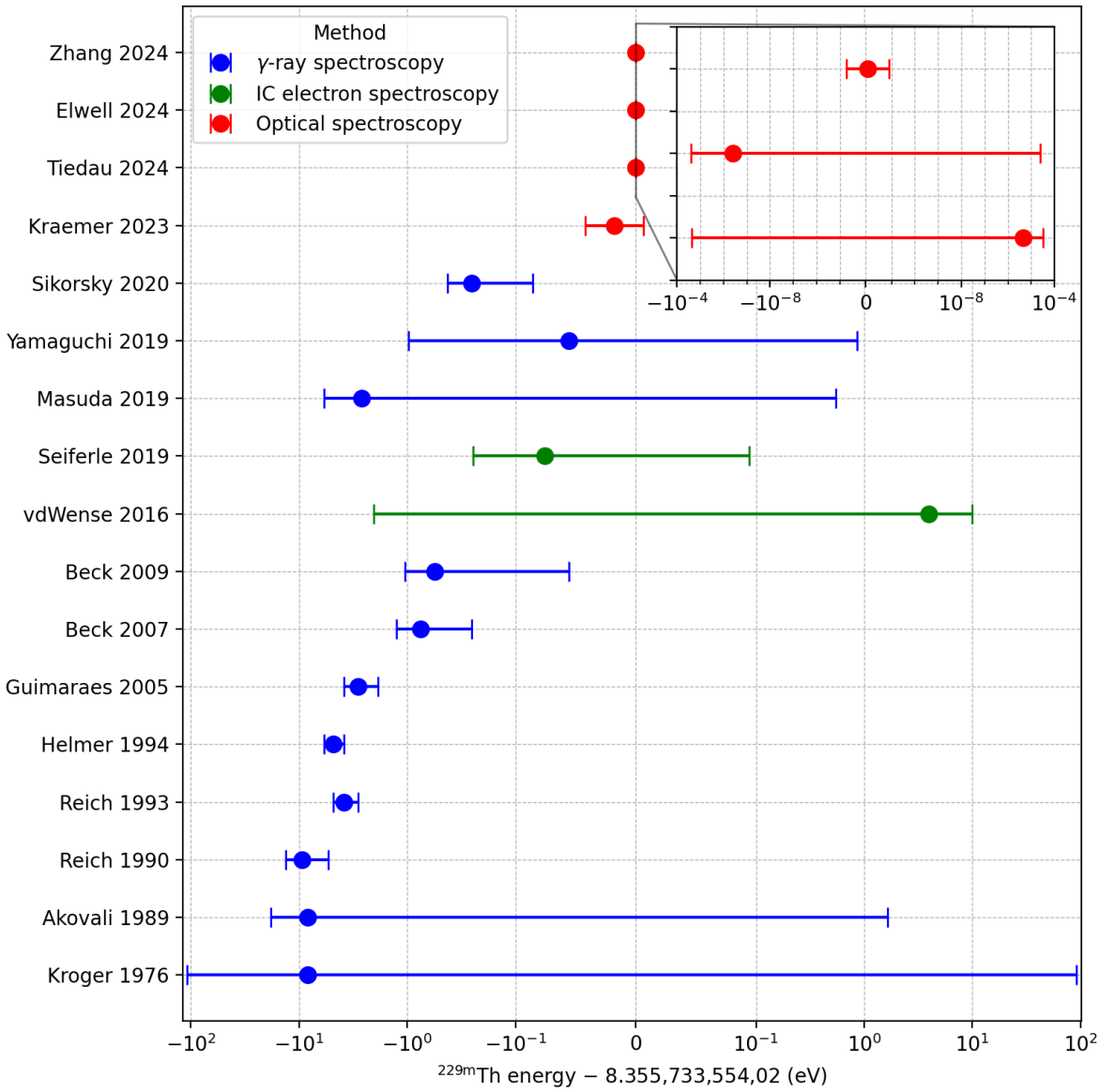

The ^{229}Th isotope used in this thesis work was primarily purchased from Oak Ridge National Laboratory (ORNL) through the National Isotope Development Center (NIDC) [82]. We also purchased two electro-deposited targets of ^{229}Th fabricated by Eckert & Ziegler [83], whose ^{229}Th material was also produced in ORNL. We are also grateful for test material chemically extracted from ^{233}U at the Johannes Gutenberg University Mainz by the Düllmann group [84].

^{229}Th is also widely used to produce ^{225}Ac, an important isotope for medical treatments of cancer [85]. ORNL recently partnered with private companies, Isotek and Terrapower, to extract ^{229}Th for medical use while safely disposing of the ^{233}U stockpile [86]. Another possible route for ^{229}Th production is nuclear transmutation with thermal neutrons from nuclear reactors [87, 88, 89]. A yield of 74 ± 7.4 MBq per gram of ^{226}Ra was demonstrated [88]. One challenge is that the neutron transmutation process typically also generates other Th isotopes. Thus, isotope purification is needed if pure ^{229}Th is desired. Production and separation of ^{229}Th in accelerator facilities such as ISOLDE, TRIUMF, and FRIB are also possible, albeit with a relatively small material yield due to the limited proton beam intensity.

Chapter 2

Frequency combs in the extreme ultraviolet (XUV)

A key enabling technology for the high-resolution spectroscopy of ^{229m}Th is coherent narrow-linewidth laser light sources in the vacuum ultraviolet (VUV). In this thesis work, we used a home-developed VUV frequency comb [90]. Here, we briefly review the vacuum and extreme ultraviolet (XUV) comb [15, 16, 17] technology and describe our VUV comb apparatus.

2.1 Frequency combs

The combination of ultrashort laser pulses with high peak intensity (suitable for nonlinear optics) and narrow laser linewidth (required for precision spectroscopy) seems fundamentally conflicting at first sight, limited by the Fourier transform.[1] However, by stacking many phase-coherent pulses in the time domain, the frequency-domain spectrum can become discretized peaks, forming a comb-like structure [91]. The repetition rate in the time domain of the pulse train, f_{rep}, corresponds directly to the frequency domain spacing between the adjacent comb lines; see Fig. 2.1. Such a pulse train can be generated in several ways, including mode-locked oscillators [92], electro-optical modulation [93] of continuous wave (CW) lasers, or soliton dynamics in optical resonators [94].

To fully control the optical phase of a frequency comb, measurement and stabilization of pulse-to-pulse phase slip $\Delta\phi$, shown in Fig. 2.1, are also required. As a pulse train is produced, say, in a mode-locked laser, the group velocity and phase velocity mismatch leads to a carrier-envelope

[1] In a scholarship interview at my college, I was asked if a laser like this can be built. After just learning the uncertainty principle in quantum mechanics, I said: "Of course not!" Luckily, I joined JILA and had the chance to work on exactly this magical laser system.

phase slip $\Delta\phi$ between adjacent pulses. In the frequency domain, this corresponds to an overall shift of the comb modes by

$$f_{\text{ceo}} = \frac{\Delta\phi}{2\pi} \times f_{\text{rep}}. \tag{2.1}$$

If the f_{ceo} can be determined and controlled, the optical frequency of each individual comb line shown in Fig. 2.1 can be described by a simple equation directly connecting optical frequencies ν_N to microwave frequencies f_{rep} and f_{ceo} as

$$\nu_N = f_{\text{ceo}} + N \times f_{\text{rep}}, \tag{2.2}$$

where N is an integer number assigned to each individual comb mode. This relationship in a frequency comb enables us to count optical frequencies using microwave electronics [95, 96].

To measure the comb f_{ceo}, we consider how f_{ceo} changes in two different nonlinear frequency generation processes.

(1) Supercontinuum generation via cascaded four-wave mixing. This is a third order process that is described by the following frequency relation:

$$2 \times \nu_N = \nu_{N-1} + \nu_{N+1}. \tag{2.3}$$

One can easily see that such a process can be cascaded to spread the power of the comb from its spectral center to wings, leading to a broadening of the spectrum. This process governs the supercontinuum generation in, for example, microstructured fibers [97]. The f_{ceo} of the comb does not change in supercontinuum generation, and one obtains

$$\nu_{\text{supercontinuum}} = \nu_{2N} = f_{\text{ceo}} + 2N f_{\text{frep}}. \tag{2.4}$$

(2) Harmonic generation. Take frequency doubling (second harmonic generation) as an example, the doubled light has an optical frequency of

$$\nu_{\text{doubling}} = 2\nu_N = 2 \times f_{\text{ceo}} + 2N \times f_{\text{rep}}. \tag{2.5}$$

Here, the f_{ceo} of the light is doubled as well.

It is therefore straightforward to use a single frequency comb, design the supercontinuum generation and frequency doubling conditions to reach the same optical frequency range with both processes, and then extract the f_{ceo} signal as [98]

$$f_{\text{ceo}} = \nu_{\text{doubling}} - \nu_{\text{supercontinuum}} \tag{2.6}$$

as the frequency difference between the doubled light and the supercontinuum light using an optical heterodyne measurement.

2.2 XUV frequency comb via cavity-enhanced high harmonic generation

Frequency combs in the infrared and visible wavelengths have enabled numerous applications in precision measurement and sensing [95, 96, 99]. Here, we take advantage of the high peak intensity of femtosecond laser pulses in a comb. This high peak intensity allows efficient nonlinear generation of the extreme ultraviolet (XUV) light via the high-order harmonic generation (HHG) process [100, 101, 102]. The mechanism of HHG and the attosecond physics involved in this process are beyond the scope of this thesis. Interested readers are referred to a few books, review articles, and dissertation theses, see Refs. [103, 104, 105, 106, 107].

To perform HHG (requiring a high peak intensity of $\sim 10^{13}$ W/cm^2) with a frequency comb (requiring a high repetition rate of $\sim$ 100 MHz), a high average power on the order of a few kW is typically required [17]. Optical enhancement cavities are used to boost the average power of the fundamental comb [15, 16] to reach this high average power level. HHG in inert gas targets is typically a low-efficiency process which leaves the fundamental light largely unperturbed, thus an optical enhancement cavity can be used to "recycle" the fundamental pulse after interaction with the HHG medium. Femtosecond enhancement cavities (fsECs) [108, 109] are developed for coherently enhancing the power of femtosecond pulses. The upconverted frequency comb in the XUV via cavity-enhanced HHG uniquely combines high photon energy, high repetition rate, and high phase coherence. Thus, it is an ideal tool for both precision frequency metrology and attosecond time-resolved dynamics studies [17]. The construction and operation of XUV combs are discussed in

Figure 2.1: Time and frequency domain of description of a frequency comb. In the time domain, it is a phase coherent pulse train with a repetition rate $f_{\text{rep}} = 1/\Delta t$, where Δt is the separation between two adjacent pulses. The phase between adjacent pulses changes by $\Delta\phi$ (modulo 2π). In the frequency domain, this corresponds to a comb structure with a separation of f_{rep} between adjacent comb modes and a common shift of f_{ceo} from zero frequency. Figure adapted from Ref. [98].

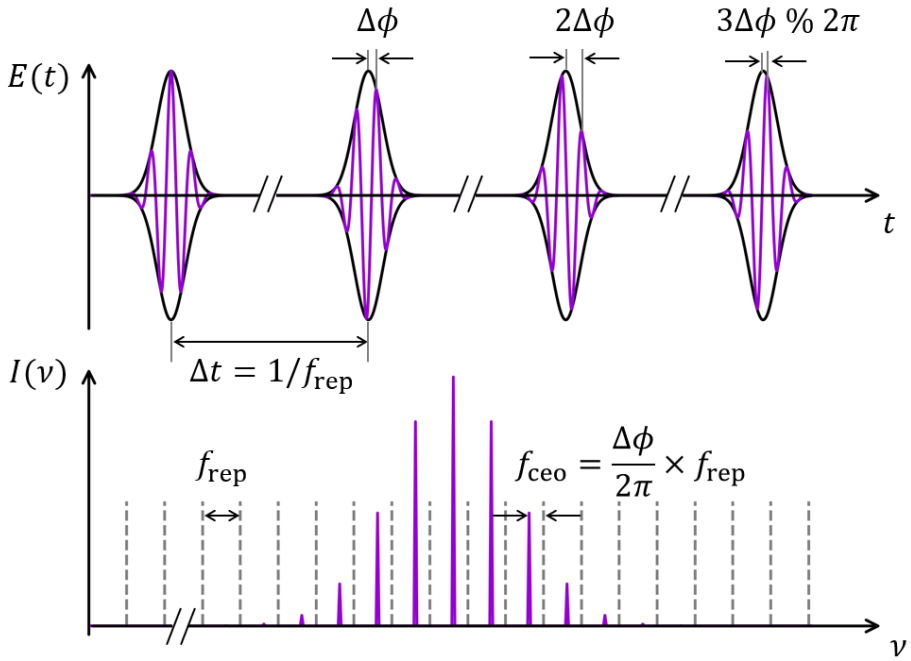

detail in Refs. [106, 107]. In this section, we provide a brief review of this field following Ref. [17].

2.2.1 Linear response of a femtosecond enhancement cavity (fsEC)

A typical XUV comb generation setup using cavity-enhanced HHG in an fsEC is illustrated in Fig. 2.2. A frequency comb (visualized as a pulse train, Fig. 2.2a) is coupled to a free-space, passive optical resonator [108, 109]. A traveling wave ring resonator is used to ensure unidirectional output of the generated XUV comb and enable separate control of the focal spot size and the cavity length. The resonator is designed to fulfill the stability criterion [110], ensuring a low diffraction loss for the intracavity fundamental light with well-defined transverse eigenmodes. Spatial mode matching is ensured by shaping the input laser beam to match the intracavity beam shape, using a suitable telescope lens system designed with ABCD matrix calculations [110].

The corresponding frequency-domain comb structure is illustrated in Figs. 2.2b and c. The resonance condition for optimal power enhancement requires that both the repetition frequency and the carrier-envelope offset of the pulses traveling in the fsEC to be matched to the corresponding parameters of the input comb. In the frequency domain, this condition is equivalent to optimizing the overlap of the input comb modes with the longitudinal modes of the fsEC. This resonance condition is typically ensured using the Pound-Drever-Hall cavity stabilization scheme [111]. Ignoring nonlinear optical effects and considering the fsEC as a linear system [1], the (field) transfer function $H(\nu)$ of the cavity reads [108, 110]:

$$H(\nu) = \frac{\sqrt{T(\nu)}}{1 - \sqrt{R(\nu)A(\nu)}\mathrm{e}^{i\phi_{\mathrm{roundtrip}}(\nu)}}, \tag{2.7}$$

where $R(\nu)$, $T(\nu)$ are the input coupler (power) reflection and transmission fraction, respectively, and $1 - A(\nu)$ is the cavity roundtrip (power) attenuation excluding the input coupler reflectivity, $\phi_{\mathrm{roundtrip}}(\nu)$ is the optical phase gained per roundtrip for the laser light at frequency ν, modulo 2π.

The frequency-dependent power enhancement $|H(\nu)|^2$ exhibits a comb-like structure with sharp Lorentzian resonances (Fig. 2.2 c) which are the cavity longitudinal modes. In contrast to a frequency comb, the chromatic dispersion in the cavity [112] leads to deviations from strictly

equidistant spacings of the cavity modes. The mismatch between the cavity and the comb causes a spectral filtering effect, limiting the bandwidth that can be enhanced simultaneously and, therefore, the pulse duration achievable in the fsEC. This effect becomes more noticeable for higher resonator finesse

$$\mathcal{F}(\nu) \approx \frac{2\pi}{1 - R(\nu)A(\nu)}, \tag{2.8}$$

which corresponds to narrower cavity resonances. It is easy to see that an over-coupled cavity, where $T(\nu) \gg [1 - A(\nu)]$, offers the highest cavity buildup for a given cavity finesse.

Today, typical fsEC-HHG systems use high-power ytterbium (Yb) fiber-based frequency combs [113, 114] as their seed. The average output powers of these Yb lasers are on the order of 100 W and pulse durations are in the 100 to 250 fs range, with a spectrum centered around 1050 nm. The high seeding power requires only moderate cavity finesse ($\sim$ a few hundred) to reach the power needed for HHG, which relaxes the limits of the spectral bandwidth. With proper mirror and cavity designs, thermal distortion of the cavity can be reduced to a negligible level for a typical fsEC operating at average power levels of $\sim$ 10 kW.

While the pulse duration of Yb-based systems are relatively long due to the small gain bandwith in Yb-doped fibers, post-broadening and compression in nonlinear medium can be employed to increase the bandwidth and compress the pulse duration to even a few cycles [115]. At high repetition rate and with high average power, post-compression in multi-pass cells are typically used [116, 117]. Recently, a high-power frequency comb based on crystal amplifiers at Yb wavelengths with ultra-low phase noise has been demonstrated [118]. There, the even more limiting bandwidth ($\sim$ 1 nm) in Yb-doped crystal amplifiers is also mitigated with post-broadening and compression in multi-pass cells.

2.2.2 Nonlinear optics inside a fsEC

By introducing a gas target (typically a supersonic expansion jet [119] of rare gases) to the focus of the cavity, HHG is performed inside the fsEC. The generated XUV light forms a train of attosecond pulses, one per half-cycle of the fundamental [101, 102]. The phase of the attosecond

Figure 2.2: a, A seeding (typically infrared) pulse train with the electric field E_{IR}, a pulse repetition period $\Delta t = 1/f_{\mathrm{rep}}$ and a pulse-to-pulse carrier-envelope offset phase slip $\Delta\phi = 2\pi f_{\mathrm{ceo}}/f_{\mathrm{rep}}$, is coupled to a passive resonator containing a gas target at the cavity focus. IC, partially transmitting input coupling mirror; HR, highly reflective mirror; FM, curved focusing HR. b, Frequency domain representation of the spectra $\left|\tilde{A}\right|$ of a frequency comb centered at frequency ν_{c}. c, Comb modes, and the power enhancement factor $|H|^2$ (gray) of the enhancement cavity, assuming a linear cavity response, H being the transfer function of the optical cavity. Due to dispersion of the cavity mirrors and medium inside the cavity, the roundtrip phase $\phi_{\mathrm{roundtrip}}$ (dotted blue, referring to the vertical axis) is not a linear function of optical frequency ν. The power enhancement factor $|H|^2$ drops to half of its peak value if the round-trip phase $\phi_{\mathrm{roundtrip}}$ deviates from a linear phase (red) by $\pi/\mathcal{F}(\nu)$ (orange corridor, see inset). d, Temporal illustration of the XUV pulse train, represented by the squared magnitude of its temporal envelope $|E_{\mathrm{XUV}}|^2$, emerging via HHG from the fundamental driving laser electric field of E_{IR}. Each half-cycle of the driving field emits an XUV pulse, phase locked to the driving field with a time lag corresponding to the electron excursion time [101, 102]. The XUV pulse intensity depends nonlinearly on the driving field amplitude. e, Generated XUV spectrum P_{XUV} (top) consisting of individual harmonics that emerges via the interference of the XUV pulses with in the attosecond pulse train with a period corresponding to half a period of the driving laser, see panel d. The substructure of a harmonic (bottom) consists of an XUV frequency comb with the same repetition rate f_{rep} as the fundamental, and an offset frequency equal to $q\times f_{\mathrm{ceo}}$ modulo f_{rep}, where q is the (odd) harmonic order. Figure taken from Ref. [17].

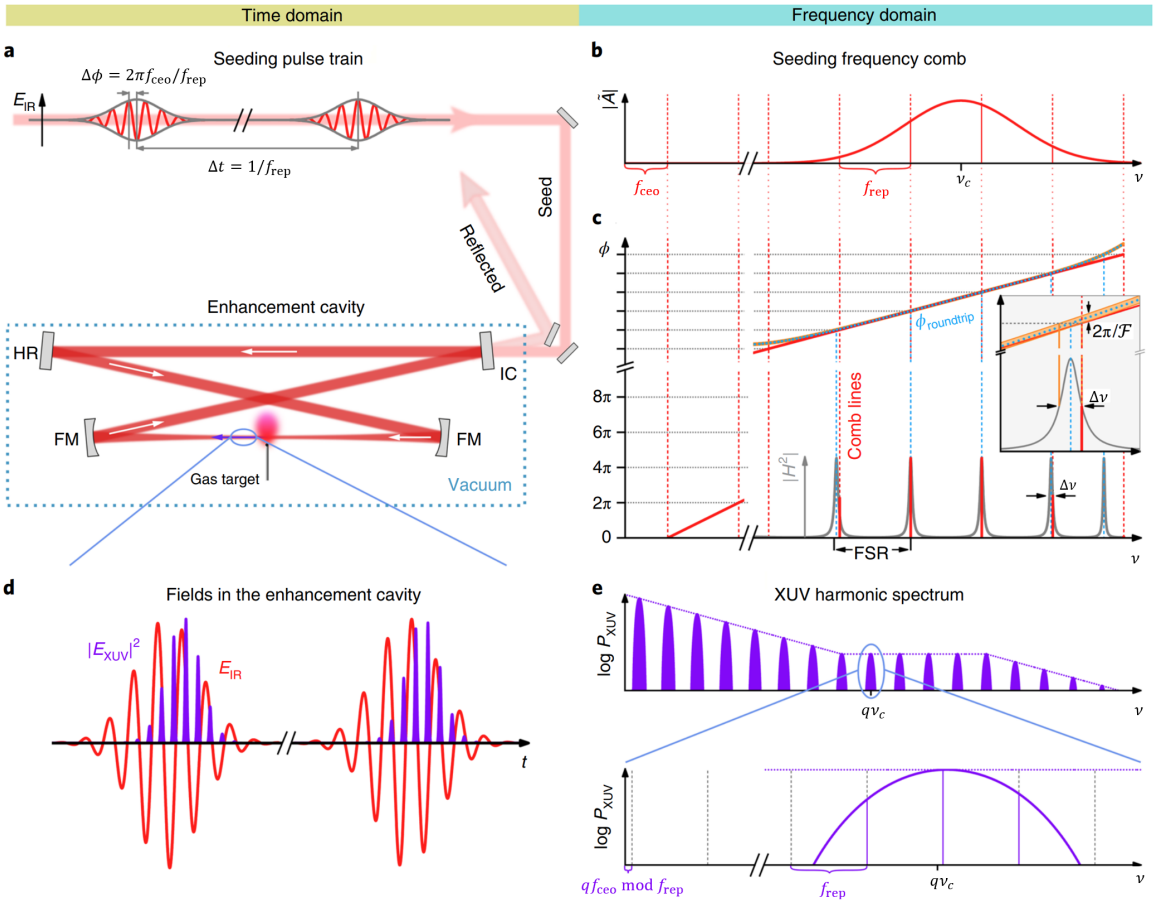

pulses is locked to that of the driving laser, ensuring the phase coherence of the XUV comb. The temporal interference of the XUV attosecond pulse train gives rise to a spectrum consisting of odd-order harmonics of the driving spectrum, extending over several tens of harmonic orders; see Fig. 2.2e top panel. Each harmonic order consists of a frequency comb with a repetition rate equal to the original comb f_{rep} and an offset frequency of $q \times f\mathrm{ceo}$, q being the harmonic order.

At the high repetition rate for HHG enabled by fsECs, each atom of the gas target typically experiences multiple laser pulses when traveling through the HHG volume; see Fig. 2.3a. This leads to the formation of a cumulative plasma in the generation volume that hurts the phase matching and considerably reduces the conversion efficiency. Plasma buildup also introduces an optical bistability that complicates cavity stabilization [120, 106, 121], see Fig. 2.3b. We define the conversion efficiency as the produced XUV power divided by the circulating power of the driving laser. Typically, a conversion efficiency below 10^{-6} is obtained in cavity-enhanced HHG inside fsECs. By accelerating the gas via heating or using gas mixtures with lower average molecular weight [122] or lowering the cavity repetition rate [123], HHG with conversion efficiencies comparable to those of single-pass experiments have been demonstrated, at repetition rates on the order of tens of megahertz.

The rapid ionization of the gas medium within the duration of a single laser pulse also introduces a dynamical plasma effect, causing a rapidly changing refractive index and thus spatial and spectral distortions; see Fig. 2.3c, d. Inside the enhancement cavities, this effect reduces the spatial and spectral mode matching between the driving and circulating fields, causing an intensity-clamping effect; see Fig. 2.3e. Quantitative modeling enables the optimization of the experimental parameters to mitigate this effect and obtain a high conversion efficiency in fsECs [121, 124].

2.2.3 XUV Outcoupling methods

A technical challenge is to separate the generated XUV comb from the fundamental beam without disrupting the cavity operation [125, 126]. The first systems employed a thin plate, placed under Brewster's angle for the fundamental wavelength after the HHG focus. Using p-polarized

Figure 2.3: Plasma effects in cavity-enhanced HHG. a, The gaseous generation medium goes through a supersonic jet expansion after existing the nozzle and traverses the interaction region given by the ionization profile σ_{ion}. The terminal velocity [119] is given by $v(x) = \sqrt{5R_{\text{g}}T_{\text{g}}/M_{\text{avg}}}$, where R_{g} is the gas constant, T_{g} is the reservoir temperature and M_{avg} is the average molar mass. The ionization fraction depends on the driving pulse intensity $I(x)$. b, When the detuning between the frequency-comb lines and the cavity resonances is scanned towards higher frequencies, for example, by decreasing the cavity length, the intracavity power considering the plasma effect (blue, theory and red, experiment) reaches its maximum at a different position than without plasma (gray). This is caused dominantly by the build-up of a cumulative plasma. Near the cavity resonance, there are two steady-state solutions of the intracavity power depending on the plasma density [106, 121]. To achieve stable operation of the cavity, the lock point of the detuning (green) must be set slightly below the maximum, after witch the high- and low-power branches unite. Panel adapted from [121] c, The electric field of an intense pulse before (black) and after (blue) passing through an ionizing medium, leading to a temporal compression due to the time-dependent plasma refractive index. d, In the frequency domain, the time compression leads to a spectral blue shift, reducing the spectral overlap with the seeding pulses. PSD, optical power spectral density. e, As a consequence, the intracavity power shows a saturation behavior when the seeding power is increased, refereed to as intensity clamping. Panel taken from Ref. [124]. Figure taken from Ref. [17].

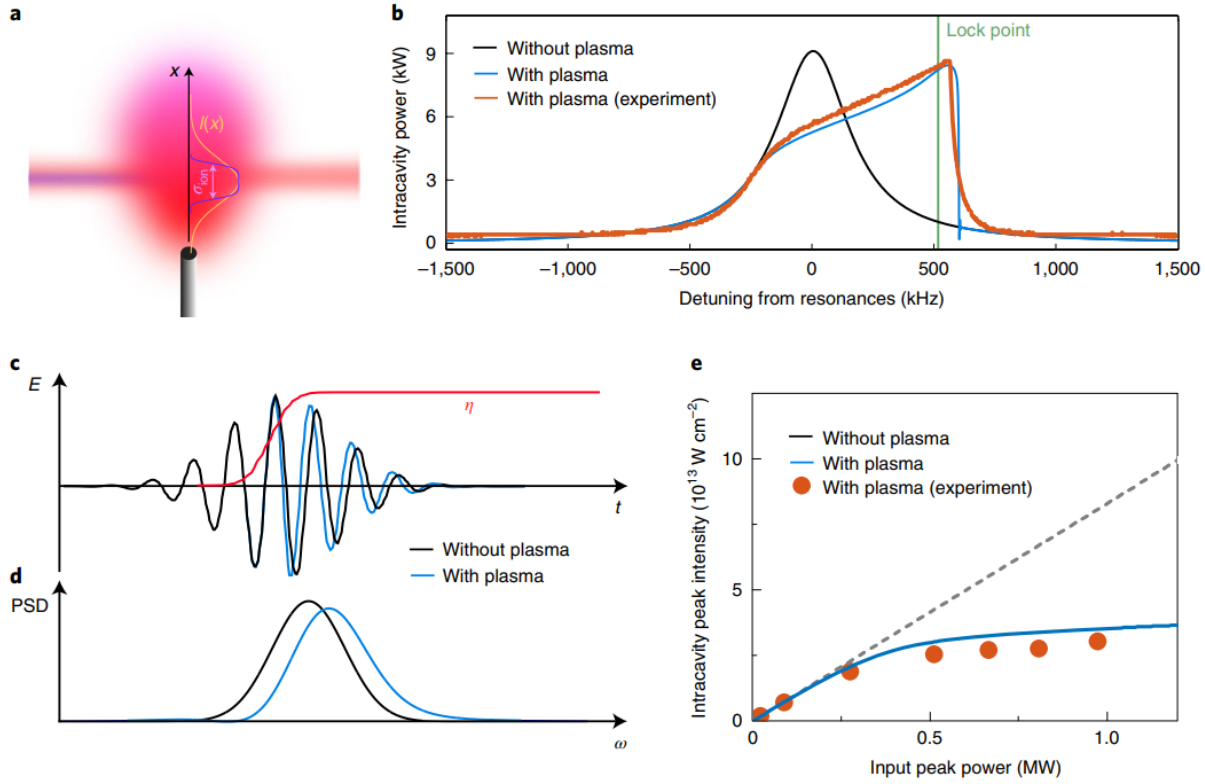

light, the cavity loss of the fundamental beam is kept low, while a small fraction of the XUV beam is coupled out from the cavity, see Fig. 2.4a. With adequately thin plates, excessive dispersion, Kerr nonlinearity, and thermal lensing can be avoided at typical cavity finesse values. This method has been applied for XUV photon energies up to 42 eV [127] and typically provides 5-15% of outcoupling efficiency. Higher outcoupling efficiencies are demonstrated by applying high-reflection coatings for VUV wavelengths to the Brewster plate [128, 129]. However, these coatings typically introduce more rapid degradation effects. In our lab, we tried out a few different Brewster plate materials with/without coatings for the outcoupling of ~ 148 nm VUV light for ^{229}Th spectroscopy. These are:

(1) Sapphire (Al_3O_2) plate ($\sim 175\,\mu$m thick) from University Wafer, uncoated. The plate withstands the cavity-enhanced HHG process. However, the Fresnel reflection of sapphire at 148 nm (desired for ^{229}Th clock) is calculated to be $< 1\%$ from its refractive index [130]. Unfortunately, typical VUV reflection-enhancing coatings cannot be applied to sapphire due to thermal expansion coefficient mismatches.

(2) Crystalline quartz plate ($\sim 350\,\mu$m thick) from University Wafer, uncoated. Strong second-order harmonic generation is observed. Intracavity power is limited to a few kW maximum.

(3) SiC plates ($\sim 350\,\mu$m thick) from University Wafer, uncoated. We are interested in SiC because of its high absorption at 148 nm, which leads to a relatively high Fresnel reflectivity [130]. However, high absorption for the fundamental light and strong thermal lensing is observed, significantly reducing the intracavity power.

(4) Diamond ($\sim 100\,\mu$m thick) from Applied Diamond, uncoated. We are also interested in diamond because of its high attenuation at 148 nm as well as its high thermal conductivity that reduces the thermal lensing effect. Unfortunately, polycrystalline diamond plates do not offer enough surface roughness to support the cavity operation. Another concern is that, although diamond has superior thermal conductivity, making it suitable for handling

high-power continuous-wave lasers [131], its damage threshold using femtosecond lasers with high peak power is relatively low, due to its relatively low bandgap. That is also why femtosecond lasers are often used for diamond machining.

(5) MgO from MTI Coorparation, uncoated. The acquired MgO substrate has high absorption at the fundamental wavelength (1040 nm) and causes obvious thermal lensing. MgO substrates and coatings from OptoSigma [129] are known to offer less absorption, but have not been tested in this work.

(6) CaF_2 plates of 150 µm to 500 µm thickness from Crystran, coated at Layertec for enhanced reflectivity at 148 nm. Although there are concerns about the surface quality and flatness of CaF_2 substrates, the ones we acquired offer a sufficiently low loss to support the cavity mode, even after the VUV reflection-enhancing coating. The coated plates are also thermally stable at high intracavity IR power without running the gas jet for HHG. However, as soon as the HHG operation starts, the plates are damaged by UV light and show a drastically increased IR absorption. The 500 µm plates typically absorb enough IR light to interrupt the HHG in a few minutes. The 150 µm plates typically allow for higher intracavity IR power and higher harmonic yield. However, when the HHG gas jet is turned on, the thermal shock leads to snapping of the CaF_2 plate within one second. We tried protecting the coating from high-energy photons by facing the VUV beam using the uncoated side or adding a second Al_3O_2 Brewster plate in front of the CaF_2 plate. However, these methods do not seem to solve the rapid degradation problem.

Another mature method typically employed for frequency domain application where angular dispersion of the harmonics is desirable is to use a reflective XUV diffraction grating (Fig. 2.2b) etched into the top layer of a highly reflective cavity mirror [132]. Outcoupling efficiencies up to 10% in the photon energy range below 20 eV have been demonstrated [132]. In our experiment, this method is deemed undesirable due to the low efficiency. Also, spatial dispersion within a single harmonic order would limit our ability to focus down the beam tightly for the IC clock operation

described in Chap. 3.

In this thesis work, a grazing-angle incidence plate outcoupler (GIP, Fig. 2.4c) and a geometric outcoupling method using noncollinear beams (Fig. 2.4d) are explored. We discuss them in detail in the following sections.

2.3 A grazing-angle incidence plate outcoupler

A major downside of the aforementioned methods is the low outcoupling efficiency. It has been proposed that a grazing angle incidence plate (GIP) can be used to replace the Brewster plate [133] for higher efficiency and broadband operation. Using s-polarized light in the fsEC, an antireflective coating has to be applied for both surfaces of the plate to reduce the loss of intracavity IR light (see Fig. 2.4c). The Fresnel reflection of s-polarized light at large grazing incidence angles can typically reach beyond 50%. Recently, a GIP has been used in the outcoupling of XUV light from HHG inside a laser oscillator [134], where the loss of GIP can be partially compensated for by the gain medium.

In our experiment, we employ a similar GIP in the passive fsEC for conducting the spectroscopy experiments described in Chap. 3 and Chap. 4, see Fig. 2.4c and Fig. 2.5. A 175 µm thick sapphire plate (University Wafer) was anti-reflection coated at LaserOptik[2] to reduce the IR loss for s-polarized light at 1040 nm wavelength (targeted reflectivity $< 0.3\%$ per surface). The top layer coating is chosen to be Ta_2O_5, whose reflectivity for s-polarized light at 148 nm is expected to be $\sim 50\%$, see Fig. 2.5b. Large 100 mm diameter sapphire wafers are diced up to 15 mm square pieces at the JILA Keck Lab after IBS coating at LaserOptik.[3] We applied two small dots of Torr Seal[4] low vapor pressure epoxy to glue the plates onto an aluminum mount. The fsEC with the sapphire GIP is thermally stable and shows no sign of degradation for hours of operation with only IR light (no HHG gas medium).

[2] Coating design B-19293, AR1025-1055 nm, 70° s-polarized light on sapphire, IBS coating

[3] We used diamond blade model 2.25M-4A-30RU7-3 (Thermocarbon Inc,), with 0.5 mm/s cutting speed, 0.05 mm cut increment and 15000 RPM spindle speed.

[4] We cure the Torr Seal at room temperature for 12 hours to avoid stress induced by high-temperature curing. The aluminum mount can be reused as the Torr Seal can be easily removed by either heating to above 120 °C or cooling to liquid nitrogen temperature.

Figure 2.4: XUV outcoupling methods. Typical efficiencies ε and maximum demonstrated photon energies $E_{\max}$ are listed. (a) A thin, transparent plate placed at Brewster's angle in the fundamental beam reflects a fraction of the collinearly propagating XUV beam while allowing p-polarized fundamental to pass with low loss. Additional coatings can be applied to enhance the XUV reflectivity at low photon energies. (b) A reflective XUV diffraction grating etched into the top layer of a highly reflective mirror for the fundamental beam, angularly disperses the individual harmonic orders. (c) A thin plate is placed at a large grazing-incidence angle in the cavity. The plate is anti-reflection coated for s-polarized fundamental beam. The generated harmonics are reflected off the first layer of the coating. (d) Nocollinear HHG using two circulating pulses in the fundamental mode, intersecting at a common focal region to generate harmonics at the bisector angle. Figure adapted from Ref. [17].

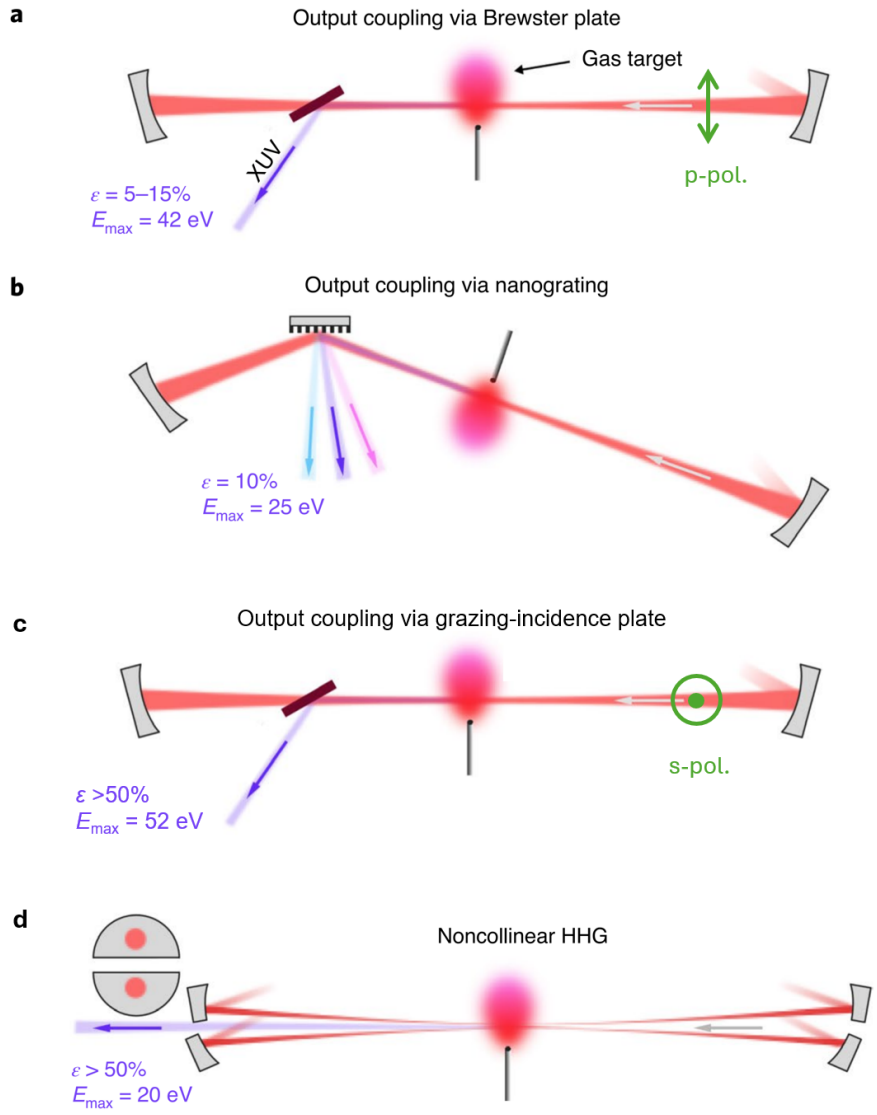

A photo of the HHG operation using this GIP is shown in Fig. 2.5a. The Xe gas jet is seen as the bright white plasma (bottom right). The generated XUV light ionizes residual gas ($\sim$ 1 mtorr O_2) inside the vacuum chamber, leaving a white/green trace visible to the naked eye. The GIP is mounted on a multiaxis stage. The angular rotation of the GIP is adjusted to optimize for small intracavity loss (high buildup power). The height of the plate is controlled with a motorized stage. When HHG is in operation, the loss of the plate increases over time scales of a few hours, reducing the intracavity power and suppressing the HHG efficiency. To facilitate the long scans required for the nuclear spectroscopy, this translation stage is used to move the plate in its plane vertically once every few hours.

2.4 A noncollinear cavity for efficient XUV comb outcoupling

In addition to separating the harmonics using reflective or dispersive optics, geometrical methods have been explored to outcouple the harmonics from the fsEC. As harmonic beams with shorter wavelengths have smaller divergences than the fundamental beam, a simple pierced mirror could suffice for outcoupling harmonics with high photon energies [125, 135]. Tailoring the mode inside the optical cavity offers increased outcoupling efficiency and reduced loss [136, 137]. To this end, we explored an outcoupling method using intracavity noncollinear HHG for high outcoupling efficiencies at high photon energies. Although this method is not used for ^{229}Th spectroscopy, it is of general interest for XUV combs. Discussions about other geometrical outcoupling methods, including quasi-imaging [136] and transverse mode gating [137], can be found in Ref. [17] and references therein.

Here, we follow our own work published in Ref. [138] and present a detailed study of a noncollinear enhancement cavity for efficient outcoupling of XUV combs generated by intra-cavity HHG. Early proposals for the noncollinear cavity can be found in Ref. [125, 139, 140]. Using two crossing beams, the generated harmonics are naturally separated from the fundamental at the bisection angle and can thus be coupled out from the cavity geometrically, while the fundamental is efficiently recycled to maintain a high cavity buildup.

Figure 2.5: A grazing incidence plate (GIP) outcoupler. a, Photo of intracavity HHG in operation with a GIP. The white/green trace is caused by VUV ionization of the oxygen ($\sim$ 1 mtorr) inside the vacuum chamber. b, Calculated Fresnel reflection coefficients on the tantalum oxide top layer [130]. Vertical dashed lines indicates the the harmonic orders of the fundamental light. Dashed part of the black line indicates that tantalum oxide is transparent in the spectral region, thus the multilayer coating effect cannot be ignored and the predicted reflectivity there (1st and 3rd order harmonic of the fundamental) is invalid.

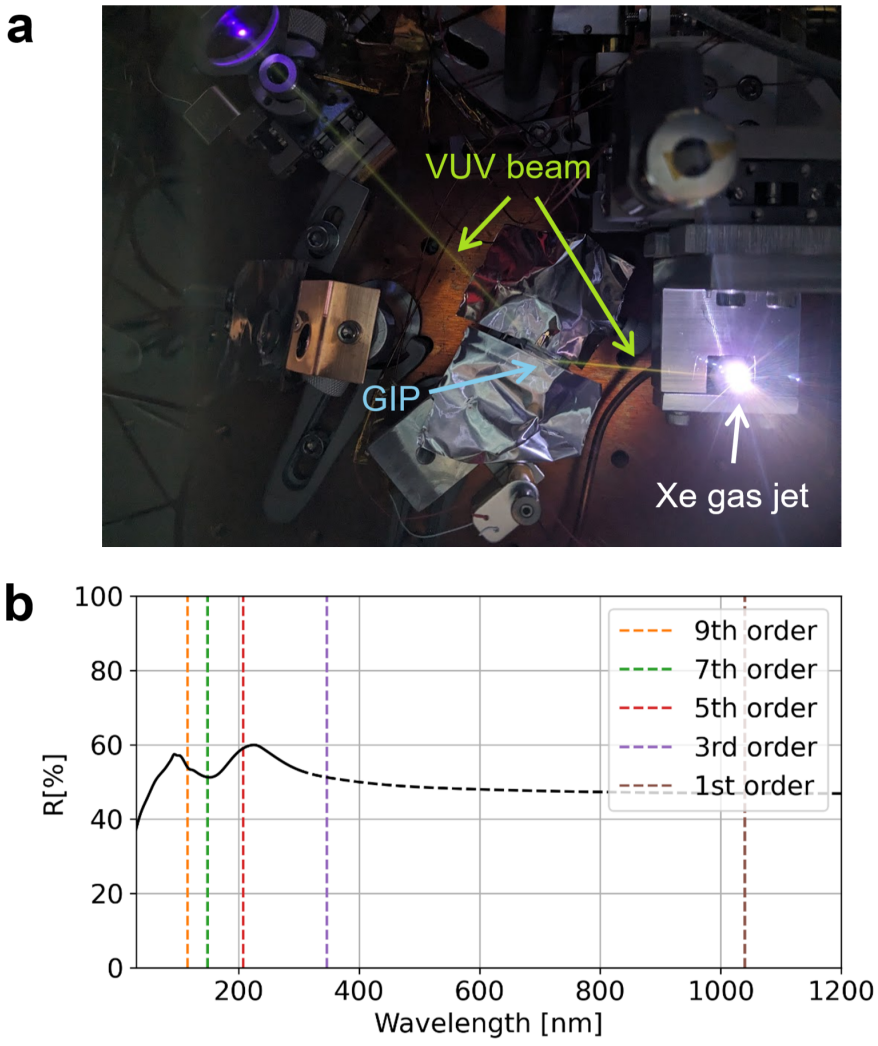

A noncollinear geometry also offers unique opportunities for studying and controlling the HHG process in single-pass experiments. Since the early proposal and demonstration [141, 142], single-pass noncollinear HHG has been used in generating circularly polarized XUV beams [143, 144], gating isolated attosecond pulses [145, 146], understanding phase-matching process [147, 148], and for fundamental studies of extreme-nonlinear optics [149, 150]. Noncollinear HHG in fsECs offers a high repetition rate, high precision system for improving the studies performed in single-pass experiments.

Our experiment setup is illustrated in Fig. 2.6a. A 120 fs, 154 MHz repetition rate Yb:fiber frequency comb [114] with up to 80 W average power, spectrally centered at 1070 nm, is used to coherently seed an fsEC. The intracavity field is linearly polarized perpendicular to the cavity plane.[5] The free spectral range of the cavity is set to $f_{\mathrm{rep}}/2 = 77$ MHz, resulting in two pulses circulating inside the fsEC at the same time.

The cavity mirrors (Layertech) are customized to have low group-delay dispersion (GDD). To fabricate the segmented input-coupling mirror (SM), a highly reflective mirror (HR) and a 1.5% transmission input coupler (IC) are cut on a diamond saw and bonded to a U-shaped substrate using Torr Seal.[6] The half HR and half IC are pressed onto the substrate with Torr Seal applied on the edge. This ensures good parallelism of the two mirrors, which can be checked using white light interferometry at the JILA Keck Lab.[7] Alternatively, a customized mirror mount where the two half mirrors can be mounted and actuated separately was also machined by the JILA Instrument Shop, but not used in this work. Layertec also offers custom coating runs for segmented mirrors with different reflectivities on the two halves.

To align the cavity, a pinhole is used to ensure spatial overlap of the two pulses. At a low input power of ~ 1 W, we can observe light transmitted through the IC easily using an infrared

[5] P-polarization works as well. This cavity is polarization insensitive.

[6] We first tried out the bonding using Crystalbond 509 wax (Ted Pella). While the flow point of Crystalbond is high (121 °C), it starts softening way below that temperature. So, the Crystalbond should not be used for optics mounting where alignment is critical. However, it is very useful for protecting optical surfaces if a mirror needs to be machined on a diamond saw, as it dissolves cleanly in Acetone.

[7] Kyle Thatcher at the JILA Instrument shop proposed that by inserting 3 small Ruby bearings in between the two bonding surfaces, a flatter surface may be obtained.

Figure 2.6: a, Schematics of a noncollinear enhancement cavity. A high-power Yb:fiber frequency comb with $f_{\mathrm{rep}} = 154$ MHz repetition rate seeds a dual-pulse fsEC whose free spectral range is set to $f_{\mathrm{rep}}/2 = 77$ MHz. The cavity is composed of 6 mirrors: four identical curved mirrors with radius of curvature $ROC = 200$ mm, one flat mirror, and one segmented input-coupling mirror (SM) which is homemade by bonding a high reflector and a 1.5% transmission input coupling mirror side by side to a flat substrate. HHG is performed at the cavity focus, where the two circulating pulses overlap temporally and spatially. The temporal delay between the two pulses is controlled via a piezo-actuated mirror (indicated by black arrows). b, Top view of the crossed beams (not to scale). Each beam forms an angle β with the bisection axis (dotted line). c, Intensity lineout at the dashed line in b. The relative carrier phase $\Delta\phi$ between the two beams changes the interference pattern. w_0 is the beam waist. d, Side view of the out-coupling mirrors. The two crossed beams, separated by a distance s on the out-coupling-mirror surface, are aligned close to the edge of mirrors with a gap size d. Figure taken from Ref. [138].

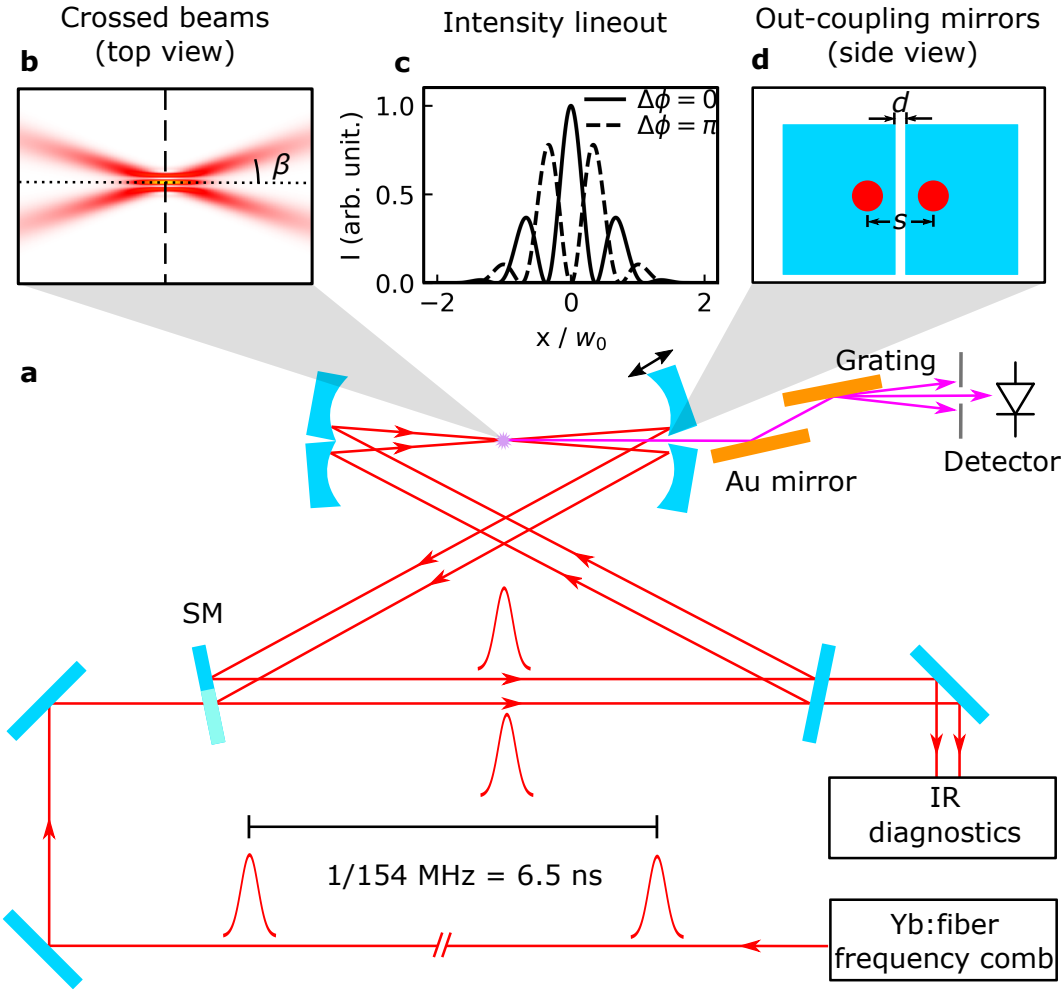

fluorescence card. We first align the beam following the first roundtrip to the proper positions on each mirror. Then, we install the pinhole at the focus of the cavity, align the pinhole position to pass the 1st roundtrip beam. We then use the 1st curved mirror of the 2nd roundtrip to steer the beam through the pinhole again. We steer the 2nd mirror of the 2nd roundtrip and the IC to complete the cavity roundtrip, at which point we can observe the cavity resonance using a camera (IR diagnostics in Fig. 2.6). The position of the pinhole and the steering of cavity mirrors need to be optimized iteratively to achieve a good spatial overlap of the two roundtrip beams at the cavity focus.

To obtain temporal overlap of the two roundtrip pulses, a ~ 0.5 mm thick barium borat (BBO) crystal is used to replace the pinhole. The noncollinear second harmonic can be observed at the bisector angle when the two roundtrip pulses overlap, and its strength can be optimized by adjusting the relative delay using the piezo-actuated curved mirror shown in Fig. 2.6a. Optimizations of the temporal and spatial overlap are performed iteratively. Finally, due to the interference of the two beams in the cavity focus, the intensity distribution changes with respect to a relative phase $\Delta\phi$ of the two beams; see Fig. 2.6b, c. This results in a small yet measurable intracavity loss and thus cavity-transmitted power difference with different $\Delta\phi$ monitored on a fast photodiode. The final optimization of the cavity alignment is thus performed by applying fast modulation ($\sim$ 10 Hz) to the cavity across its main resonance peak and slow modulation ($\sim$ 1 Hz) on the crossed beam relative phase by $\sim \pi$ simultaneously. With a pinhole placed at the cavity focus, we walk the cavity mirrors to optimize for both the highest cavity transmission and highest contrast between in-phase and out-of-phase configuration. After optimization, the temporal delay between the two laser pulses stays intrinsically stable throughout the course of our experiment. The relative phase is adjusted in real time to optimize the harmonic yield.

Before adding the gas medium, a single-beam power enhancement of ~ 170 is obtained in the cavity, resulting in a peak intensity of 8×10^{13} W/cm^2 using a focal spot size $w_0 = 44\,\mu$m ($1/e^2$ intensity radius). Note that the interference between the two beams at the center doubles the laser electric field, leading to a 4 times higher intensity than that of a single beam. Using a glass

nozzle [151] with an orifice diameter of 50 µm, we inject Xe or He:Xe mixtures into the cavity focus as HHG medium. The 11th harmonic is selected using a dispersive gold grating and is directed to a NIST-calibrated windowless photodiode transfer standard [152].[8]

With a beam waist $w_0 = 44\,\mu\text{m}$, one can easily obtain the Gaussian beam divergence half angle $\gamma = 0.44°$. We define the noncollinear half-angle β as shown in Fig. 2.6b. For $\beta \gg \gamma$, the XUV photons are generated at discrete angles dictated by the conservation of the photon energy and momentum [149]. In the wave picture, interference between the harmonics generated by different fringes at the focus causes the angular separation of the harmonics in the far field [145]. As we gradually reduce β, the far-field harmonics start to overlap and eventually merge together, visualized in Fig. 2.7a. This occurs because significant harmonic power is generated only from the central fringe when $\beta \sim \gamma$. For applications requiring unidirectional harmonic emission, it is therefore important to keep β small. However, clipping loss on the mirror edges increases dramatically as β decreases to $\sim 2\gamma$, reducing the finesse and power buildup of the cavity, limiting the smallest useful angle β. In Fig. 2.7, we show the cavity power enhancement and outcoupling efficiency at different mirror gap sizes d and noncollinear half-angles β.

Another important consideration for the choice of β is the phase-velocity match between the harmonics and the fundamental. In addition to the dispersion caused by the neutral atom and the plasma at the focus, one can show that a geometric wave vector mismatch arises from the noncollinear geometry. In the small-angle approximation $\beta \ll 1$, this dispersion term is given by

$$\Delta k_{\text{nc}}^{q} \approx \Delta k_{\text{c}}^{q} \left(1 + \frac{\pi \beta^2 z_{\text{R}}}{\lambda} - \frac{\beta^2}{2}\right) \tag{2.9}$$

for harmonic order q, where Δk_{c}^{q} is the Gouy phase mismatch from a single Gaussian beam [147, 148]. Here, λ and z_{R} are the wavelength and Rayleigh length of the fundamental beam, respectively. The noncollinear phase mismatch is shown in Fig. 2.7. The intensity-dependent dipole phase of HHG in our experiment can be neglected, as the generation medium is much shorter than the Rayleigh length [153].

[8] While it is called a photodiode, this detector actually works by measuring the photocurrent on an Al_3O_2 surface, thus is solar blind (insensitive to visible/infrared light).

Figure 2.7: a, Cavity buildup factor as a function of noncollinear half-angle β, shown for different mirror gaps d. Inset shows the simulated 11th harmonic far-field intensity distribution at the plane of the outcoupling mirrors. For large β, the harmonics split into separated spots. b, The outcoupling efficiency (OCE) for the 11th harmonic with different mirror gap d, and the geometrical phase mismatch of the 11th harmonic $\Delta k_{\mathrm{nc}}^{11}$, as a function of β. Our experimental conditions are $d = 0.5$ mm (blue line) and $\beta = 0.94°$ (black dashed line). Figure taken from Ref. [138].

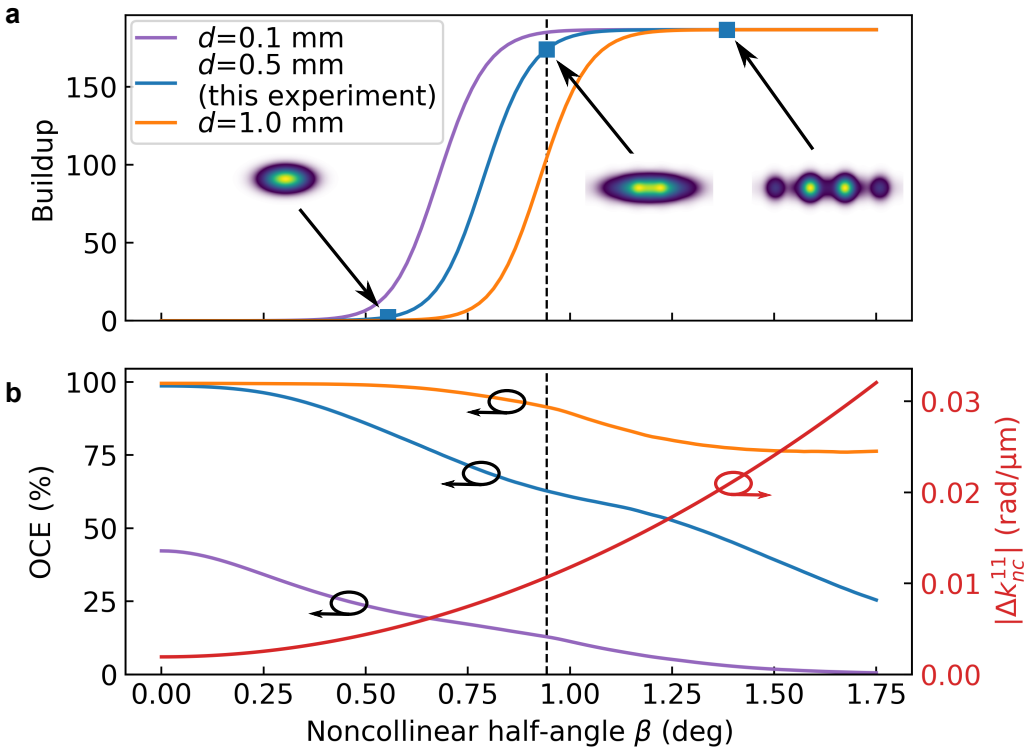

Although $\Delta k_{\mathrm{nc}}^{q}$ can be compensated for by a gas medium below the critical ionization threshold, in which the dispersion of neutral atoms dominates over that from plasma [147, 148], it is advantageous to keep the geometric phase mismatch small in the first place. This is because, in fsECs, nonlinearity from the gas target disturbs the resonant condition between the laser and cavity and causes transverse-mode coupling, resulting in a clamping effect on the intensity buildup of the fundamental beam [121, 124]. Thus, a small $\Delta k_{\mathrm{nc}}^{q}$ allows us to operate at low phase matching pressures and reduce the intensity clamping effect. To simultaneously obtain a useful cavity buildup, a uniform beam profile, a good out-coupling efficiency (OCE) and a small phase mismatch, we operate our experiment at $d = 0.5$ mm and $\beta = 0.94^{\circ}$ (see Fig. 2.7).

We perform a numerical simulation to aid in the understanding of the experimental results. In the semi-classical model for HHG [101, 102], electrons ionized in the strong laser field can go through two distinct types of trajectories, known as the long trajectory and the short trajectory, before returning to the parent ion and emitting a high-energy photon. Harmonics generated from the long-trajectory exhibit a fast-varying intensity-dependent phase and therefore a strong phase-front curvature at the laser focus. This leads to a large divergence. Thus, long-trajectory harmonic beams typically appear as large halos [154] in the far field. In contrast, the short-trajectory beam has a small beam divergence and on-axis emission [154], and can be selected by proper phase matching conditions [155]. We start from the HHG dipole yield and phase obtained as the solution of a time-dependent Schrödinger equation (TDSE) [156] assuming a continuous wave 1070 nm laser interacting with Xe atoms. This solution contains both long- and short-trajectory information. We then numerically extract the short-trajectory dipole contribution for the beam-shape simulations.

For harmonics well above the ionization threshold of the generation medium, the intensity-dependent dipole is written semiclassically as (in atomic units):

$$d_q(I) = \sum_j A_j \mathrm{e}^{-i\alpha_j U_p(I)/\omega}, \tag{2.10}$$

where $U_P(I) = \frac{I}{4\omega^2}$ is the ponderomotive energy, proportional to the laser intensity I, ω is the laser angular frequency. Each amplitude A_j and the corresponding phase coefficient α_j represent the

contribution of a particular quantum mechanical trajectory j. For long trajectories, $\alpha_j > \pi$.

This can be generalized [154, 157, 158, 159] to a full quantum-mechanical HHG dipole expression as

$$d_q(I) = \int \tilde{d}_q(\alpha) \mathrm{e}^{-i\alpha U_p(I)/\omega} \mathrm{d}\alpha, \tag{2.11}$$

where the weight of the quantum-path distribution is obtained using a Fourier transform with respect to α as

$$\tilde{d}_q(\alpha, I_0) = \int d_q(I) \mathrm{e}^{i\alpha U_p(I)/\omega} W(I - I_0) \mathrm{dI} \tag{2.12}$$

for a continuous phase coefficient α near intensities I_0. We use a Hann window for $W(I-I_0)$ peaked at I_0 and treat the amplitude of $d_q(I)$ as a constant in this transformation. The HHG dipole and the corresponding quantum path distribution for the 11th harmonic in Xe driven with a 1070 nm wavelength laser is shown in Fig. 2.8a and b, respectively.

In the semi-classical model [101, 102], the highest photon energy that can be generated in an HHG process at a given laser intensity is $I_p + 3.2U_p$, where I_p is the ionization potential of the atom and U_p is the ponderomotive potential of the electron in the laser field. For harmonics with a photon energy larger than I_p, one can find a threshold laser intensity where the given harmonic order is exactly at the cutoff. Below this intensity, the generalized long and short trajectory merge together and cannot be separated. We therefore leave the dipole data below this cutoff intensity unchanged. For dipole data above the cutoff intensity, we use Eqn. 2.12 to extract the corresponding short-trajectory contribution at $|\alpha| < \pi$. The filtered data is transformed back using Eqn. 2.11. We apply a moving average filter to smooth the data, removing the fast oscillations that arise from interferences between the quantum paths. The resulting dipole data as well as the quantum path distribution are shown in Figs. 2.9c and d.

Neglecting phase-matching effects, we calculate the HHG emission from the focal plane and then propagate to the far field using the Huygens integral in the Fresnel approximation [110]. We use a peak intensity of 5×10^{13} W/cm^2 in the simulation to reproduce the laser intensity used in the experiment. The harmonic beam shapes in the outcoupling mirror surface plane (103 mm away

Figure 2.8: a, HHG dipole $d_q(I)$ yield and phase from TDSE solutions for the 11th harmonic in Xe driven by a laser at 1070 nm. b, Corresponding quantum path distribution, $\tilde{d}_q(\alpha, I_0)$. c, Filtered HHG dipole yield and phase for the 11th harmonic in Xe, containing only the short trajectory. d, Corresponding quantum path distribution of c. See supplementary material of Ref. [138] for more details.

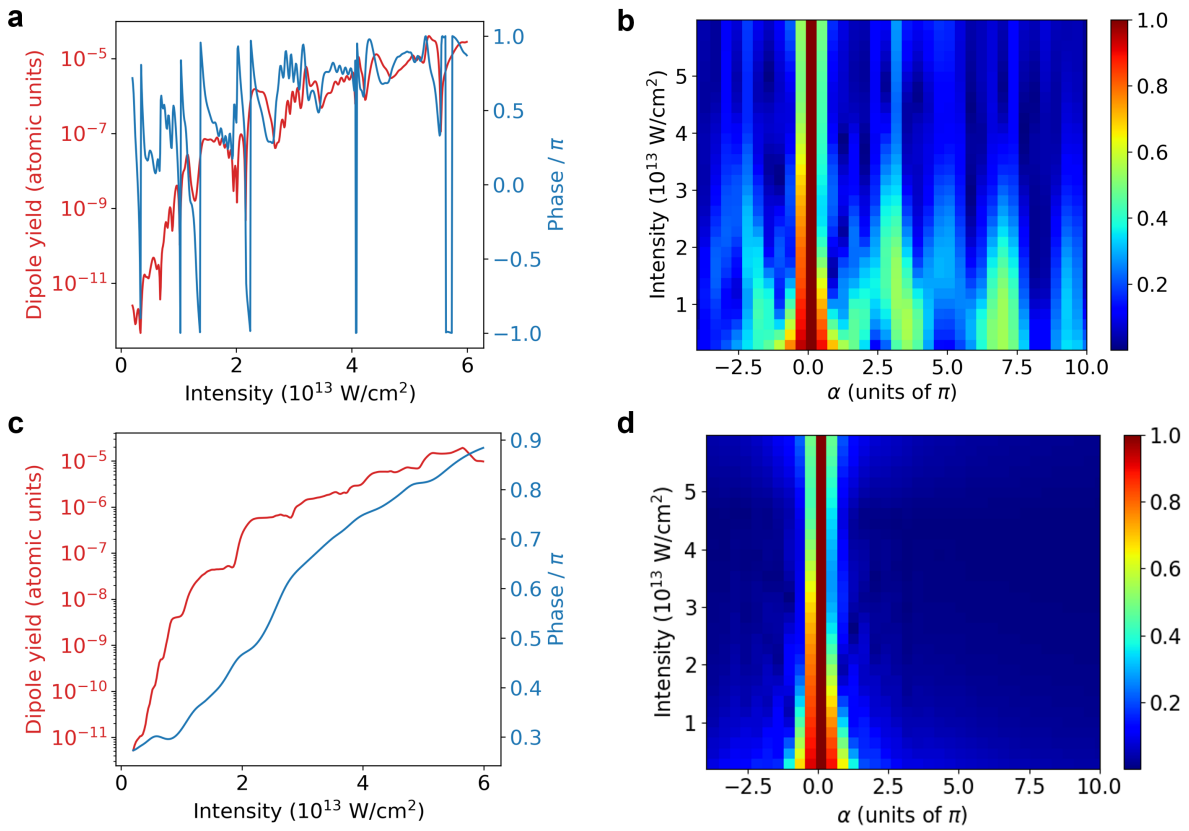

from the focus) and in the far field (700 mm behind the outcoupling mirrors) are shown in Fig. 2.9, after accounting for diffraction at the edges of the outcoupling mirror. The relative carrier phase $\Delta\phi$ between the two pulses of the crossed beams changes the interference pattern at the focus and thus the generated harmonic profile in the far field. When $\Delta\phi = \pi$, the harmonics generated from different parts of the fundamental interfere destructively on the bisection axis. This causes the harmonic beam to split into a doublet in the far field. Simulated harmonic far-field beam shape qualitatively matches the experimental observation.

Harmonics of order 9 to 19 are observed on a sodium salicylate screen and are recorded in Fig. 2.10. Sodium salicylate is known to have a nearly constant quantum efficiency in the extreme ultraviolet range; see Ref. [160] and references therein. Thus, the integrated brightness of the harmonics serves as a crude guide for the ratio of harmonic powers [161]. Experimentally, we noticed a rapid degradation of the fluorescence intensity of sodium salicylate in our vacuum chamber over the course of a week. This degradation appears to be uniform for the 9th harmonic and above, but is much less prominent for the 7th harmonic. Thus, using just the fluorescence brightness ratio and the power of high-order harmonics may lead to an overestimation of the 7th harmonic power (not included in Fig. 2.10). A slight asymmetry is observed in the experimentally recorded beam profile, caused by a misalignment between the bisection axis of the crossed beams and the center of the mirror gap. Theoretically estimated OCEs for these harmonic orders are shown in Fig. 2.10c.

We record the XUV power in the 11th harmonic as a function of the intracavity fundamental power. Inspired by Ref. [122], we also compare the harmonic yield using pure Xe or a He:Xe mixture with 9:1 volume ratio, see Fig. 2.11a. We observe that, with pure Xe as the generation medium (green traces), the XUV output power is higher when $\Delta\phi = \pi$ for the same fundamental power. This trend is reversed for He:Xe gas mixture (purple traces), yet the highest harmonic yield is still obtained when $\Delta\phi = \pi$ due to the higher intracavity power achieved.

We show that the seemingly contradictory behavior when comparing the pure Xe or He:Xe mixture medium can be understood simply as a result of the change of the focal volume. As shown

Figure 2.9: a,b, Simulated 11th harmonic profile on the outcoupling-mirror surface, for $\Delta\phi = 0$ and $\Delta\phi = \pi$, respectively. The shaded area is blocked by the out-coupling mirrors, and most of the harmonic power is coupled out through the gap. c,d The simulated harmonic profile at a far distance away (0.7 m) from the mirror gap. Gray curves show integrated power distribution along the horizontal (x) and vertical (y) directions. Inset photos: experimentally observed 11th harmonic beam profiles. Figure taken from Ref. [138].

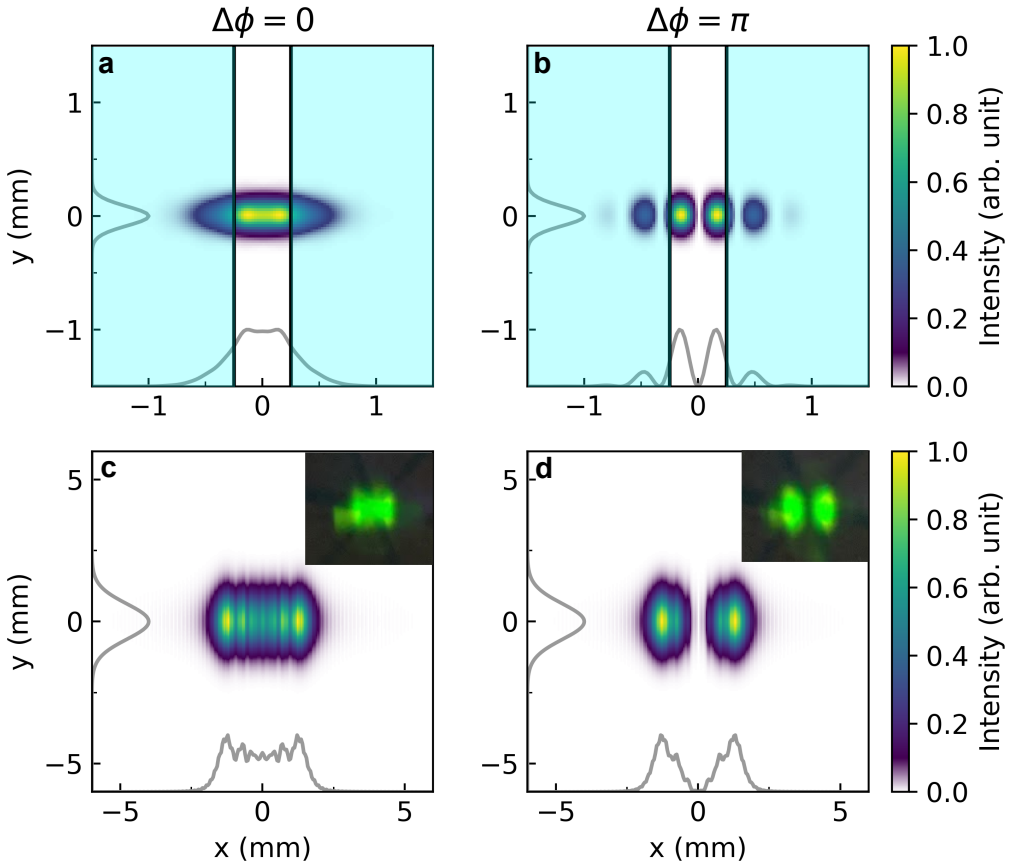

Figure 2.10: a,b, Upper panel: images of harmonics dispersed on a fluorescent plate. Lower panel: harmonic photon flux integrated in the vertical direction. Results in a and b are shown for $\Delta\phi = 0$ and $\Delta\phi = \pi$, respectively. A two-dimensional low-pass filter in Fourier domain (not shown) is used to remove a high frequency noise pattern on the image originating from the camera. Asymmetry of the harmonics is caused by a slight misalignment between the mirror gap and the bisection axis. The images shown here are taken with the cavity locked and using pure Xe gas at room temperature. c, Theoretically estimated out-coupling efficiencies from the cavity for harmonic orders 9 to 19 (119 to 56 nm) and different $\Delta\phi$. Figure taken from Ref. [138].

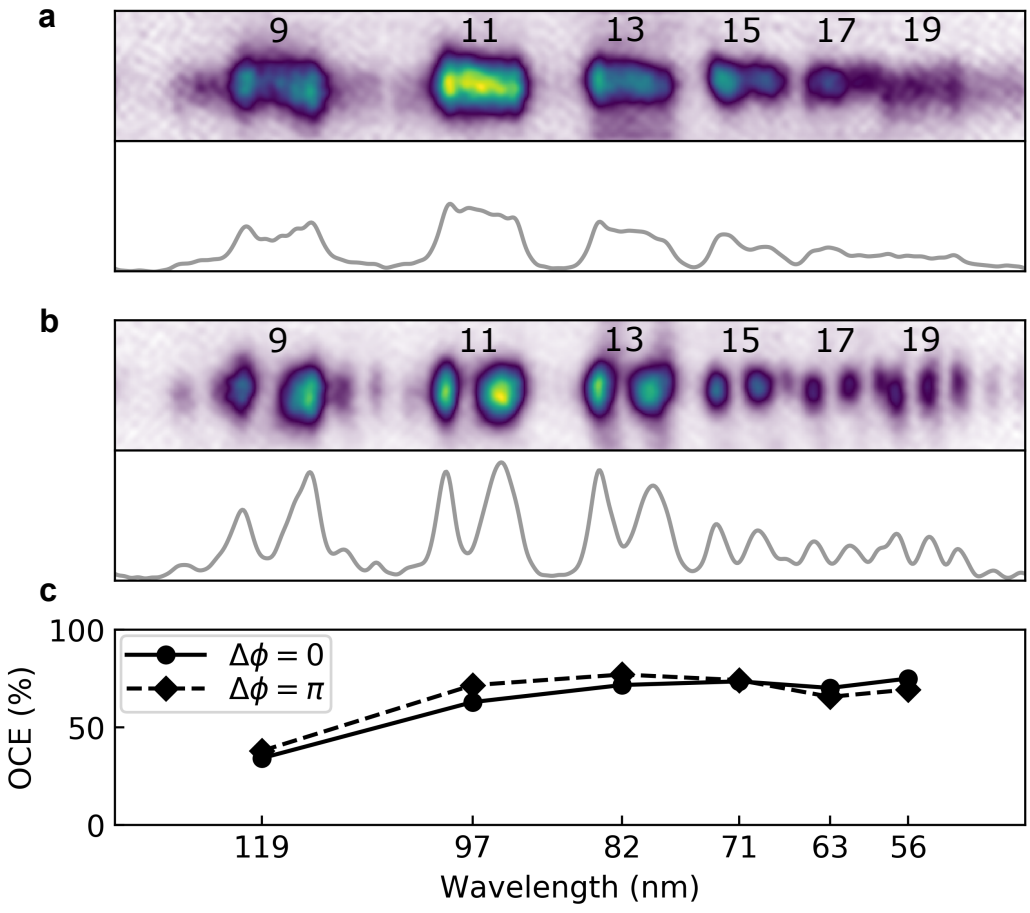

in Fig. 2.6c, the relative phase $\Delta\phi$ changes the intensity grating at the focus and therefore the peak intensity. Since HHG is an extremely nonlinear process, the harmonic power generated is mainly from the central peak for $\Delta\phi = 0$, or the innermost two symmetric peaks for $\Delta\phi = \pi$. With our beam parameters, the fundamental power in the central peaks amounts to 57% and 88%, for $\Delta\phi = 0$ and $\Delta\phi = \pi$, respectively. That is, when changing from $\Delta\phi = 0$ to $\Delta\phi = \pi$, we can employ a larger fraction of the fundamental power for HHG. We thus define an effective generation efficiency as the the ratio between the generated harmonics to the power inside the central fringe(s) in the generation volume; see Fig. 2.11b. Remarkably, the effective conversion efficiency is approximately identical for $\Delta\phi = 0$ and $\Delta\phi = \pi$ throughout the entire range of peak intensities, for both the pure Xe and He:Xe mixture, respectively.

The motivation to use a 9:1 He:Xe mixture is to reduce the plasma effect and improve phase matching. As is shown in Ref. [122], the harmonic yield limited by accumulated plasma is characterized by a dimensionless parameter

$$\xi_{\text{beam}} = \sigma_{\text{FWHM}}/v_{\text{gas}} \times f_{\text{rep}}, \tag{2.13}$$

which represents the number of laser pulses that one atom "sees" as it transits through the laser beam. Here, σ_{FWHM} is the full width at half-maximum of the focus and ν_{gas} is the average atomic velocity in the jet. Following Ref. [122], we used a 9:1 He:Xe mixture heated to 560 °C as the generation medium, corresponding to $\xi_{\text{beam}} \sim 5$ with our laser repetition rate of 154 MHz. As expected, a significant gain in harmonic yield is observed compared to using pure Xe (Fig. 2.11), due to both the reduced depletion of neutral atoms and the improved phase-matching conditions. In Fig. 2.11b inset, we see that as we sweep across resonance with Xe or He:Xe gases, the resonance peak is broadened due to the intracavity plasma [121, 124]. This effect is reduced, but still significant, when we use the heated He:Xe mixture, indicating that a large plasma density remains [122]. Improvements in harmonic conversion can be anticipated if the parameter ξ_{beam} is further reduced.

The demonstration of the dual-pulse noncollinear fsEC enabled us to understand the phase matching and power scaling of the crossed beam HHG at high repetition rate. In addition to spec-

Figure 2.11: Out-coupled 11th harmonic power (back-calculated to the point right after the out-coupling mirror pair) as a function of intracavity (single beam) fundamental drive power, shown for different generation media and relative phases. Data is taken when the cavity is swept across the resonance. As shown in Ref. [122], similar harmonic power is expected when the cavity is locked with a similar intracavity power level. b, Effective conversion efficiency (defined in the text) as a function of peak drive intensity. Inset shows intracavity IR power when the cavity is swept across a resonance, with $\Delta\phi = 0$ (continuous black) and $\Delta\phi = \pi$ (dashed black) configurations using a He:Xe mixture gas target, displaying clear deviations from the Lorentzian line shape obtained without a gas target (gray), indicating significant plasma density. Green traces are recorded with pure Xe with 260 kPa backing pressure at room temperature. Purple traces are recorded with 9:1 He:Xe mixture with 4100 kPa backing pressure heated to ~ 560 °C. Figure taken from Ref. [138].

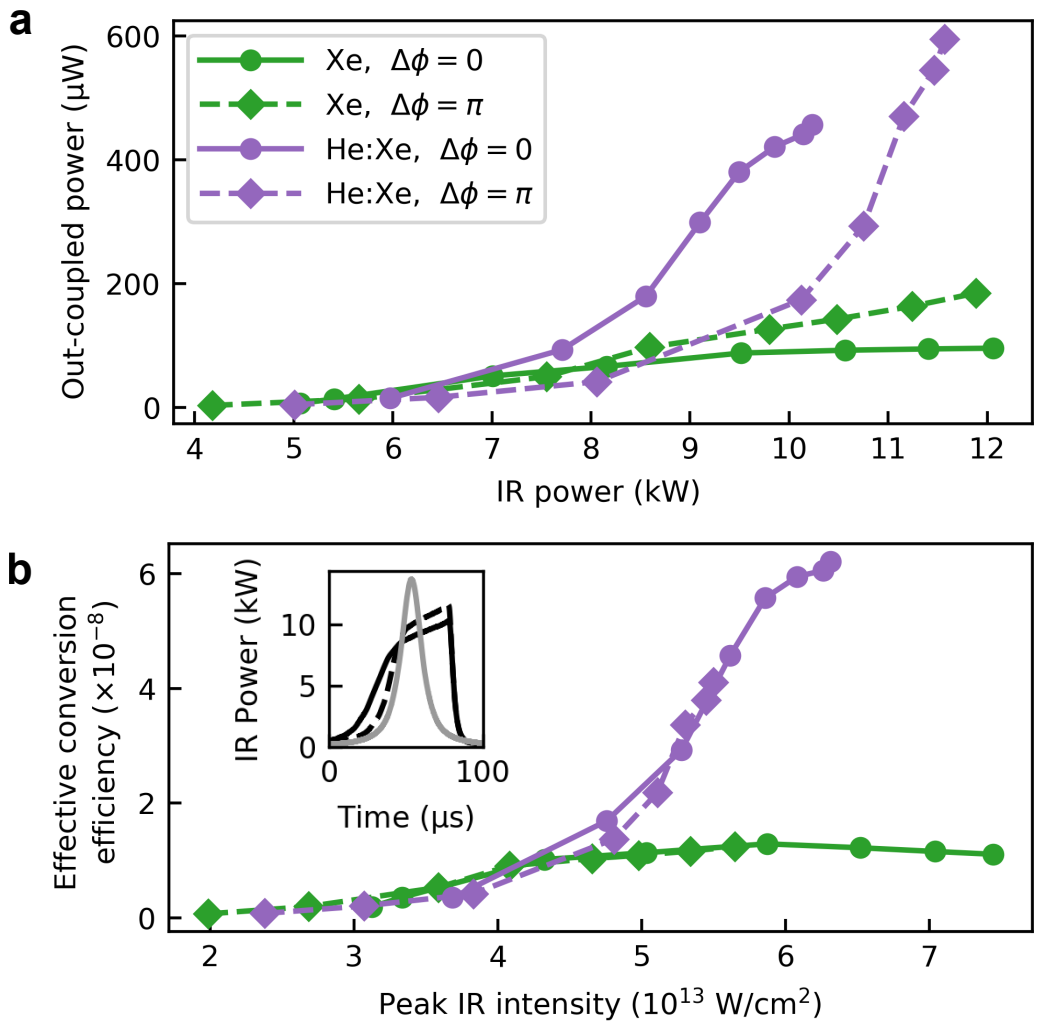

troscopy applications, the system could also benefit ultrafast time-resolved studies using isolated attosecond pulses via wavefront rotation streaking [145, 146, 162].

For the ^{229}Th nuclear clock project, the 7th harmonic generation of an Yb:fiber comb will cover the correct spectral region. However, at the 7th harmonic, the outcoupling efficiency of the noncollinear cavity drops rapidly to $\sim$ 30%. Considering also the difficulty in aligning and maintaining the cavity operation, we chose to switch to an outcoupling method using a grazing-incidence plate described in Sect. 2.3. Recently, a novel monolithic noncollinear cavity geometry is briefly described in Ref. [163], using custom wedged mirrors and un-split curved focusing mirrors, providing increased stability and ease of alignment [164].

We observe that the 7th harmonic yield remained almost the same between the pure Xe and the He:Xe mixture. This is possibly due to the large dispersion of Xe near our 7th harmonic wavelength [165] leading to a extremely difficult phase-matching condition. It will be interesting to consider other methods for phase matching of the 7th harmonic generation process, say using different gas mixtures with different dispersion properties or even using coherent light manipulation of optical resonance [166, 167]. However, for the ^{229}Th spectroscopy presented in this thesis, we use pure Xe for simplicity.

2.5 A tunable VUV comb for ^{229}Th nuclear spectroscopy

When we started building the ^{229}Th spectroscopy experiment, the uncertainty region of the nuclear transition is larger than the typical spectral coverage of a VUV comb based on fsEC. Thus, we developed a VUV comb system with a tunable center wavelength by adjusting the spectral coverage of the fundamental infrared (IR) comb. In this section, we document this effort following our own published work in Ref. [90].

The IR comb seeding the fsEC is presented in Fig. 2.12. We start from a low-noise 75 MHz Yb-fiber oscillator [168] and amplify its output in cascaded linear (PM-YSF from Coherent) and nonlinear (PLMA-YDF-25/250 from Coherent) similariton [169] amplifiers. The output of the nonlinear amplifier gives us a coherent broadband frequency comb covering a $\sim$ 100 nm bandwidth

(Fig. 2.12b). A fraction ($\sim$ 10%) of the nonlinear amplifier output is sent to a highly nonlinear photonic crystal fiber (HNL PCF, NL-1050-Zero-2 from NKT) for supercontinuum generation. We stabilized the comb carrier-envelope offset frequency f_{ceo} by the $f-2f$ scheme [98] using an all-fiber setup similar to that presented in Ref. [170]. To fully stabilize the frequency comb, we also phase lock one of the comb lines in the supercontinuum to the Sr clock laser at 698 nm [171] (see also Sect. 2.6). Then, by simply shifting the offset frequency between one comb line and the Sr clock laser, all comb lines can be scanned in parallel [161] to search for the ^{229}Th nuclear transition.

To achieve the desired spectral tunability, we select a part of the spectrum from the nonlinear amplifier output using an interference bandpass filter(Edmund Optics #87-824, 1050 nm center wavelength, 25 nm bandwidth). The center wavelength can be continuously tuned from 1040 nm to 1070 nm by varying the incidence angle of the comb on the bandpass filter, or by using different bandpass filters. The filtered light is stretched using a grating-based pulse stretcher (not shown) and a stretcher fiber, then further amplified in a large-mode-area fiber (LMF, customized at IMRA) power amplifier to obtain high spectral power. The optical spectra of the nonlinear amplifier and the power amplifier at several different wavelength settings are shown in Fig. 2.12b. The spectral filtering, temporal stretching, and subsequent amplification allowed us to mitigate nonlinear self-phase modulation in the LMF gain fiber and obtain high output spectral power with a clean pulse shape. The output is compressed with a grating compressor to produce an infrared frequency comb with $>$ 50 W average power and $<$ 200 fs pulse duration.

The tunable IR comb is first used to seed a noncollinear fsEC [138, 90] which was later swapped to a collinear fsEC using a grazing-incident plate outcoupler [24]. In Fig. 2.13, we show the cavity-enhanced IR comb spectra measured using a grating-based optical spectrum analyzer, and the corresponding VUV frequency comb spectra using a grating-based VUV spectrometer (HP Spectroscopy, easyLIGHT) with $<$ 0.1 nm resolution. The VUV comb power per line is estimated to be approximately 1 nW delivered to our spectroscopy setup. The tunable comb was originally designed to cover the energy range given in Ref. [62]. More recent measurements presented in Ref. [45, 25] are published after the design phase of the VUV comb. Fortunately, our

Figure 2.12: a, Tunable Yb-fiber frequency comb. Black lines represent passive fibers. Green lines represent active fiber amplifiers. Red lines are free-space laser paths. Grating pairs (yellow) are used for temporal compression of the laser pulses. A slit is used in combination with the first grating pair to clean up the spectral output from the oscillator. WDM, wavelength-division multiplexer; PM-YSF, polarization-maintaining Yb-doped single-clad fiber; PLMA-YDF-25/250, polarization-maintaining large-mode-area Yb-doped double-clad fiber with 25/250 µm core/cladding diameter; HNL PCF, highly nonlinear photonic-crystal fiber; and LMF, large-mode-area fiber module with 50 µm core diameter. b, Spectra of the nonlinear similariton amplifier and LMF amplifier output at different wavelength settings. Figure taken from Ref. [90].

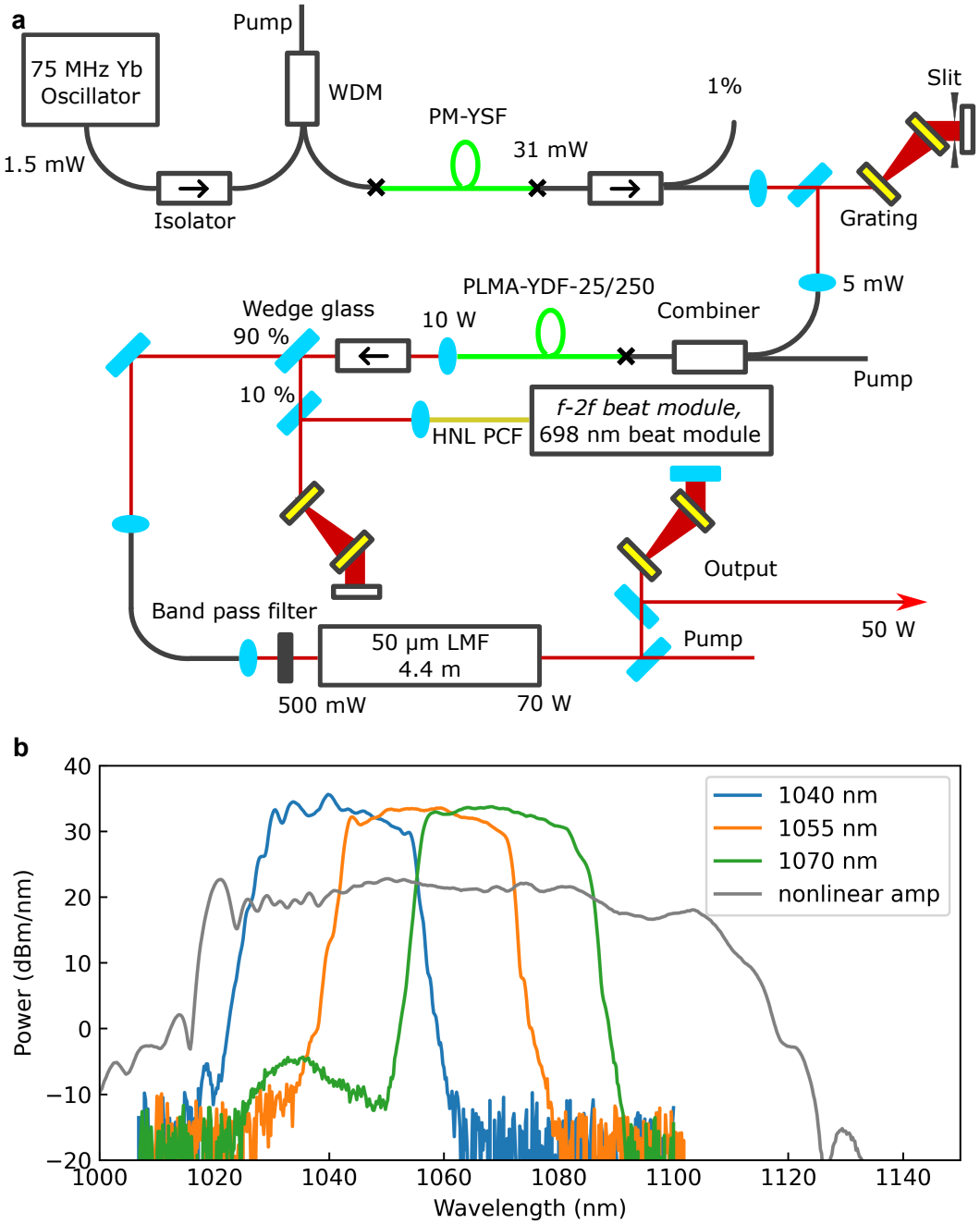

comb tunability range covers the more precise energy range determined in Ref. [25]. Recent direct laser excitation measurements in Refs. [27, 28] further confirm the desired comb coverage.

2.6 Comb stabilization to the Sr clock

For the comb spectroscopy of the ^{229}Th nuclear transition, we need to be able to scan our comb frequencies in a controlled way. Luckily, we can easily lock our comb to the ^{87}Sr optical clock [5] which provides the most stable optical standard in the world, thanks to the JILA ^{87}Sr clock and Stable Lasers team in the Ye group. Here, we present the details of the locking scheme.

As mentioned above, the comb f_{ceo} is stabilized using the f-$2f$ detection scheme (see also Sect. 2.1). We fix the comb f_{ceo} to -8 MHz, which matches the dispersion of the fsEC. This allows us to couple all comb modes into the fsEC and obtain good cavity enhancement [106].

Since the comb has two degrees of freedom, we need another lock point with known frequency. The simplest way is to lock one of the comb lines to the ^{87}Sr optical clock laser [172] at the ~ 698 nm wavelength, which offers a convenient known optical frequency reference for our experiment. For convenience, we picked off the ^{87}Sr clock laser from the distribution center in the Ye lab, whose frequency is shifted by a few acousto-optic modulators (AOM) before reaching the ^{87}Sr clock setup. Thus, the clock laser we use has a (changing but known) frequency offset from the ^{87}Sr clock transition. On March 28th, 2023, we set up our locking system as shown in Fig. 2.14. On that specific day, the ^{87}Sr clock laser frequency at our pickup port is

$$\nu_{\mathrm{clock\_laser}} = 429,228,141,703,262.2 \text{ Hz}, \tag{2.14}$$

provided by the ^{87}Sr clock measurement and AOM offset settings. With the comb stabilized as shown in Fig. 2.14, the f_{rep} is measured using a frequency counter to be

$$f_{\mathrm{rep}} = 75054008.3594 \text{ Hz} \tag{2.15}$$

Figure 2.13: VUV comb spectral tunability. (a) Fundamental comb spectrum, measured as the leakage transmission from one of the enhancement cavity mirrors. (b) VUV spectrum of the outcoupled harmonics, measured with a grating-based VUV spectrometer. Horizontal error bars indicate the ^{229m}Th transition uncertainty (1-σ) ranges given in Seiferle et al. [62], Sikorsky et al. [45] and Kraemer et al. [25]. Recent measurements by Tiedau et al. [27] and Elwell et al. [28] further confirm that our comb covers the nuclear clock transition. The uncertainties for these two measurements are too small to be visualized on this plot. We obtain similar overall VUV powers at each wavelength setting. Vertical scales in the plots are normalized to unity. Figure taken from Ref. [90].

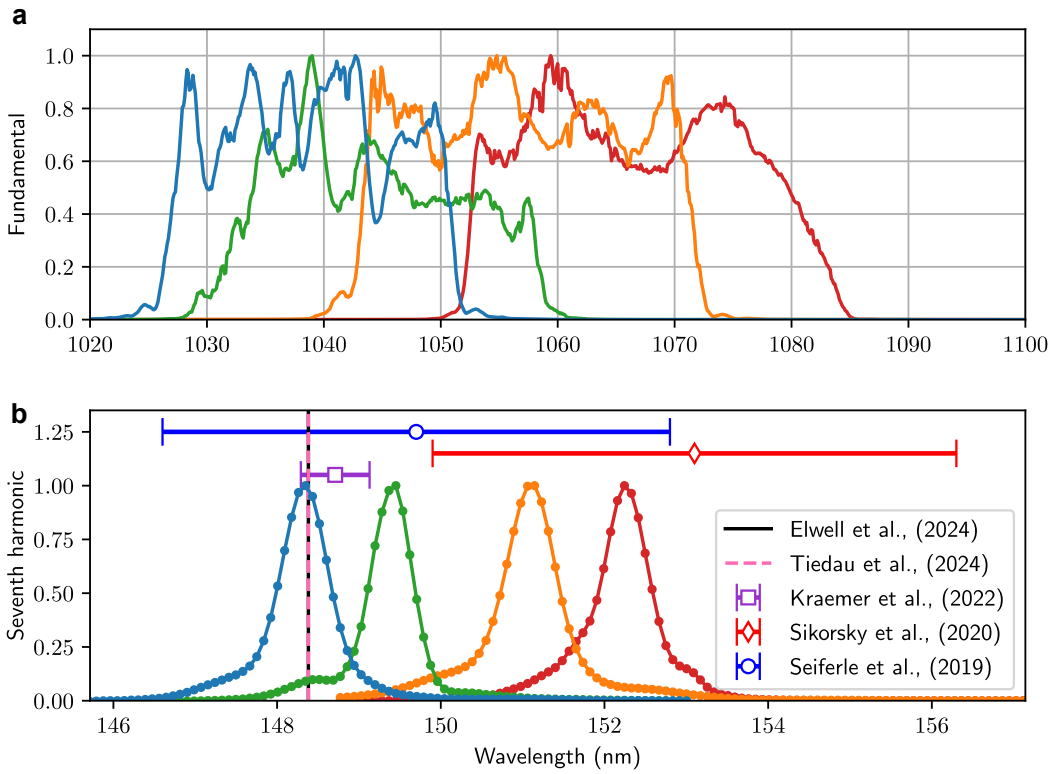

with the counter referenced to the NIST hydrogen maser. It is easy to see from Fig. 2.14a that[9]

$$\nu_{\text{clock\_laser}} = N_0 \times f_{\text{rep}} - f_{\text{ceo}} - f_{\text{beat}}. \tag{2.16}$$

Directly solving this equation leads to

$$N_0 = [5718924].000007, \tag{2.17}$$

where we only take the integer part to be the actual comb mode. The residual of the integer corresponds to ~ 0.1 mHz error on the f_{rep} measurement, which is the last digit in the frequency counter. It is easy to ensure that the same comb mode is locked to the ^{87}Sr clock laser every time. If we were off by one mode, the f_{rep} on the counter would be different by $f_{\text{rep}}/N_0 \sim 13$ Hz, which is easily noticeable.

The f_{ceo}, f_{beat} detection and locking electronics are shown in Fig. 2.14b. About 600 mW of light from the comb is sent into a PCF (NL-1050-Zero-2 from NKT Photonics) for supercontinuum generation and subsequent frequency doubling in a periodically-poled lithium niobate (PPLN). The detection of f_{ceo} is performed using an all-fiber setup similar to that used in Ref. [170]. Part of the generated supercontinuum light at 698 nm is filtered out to perform an optical beat with the ^{87}Sr clock laser. Both f_{ceo} and f_{beat} are detected using balanced photodiodes to reject the intensity noise of the laser.

To scan the VUV comb at 148 nm by ~ 75 MHz for covering the entire f_{rep} range, the comb mode at the 698 nm needs to be scanned by $\sim 75/4.7 \approx 16$ MHz, where 4.7 is the ratio between the ^{229}Th and ^{87}Sr clock transition frequency [24]. A superheterodyne method is used to shift the radio frequency (RF) signal of f_{beat} by beating it with an auxiliary RF tone from a direct digital synthesizer (DDS) using a frequency mixer (Fig. 2.14). The mixed signal is band-pass-filtered before reaching a phase-frequency detector. The phase difference between this mixed signal and a stable RF reference is fed back to the laser oscillation to stabilize the phase of the f_{rep} signal, closing the loop for the phase lock of f_{beat}. In this way, the frequency of f_{beat} can be digitally

[9] The signs of the locked frequency offset can be easily verified by slightly changing the offset frequency and observing the change of f_{rep}.

scanned by changing the DDS frequency set point without having to change the bandpass filter. A similar design is used for the f_{ceo} lock; see Fig. 2.14. Suitable servo loop filters are needed to shape the feedback transfer function for obtaining a low-noise phase lock. For phase lock loop designs and general feedback control techniques, interested readers are referred to Refs. [173, 174, 175].

Although simple, this comb locking scheme has a practical disadvantage. The f_{ceo} lock (feeding back to oscillator pump current) and f_{rep} lock (feeding back to the intra-oscillator EOM) are not orthogonal to each other (i.e. the oscillator pump current, for example, affects both the f_{ceo} and f_{rep} frequency). Thus, it is difficult to optimize both locks simultaneously to obtain a low phase noise of the comb. However, the correlated noises in f_{beat} and f_{ceo} can cancel each other out and lead to a narrow comb line at ~ 148 nm, although the phase noises of f_{beat} and f_{ceo} are both relatively high. Thus, to reduce the linewidth of the comb, we only need to reduce the phase noise of the comb mode at the IR wavelength that contributes to the HHG process (~ 1040 nm). We modify the locking scheme to include an auxiliary continuous wave laser (Coherent Mephisto) at 1064 nm wavelength which has a low phase noise. The comb is tightly locked to the Mephisto laser at 1064 nm, while the absolute frequency of the Mephisto laser is slowly steered to keep another comb mode phase locked to the Sr clock laser; see Fig. 2.15. Additionally, the fsEC is now stabilized directly using the auxiliary Mephisto laser; see Fig. 2.15b. This allows us to keep the cavity length stabilized even if the comb output is turned off, say, for $^{229\mathrm{m}}$Th detection. Moreover, the offset between the comb and cavity can now be arbitrarily adjusted, making it easier to mitigate the cavity bistability caused by the effects of intracavity plasma [126, 121].

The locked beat notes of f_{ceo}, $f_{\mathrm{beat,\ 698nm}}$, and $f_{\mathrm{beat,\ 1064nm}}$ are shown in Figs.2.16a, b, and c, respectively. The observed larger noises for f_{ceo} and $f_{\mathrm{beat,\ 698nm}}$ are anti-correlated when we tightly lock one comb mode to the low noise 1064 nm reference laser. Thus, $f_{\mathrm{beat,\ 1064nm}}$ shows a higher signal-to-noise (SNR) ratio than f_{ceo} and $f_{\mathrm{beat,\ 698nm}}$.

Another practical issue motivated us to further change the locking scheme. The fiber-based f_{ceo} detection module [170] shown in Fig. 2.14b requires a fixed polarization of the supercontinuum light. However, at ~ 1050 nm fundamental wavelength, it is difficult to obtain a highly nonlinear

Figure 2.14: A simple comb locking scheme. a, Illustration of the lock points and frequencies. Consider the comb as a rubber band with two degrees of freedom, we can fully stabilize the comb by locking its f_{ceo} and a beat f_{beat} with the ^{87}Sr clock laser. b, Schematic of the implementation of the comb locking scheme including the optical detection and the feedback loop design. Red lines represent free-space optical beam path, green lines represent optical fibers, and black lines represent electrical connections. PCF, photonic crystal fiber. PPLN, periodically poled lithium niobate. WDM, wavelength division multiplexer. DDS, direct digital synthesizer. PFD, phase-frequency detector. EOM, electro-optical modulator. PZT, piezoelectric transducer.

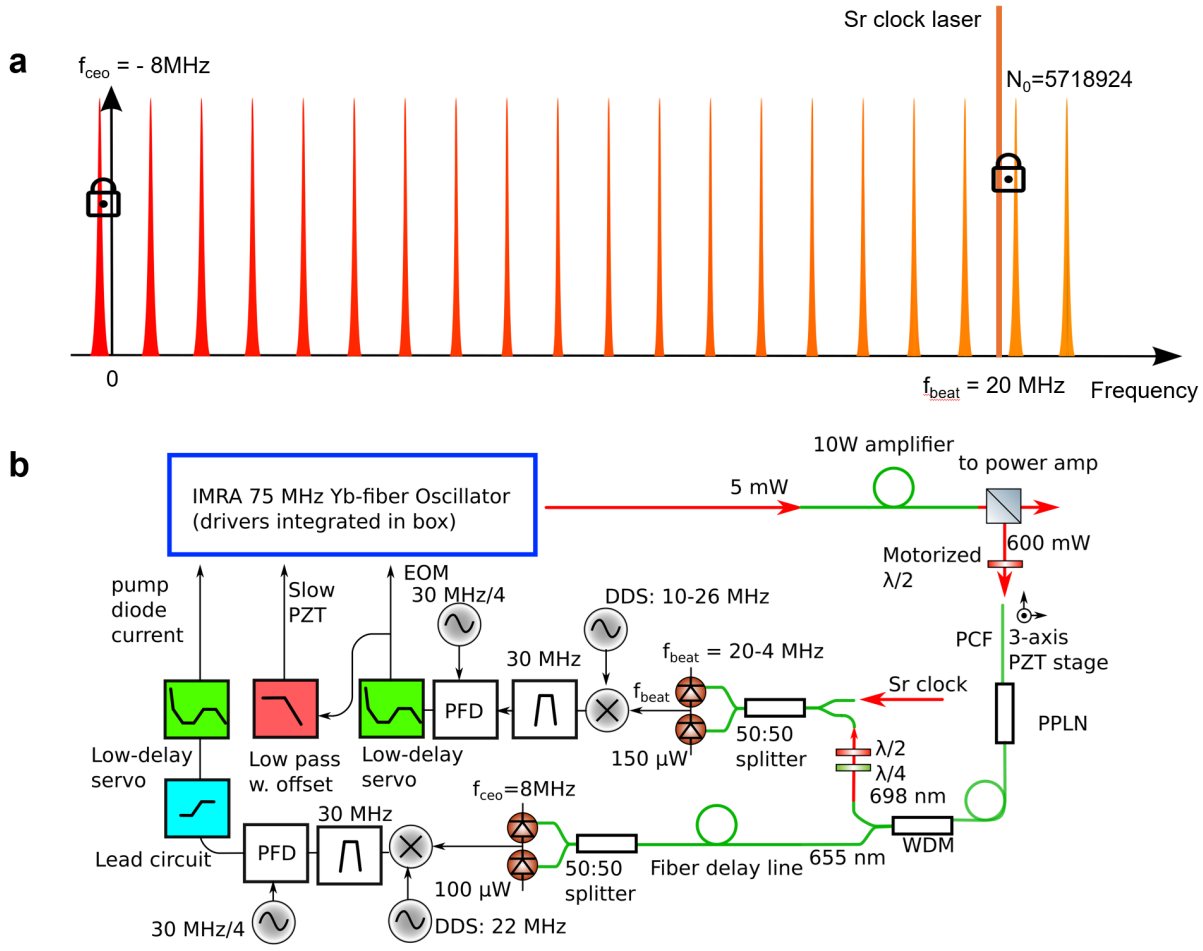

Figure 2.15: Comb locking scheme with improved linewidth. a, Illustration of the lock in the frequency domain. The locking scheme is similar to that in Fig. 2.14a, except with an auxiliary Mephisto laser. b, Schematic of the implementation of the lock showing the stabilization of both the comb and the fsEC using auxiliary Mephisto laser. Figure taken from Ref. [24].

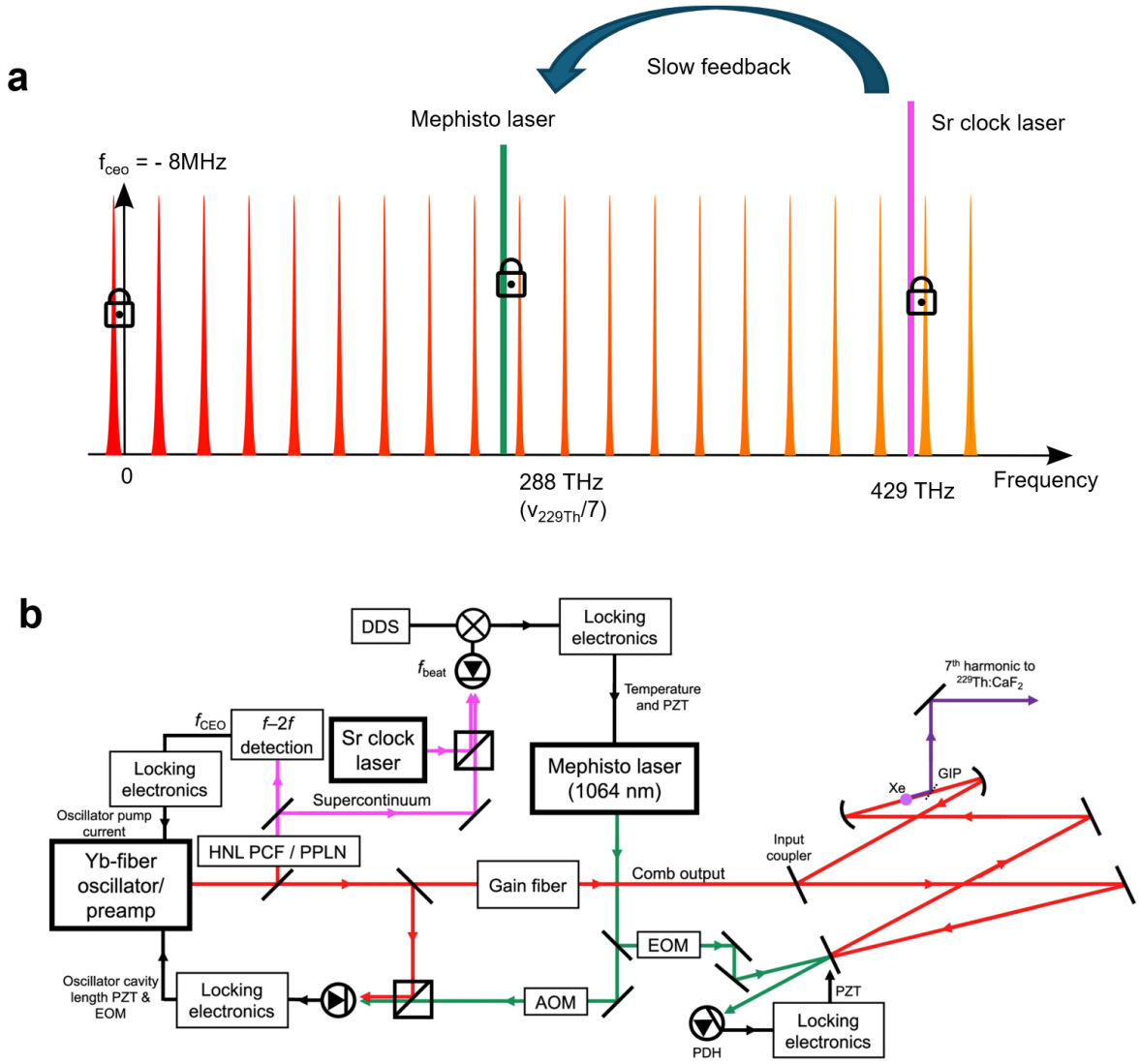

fiber that is polarization-maintaining.[10] Thus, thermal drifts of the polarization in the supercontinuum broadening fiber make the f_{ceo} detection unstable. As the comb can be fully stabilized by locking at any two frequencies separated far away from each other, we can alternatively stabilize the comb by just locking the $f_{\mathrm{beat,\ 698nm}}$ and $f_{\mathrm{beat,\ 1064nm}}$, provided that the laser frequencies are known. The 698 nm reference laser is provided by the Sr clock/stable laser team with frequency calibrated by the JILA ^{87}Sr clock [5]. We stabilize our Mephisto 1064 nm laser to the Menlo frequency comb used to transfer the stability of the JILA Si cavity [57, 176] stability to the clock laser [172]. Using this new locking scheme, we bypass the need to detect the comb f_{ceo} and obtain a more stable operation of the comb locks.

How good is the VUV comb linewidth? In the beatnote data shown in Fig. 2.16, the (relative) sideband noise power is a direct indication of the amount of phase noise present in the system [177]. For understanding laser phase noise and linewidth, interested readers are referred to Refs. [177, 57, 178, 4, 179]. Briefly, considering a single-tone carrier, adding (small) phase modulations on the carrier would generate sidebands whose power is proportional to the mean square phase deviation $(\Delta\phi)^2$. The power ratio between the coherent carrier and the noise sideband can then be quantified by integrating the laser phase noise [177].

A complication comes from the 7th harmonic generation process employed in our experiment. In the case of noiseless harmonic generation [180], the timing jitter in the fundamental laser is faithfully transferred to the harmonics. However, in the 7th harmonic, the phase jitter is 7 times larger than that in the fundamental, due to the higher carrier frequency (see Fig. 2.17a. The corresponding phase noise power spectral density, $S_\phi(f) \propto (\Delta\phi)^2$, is thus scaled up by a factor of 49 ($\sim$ 17 dB) in the 7th harmonic.

Assuming the phase noise comes purely from the comb itself (i.e. the noise of the Mephisto reference laser is much smaller than that of the comb), the beatnote power distribution in the RF (see Fig. 2.16) is identical to the optical power distribution for the light generating the beat. One

[10] Waveguide-based solutions may offer higher nonlinearity while maintaining the polarization, see, for example, the Comb-Offset-Stabilization Module from Octave Photonics.

Figure 2.16: Beatnotes of the comb lock. a, comb f_{ceo}, b, comb beat with 698 nm clock laser $f_{\mathrm{beat,\ 698nm}}$ and c. comb beat note with the 1064 nm Mephisto laser $f_{\mathrm{beat,\ 1064nm}}$.

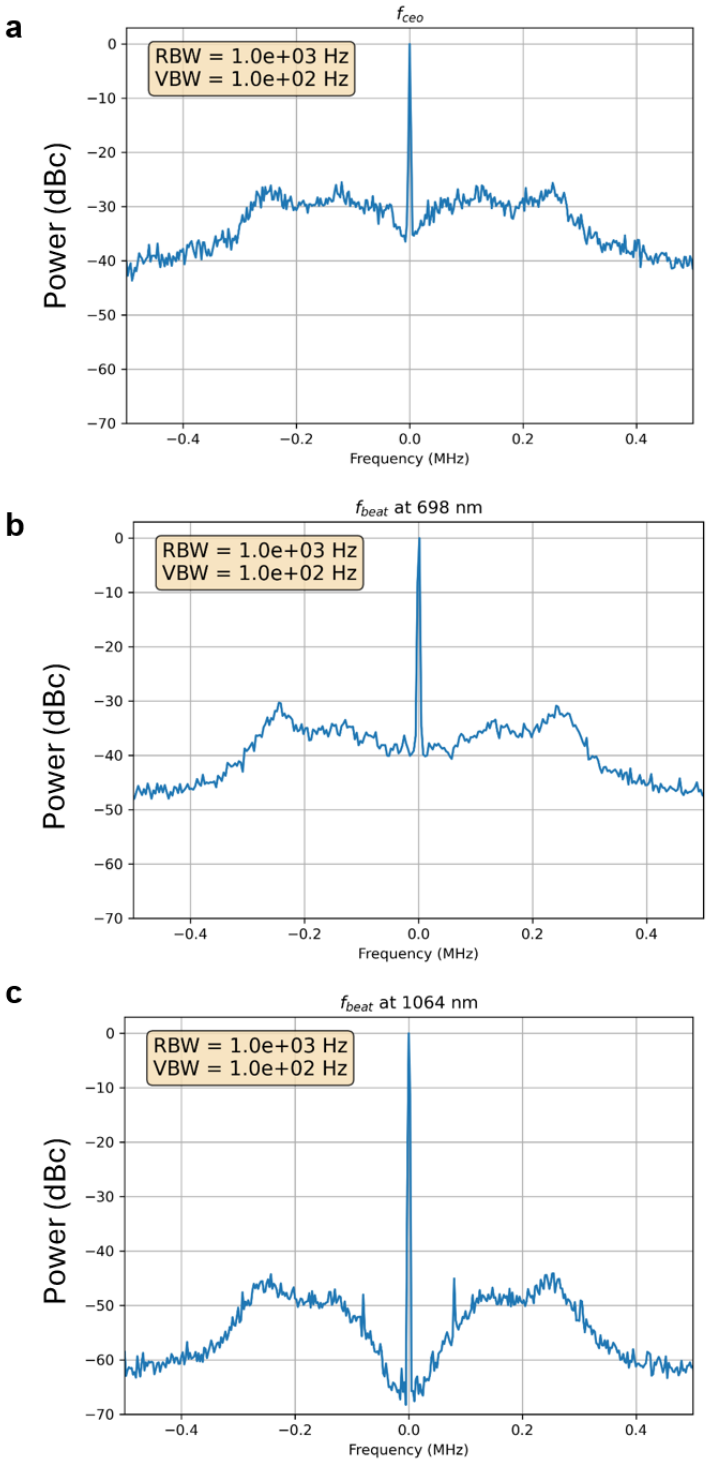

may ask what SNR we need for the $f_{\text{beat, 1064nm}}$ signal to ensure a good comb linewidth at the 7th harmonic. We can do an order-of-magnitude estimation. We define the linewidth δ as where half of the optical power is within $\pm\delta/2$ of the carrier frequency, while the other half is in the noise outside the narrow coherent tone. We observe that most of the noise comes within a 1 MHz window near the carrier, as shown in Fig. 2.16. With a 1 kHz resolution bandwidth (RBW) as in Fig. 2.16, we have $\sim 10^3$ more frequency bins containing noise in a 1 MHz window. Only one bin contains the coherent carrier with a linewidth below 1 kHz. Thus, an SNR of 30 at a 1 kHz RBW would be sufficient to ensure that a large portion of optical power is contained in the coherent carrier with a linewidth smaller than $\delta = 1$ kHz. Considering the additional 17 dB scaling from the 7th harmonic generation, we would like to keep the $f_{\text{beat, 1064nm}}$ SNR > 47 dB at 1 kHz RBW. Fig. 2.16c shows that this is indeed the case.

Additionally, the fsEC provides a low-pass filter that removes high-frequency laser phase noise, further helping in reducing the 7th harmonic linewidth; see [90]. The estimated integrated phase noise of the VUV comb, considering the scaling relation shown in Fig. 2.17a is significantly below 1 radian (Fig. 2.17b), indicating that most of the VUV comb power should be contained in a narrow frequency carrier even down to 10 Hz Fourier frequency. However, path length jitter may lead to additional out-of-loop phase noise that is not analyzed in Fig. 2.17b. We estimate that the path length fluctuation can introduce a linewidth broadening on the order of kHz [181, 180].

Another source of the comb phase noise comes from the HHG process itself. The electrons ionized from the Xe gas atom experience a slightly different phase shift depending on the laser intensity (see, for example, Eqn. 2.11). The effect is likely negligible due to the small phase coefficient α_j for the 7th harmonic [158, 180], at least for the short trajectory component that shows a good beam shape [154]. Intentionally modulating the IR comb intensity may help us verify the α_j amplitude, as shown in Ref. [180]. Ultimately, the VUV comb linewidth is benchmarked against the ^{229}Th nuclear clock transition in Chap. 5.

Figure 2.17: a, Illustration of the phase noise scaling in 7th harmonic generation process. Even without any additional noise, the same timing jitter corresponding to a phase of ϕ_1 would result in a larger phase noise of $7 \times \phi_1$ in the 7th harmonic. Figure adapted from Ref. [179]. b, Phase noise performance of the VUV comb. A low-pass filtering function (corner frequency: 93.75 kHz) corresponding to the transfer function of our enhancement cavity has been applied, which reduces the high-frequency phase noise. The left axis is for phase noise power spectral density (blue curve), and the right axis is for the integrated phase noise (orange curve) integrated from 1 MHz down to the corresponding value of the x-axis. Figure taken from Ref. [90].

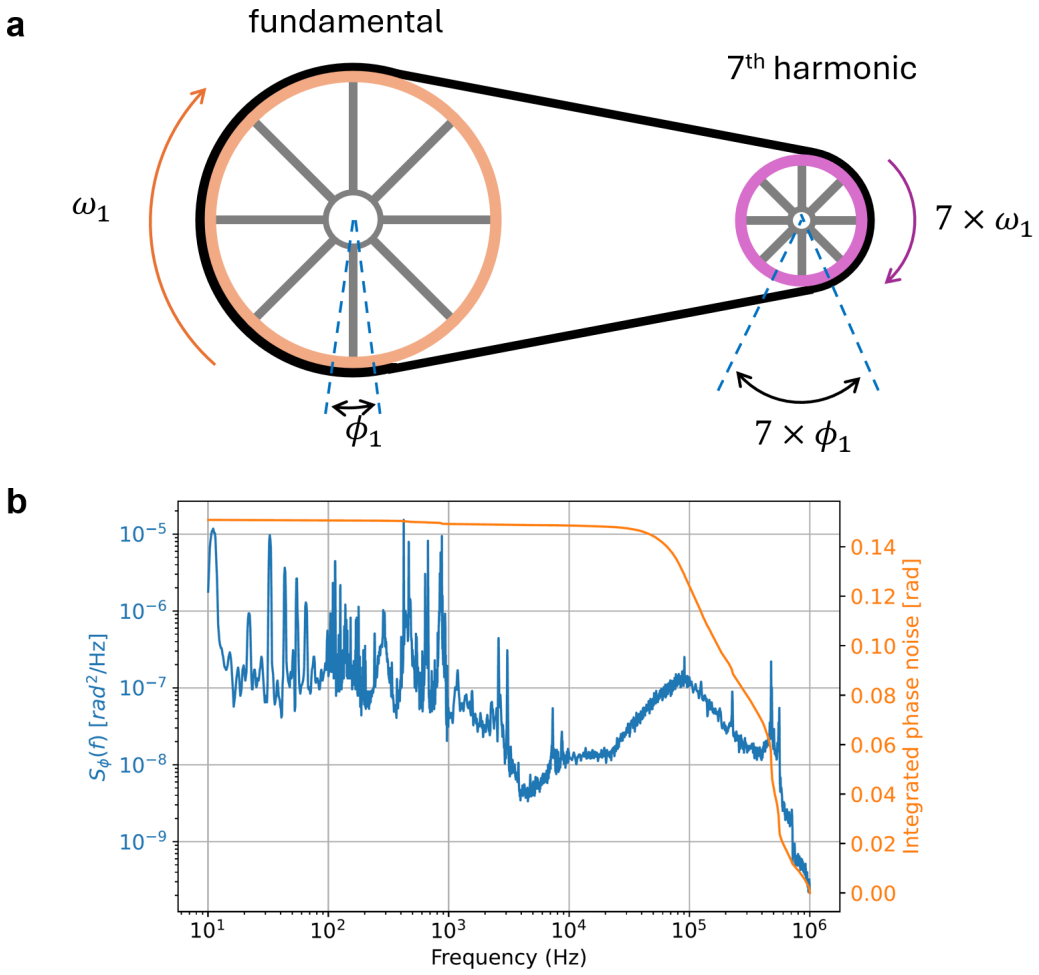

2.7 A Xe recycling system

To obtain a good 7th harmonic generation efficiency, we choose Xe gas as the generation medium because of its large polarizability. The Xe gas is relatively expensive. The market price of the Xe gas is about \$40 per standard liter in January 2025. Using a 100 µm diameter nozzle and operating at a backing pressure of 30 psi, we can calculate the mass flow rate of the Xe gas jet following equation (2.43) in Ref. [119]:

$$\hat{T}\ (\text{torr·L/s}) = C\left(\frac{T_\text{c}}{T_0}\right)\sqrt{\frac{300}{T_0}}P_0 d^2. \tag{2.18}$$

Here, T_c is the temperature of the vacuum chamber, which is usually assumed to be at room temperature. T_0 is the temperature of the gas inside the nozzle, P_0 is the stagnation pressure in torr, d is the diameter of the nozzle in cm, and C is a numerical value for specific gases. For Xe, we take $C = 7.9$ L/cm^2/s given in Table 2.5 in Ref. [119]. Assuming $T_\text{c} = T_0 = 300$ K and a typical stagnation pressure of ~ 20 psi used in our experiment, the corresponding mass flow rate is calculated as

$$\hat{T} = \ 0.82\ (\text{torr·L/s}) \approx 1.1 \times 10^{-3}\ \text{atm·L / s}. \tag{2.19}$$

We typically use 250 standard liters (atm· L) Xe gas bottles, which cost 250 L × (\$40/L) = \$10,000 but only last about $250/1 \times 10^{-3}/3600 \approx 63$ hours. The cost of running the experiment continuously will be prohibitively high. Thus, we implement a simple Xe recycling system to reduce the consumption of Xe gas when operating the VUV comb.[11] It is also possible to build a more sophisticated closed-loop gas recycling system [182], but a significant investment is required.

A mixture of oxygen and ozone is injected into the vacuum chamber to avoid hydrocarbon buildup on the optics caused by VUV irradiation [107]. This O_2, O_3 gas mixes with Xe in the vacuum chamber and is pumped out using a turbo molecular pump backed by a dry scroll pump.[12]

[11] We had inspiring discussions with Johannes Weitenberg and Akira Ozawa about this design. A similar system is implemented in MPQ for the recycling of Xe.

We collect this gas mixture from the exhaust of the scroll pump. Their vapor pressures at low temperatures are shown in Fig. 2.18.

We see that O_3 has a similar vapor pressure to Xe and is therefore difficult to separate by distillation. In addition, frozen ozone poses an explosion risk as conversion from O_2 to O_3 is exothermic [189]. Thus, we use a catalytic ozone destruct device (OxidationTech, CDU-15) to convert O_3 to O_2 before filling the exhaust gas from the pumps into storage tedlar gas bags (Restek, Tedlar Sampling Bag, 40 L). The tedlar bags are convenient, but start leaking after multiple uses. In the future, a more robust product should be used.

The gas collected in the bags is then transferred to a stainless steel gas bottle dipped in liquid nitrogen (LN2), since at the LN2 temperature the vapor pressures of Xe and O_2 are below atmospheric pressure. To complete the transfer, a suitable Nalgen Dewar is used with the bottom of a stainless steel gas cylinder dipped in the LN2. A heat gun is used to warm up the inlet of the gas cylinder to avoid clogging due to frozen Xe solid.

We then connect the collected O_2 and Xe mixture bottle to a roughing pump with an ultimate pressure of $\sim$ 10 torr. This is good enough to pump out O_2 at LN2 temperature, as its vapor pressure is still high (Fig. 2.18), while the frozen Xe solid remains inside the bottle. In this process, the vapor pressure of O_2 is monitored to indicate when the pumping process has finished. In this process, the gas bottle is thawed and frozen a few times to avoid trapping O_2 in frozen Xe.

Finally, we perform another transfer process to further purify the gas. With the Xe gas cylinder cooled by dry ice, we flow the Xe to another clean cylinder dipped in LN2. A few in-line filters (Restek, Click-On In-line filters) made for gas chromatography mass spectrometry are used to further remove moisture, oxygen, and hydrocarbon. Finally, a particle filter with 2 µm pore size is installed in the gas line to avoid clogging the gas nozzle. We confirm that the harmonic power generated using recycled Xe is identical to that generated by using a fresh Research Grade Xe bottle.

[12] Dry scroll pumps require regular maintenance and add dust particles to their exhaust. A possibly better option is a multi-stage roots blower. However, roots pumps are inefficient for pumping He gas.

Figure 2.18: Vapor pressure of O_2, O_3, and Xe. The vapor pressure of O_2 is obtained using the Antoine equation [183] with data compiled from Ref. [184]. The vapor pressure of O_3 is taken from Ref. [185]. The vapor pressure of Xe is taken from Ref. [186], which we also cross-checked with data from Refs. [187, 188].

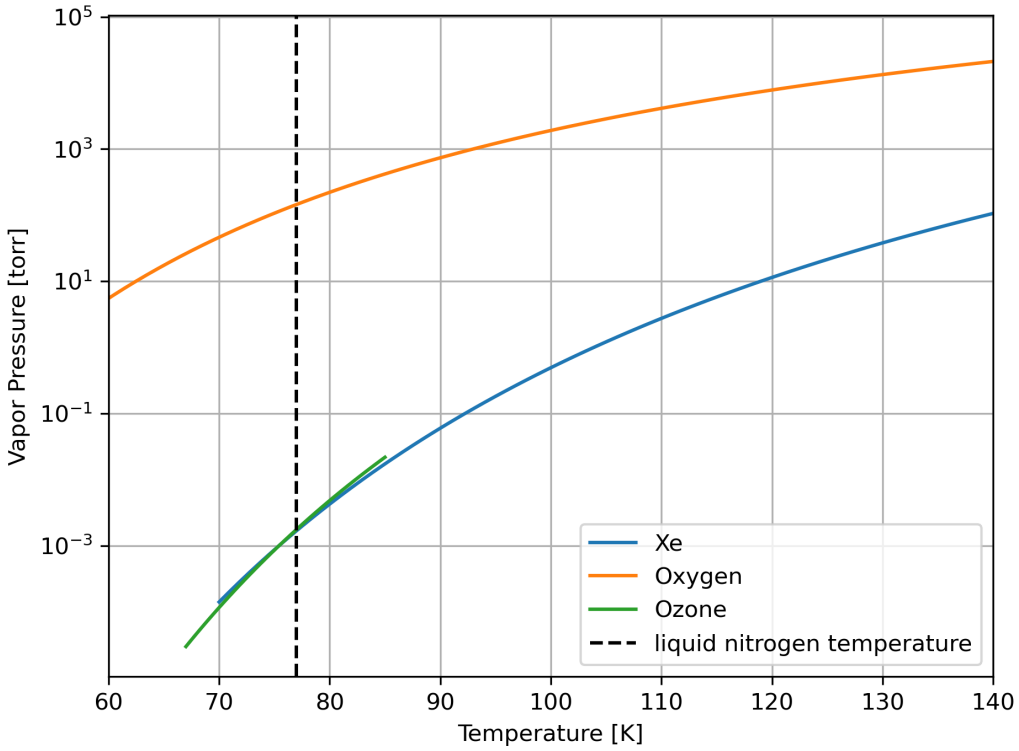

Chapter 3

Thin-film ^{229}Th targets for nuclear spectroscopy

Motivated by the progress in nuclear clock research [42, 43, 59, 190, 29] detailed in Chap. 1, we started working on building a thin-film nuclear clock in 2019 [191]. Although we have not yet observed state-resolved nuclear transition lines in thin-film targets, the first stage of research did produce satisfactory results in observing the nuclear excitation signal using a four-wave mixing laser [76]. The initial spectroscopy setup is designed to use the internal conversion (IC) scheme [190, 191], as the IC decay channel has already been observed [59, 29]. In this chapter, we document our effort in this direction, including target fabrication, detection setup, and data analysis. The spectroscopy data is attached in Appendix A, even though no clear nuclear transition is observed. After the report of the radiative decay [25] of ^{229m}Th from ISOLDE, we shifted our focus looking for fluorescence photons; see Sect. 3.6.

3.1 Laser excitation rate of ^{229m}Th

With a VUV frequency comb laser presented in Chap. 2, how can we calculate the excitation rate of the ^{229m}Th isomer? In this chapter, we first consider the ^{229}Th nucleus as a two-level system and calculate the nuclear excitation rate when irradiated with a laser.[1] We then present our effort in making $^{229}ThO_2$ and $^{229}ThF_4$ thin film targets. The spectroscopy results with them are shown in the end, as well as in Appendix A.

[1] Shielding effects from the electronic shell [192] is not included in our analysis.

3.1.1 Full solution of the optical Bloch equation

The laser excitation rate of the nucleus can be described by the optical Bloch equation, similar to any two-level system. We define a Rabi frequency as

$$\Omega = \sqrt{\frac{2\pi c^2 I C_{\mathrm{ge}}^2 \Gamma_\gamma}{\hbar \omega_0^3}}, \tag{3.1}$$

where c is the speed of light, I is the intensity of the laser, C_{ge} is the Clebsch-Gordan coefficient of the transition, Γ_γ is the radiative decay rate, $\hbar$ is reduced Planck's constant, and ω_0 is the resonance frequency of the two-level system. We can write down the optical Bloch equation that describes the evolution of the system as [193]:

$$\begin{aligned} \dot{u} &= -\frac{\tilde{\Gamma}}{2} u + \delta v \\ \dot{v} &= -\delta u - \tilde{\Gamma} v + \frac{\Omega}{2} w \\ \dot{w} &= -2\Omega v - \Gamma w + \Gamma, \end{aligned} \tag{3.2}$$

where

$$u = \rho_{12} \mathrm{e}^{-i\delta t} + \rho_{21} \mathrm{e}^{i\delta t} \tag{3.3}$$

$$v = -i(\rho_{12} \mathrm{e}^{-i\delta t} + \rho_{21} \mathrm{e}^{i\delta t}) \tag{3.4}$$

$$w = 1 - 2\rho_{22} \tag{3.5}$$

and $\delta = \omega - \omega_0$ is the detuning between the laser and the nuclear transition frequency. ρ_{ij} are the density matrix elements. We use $\Gamma = \Gamma_\gamma + \Gamma_{\mathrm{nr}}$ to denote the total decay rate of $^{229\mathrm{m}}$Th, including the γ-decay rate Γ_γ as well as a non-radiative decay rate Γ_{nr} coming from the IC decay channel. Further,

$$\tilde{\Gamma} = \frac{\Gamma + \Gamma_{\mathrm{L}}}{2} + \tilde{\Gamma}_{\mathrm{add}} \tag{3.6}$$

is the total decoherence rate, with Γ_{L} the linewidth of the laser light and $\tilde{\Gamma}_{\mathrm{add}}$ capturing additional decoherence mechanisms. The corresponding nuclear excited state population can be solved by

numerically integrating Eqns. 3.2.[2] In the specific case when the laser field is on resonance with the nuclear transition, the dynamics can also be described using Torrey's solution of the optical Bloch equations [195, 194] below:

$$\rho_{22} = \frac{\Omega^2}{2(\Gamma\tilde{\Gamma} + \Omega^2)} \left[1 - \mathrm{e}^{-\frac{1}{2}(\Gamma+\tilde{\Gamma})t} \left(\cos(\Lambda t) + \frac{\Gamma + \tilde{\Gamma}}{2\Lambda} \sin(\Lambda t) \right) \right], \tag{3.7}$$

where

$$\Lambda = \left| \Omega^2 - (\tilde{\Gamma} - \Gamma)^2/4 \right|^{1/2}. \tag{3.8}$$

When $\Omega < \left|\tilde{\Gamma} - \Gamma\right|/2$, the sin and cos functions in Eqn. 3.7 should be replaced with sinh and cosh, respectively.[3]

3.1.2 Simple excitation rate estimations

To gain more insight into the laser excitation rate of $^{229\mathrm{m}}$Th, we try to make a few approximations and simplify the solution. In cases where a laser linewidth is much larger than the transition linewidth, i.e. $\Gamma_\mathrm{L} \gg \Gamma$, and with a low excitation fraction, $\tilde{\Gamma} \gg \Gamma \gg \Omega$, Eqn. 3.7 simplifies to

$$\rho_{22}(t) = \frac{\Omega^2}{2\tilde{\Gamma}\Gamma}(1 - \mathrm{e}^{-\Gamma t}). \tag{3.9}$$

At $t = 0$, the excitation rate is thus

$$\Gamma_\mathrm{exc,peak} \approx \frac{\Omega^2}{2\tilde{\Gamma}} = \frac{\pi c^2 I C_g e^2 \Gamma_\gamma}{\hbar\omega_0^3 \tilde{\Gamma}}. \tag{3.10}$$

Note that Γ_exc is derived from Eqn. 3.7 assumed $\delta = 0$, i.e. the laser is on resonance with the transition. With a broadband laser and a Lorentzian lineshape, this assumption breaks down. The actual integrated excitation rate can be corrected to be

$$\Gamma_\mathrm{exc} = \frac{\pi}{2}\Gamma_\mathrm{exc,peak} = \frac{\pi^2 c^2}{2\hbar\omega_0^3} \times I \times \frac{\Gamma_\gamma}{\tilde{\Gamma}} \times C_\mathrm{ge}^2 = \frac{\lambda^3}{8\pi\hbar c} \times \frac{\Gamma_\gamma}{\Gamma_\mathrm{L}} \times I \times C_\mathrm{ge}^2 \tag{3.11}$$

where we also used the approximation $\tilde{\Gamma} \approx \frac{\Gamma_\mathrm{L}}{2}$, assuming the laser linewidth dominates the decoherence, and λ is the transition wavelength.

[2] Analytic solutions of the full equation exist as well, see Ref. [194].

[3] Directly evaluating sinh and cosh at certain numerical conditions may lead to divergent results due to the precision of computers. This can be avoided by breaking down the hyperbolic functions to exponential functions and properly combining them before plugging in numbers.

A full derivation of the above discussion can be found in Refs. [191, 196]. For the moment, let us assume $C_{\mathrm{ge}} = 1$ and see if we can obtain the same result from other simple considerations.

3.1.2.1 Estimation using the steady-state scattering rate

We know the $^{229\mathrm{m}}$Th excitation fraction stays low throughout our experiment, i.e. most of the ^{229}Th atoms stay in the ground state. We absorb any additional decoherence, such as inhomogeneous broadening, into the laser linewidth Γ_{L}. The excitation rate is estimated using a few different simple ways as follows. Interested readers can also refer to Refs. [193, 197] for more details.

The scattering rate of a two-level system can be written as

$$R(\Delta) = \frac{\Gamma_\gamma}{2} \frac{s}{1 + s + 4\Delta^2/\Gamma_\gamma^2} \tag{3.12}$$

where $\Gamma_\gamma = 1/\tau$ is the angular transition linewidth, $s = I/I_{\mathrm{sat}}$ is the saturation parameter, and Δ is the angular frequency detuning. Using the formula for the saturation intensity of a two-level system as

$$I_{\mathrm{sat}} = \frac{2\pi^2 \hbar c}{3\lambda^2} \Gamma_\gamma \tag{3.13}$$

and integrating over the detuning Δ, we can get the photon scattering rate as

$$R = \frac{3\lambda^3}{8\pi\hbar c} \times \Gamma_\gamma/\Gamma_{\mathrm{L}} \times I \tag{3.14}$$

where $I = P/A$ is the laser intensity. Considering in reality that the quantization axis of the nuclei are randomly oriented, we need to divide the result by another factor of 3, making the result agree with Eqn. 3.11.

3.1.2.2 Estimation using Einstein coefficients

We may also perform this estimation using the Einstein coefficients. Again, assuming a simple two-level system with the Einstein B coefficient written as

$$B = \frac{\pi^2 c^3}{\hbar\omega^3} A \tag{3.15}$$

where $A = \Gamma_\gamma = 1/\tau$ is the Einstein A coefficient, the excitation rate is simply calculated as

$$R = B\rho(\omega) = B \times \frac{I}{C \times \Gamma_\mathrm{L}} = \frac{\lambda^3}{8\pi\hbar c} \times \frac{\Gamma_\gamma}{\Gamma_\mathrm{L}} \times I \tag{3.16}$$

which agrees with the previous result in Eqn. 3.11.

3.1.2.3 Estimation using integrated absorption cross section

We know that the integrated cross section of a two-level system is written as

$$\sigma = \frac{\lambda^2}{4} \tag{3.17}$$

Considering the photon absorption rate with only a fraction of $\Gamma_\gamma/\Gamma_\mathrm{L}$ photons on resonance, the absorption rate (and thus the nuclear excitation rate) is

$$R = \frac{\sigma}{\hbar\omega} I \times \frac{\Gamma_\gamma}{\Gamma_\mathrm{L}} = \frac{\lambda^3}{8\pi\hbar c} \times \frac{\Gamma_\gamma}{\Gamma_\mathrm{L}} \times I, \tag{3.18}$$

again in agreement with Eqn. 3.11.

3.2 Nuclear spectroscopy based on internal conversion decay

At the beginning of the thesis work, radiative decay from the thorium nuclear transition had not yet been observed, while the internal conversion (IC) decay channel has been observed [59] and well characterized [29, 62]. Thus, we started building the experiment based on the concept of a nuclear clock based on internal conversion (IC) decay in thin film ^{229}Th targets, as proposed in Refs. [190, 191].

We consider a generic experiment setup where we have a time-gated laser system which irradiates a ^{229}Th spectroscopy target. The internal conversion (IC) process is used for $^{229\mathrm{m}}$Th detection, as illustrated in Fig. 3.1. In IC decay, $^{229\mathrm{m}}$Th transfers its energy directly to an electron and ejects the electron out of neutral thorium samples [59, 29]. We first irradiate a thin film containing many ^{229}Th nuclei, during which a fraction of ^{229}Th is brought to the excited state resonantly if the laser is on resonance with the nuclear transition; see Fig. 3.1b. The excitation rate

can be calculated following the notation in Fig. 3.1a and Sect. 3.1. After a certain irradiation time, the laser is turned off. IC decay of ^{229m}Th gives energy to the electrons. The energetic electrons are subsequently released into free space as the spectroscopy signal; see Fig. 3.1c.

Two types of lasers can be used for this IC-based spectroscopy experiment; see Fig. 3.2. In Fig. 3.2a, a four-wave mixing (FWM) scheme is shown for broadband tunable VUV laser generation [70, 75]. Two UV photons are tuned to a two-photon transition in Xe gas. A visible photon is used to tune the wavelength of the generated VUV photon. The broadband laser system operates with nanosecond laser pulses, offering a natural gating for IC decay detection [190]. Broadband tunability is also advantageous for the initial search of the transition. In parallel to our IC decay search using a VUV frequency comb (Fig. 3.2b) at JILA , a similar experiment was carried out at UCLA [74] using a pulsed FWM laser. The same laser system was later used for the radiative spectroscopy experiment of ^{229m}Th in $LiSrAlF_6$ crystals [28], as well as spectroscopy of $^{229}ThF_4$ thin films [76].

Although having broadband tunability, FWM lasers using the scheme shown in Fig. 3.2 are naturally broadband, limited by the short pulse duration. To obtain a narrow linewidth, a VUV frequency comb is built at JILA using cavity-enhanced high-order harmonic generation [15, 16, 17] in a Xe gas jet (see Chap. 2), shown in Fig. 3.2. The frequency comb consists of 10^5 comb modes, each having ~ 1 nW of comb power [90]. Taking into account the $\sim 10\,\mu$s lifetime of IC decay [29], the lifetime-limited linewidth of the ^{229}Th nuclear transition would be ~ 16 kHz, shown in Fig. 3.2. The narrow linewidth frequency comb lines thus may offer much higher spectroscopy resolution, where each comb mode can be used individually to excite the ^{229m}Th isomer. The large number of comb modes offers a parallel advantage allowing us to cover a wide range of spectrum quickly with a fine step size. Experiments for direct comb spectroscopy of the ^{229}Th nuclear transition are performed at JILA [191].

The VUV comb is directed to a detection setup for the IC decay electrons, shown in Fig. 3.3. As the ^{229m}Th lifetime is around $10\,\mu$s with the IC decay channel [29], it is important for us to remove the VUV beam within a $\sim 1\,\mu$s time scale. While gating the fundamental laser light using

Figure 3.1: Concept of nuclear laser spectroscopy using the internal conversion channel. a, We consider the nuclear excitation via laser with a rate Γ_{exc}. The nuclear decay rate contains two parts, Γ_γ is the radiative decay rate while Γ_{IC} describes the internal conversion (IC) decay rate. b, Nuclear excitation via photon absorption. ^{229}Th embedded in a thin film are irradiated with a laser. One of the resonant photon is absorbed, exciting the ^{229}Th from its ground state, $^{229\mathrm{g}}$Th to its excited state, $^{229\mathrm{m}}$Th. c, Nuclear decay via internal conversion. $^{229\mathrm{m}}$Th transfers its energy to an electron (red dot) through a virtual photon. The electron gains enough kinetic energy to fly off from the surface of the thin film.

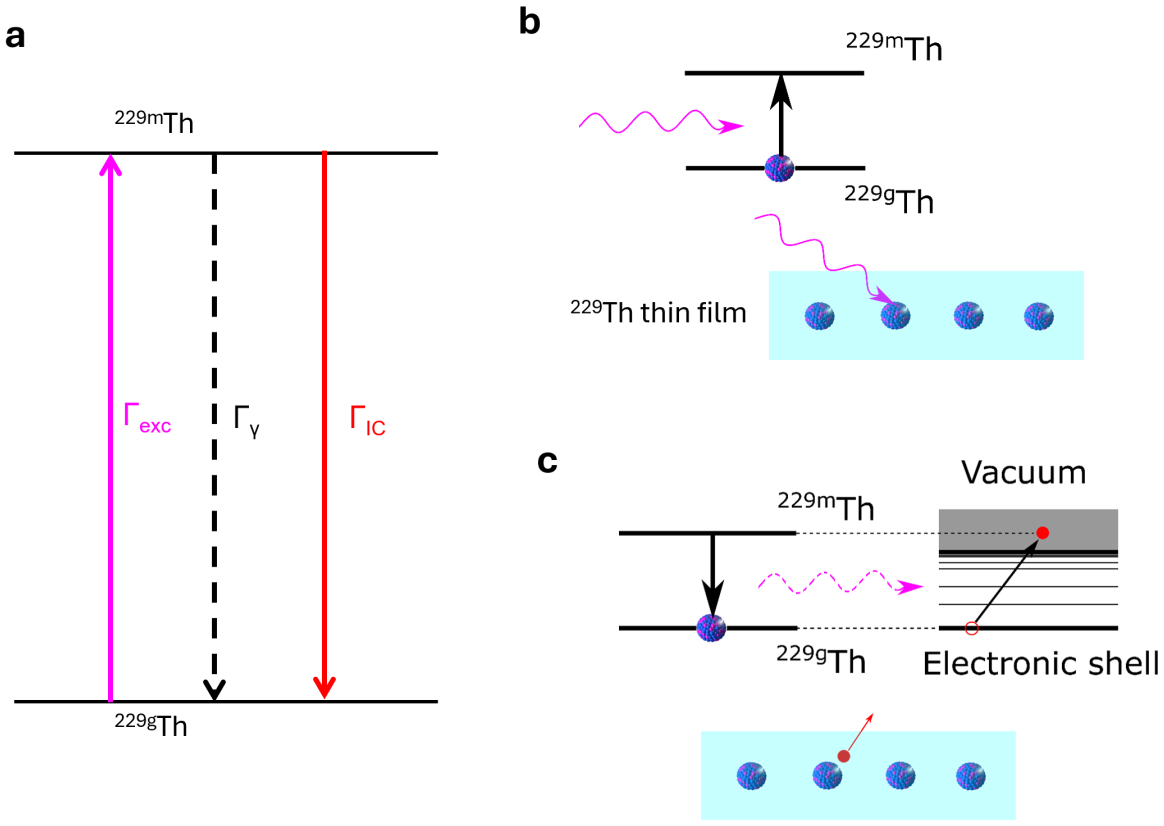

Figure 3.2: Laser systems for nuclear spectroscopy. a, A widely tunable laser generated through a four-wave mixing process in xenon gas. Figure taken from Ref. [70]. b, a vacuum ultraviolet (VUV) frequency comb for the nuclear transition search. We show an idealized nuclear transition line with ~ 16 kHz lifetime-limited linewidth. All comb lines can be scanned in parallel to search for this narrow transition.

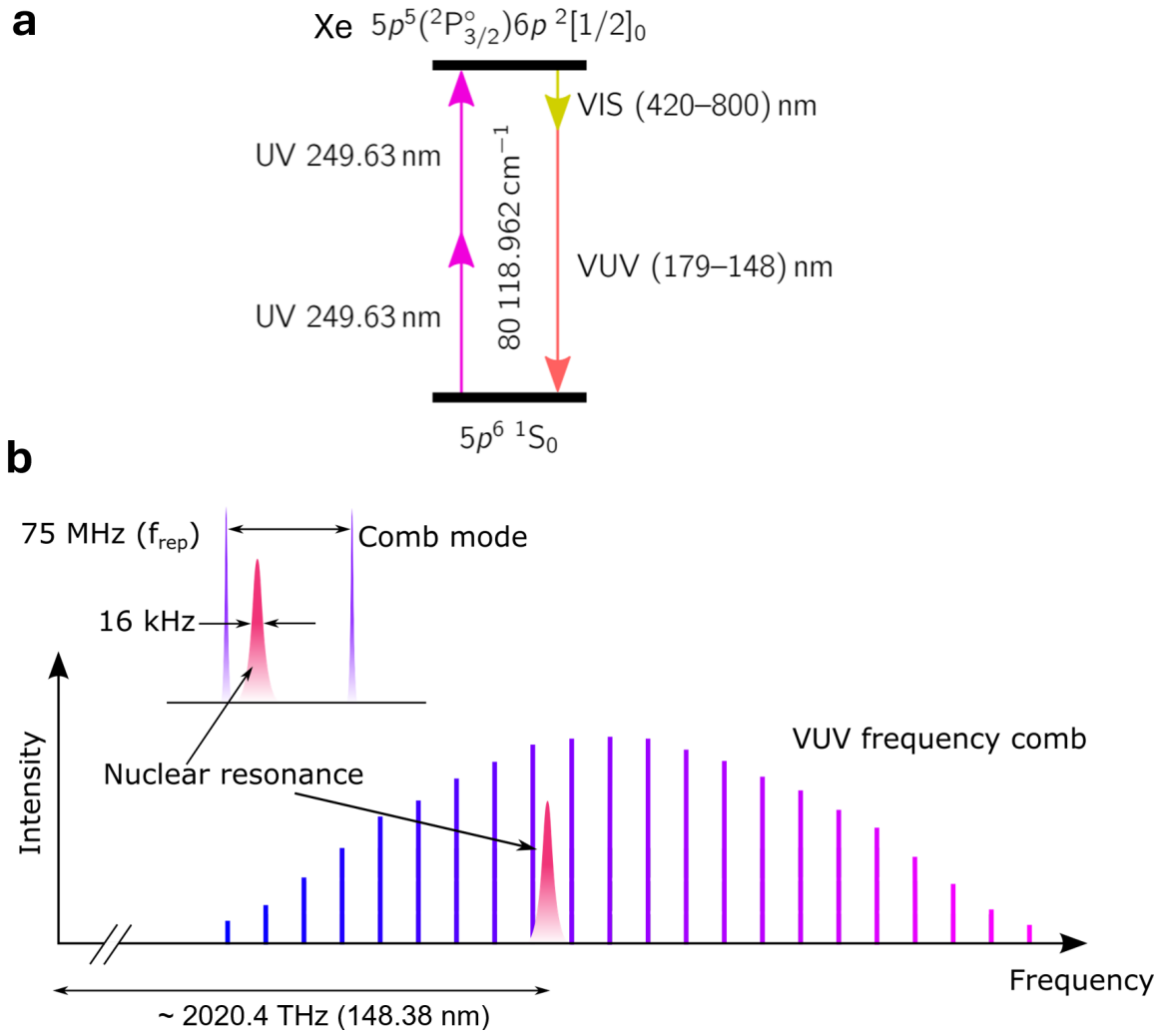

an acousto-optical modulator (AOM) is in principle possible and fast enough, we observed a high background photoelectron count rate with decay lifetimes on the order of tens of µs in practice when the fundamental light is quickly turned off. This is possibly caused by the fluorescence of the Xe plasma jet[4] [198] that gets imaged to the target, kicking off photoelectrons during the detection cycle. A quick estimation of the Xe gas speed in the supersonic jet [119] together with the observed plasma dimension of $\sim$ a few mm also gives a plasma decay lifetime of the same order of magnitude.

To achieve fast gating despite lingering plasma fluorescence, a mechanical chopper wheel is implemented. The VUV comb is focused down tightly through a 200 µm diameter pinhole to reduce the dimensions of the beam to obtain a fast turn-on / turn-off time of ~ 1 µs. A significant amount of fundamental laser power (100 mW $\sim$ 1 W) is reflected off of the GIP outcoupler and travels in the same direction as the VUV comb. However, because of the dispersion of the lens material, the fundamental beam focuses to a different position compared to the VUV beam. The pinhole therefore also serves as a spatial filter to remove residual IR light and other harmonics directed to the target. Due to the high thermal load caused by residual IR light, conventional pinholes made out of laser-drilled tungsten films cannot be used.[5] Instead, a 1 inch diameter, $\sim$ 2 mm thick copper disk was drilled through using a $\sim$ 200 µm diameter drill, with the back side cleared conically, to serve as the pinhole.

Right in front of the pinhole, a chopper wheel driven with a vacuum-compatible motor is installed, see Fig. 3.3b. Several brushless DC motors from Koford Engineering have been tested as the drive for the chopper.[6] We eventually operated a motor at a speed of 30 kRPM. With

[4] Xe is the medium used for generation of the VUV comb, see Chap. 2.

[5] We tried one out. The pinhole mask heats up enough to glow in red.

[6] See `https://www.koford.com/`. Several technical issues are encountered during the tests. Some of the vacuum-compatible motors are contaminated with lubricant oil from the manufacturer, thus careful checks and prebakes monitored using a residual gas analyzer is required. In addition, the Hall sensors for motor control break down at 150 °C, although that is still within the rated operating temperature. Thus, pre-bakes are performed at 100 °C instead. Motor bearings are susceptible to dust contamination that leads to abrupt increases in mechanical friction. Closed-loop motor controllers from the vendor do not allow adjustments of the feed-back loop parameters, thus only open-loop control was implemented. With the motor mounted to the vacuum chamber wall that is isolated from the optical table using thick viton blocks, mechanical vibrations of the motor do not cause an issue for the laser cavity stabilization.

30 slots machined on the chopper wheel, this gives us an operation frequency of 15 kHz. Each cycle consists of $\sim 33\,\mu s$ laser on time for nuclear excitation and a $\sim 33\,\mu s$ laser off time for signal detection. The chopper wheel is machined out of a solid aluminum block and dynamically balanced to less than 2.5 g-in by trimming the edge, limited by the repeatability of the collet.[7] The exact on/off time of the VUV laser beam was monitored using a visible laser beam aligned at a small angle to the VUV laser (red dot in Fig. 3.2b). This small angle allows the visible laser beam to be turned on/off slightly earlier than the VUV laser, giving us a convenient time delay to trigger the control sequences of the detection setup. To reduce the background from scattered photons, we also covered most of the inner side with aluminum foils painted with a vacuum-compatible black paint (Alion MH2200, cured at 400 F).[8]

Efforts are made in the designed detection setup to avoid excess background during the detection window. We use a voltage gating scheme illustrated in Fig. 3.4a. The voltage on the target itself and the voltage on the mount (effectively a ring electrode around the target) are controlled separately. During laser irradiation, the target disk voltage is kept positive (+20 V), so that the photoelectrons coming from the target will not be energetic enough to reach the detector, causing saturation. The mount also serves as a ring electrode and is kept at a large negative voltage (−80 V) such that the photoelectrons freed up from the target surface during irradiation get repelled away quickly. Voltage switching is implemented using an arbitrary wave generator and home-built high voltage amplifiers using a high voltage, high slew rate operational amplifier (PA-85, Apex Microtechnology).

We avoided the use of a magnetic bottle with a permanent magnet as in Refs. [29]. This is because, experimentally, we observe that a significant number of electrons are trapped in the magnetic bottle spectrometer near the target surface during the laser irradiation. Magnetic trapping leads to a large bunch of electrons at the beginning of the detection cycle when the voltage of the

[7] We tried commercial sheet-metal chopper wheel blades. However, their imbalance is too large to allow for operation at the desired speed. In the end, the dynamical balance is performed by NextGen Balancing `https://ngbalancingtechnologies.com/`. A better balancing result can probably be achieved using shrink-fitting, if desired.

[8] According to the JILA machine shop, Krylon K01602A07 ultra flat black paint offers a cheaper and easier solution for applications less demanding for vacuum, after proper heat treatment. Surprisingly, black Sharpie marks are acceptable in ultra-high vacuum.

Figure 3.3: Detection system for IC spectroscopy. a, Schematic of the detection setup. Time gating of a VUV comb is implemented using a mechanical chopper wheel and a pinhole. The gated VUV comb is focused onto a thin-film target on a target mount, with the target voltage and mount voltage separately controlled. Conductive wire-grid meshes are used to control the flow of electrons. A magnetic field generated by a coil wrapped around the vacuum chamber is used to guide the electrons to a MicroChannel Plate (MCP) detector for single electron counting. b, Photo of the mechanical chopper wheel.

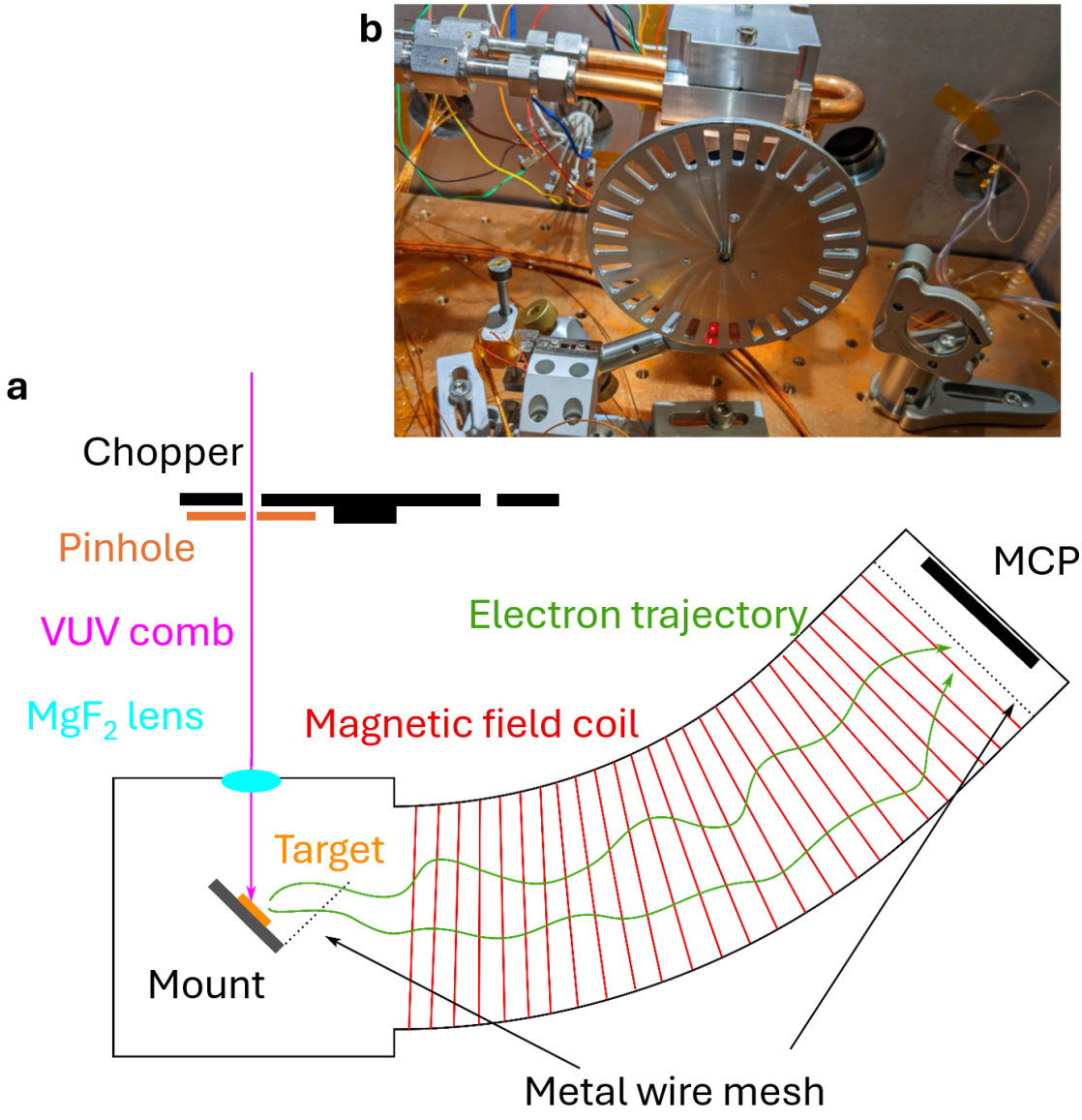

target is rapidly switched. We observe that the surface quality has a significant impact on the background photon count rate. We use an argon sputtering gun to clean the surface. Ar ions with 500 eV of kinetic energy are used to sputter the surface for 30 seconds before the experiment cycle to remove the hydrocarbon coating on the target.

Signal collection efficiency is estimated by turning off the high bias on the MCP detector and measuring the photoelectron current from the target and to the MCP detector front surface. The collection efficiency is estimated to be ~ 0.5. Insulators near the target area, such as Kapton tape, may charge up significantly under VUV irradiation, which leads to bending of the electron trajectory and significantly reduces the signal count rate. Thus, we ensure that the front surface of the target mount is made of conductive metal.

The result of a typical scan cycle is shown in Fig. 3.4b. During the first $\sim 30\,\mu s$, the chopper wheel is open so that the VUV laser is irradiating the target. Although no electrons can fly to the detector due to voltage gating, a small amount of scattered light may reach the detector. The scattered photons lead to a constant high count rate on the MCP during the laser irradiation cycle. At $\sim 30\,\mu s$, the chopper wheel closes and the target / mount voltages are switched according to Fig. 3.4a. As ^{229}Th is radioactive, electrons are automatically ejected from the target when a radioactive decay event occurs. With the proper voltage gating scheme presented in Fig. 3.4, the electron counts collected in this region of interest originate dominantly from the intrinsic radioactivity of the target itself. At $\sim 90\,\mu s$, we switch the voltage of the electrodes again so that the electrons from the target cannot reach the detector. The count rate is then limited by the intrinsic background of the detector itself. After $\sim 110\,\mu s$, the chopper opens again and the irradiation/detection cycle repeats. If the nuclear transition is successfully excited, an elevated count rate is expected in the first $\sim 10\,\mu s$ after the laser irradiation.

For this concept, we would need a target with a low band gap to enable the IC decay and a low work function/electron affinity to enable the release of free electrons. Ideally, what we are looking for is a good photocathode, as the photoelectric field is similar to the IC electron ejection mechanism that we plan to use for nuclear excitation signal detection; see Fig. 3.5. In general,

Figure 3.4: Voltage gating scheme for background suppression. a, Voltage switching scheme of the target disk and the ring electrode (target mount) synchronized with the chopper. b, Signal count rate as a function of time during the detection cycle, dependent on the voltage switching times.

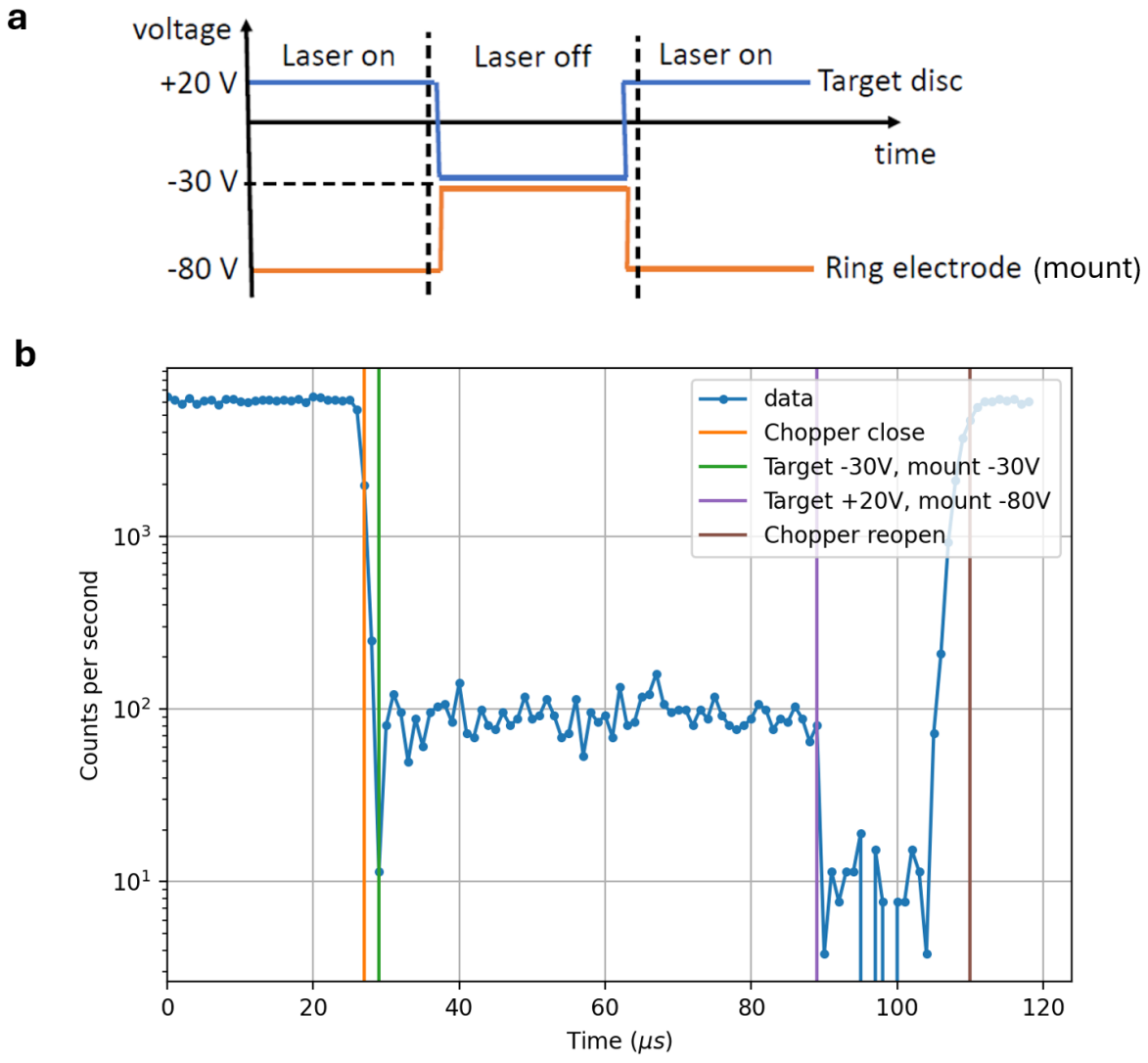

low band gap insulators have longer inelastic scattering mean-free-paths of electrons compared to those of metals, thus offering higher quantum efficiency for photocathode applications. We choose $^{229}ThO_2$ for the experiment due to its chemical stability and the potentially relatively high electron emission efficiency predicted theoretically.

We also ensure that the sample is thin enough for VUV photons to penetrate efficiently into the material for nuclear excitation. Using the attenuation coefficient of $\alpha \sim 0.1$ nm^{-1} reported in Ref. [199] for $^{229}ThO_2$, for a 10 nm thick layer, the nuclear excitation rate decreases by a factor of $\eta_{abs} = 0.63$ [191] due to material absorption.

Figure 3.5: Comparison of IC decay and photoelectric effect. a, IC decay effect considered in the proposed scheme. The ^{229m}Th state decays, transferring its energy to an electron in the bulk by a virtual photon. The electron (orange) scatters around in the bulk material (light blue) and escapes through a surface potential barrier (dark blue) to vacuum. b, Photoelectric effect, where the electron gains energy by absorption of a photon. Note, the electron scattering process and escape efficiency is the same as the IC electron ejection. c, A three-step model for calculating the photoemission efficiency, adapted from Ref. [200].

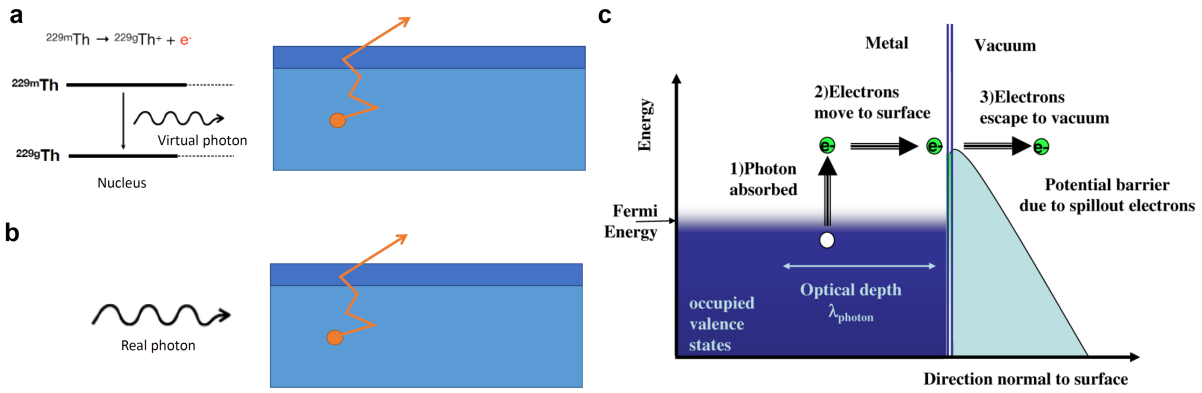

To predict the efficiency of IC electron ejection, we consider the band structure of $^{229}ThO_2$ shown in Fig. 3.6. The relevant parameters can be found in Ref. [191]. The photoelectron efficiency can then be calculated accordingly [200].

However, the predicted photoelectron quantum efficiency (QE) on the order of $\sim 10\%$ in Ref. [191] deviates a lot from our experimentally measured results of $< 0.1\%$. There are several corrections that need to be applied to the calculations presented; see Sect. 3.5 for more details and

Figure 3.6: Band structure of $^{229}ThO_2$. The parameters noted are used for estimating the IC electron escape efficiency: E_F is the Fermi energy, E_{vac} the vacuum energy, E_{wf} is the work function, E_{cbm} denotes the conduction-band minimum and E_{vbm} the valence-band maximum, E_{gap} band gap, E_{iso} the isomer energy, and E_{kin} is the kinetic energy of the IC electron. Figure adapted from the Ref. [191].

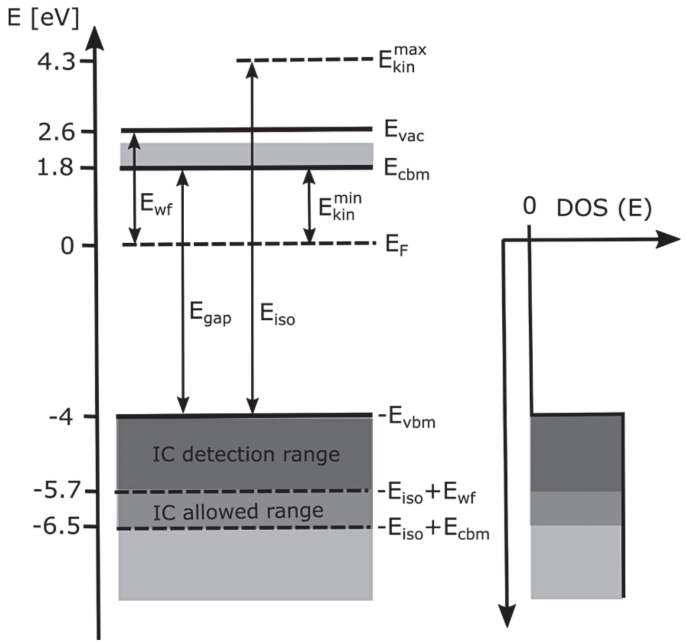

potential solutions.

3.3 Experimental fabrication of $^{229}ThF_4$ and $^{229}ThO_2$ thin films

There is no commercially available high-quality thin-film $^{229}ThO_2$ target. Here we present our effort to obtain thin-film $^{229}ThO_2$ targets using a few different ways.

Figure 3.7: Photos of ^{229}Th targets. a, Target fabricated using drop-on-demand technique. b, Target T5-306, electroplated on stainless steel. c, Target T5-307, electroplated on platinum.

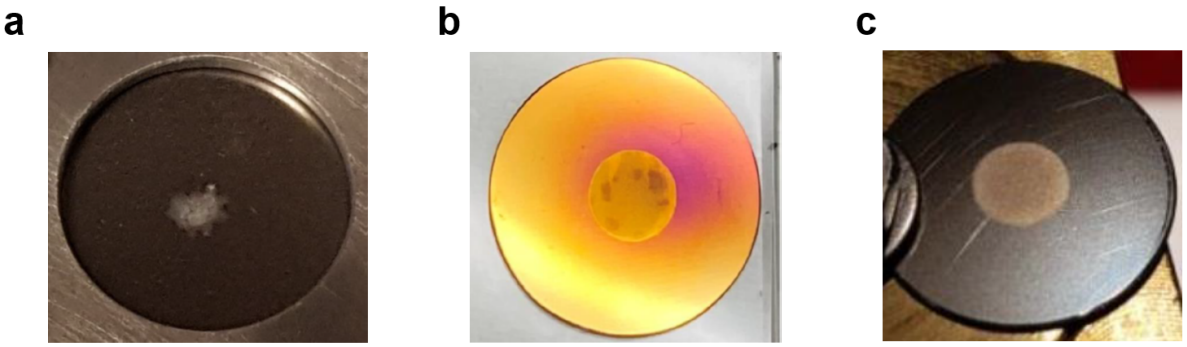

3.3.1 Drop-on-demand target fabrication

A first attempt is made using the drop-on-demand technique described in Ref. [201], carried out by our collaborators in Johannes Gutenberg-Universität Mainz [84]. In this process, $^{229}Th(NO_3)_4$ dissolved in water is dropped onto a titanium substrate plate using microdroplets. The dried $^{229}Th(NO_3)_4$ are then heated to 110 °C for annealing. In this effort, only one target is produced, which contains a ^{229}Th activity of 4.1 kBq and a 5.8 kBq activity of ^{228}Th contaminant. The large activity of ^{228}Th comes from the much shorter lifetime of ^{228}Th compared to ^{229}Th, and does not significantly dilute the content of ^{229}Th. However, its powdery appearance raises concerns about its mechanical integrity; see Fig. 3.7a. Thus, we eventually disposed of this target after using it for some preliminary tests.

There are a few possible improvements that may lead to better results.

(1) Material purity. The target contains 4.1 kBq of ^{229}Th which amounts to $< 1\,\mu$g of material. However, visually the content on the target substrate seems much greater than 1 µg. Possible contaminants in the water solution of $^{229}Th(NO_3)_4$ should be analyzed and further purification should be performed.

(2) Droplet size. It is unclear if the printing technique using microdroplets [201] was used or if a larger droplet was dispensed directly. Smaller droplets tend to leave a more uniform residue after evaporation [202]. Given the specific need of our experiment, smaller targets would be favorable. Simple picoliter dispensers based on piezo [203, 204], pneumatic systems [205], or electrospray techniques [206] may suffice for this task.

(3) Different material choice. Although band gap calculations were performed here only for $^{229}ThO_2$, other chemical forms of ^{229}Th could be favorable for thin film fabrication. A simple idea is to fabricate $^{229}Th(NO_3)_4$ thin films directly. Experimentally, dry $^{229}Th(NO_3)_4$ (or possibly its hydrates) is observed to form a smooth surface when the water solution evaporates slowly. Further heating beyond 55 °C leads to melting and bubbling of the dried residue that destroys the smooth surface.

3.3.2 Electro-plating of ^{229}Th

Motivated by thin-film ^{233}U targets used in Ref. [59], we also tried electroplating [207] to obtain a thin-film target. As electroplating is a standard procedure in the fabrication of calibration targets for α spectrometers, we acquired two separate targets through a company (Eckert & Ziegler) using different procedures.

(1) Target T5-306, see Fig. 3.7b. 11.5 kBq ^{229}Th electroplated on a $\varnothing$= 5 mm surface of a stainless steel disc ($\varnothing$= 15.875 mm, 0.5 mm thick, polished in the JILA glass shop). The surface of the stainless steel was first etched using a 5% H_2SO_4 solution before the plating. ^{229}Th was plated using a bath of $(NH_4)_2SO_4$ for about 1 hour. After plating, the target was annealed over a Bunsen flame for diffusion bounding.

(2) Target T5-307, see Fig. 3.7c. 19.9 kBq electroplated on a $\varnothing = 5$ mm surface of a pure platinum disc ($\varnothing = 15.875$ mm, 0.5 mm thick, polished in the JILA glass shop). After learning from the previous plating results, we made the following changes [208]:

- Use all new components in the plating cell (including the platinum wire and plate insert).
- A blind plating run was performed before adding the ^{229}Th on a dummy substrate to further purify the solution.
- No chemical or mechanical cleaning is involved on the platinum plate. It is electroplated after alcohol rinsing. This is to help facilitate AFM measurements of the plated surface height.
- Use ultrapure reagents:
  - HPLC grade or ultrapure isopropanol instead of acetone as the electrolyte.
  - Ultrapure nitric acid to adjust current density.
  - Ultrapure ammonium hydroxide to stop the plating.
  - Ultrapure water and ethanol to rinse the platinum foil after plating.
- Th-229 batch to be used is "as is" condition as provided by radiochemistry. The volume is likely to be $10-20\,\mu$L.
- Plate at $30-50$ V; $5-7$ mA. The dwell time for plating is 30 minutes.
- Plated platinum annealing on a hot plate at the highest setting for 1 hour.
- Electrodeposited and diffusion-bonded on customer-supplied platinum foil on a modified PM shipping holder, 15.8 OD $\times$ 5 mm ID $\times$ 0.5 mm Pt.

Before using a solid disc of Pt, a Pt-coated Si wafer (150 nm thick Pt on top of a $\sim$ 30 nm TiO_2 bonding layer, custom made at the University Wafer) was tried for the electroplating procedure. However, the Pt film peeled off during the plating tests, and thus we opt for a solid Pt disk instead.

The activities of the two targets are calibrated by the manufacturer by measuring the kinetic energy spectrum of the α particles from the target, shown in Fig. 3.8. These targets also served as calibration sources for our own α spectrometer to characterize the targets fabricated in-house.

We characterize the two electroplated targets using various tools.[9] A microscope picture and the atomic force microscope (AFM) scan image of target T5-306 are presented in Fig. 3.9. The images are taken close to the edge of the electroplated area. From the optical microscope image, one can already see the obvious clustering of black material on the coated area. The AFM image further confirms that the coated area consists of peaks and valleys with a height of the order of $\sim$ 100 nm, much thicker than the designed thickness of 10 nm corresponding to the quantity of ^{229}Th material used. Evidently, the target contains a significant amount of contaminants that dilute the ^{229}Th content in the top layer. Target T5-307 shows a very similar behavior in which the material clusters to high peaks in the coated area.

To understand what contaminants are in the ^{229}Th targets, we performed X-ray photoelectron spectroscopy (XPS) of the ^{229}Th targets.[10] Results are shown in Fig. 3.10. Using a monochromatic X-ray source, photoelectrons are ejected from the target. The kinetic energy of photoelectrons is analyzed using a hemispherical electron energy analyzer. Electrons coming from different specific orbitals of elements carry different kinetic energy, therefore offering elemental resolution of the target material.[11] Data are analyzed according to Ref. [209]. Taking into account the emission efficiency of each element, the atomic percentage of ^{229}Th in the targets is estimated to be $\sim 1\%$. Therefore, these targets are deemed not suitable for the ^{229}Th nuclear spectroscopy experiment.

[9] We would like to acknowledge the JILA Keck Lab staff, including Dave Alchenberger, Curtis Beimborn, Amy Ekiriwang, Scot Bohnenstiehl, Alan Copley for technical assistance on these measurements.

[10] We would like to acknowledge Andrew S. Cavanagh for technical assistance on XPS data collection and interpretation.

[11] Another way to analyze the element on a surface is through Energy Dispersive Spectroscopy (EDS), where a scanning electron microscope or a focused ion beam is used to excite the electronic states, and the X-ray emission is measured to analyze the elemental composition. This could even allow one to map out the spatial distribution of different elements. The Colorado Shared Instrumentation in Nanofabrication and Characterization (COSINC) is facilitated with EDS measurements. We acknowledge Tomoko Borsa for discussions about COSINC capabilities.

Figure 3.8: α-spectrum of T5-306. a, α-spectrum of target T5-306 supplied by Eckert & Ziegler Isotope Products. Zoom-in view of the region containing the α-peaks of ^{229}Thclose to 5000 keV. The full-width half maximum of the peaks are $\sim$ 30 keV. b, Zoom-out view of the α-spectrum of target T5-306. Data provided by Eckert & Ziegler Isotope Products.

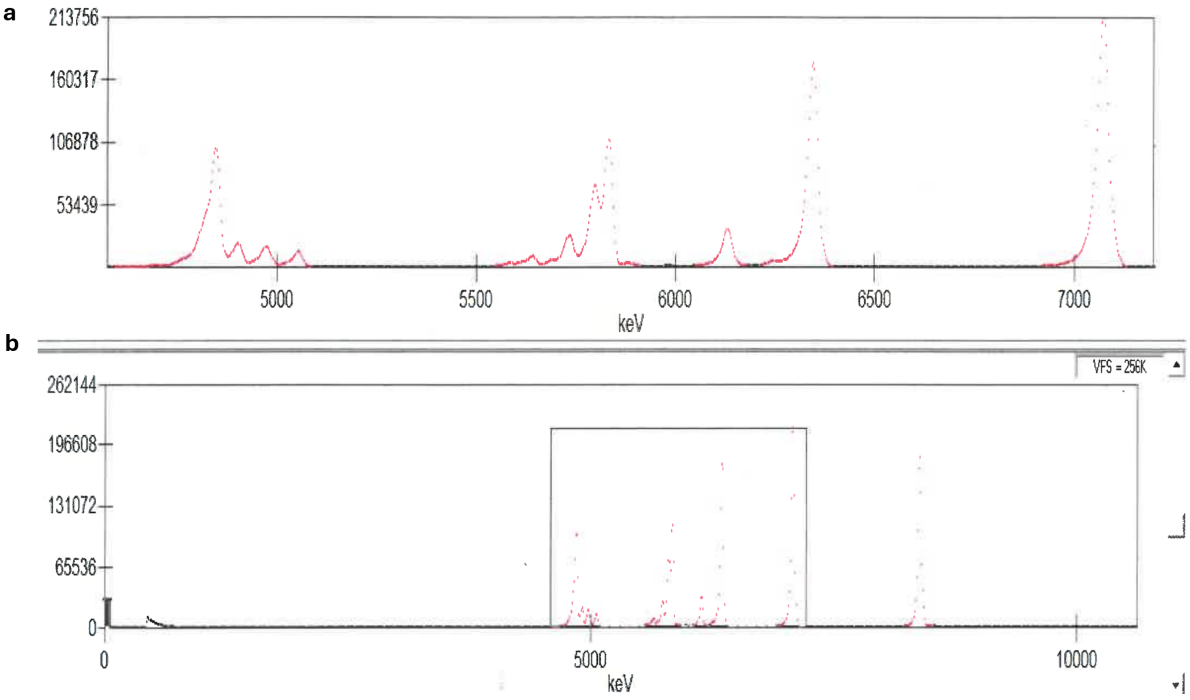

Figure 3.9: Microscope and AFM photos of T5-306. a, Optical microscope image. Bottom left corner is uncoated substrate. Top right side is the coated area of the target. A possible triangular scratch to the surface in the center is shown, where some black material appears to have been removed. This scratch is already present with the target received as is. b, Atomic force microscope (AFM) image of the target. Similar to that in a, the bottom left corner shows the uncoated area with good surface flatness. The top right corner shows the ^{229}Th coated area, where obvious etching of the substrate is present, evident by the $\sim$ 100 nm high peak and valleys.

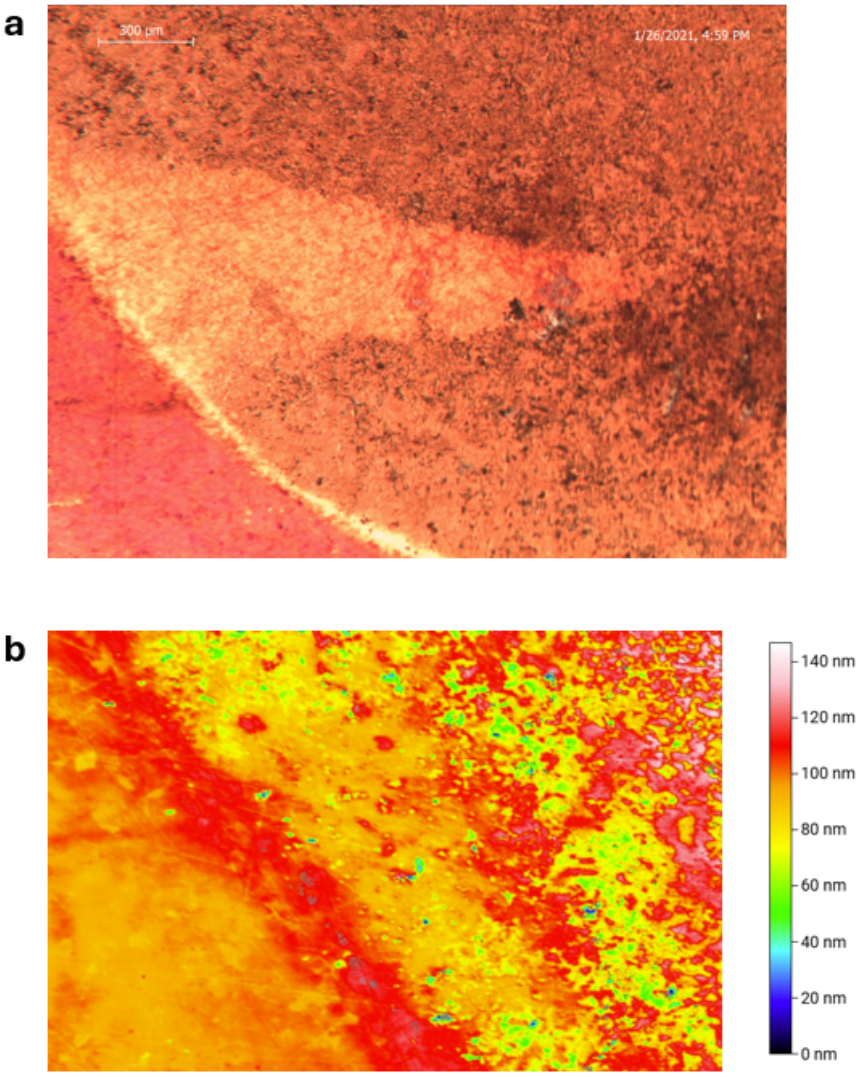

Figure 3.10: X-ray photoelectron spectroscopy results of the electro-plated targets. Peaks of the electron energy originates from specific orbitals in certain elements. A few dominant peaks are labeled in the plot with their origin.

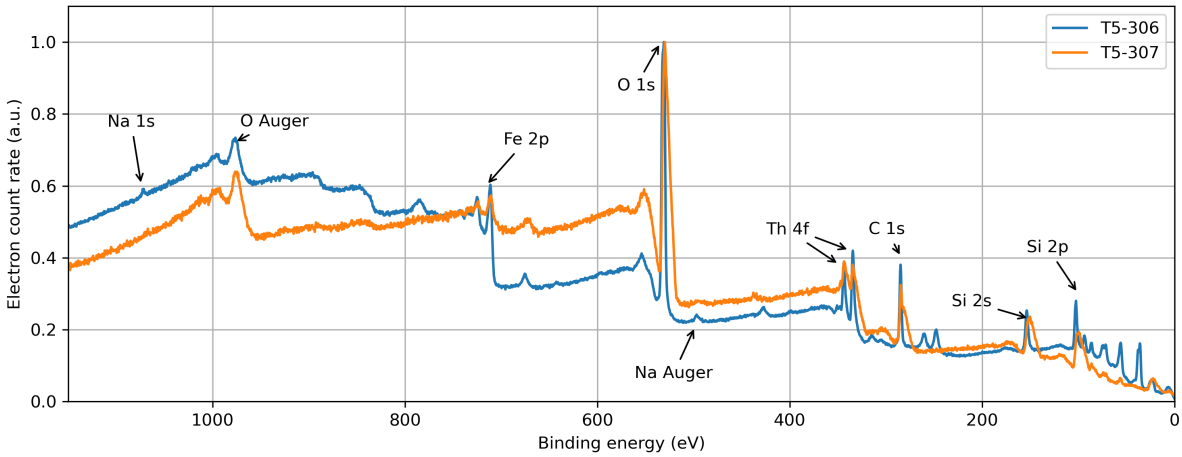

3.3.3 Radioactive physical vapor deposition

In order to obtain a high quality $^{229}ThO_2$ target, we built a new machine to perform physical vapor deposition (PVD).

To perform thin film deposition, coating materials can be heated up by either electrical heaters or electron beams. Alternatively, ion beams can be used to directly sputter the material. With the small quantity of ^{229}Th material available, it is impractical to use an electron beam or ion beam to evaporate ^{229}Th material specifically without also evaporating its container material. Thus, we choose to use physical vapor deposition using a resistive crucible heater.

The vapor pressures of a few common thorium compounds are shown in Fig. 3.11. $^{229}ThF_4$ with much higher vapor pressure at low evaporation temperature is chosen as the material for evaporation coating. However, $^{229}ThO_2$ is a better candidate [191] for IC electron spectroscopy because of its low band gap. Thus, chemical conversion of the $^{229}ThF_4$ thin film to the $^{229}ThO_2$ thin film is later performed using a pyrohydrolysis process [210, 211]. Commercially available $^{232}ThF_4$ coating [212] are first purchased from Infinite Optics to validate the idea, with XPS measurements that confirm the successful conversion from ThF_4 to $^{232}ThO_2$. A setup for the $^{229}ThF_4$ coating is developed to minimize the amount of ^{229}Th material used in each coating run.

Physical vapor deposition of rare radioactive isotopes, especially actinides, has been a standard technique for the fabrication of nuclear targets used in accelerator facilities for nuclear physics experiments [216, 217, 218, 219, 220, 221]. However, in recent years, there have been fewer reports on the fabrication of vapor-deposited radioactive targets [222]. Thus, we decided to build a new machine for the fabrication of ^{229}Th targets in the lab.

For target fabrication, a quantity of $\sim$ 5.1 MBq ($\sim$ 700 µg) of ^{229}Th material (Batch No. UTHX1-Th229-C-8, isotopic purity: 99.96%, chemical purity: 99.99%) is purchased from the Oak Ridge National Lab through the National Isotope Development Center (NIDC), at a price of $ 112 per µg. A later batch (Batch: TH229BATCH) of 100 µg of ^{229}Th is purchased at a price of $ 120 per µg but is not used in the work presented in this thesis. The material is delivered in

Figure 3.11: Vapor pressure of thorium compounds. Analytical pressure curves are taken from Ref. [213] for Th metal, Ref. [214] for $^{229}ThO_2$, and Ref. [215] for $^{229}ThF_4$.

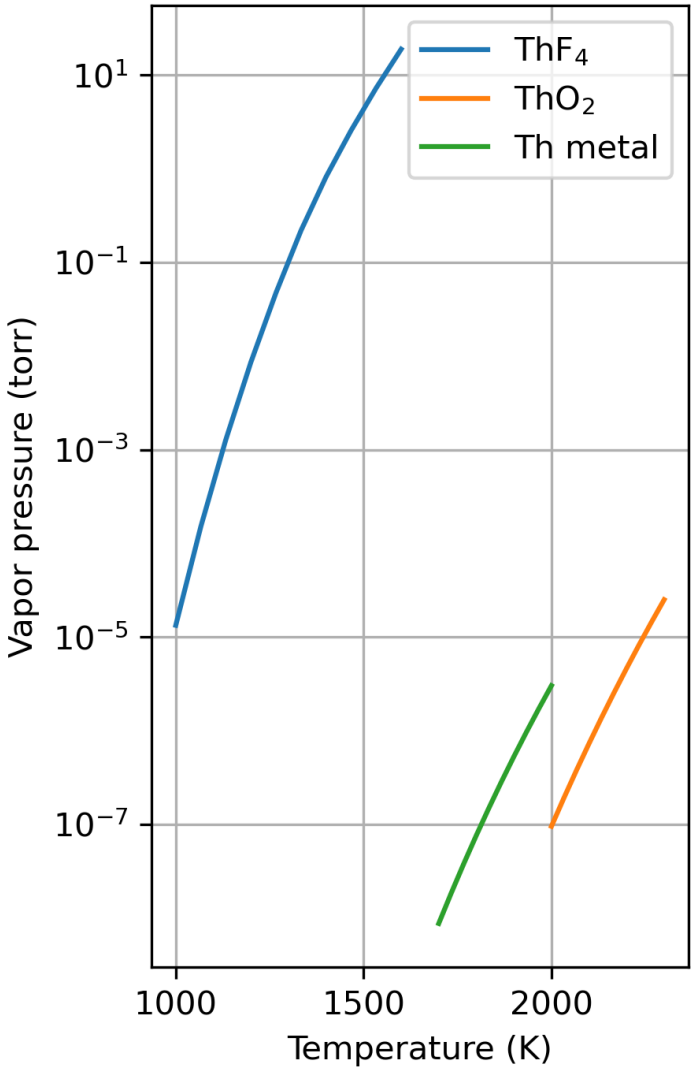

the chemical form of $^{229}Th(NO_3)_4$ and the mass quantity refers to the pure ^{229}Th mass contained. One gram of $^{232}Th(NO_3)_4$ material is purchased from United Nuclear at a price of $34.5 per gram for tests to avoid waste of the expensive ^{229}Th isotope and minimize radioactive exposure to us when performing the experiment.

We dissolve the received $^{229}Th(NO_3)_4$ material in 540 µL of Ultrapur Water from Millipore Sigma. From the solution, 10 µL is transferred to a different vial using a pipette.[12] This new vial is further diluted with 290 µL ultrapure water. For each coating run, we typically transfer ∼ 20 µL of the diluted solution containing ∼ 6 kBq of $^{229}Th(NO_3)_4$ material to a small glassy carbon crucible shown in Fig. 3.12a.[13] Then ∼ 10 µL of 40% HF is added to the crucible to form $^{229}ThF_4$ precipitates, following the reaction

$$[Th(NO_3)_4]_{aqu} + 4\,[HF]_{aqu} \longrightarrow ThF_4 \downarrow + 4\,[HNO_3]_{aqu}\,. \tag{3.19}$$

The crucible is then heated to 130 °C on a hot plate for 30 minutes to dry the excess water, hydrofluoric acid and nitric acid. A tight-fit lid (Fig. 3.12a) is added on top of the crucible to further reduce the area of the evaporated $^{229}ThF_4$ molecular beam during coating. The crucible weight is measured using a microbalance (Mettler Toledo MX5, resolution of 1 µg) before and after adding ^{229}Th material to confirm weight increase.

We load the crucible containing dry $^{229}ThF_4$ into a tantalum crucible heater installed in a 6-inch cubic vacuum chamber, see 3.12b and c.[14] A small piece of glassy carbon rod is used to support the crucible to reach the desired height. The heater is directly clamped to a high-current vacuum feedthrough (Kurt J. Lesker, Type EFT0823373, 330 A, 8 kV) using a copper mounting structure. Other substrates such as MgF_2, Al_3O_2, Ce:YAG, and Si have also been tested.

Platinum-coated Si wafers of 0.5 mm thickness and 5/8 inch diameter are typically used as

[12] A set of pipettes are used, model Eppendorf Research plus, ranges 0.5 – 10 µL, 10 – 100 µL, 100 – 1,000 µL.

[13] The glassy carbon crucible material is purchased from HTW Hochtemperatur Werkstoffe GmbH. The crucible shape is machined in the JILA Instrument Shop. Glassy carbon is used for its resistance to fluoride-containing material.

[14] The crucible heater is Kurt J. Lesker, Type EVCH7, with its shape slightly modified in the JILA Machine Shop.

Figure 3.12: Vapor deposition setup. a, Photo of the glassy carbon crucible. b, Photo of the vapor deposition chamber in operation. c, Conceptual sketch of the vapor deposition setup.

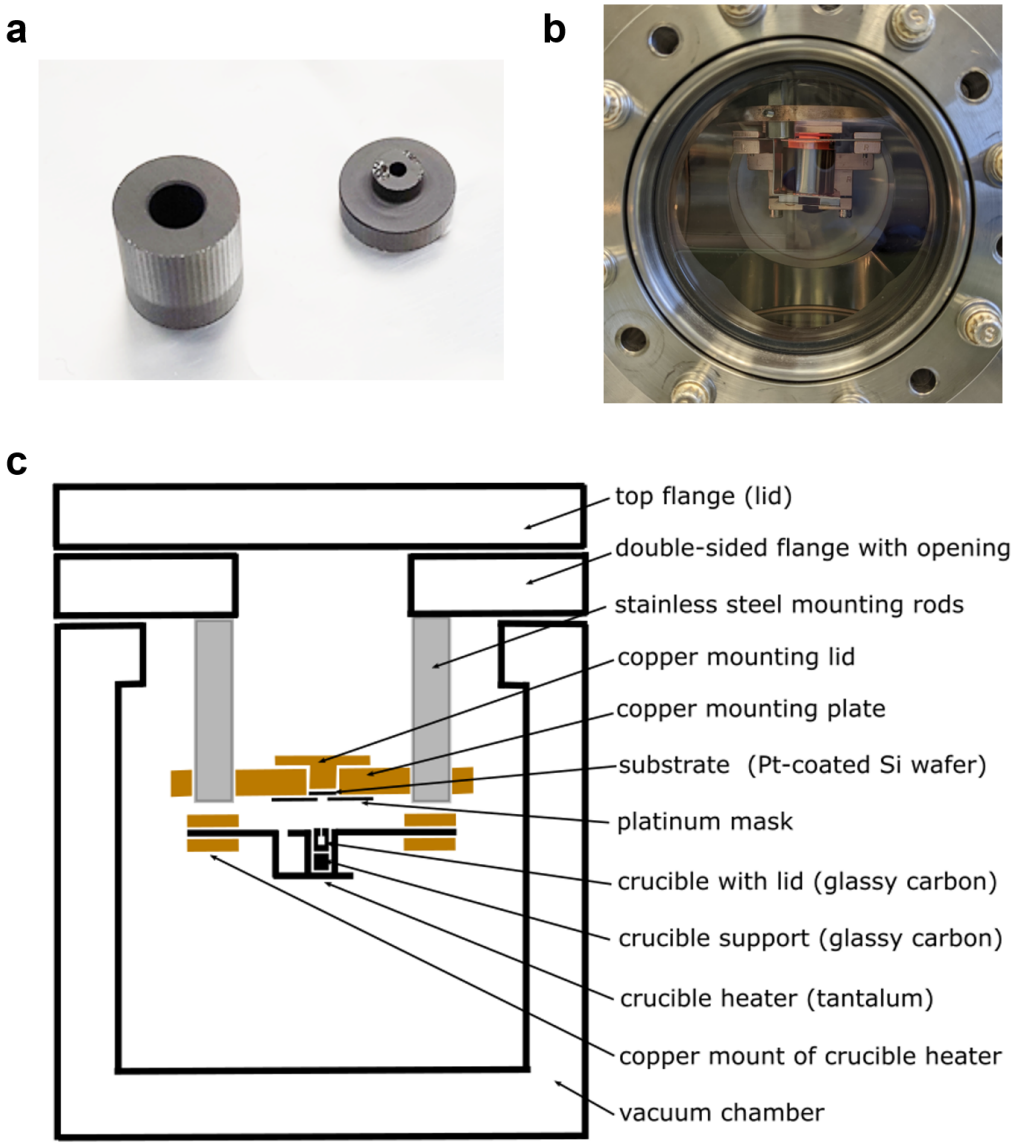

the coating substrate.[15] A platinum mask (GoodFellow PT00-FL-000171, 25×25 mm size, 0.25 mm thick) with a ~ 5 mm center hole is used to hold the substrate with a copper lid pushing from the top side. Smaller Pt pinhole masks are used to further reduce the coating area if a small target is desired.[16] Pt is chosen to allow easier recovery of the ^{229}Th material if needed in the future.

The copper mounting structure for the substrate is installed on a 6-inch double-sided flange. The height of the substrate can be adjusted using the stainless steel mounting rods. The double-sided flange design allows us to easily load/unload the substrate from the top side (Fig. 3.12c). A turbo pump is directly connected to the chamber, allowing us to reach a 10^{-6} torr vacuum pressure ~ 30 minutes after the start of the pumping procedure, when coating runs are performed. Up to 10^{-9} torr vacuum level can also be easily reached in longer waiting times.

Before coating runs, the crucible heater and the crucible (without $^{229}ThF_4$ loaded) are cleaned by rinsing with distilled water and methanol and loaded into the crucible heater for a dummy coating run. In this dummy coating run, the crucible heater is heated to 1600 °C at 187 A current for 30 min to evaporate any residual contaminant. For vapor deposition, the current that passes through the crucible heater is slowly increased to 130 A and held there for 10 minutes before termination. The corresponding temperature of the heater is 1208 °C, precalibrated with an optical pyrometer.[17] After the coating run, the chamber is left to cool for about 2 hours before venting. Removal of the coated substrate is easy with a vacuum tweezer (Chip Quik TV-1000).

The $^{229}ThF_4$ samples are then converted to $^{229}ThO_2$ using a pyrohydrolysis procedure [210, 211] following the reaction

$$ThF_4 + 2H_2O \xrightarrow{550\,^\circ C} ThO_2 + 4HF. \tag{3.20}$$

The setup is shown in Fig. 3.13. Argon gas is saturated with water vapor by bubbling through distilled water and sent to the target through a glass tube to supply the moisture needed for this

[15] The wafers are custom made at University Wafer, with 150 nm thick Pt coating on top of 30 nm TiO_2 bonding layer.

[16] We purchased 0.05 mm thick Pt foil from Alfa Aesar. The 50 µm or 100 µm diameter holes are laser drilled at Lenox Laser.

[17] A discontinued model of optical pyrometer is used from https://www.pyrometer.com/ A tungsten wire is heated inside the pyrometer with a pre-calibrated current-to-temperature relation. We match the brightness of the tungsten wire with the hot device under test in the field of view of the pyrometer.

Figure 3.13: Pyrohydrolysis. a, Schematic of the pyrohydrolysis setup for converting $^{229}ThF_4$ thin films to $^{229}ThO_2$ thin films. b, Photo of the pyrohydrolysis setup.

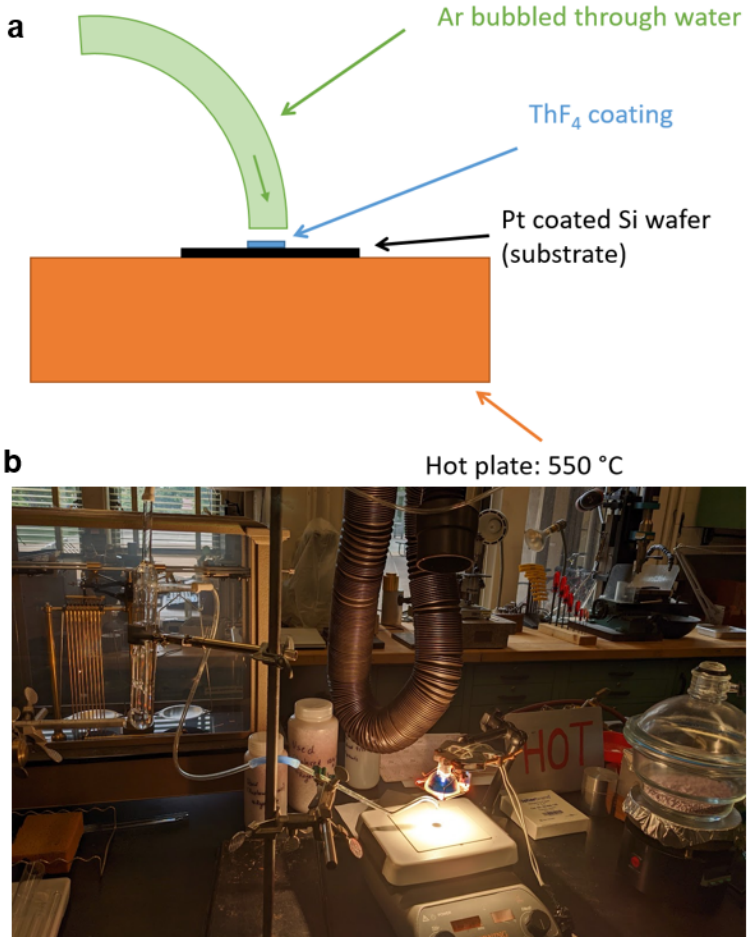

reaction. The target is placed on a hot plate (Corning, PC-420D) set at a temperature of 550 °C. A 300 W halogen lamp (Omnilux ELH, 120 V) is placed a few cm above the target to further increase the temperature. We run the process for 1 hour, although significantly shorter reaction times may be sufficient. The surface of the substrate remains intact and the $^{229}ThO_2$ layer remains attached to the surface after this process.

The chemical compositions of the targets are checked with XPS again; see Fig. 3.14. Before pyrohydrolysis, the target is dominantly $^{229}ThF_4$, with a small amount of carbon and oxygen from surface hydrocarbon contamination. After pyrohydrolysis, the fluorine peak completely disappears and the target is fully converted to $^{229}ThO_2$.

Figure 3.14: X-ray photoelectron spectroscopy results of the physical vapor deposited (PVD) targets, before ($^{229}ThF_4$) and after($^{229}ThO_2$) pyrohydrolysis. Peaks of the electron energy originates from specific orbitals in certain elements. A few dominant peaks are labeled in the plot. Figure adapted from Ref. [76].

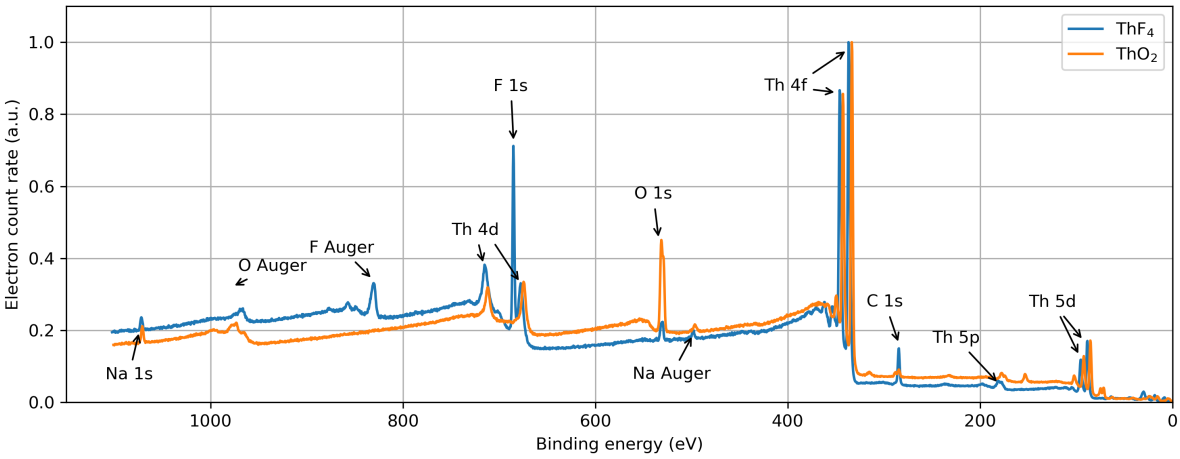

We also characterized the PVD targets using AFM before and after the pyrohydrolysis treatment. For this, a 50 µm diameter target is produced. The layer thickness of the $^{229}ThF_4$ target as deposited is measured to be 32 ± 2 nm, while after pyrohydrolysis it shrinks down to 23 ± 2 nm; see Fig. 3.15. Due to the density difference between thorium oxide and thorium fluoride, the expected volume shrinking factor is

$$\rho_{ThF_4}/\rho_{ThO_2} \cdot M_{ThO_2}/M_{ThF_4} \approx 0.54, \tag{3.21}$$

where ρ denotes the density and M the molecular mass of the corresponding chemical form. The deviation of the observed shrinking factor of $23/33 \sim 0.70$ is likely due to the amorphous structure of the thin films, resulting in a density different from that of the bulk samples.

We also investigate the PVD targets using α spectroscopy. The energy of the α particles emitted from the surface is investigated using a single channel α spectrometer.[18] A sample α spectrum is shown in Fig. 3.16 compared to a spectrum taken using the calibration target T5-306 purchased from Eckert & Ziegler Isotope Products, shown in Fig. 3.8. By comparing the integrated count rate in the region of interest (ROI) highlighted in Fig. 3.16 and using the activity of T5-306 being 11.49 kBq, the activity of the 50 µm target is measured to be 3.0 Bq. This is reasonably close to the activity of a $\sim$ 30 nm thick, $\sim$ 50 µm diameter $^{229}ThF_4$ disk. We also note that the daughter isotope concentration in the vapor-deposited target appears to be lower than that of the electroplated T5-306 target. This is likely because the PVD process distills the ^{229}Th material. It will return to equilibrium after a long enough waiting time.

Originally, $^{229}ThF_4$ was assumed to have a band gap of 6.53 eV [223], thus not being transparent to the VUV light at 148.4 nm ($\sim$ 8.4 eV). However, recent work indicates that $^{229}ThF_4$ actually has a band gap of around 10 eV [224, 225], making it possible to observe radiative decay photons in $^{229}ThF_4$ samples. To experimentally test this, we made a thick ($\sim$ 1 µm) ThF_4 target with a diameter of 5 mm, covering part of a 10 mm square MgF_2 substrate. Using the setup shown in Fig. 3.17a, we measured the ratio of the transmitted power of a D_2 lamp (Hamamatsu L7293) on the coated/uncoated area of the MgF_2 substrate, shown in Fig. 3.17b. The VUV transmission is spectrally dispersed using a grating spectrometer (HP Spectroscopy, easyLIGHT), with the wavelength axis calibrated using the D_2 lamp spectrum [226]. The high transmission down to nearly 125 nm wavelength agrees with the large bandgap of ThF_4 reported in Refs. [224, 225] and inspired us to try the nuclear transition search also with radiative photons [76], see Sect. 3.6.2.

A further check of the VUV transparency is made with thorium oxide. A similar ThF_4 coating is fabricated on a sapphire (Al_3O_2) substrate. Al_3O_2 is chosen for its transparency at 148 nm [130]

[18] Ortec/Ametek, alpha-aria, using a Ortec/Ametek, U-019-300-AS silicon charge detector.

Figure 3.15: AFM measurement of PVD targets, before (a, c) and after (b, d) pyrohydrolysis. Figure adapted from Ref. [76].

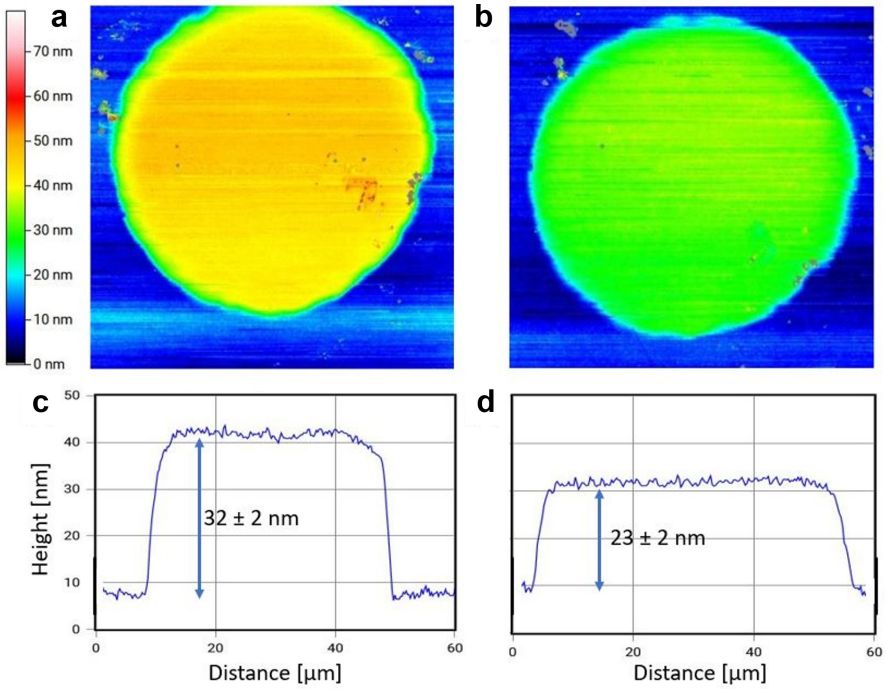

Figure 3.16: α spectrum of a PVD target, $^{229}ThF_4$ #8, shown in comparison with the α calibration source, T5-306, in Fig. 3.8. ROI, region of interest corresponding to ^{229}Th decay. arb. stands for arbitrary unit. A few peaks are labeled with their corresponding isotopes. Figure adapted from Ref. [76].

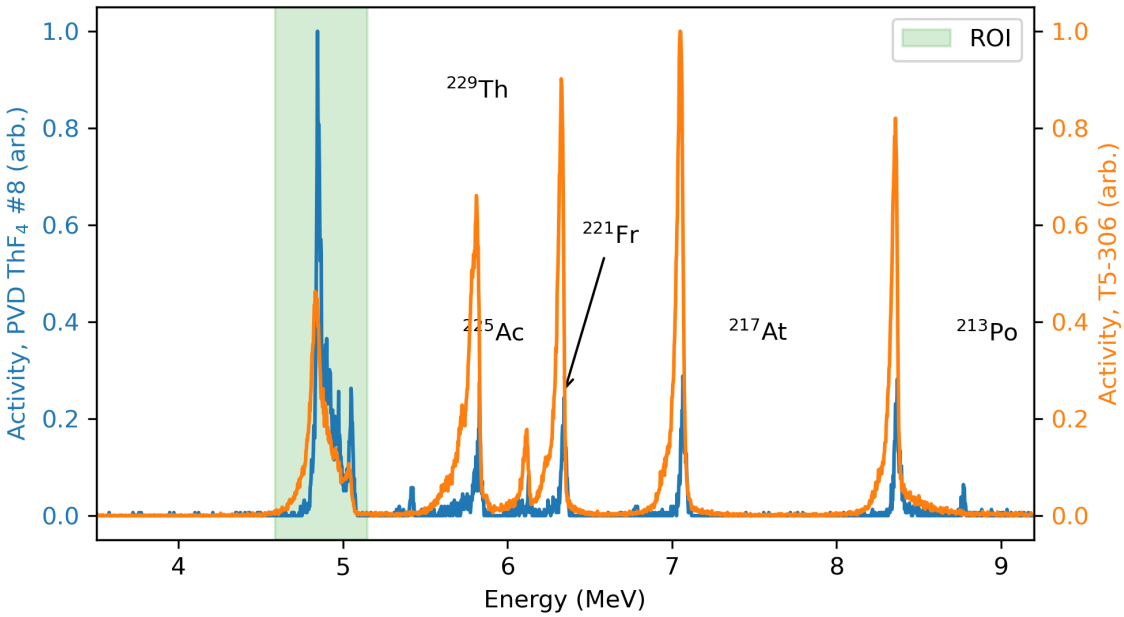

and also its resistance to the pyrohydrolysis procedure. We observe no additional absorption of the ThF_4 thin film in the VUV but complete absorption in the $\sim$ 150 nm range from the ThO_2 thin film after pyrohydrolysis, confirming that our measurement provides trustworthy information on the sample band gap.

Figure 3.17: VUV transmission of a PVD ThF_4 target. a, Measurement setup for characterizing the transmission of a PVD target. b, Measured optical transmission of a $^{229}ThF_4$ thin film. Figure adapted from Ref.[76].

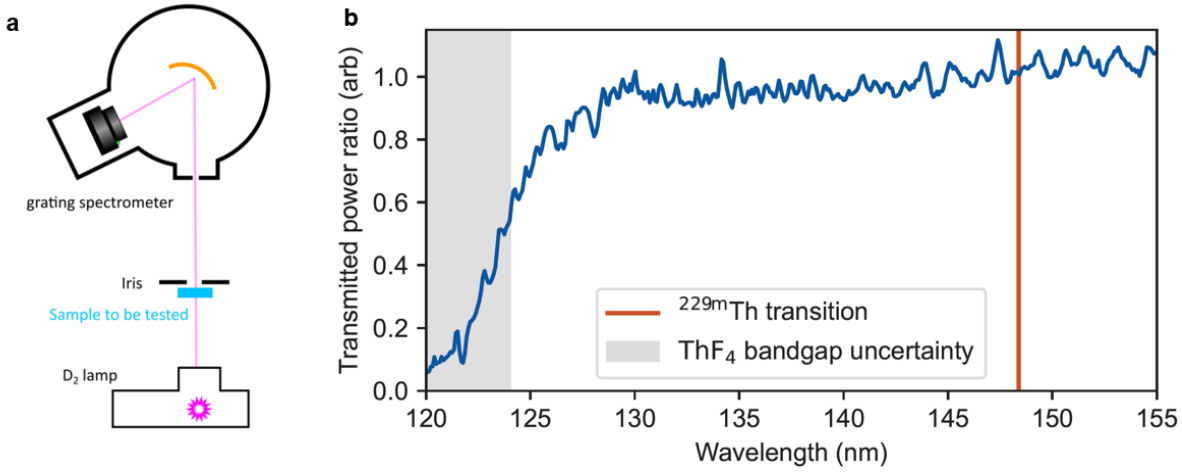

The thin-film targets are likely amorphous. Preliminary characterization of the crystallinity of the PVD targets is carried out at the Materials Research X-Ray Diffraction (XRD) Facility at the University of Colorado, Boulder.[19] Using Grazing-incidence wide angle scattering XRD [227], the average grain size of the samples is estimated as the correlation length obtained by the Scherrer equation [227] to be about 30 Å. Annealing at high temperature may help crystallize the thin-film samples. Diffusion of ^{229}Th atoms into VUV transparent substrates at elevated temperatures may also be possible [228].

[19] We would like to thank Viki Martinez and Joseph MacLennan for technical assistance on the XRD data collection and interpretation.

3.4 Attempts of VUV comb spectroscopy on $^{229}ThO_2$ thin films

Several attempts of VUV comb spectroscopy have been made on $^{229}ThO_2$ thin films, albeit without observation of a clear signal. In this section, we describe the operation and results of the spectroscopy, with the raw data presented in Appendix A.

Since the laser excitation rate of the nuclear transition is low, we choose to use a tight focus and a small target to minimize the target radioactivity and thus the background coming from shake-off electrons, which dominates the background in Fig. 3.4. Due to chromatic dispersion and spherical dispersion, the focal spot size of the laser on the target is designed to be $\sim 50\,\mu m$ (simulated using the Zemax [229] software package and experimentally verified using a $\sim 50\,\mu m$ diameter pinhole). However, practically aligning the laser beam to a target smaller than $100\,\mu m$ becomes challenging. Thus, $100\,\mu m$ targets are used in the end.

The alignment procedure of the laser beam to the target is shown in Fig. 3.18 using two steps. We first perform an initial alignment using a camera imaging system shown in Fig. 3.18a. Using a cerium-doped yttrium aluminum garnet (Ce:YAG) fluorescent screen mounted on a 3-axis translation stage, we mark the position of the laser beam. We use a $50\,\mu m$ pinhole to check if the mount is in the focal plane of the laser beam. We then align the marked position of the laser beam onto the $100\,\mu m$ diameter target, which can be seen in the camera imaging system as shown in Fig. 3.18b. The Ce:YAG screen, the pinhole, and the $^{229}ThO_2$ target are mounted in the same vertical plane. We then measure the photocurrent from the target with a $\sim 10\,\mu s$ long VUV burst generated simply by sweeping the fsEC across its resonance with the comb. The target is biased to -30 V and the photocurrent AC-coupled to a transimpedance amplifier using the schematic shown in Fig. 3.18c. The measured photocurrent is shown on Fig. 3.18d, where we can observe a clear reduction of the photocurrent when the laser is aligned to the $^{229}ThO_2$ target. This is likely due to the fact that the work function of ^{229}Th is lower than that of the Pt metal. Thus, a local electric field establishes on the target surface, as shown in Fig. 3.18e. The order of magnitude of this E-field is 1 V/$100\,\mu m$. To reduce this effect, we simply installed a wire-grid mesh ~ 1 cm away

with +100 V bias voltage. With the wire mesh biased, the photocurrent difference on the $^{229}ThO_2$ surface doubles, but on the Pt surface the photocurrent remains the same, confirming the theory proposed in Fig. 3.18 e. This wire mesh is used in the experiment shown in Fig. 4.1a.

As described in Sect. 2.6, we use the JILA Sr optical clock as an absolute frequency reference to calibrate our comb optical frequency. The scan results can then be parametrized using the comb repetition rate, f_{rep}, calculated from a fixed parameter $f_{\mathrm{ceo}} = -8$ MHz and an adjustable parameter f_{beat} with the ^{87}Sr optical clock laser, which is set by a computer-controlled direct digital synthesizer (DDS). Every second of experimental time, we change the VUV laser frequency at 148.7 nm with a 2 kHz step size set by the DDS. The small step size is chosen so that we can easily apply binning or smoothing in later steps in data processing. Using the 2 kHz/s scanning speed, we can cover the 75 MHz comb repetition rate in the VUV in around 10 hours.

A sample of raw scanning data is shown in Fig. 3.19. In the top panel, we show the scattered photon counts per second as a function of lab time. Besides a slow drop caused by slow degradation of the VUV laser power over time, there is also a fast, small-amplitude oscillation observable in this trace. This periodic oscillation correlates well with the speed of the chopper wheel, indicating that it comes from a small oscillation in the chopper speed control loop leading to a time-dependent vibration on the optical table that slightly changes the laser power. Toward the end of the trace, the laser goes unlocked, and the average scattered photon count rate goes to 0.

The signal count numbers in the collection window of each scan step size are summed and displayed in the middle panel of Fig. 3.19. When the average scattered photon count rate is low, which indicates that the laser is unlocked, the data points are marked in red and discarded.

The bottom panel of Fig. 3.19 shows the f_{rep} of the comb. The solid blue line is calculated directly from the DDS frequency settings and the known ^{87}Sr clock laser optical frequency, knowing the comb mode number determined in Sect. 2.6. The orange circles are taken with a frequency counter and are used to roughly check if we are locked to the correct comb mode.[20]

[20] Hewlett-Packard 5313A, 15 seconds of gate time. We used several different radiofrequency references in the work presented in this thesis, including the hydrogen maser maintained by the National Institute of Standards and Technology and a Stanford Research Systems FS725 Rb clock. However, because we are directly referencing to the

Figure 3.18: Alignment of VUV laser to $^{229}ThO_2$ thin films. a, Schematic illustration of the camera setup for initial alignment. The VUV comb is first focused on a cerium-doped yttrium aluminum garnet (Ce:YAG) fluorescent screen. A camera is used to monitor the fluorescence and show the beam position. The Ce:YAG screen, a 50 µm pinhole, and The $^{229}ThO_2$ target coated on a Pt substrate is mounted in the same vertical plane on a 3-axis translation stage. b, A camera image of the fluorescent screen. The location of the $^{229}ThO_2$ coating is marked with the arrow. c, Schematic of final alignment using photocurrent. TIA, transimpedance amplifier. d, Photocurrent difference measured on the $^{229}ThO_2$ thin film vs on the Pt substrate, as shown in the two configurations in c. e, Local electric field causing the electrons to bend back to the Pt surface, leading to a lower quantum efficiency of the $^{229}ThO_2$ sample.

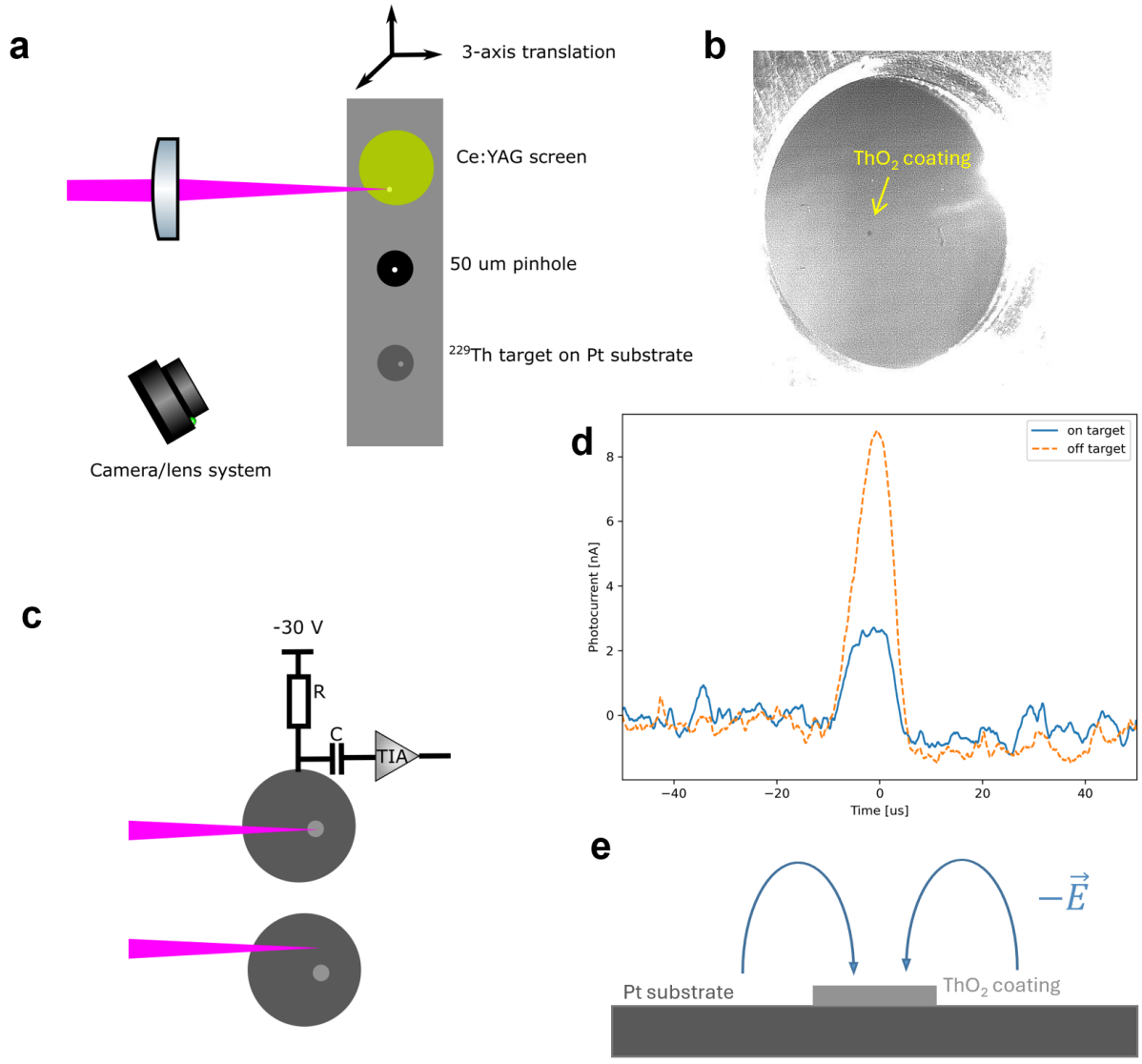

Figure 3.19: Sample raw data of $^{229}ThO_2$ spectroscopy. Top panel shows the scattered photon count rate during the laser irradiation cycle. Middle panel shows the signal collected at each f_{rep} data point, and the bottom panel shows the corresponding comb f_{rep} both calculated from the ^{87}Sr clock laser frequency and the direct digital synthesizer (DDS) settings, and measured directly using a frequency counter.

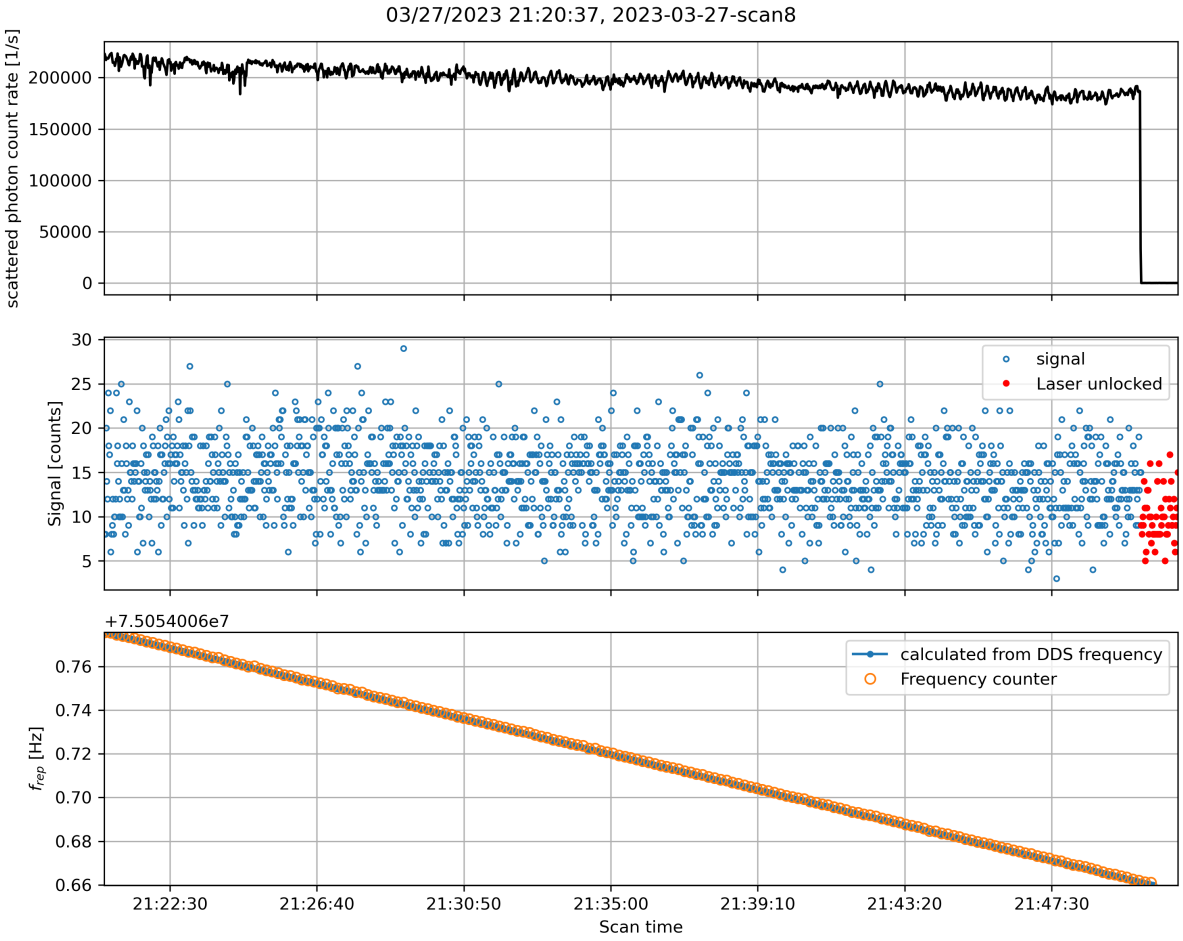

A collection of the scan data can be found in Appendix A. Unfortunately, no repeatable signals are found across the scans performed in this measurement.

3.5 Future directions on IC-based nuclear clocks

Though we have yet to observe the ^{229}Th transition in thin films using the IC channel, we have discovered several issues in the concept initially proposed [190, 191]. In this section, we discuss the problems and potential solutions that should be investigated in the future.

The work function of ThO_2 ($\Phi = 2.6$ eV) used in Ref. [191] (see also Fig. 3.6) comes from Ref. [230] without a clear description of the measurement technique. However, it is reported in Ref. [231] that such a low work function is only obtained after a high-temperature activation process, during which the surface layer of thorium oxide possibly becomes reduced to thorium metal, lowering the work function. This could partly explain the discrepancy in theoretical quantum efficiency (QE) calculated through the $^{229}ThO_2$ band structure in Fig. 3.6 and the experimentally observed QE in the $^{229}ThO_2$ samples. To test this hypothesis, we proposed to fabricate the $^{229}ThO_2$ target on iridium disks and anneal in situ inside the vacuum chamber to "activate" the $^{229}ThO_2$ sample and reduce its work function. Custom Iridium Disc Cathodes were obtained from Kimball Physics to test out this concept. However, the surface roughness of the Ir cathode is too high for $^{229}ThO_2$ thin film fabrication.[21] Solid Ir substrates can be mechanically polished for this purpose. We have not yet experimentally investigated the viability of this approach.

In Ref. [191], it is also assumed that the electrical resistivity of ThO_2 is 10^6 $\Omega\,$m, taken from the measurement in Ref. [205]. However, in Ref. [232], a detailed review of past experiments shows that ThO_2 electrical conductivity depends significantly on impurity level. The projected room-temperature electrical resistivity of $^{229}ThO_2$ from Ref. [232] should be $> 10^{14}$ $\Omega\,$m, several orders of magnitude higher than that presented in Ref. [205]. Following the analysis in Ref. [191],

[87]Sr optical clock, the absolute frequency accuracy of the f_{rep} counter does not cause a problem in the spectroscopy data collection.

[21] An attempt to coat ThO_2 on the Ir cathode is made. However, with the small (∼µg thorium material, we did not observe a change in its thermionic emission efficiency

significant surface charge-up is expected, reducing the possibility of electron emission from the $^{229}ThO_2$ target.

A monolayer graphene is expected to be highly transparent to VUV laser [233] as well as low-energy electrons [234, 235], and has been used in XPS study of insulators [236], gaseous material [237], or protection of photocathode material from oxidation [238]. Therefore, to reduce the charge-up effect, we applied monolayer graphene coatings on the surface of $^{229}ThO_2$ targets.[22]

Another possible trivial explanation for the missing signal is that the $^{229}ThO_2$ target is misaligned with the VUV laser beam. To test this hypothesis, we also changed the substrate to a Ce:YAG fluorescent screen. In order to provide good electrical conductivity on the surface while still being able to check the alignment in-situ, a 5 nm thick Ti coating and a 10 nm thick gold coating are applied to the Ce:YAG substrate before the $^{229}ThO_2$ target deposition. The top layer is further coated with graphene; see Fig. 3.20.

This graphene-coated target fabricated on a gold-coated Ce:YAG substrate is tested out in the spectroscopy setup. It shows a higher background count rate; see Fig. A.1 trace j, k. However, the count rate decreases significantly within the 10-hour scanning time, indicating a possible degradation of the graphene top coating due to VUV irradiation. The scan data show no obvious signal. However, further tests using cleaner technologies for monolayer graphene transfer should be investigated to reduce the residue on the target, see Fig. 3.20c.

Instead of detecting the free electrons that fly off from the surface, detection methods using solid-state sensors for energetic electrons in bulk material are investigated. One promising route is to use a superconducting nanowire single photon detector (SNSPD), as mentioned in Ref. [191]. In an SNSPD, the energy deposited by a single photon causes a hot spot on a superconducting nanowire, causing it to locally heat up enough and lose superconductivity. A good review of the SNSPD operation principle can be found in Ref. [239]. It is conceivable that, by applying a thin ($\sim$ 10 nm) ^{229}Th coating on top of the SNSPD, a large fraction of the thermal energy deposited in

[22] We used ACS Material, Trivial Transfer Graphene in this experiment. A similar product called "Easy Transfer" is sold by Graphenea but not used in this experiment.

Figure 3.20: Target 229Th#20, $^{229}ThO_2$ deposited on gold-coated Ce:YAG. The $^{229}ThO_2$ target is covered with a monolayer graphene after the vapor deposition and pyrohydrolysis. a, Illustration of the concept. b, Microscope image of the target. The small dot in the center is the $^{229}ThO_2$ coating. c, Zoom-in view of the $^{229}ThO_2$ coating on the target, covered with graphene. Some white residues are visible, likely from the polymethyl methacrylate used in the graphene transfer procedure.

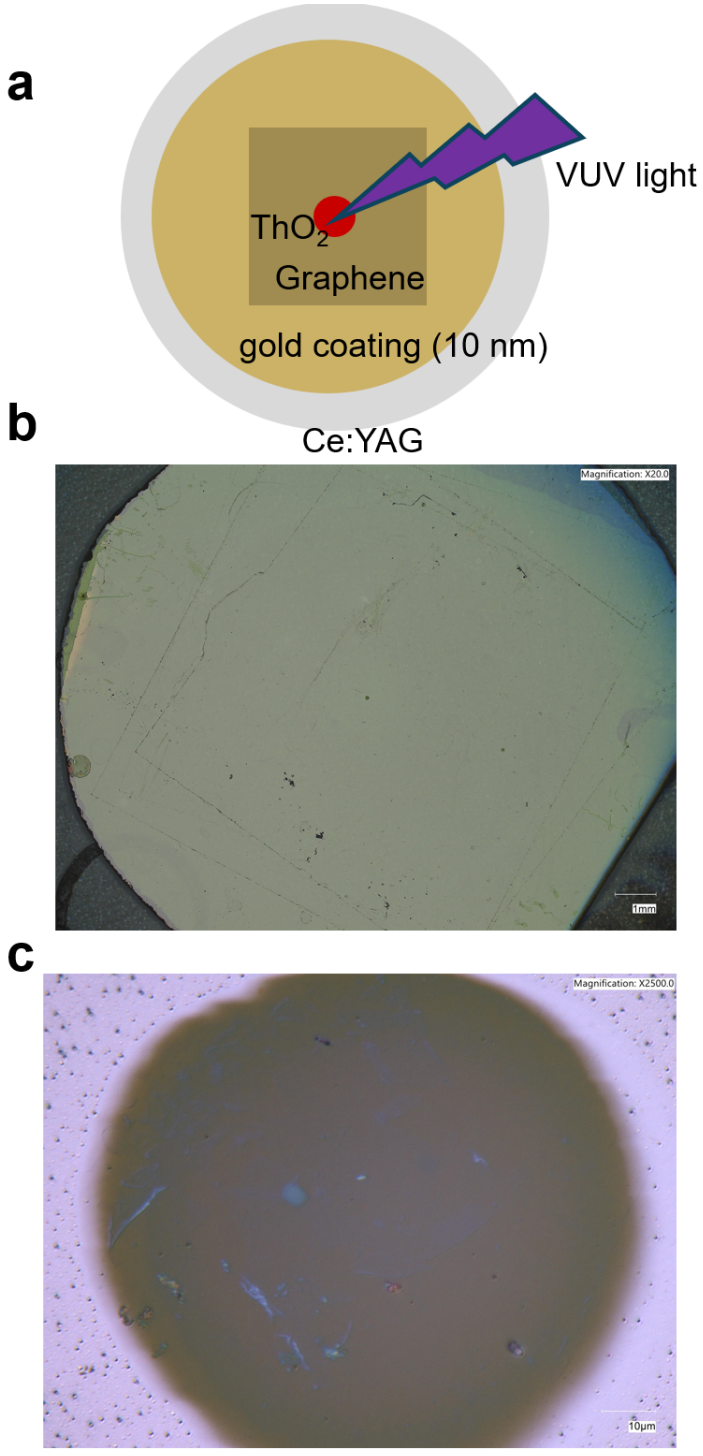

the ^{229}Th thin film may be transferred into the SNSPD and trigger a click similar to a single photon event. We note that the detection of ^{229}Th nuclear IC decay events has also been investigated using ^{229}Th implanted into SNSPDs in Refs. [70, 28, 240].

Toward this direction, an NbN SNSPD is coated with ThF_4 for tests; see Fig. 3.21. However, after the $^{229}ThF_4$ deposition, the thin nanowires lost superconductivity. Future tests should be performed to check the reactivity between $^{229}ThF_4$ and the superconducting nanowire materials at the high temperatures used for the vapor deposition. The thermal load from the laser irradiation should also be small enough such that the SNSPD does not heat up above its operational temperature.

3.6 Spectroscopy of $^{229}ThF_4$ using the radiative decay channel

3.6.1 Null results with a VUV frequency comb

Given the wide band gap (see Refs. [224, 225] and Fig. 3.17) of ThF_4, observation of radiative decay in $^{229}ThF_4$ material should be feasible. Recently, the background luminescence of thin ThF_4 films is characterized towards this goal [241]. Using a setup similar to that in Ref. [24], we performed spectroscopy on $^{229}ThF_4$ thin film targets using our VUV frequency comb. However, no signal was observed.

To maximize the expected signal, a $\sim$ 150 nm thick $^{229}ThF_4$ target is fabricated. The target (229Th#23) is fabricated in our coating chamber with $\sim$ 5 mm diameter, with a total activity of 58 kBq. The areal density of the ^{229}Th emitter can be estimated simply from the density of $^{229}ThF_4$ to be $\sim 2 \times 10^{15}$ ^{229}Th atoms per mm^2. With a 1 nW laser power, and 240 kHz scanning range per step, $\sim$ 400 seconds of excitation time, a signal rate of $\sim 10^4$ is expected.

To reduce the background without losing the signal, we cover the $^{229}ThF_4$ thin film using a 50 µm thick, 500 µm diameter Pt mask (Lenox laser), effectively reducing the target area while still making the system easy to align. The background obtained from the thin film is low, probably due to the thin film reducing the path for the generation of Cherenkov radiation and color centers [25].

Figure 3.21: ThF_4 coated superconducting nanowire single photon detector (SNSPD). The color comes from interference of light due to the ThF_4 coating.

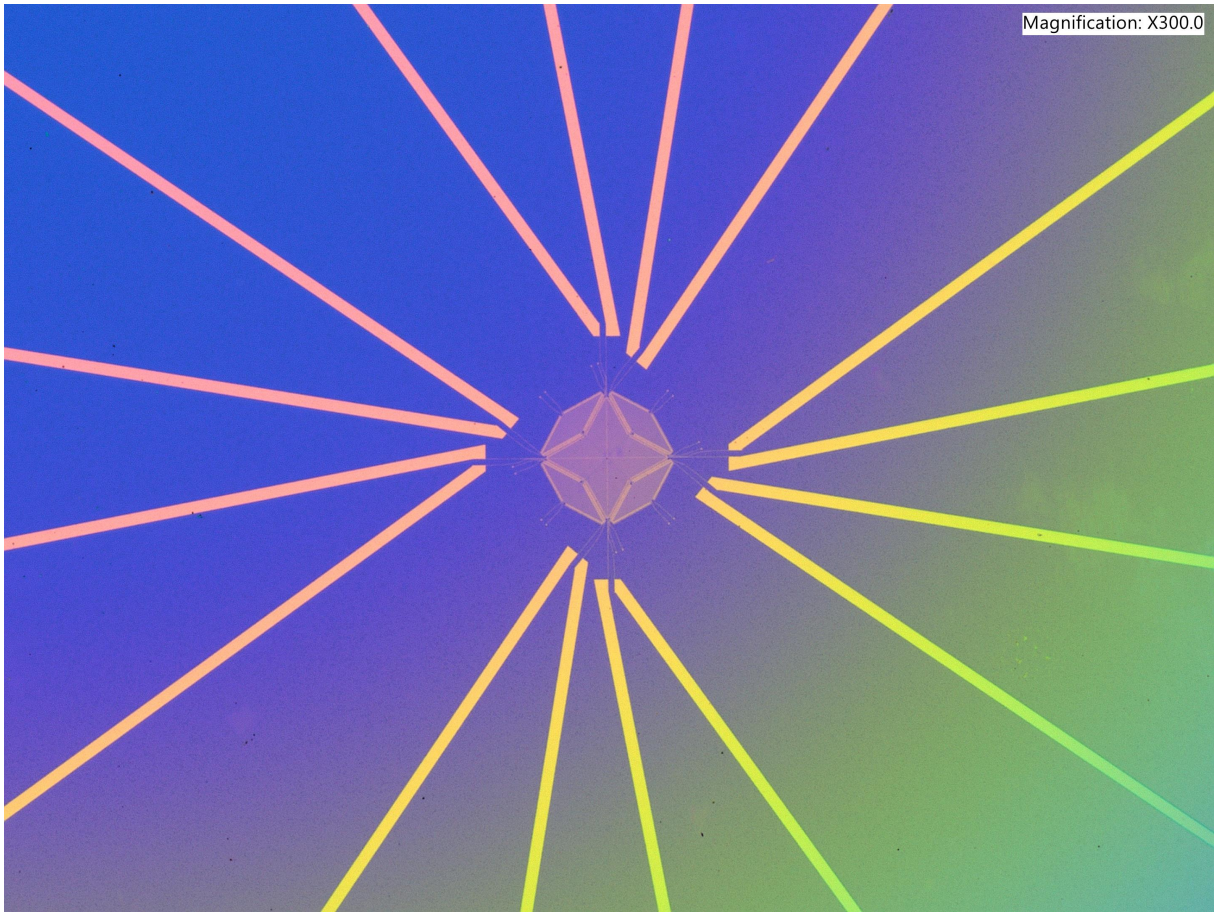

Thus, no additional spectral filtering is implemented. The setup of the experiment is illustrated in Fig. 3.22.

The background observed in the experiment shows a strong time dependence. The target used for this experiment (229Th#23) was fabricated on 2024-04-23. The observed background count rate, whether we are performing laser scans or not, shows a linear rise across the days when the experiment was performed; see Fig. 3.23a. This likely comes from the accumulation process of daughter isotopes after vapor deposition or radiation damage to the MgF_2 substrate.

We perform the scan with 400 seconds of VUV irradiation, then with 200 seconds of VUV photon collection while the VUV laser is turned off. The average count rate in the 200 seconds of time bin is shown in Fig. 3.23b. We see that there is an enhanced signal in the first few seconds. After that, the count rate is rather flat, indicating that there is no time-dependent decay of the photon count rate on ~ 100 s time scales.

The background count rate shown in Fig. 3.23a can be piecewise fit to linear functions and subtracted away to show the spectroscopy signal of $^{229}ThF_4$ on a background-free plot. In Fig. 3.23c, we show this background-subtracted VUV photon count rate as a function of the laser f_{rep} used in the scan. The horizontal axis range corresponds to a full scan that bridges the comb f_{rep} gap. No obvious signal is observed. We also re-measured the top five highest points. However, they do not appear to be reproducibly higher than the background.

The missing signal contradicts the high anticipated signal count rate. As we will learn from Sect. 3.6.2, only a small number ($< 1\%$) of the ^{229}Th nuclei in the $^{229}ThF_4$ thin film actually contributes to the radiative decay signal. In addition, significant inhomogeneous broadening may be expected in a thin-film environment, leading to further dilution of the signal count rate when a comb is used to perform the scan.

3.6.2 Successful observation with a broadband VUV laser

As discussed above, a possible broadening in $^{229}ThF_4$ thin films will lead to a significant reduction in excitation number in our comb-based scan using a narrow-linewidth laser. If the

Figure 3.22: VUV comb spectroscopy setup of a $^{229}ThF_4$ thin film. The $^{229}ThF_4$ film coated on MgF_2 substrate is covered with a $\sim 500\,\mu m$ size pinhole mask to reduce the exposed radioactivity. The exposed $^{229}ThF_4$ is placed at the focus of a parabolic mirror. The parabolic mirror collects the VUV fluorescence photons and sends them to a photomultiplier tube (PMT) through a MgF_2 lens and a MgF_2 window. the MgF_2 window is mounted on a flange to separate the PMT chamber from the $^{229}ThF_4$ chamber in order to keep the ultrahigh vacuum condition in the $^{229}ThF_4$ chamber.

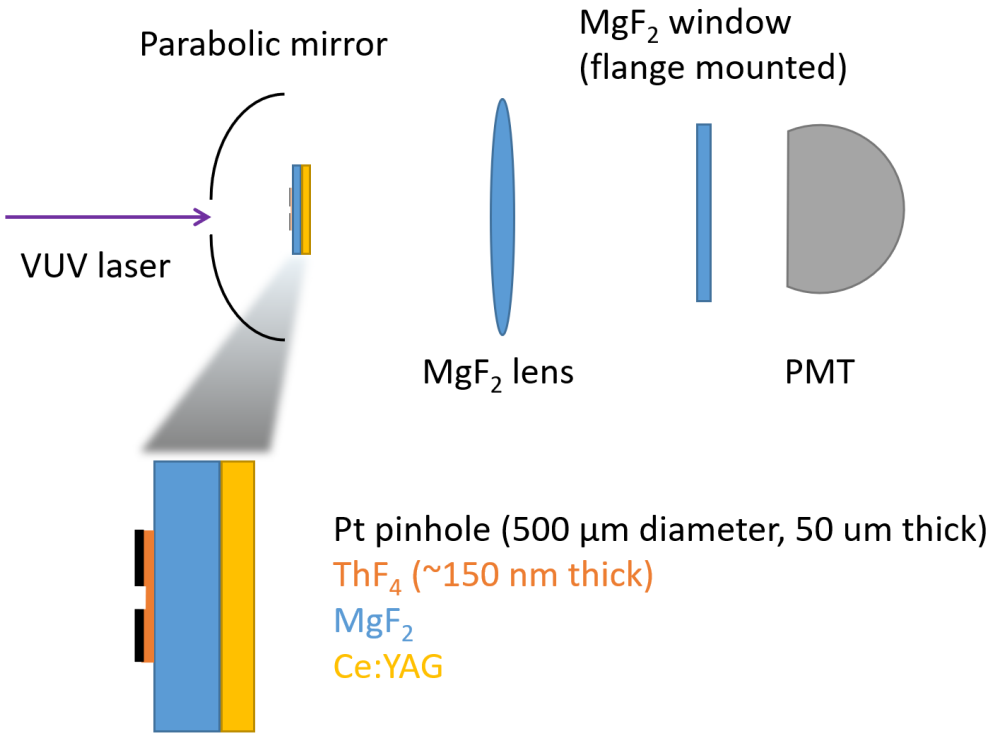

Figure 3.23: VUV comb spectroscopy data with a $^{229}ThF_4$ thin film. a, Background count rate as a function of time after the target was fabricated and installed in the spectroscopy setup. b, Background count rate as a function of time after the laser irradiation in the spectroscopy scans. c, Background-removed VUV photon count rate as a function of laser frequency. Cps, counts per second.

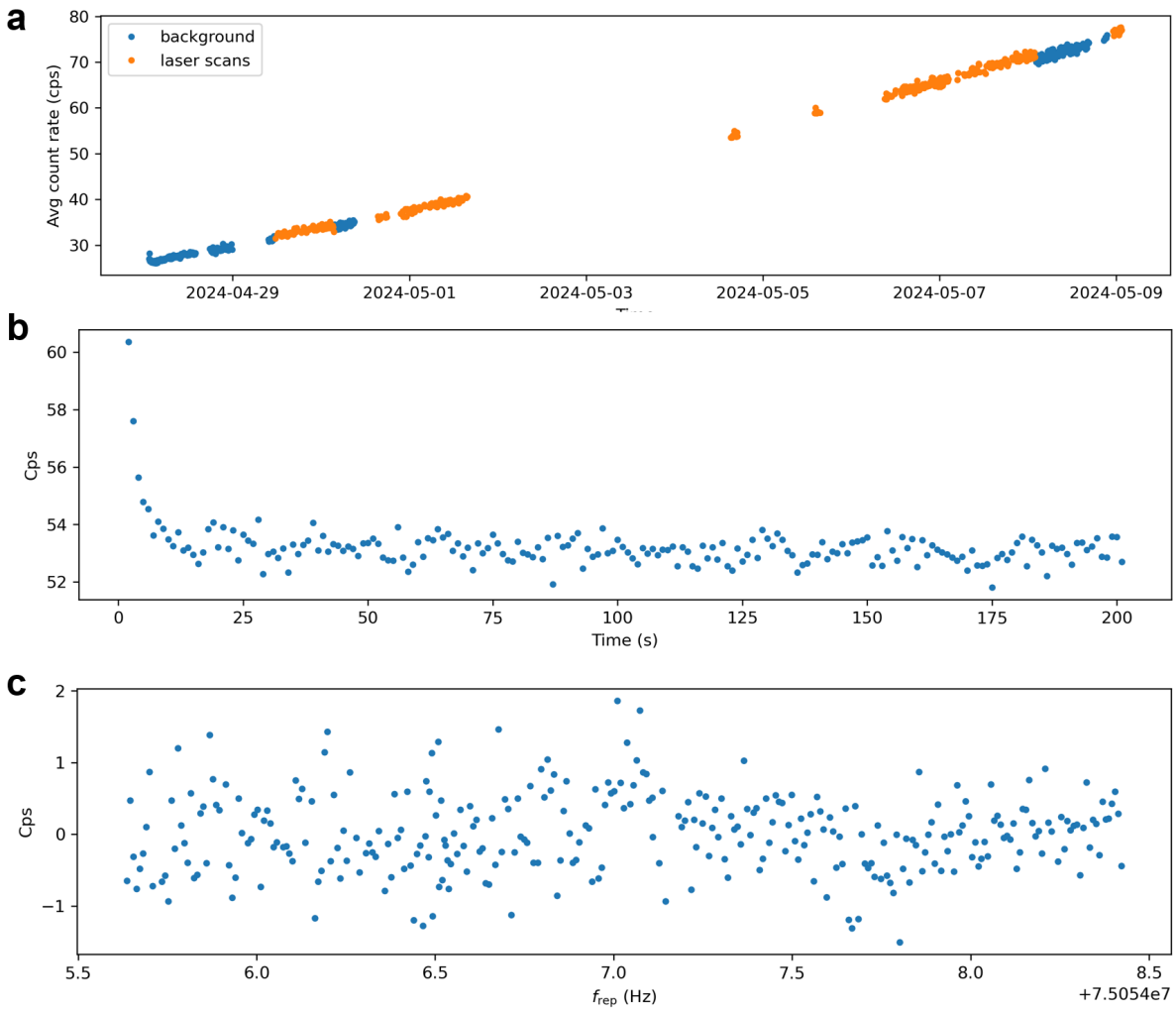

broadened linewidth exceeds $f_{\text{rep}} \sim 75$ MHz, we will not be able to obtain a clear spectroscopy signal as we change the comb f_{rep}. Thus, we collaborated with Prof. Eric Hudson's group in UCLA to perform a scan using their broadband four-wave mixing laser [70, 28, 75]. This laser system offers nanosecond VUV laser pulses with typically $\sim 2\,\mu$J per pulse at a 30 Hz repetition rate. The linewidth of the laser is ~ 10 GHz, limiting the final resolution of the result, but works perfectly for a sample with potentially broad transition linewidth.

To mount the $^{229}ThF_4$ thin films in the UCLA VUV spectroscopy setup shown in Ref. [69], an adapter mount is made; see Fig. 3.24. Two pieces of ~ 8 mm by 4 mm substrates (175 µm thick for Al_3O_2 substrate (from University Wafer) and 250 µm for the MgF_2 substrate (from Crystran) are coated side by side in the same plane in the vapor deposition setup (Fig. 3.12), leading to two half circles at the edges of the substrates. The two plates are then mounted at $\sim 70°$ angle with respect to the VUV laser beam; see Fig. 3.24a. The large incidence angle is used primarily to allow the thin film $^{229}ThF_4$ targets to fit inside the mount. Although the reflection of the laser beam (s-polarization) from the substrate significantly reduces the VUV laser power for spectroscopy, the large incidence angle also allows us to effectively illuminate more ^{229}Th atoms.

Two plates with the same coating material are sandwiched together, providing two advantages. Firstly, each $^{229}ThF_4$ coating run produces two symmetric substrates. Using both of them increases the number of atoms irradiated with the laser. Secondly, with the $^{229}ThF_4$ coatings facing each other, the radioactive daughter isotopes emitted from the $^{229}ThF_4$ surfaces are contained within the target mount itself, eliminating radioactive contamination of the detection setup. An aluminum mount is machined at JILA for the $^{229}ThF_4$ thin films; see Fig. 3.24b. The substrate plates are taped onto a thin aluminum side wall using vacuum-compatible double-sided tape.[23]

A clear nuclear resonance signal is observed and reported in $^{229}ThF_4$ thin films, on both Al_3O_2 and MgF_2 substrates [76]. The transition frequency coincides well with that reported in ^{229}Th-doped $LiSrAlF_6$ crystals [28], see Fig. 3.25a. The observed signal amplitude is relatively low

[23] SPI Supplies, Die-Cut Double Sided Adhesive Conductive Carbon Discs. Their online technical notes for this product claim good vacuum compatibility. An alternative is Double Sided Kapton Polyimide Tape from Ted Pella.

Figure 3.24: $^{229}ThF_4$ mount for VUV spectroscopy. a, Schematic showing the setup concept. PMT, photomultiplier tube. b, Photos of the target mount taken at different viewing angles.

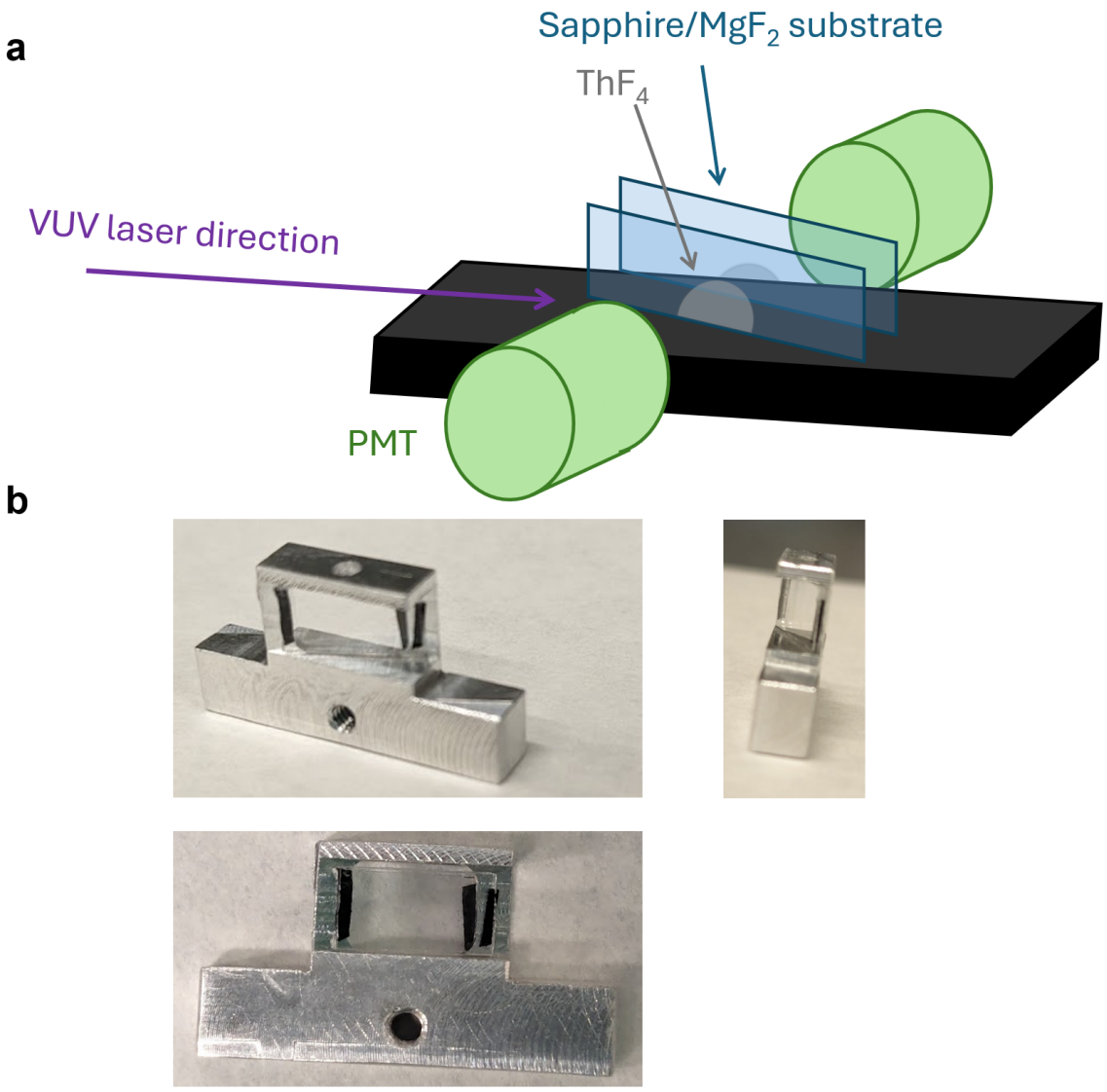

$\sim 10^{-3}$ compared to that estimated using laser power and ^{229}Th density, indicating a significant quenching effect on the surface.

Another interesting observation is that the lifetime of ^{229m}Th is reduced to ~ 160 s, compared to that of ~ 600 s in other doped crystals [28] (shown as the black line for reference in Fig. 3.25b). It is well known that the lifetime of optical emitters depends on the refractive index of the material due to the Purcell effect [242]. For magnetic dipole transitions, the lifetime of the excited state atom scales as $1/n^3$. General discussions of this effect can be found in Refs. [243, 244]. Specifically for ^{229m}Th, this effect is discussed in Refs. [245, 61]. The application of this effect in thin slabs can be understood following Ref. [246], or equivalently using a purely classical antenna model presented in Refs. [247, 248, 249]. However, this effect cannot fully explain the short ^{229m}Th lifetime in $^{229}ThF_4$ films. First, if the films are sufficiently thin ($\ll \lambda \sim 148$ nm), the ^{229m}Th lifetime will be significantly dependent on the refractive index of the substrate material. However, we did not observe a statistically significant difference between $^{229}ThF_4$ on Al_3O_2 and MgF_2 substrates, although their large difference in refractive index [130]. Secondly, if the films are thick enough that the lifetime is dominated by the $^{229}ThF_4$ index [212], the expected lifetime reduction is still significantly smaller than the experimental observation. Other quenching mechanisms should be considered.

The superradiance effect causing a reduction in lifetime is also unlikely, due to the rapid dephasing caused by the large inhomogeneous broadening in the ^{229}Th films used in this experiment. However, the high emitter density of the ^{229}Th nucleus in $^{229}ThF_4$ ($(\lambda/n_{ThF_4})^3/\rho_{Th} \sim 10^7$ provides a unique system for collective quantum optics studies involving nuclear superradiance [250] and nuclear forward scattering [251], especially in combination with photonic structures such as waveguides and resonators manufactured with $^{229}ThF_4$.

A fundamental limitation to the thin-film nuclear clock is the line broadening in thin-film targets. It is well known that in Mössbauer spectroscopy, interactions between the nucleus with the environment, such as electric monopole, electric quadrupole, and magnetic dipole interactions, can lead to broadening of the line shape (see Fig. 5.1). In order to obtain narrow line widths

Figure 3.25: $^{229}ThF_4$ spectroscopy signal using a broadband laser. a, Recorded nuclear fluorescence counts N_γ normalized by laser power P_L versus VUV laser frequency. The observed power-normalized fluorescence for the $^{229}ThF_4$ film on a Al_3O_2 (MgF_2) substrate is shown in blue (red). All error bars represent the standard error of the mean. b, Recorded nuclear fluorescence rate $\dot{N}_\gamma$ versus time after the laser is extinguished. The observed radiative decay for $^{229}ThF_4$ on a Al_3O_2 (MgF_2) substrate is shown in blue (red). The peak of all curves are normalized to unity. The corresponding result observed in ^{229}Th:$LiSrAlF_6$ [74] is shown in black for comparison. Figure taken from Ref. [76].

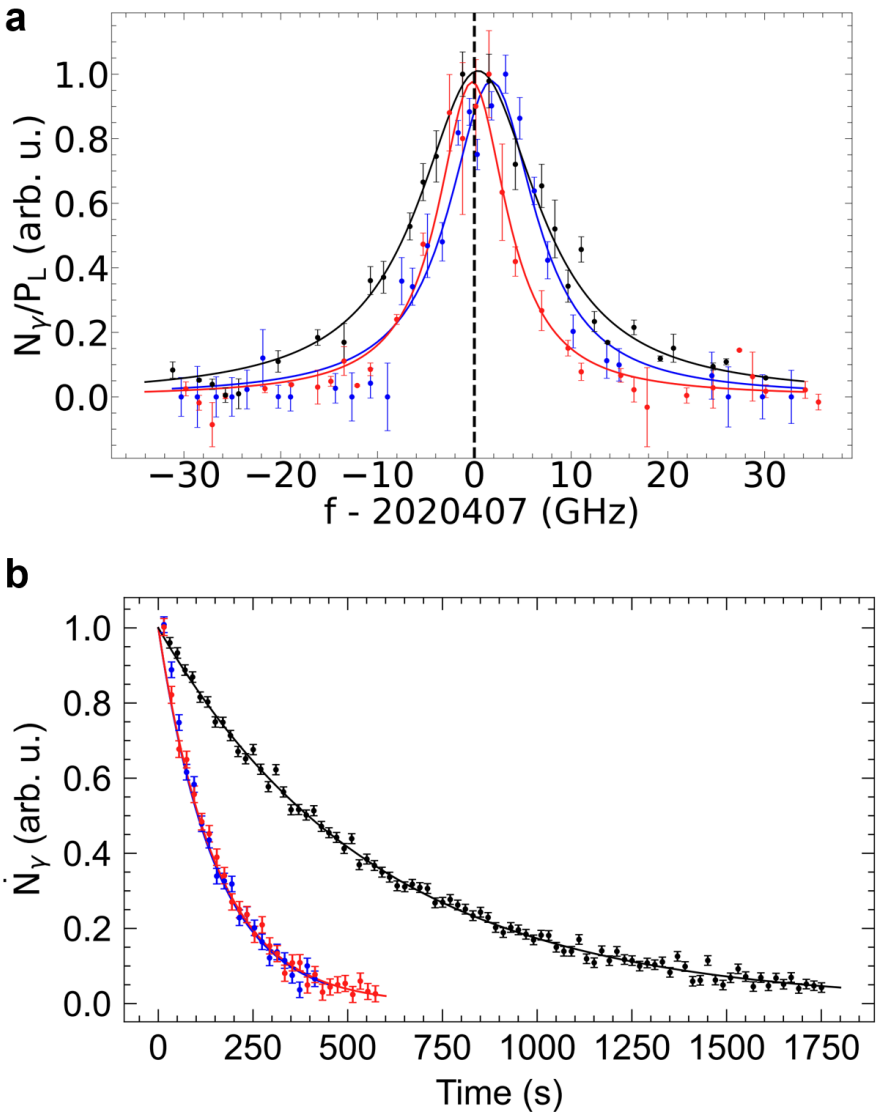

in Mössbauer spectroscopy, careful sample preparation procedures are required [35, 10, 252, 253] which often involve proper annealing procedures to obtain the crystalline structure of the source and sample. This annealing procedure likely leads to the diffusion of a thin layer of material for Mössbauer spectroscopy into the host sample; see, for example, Ref. [254]. In the future, the annealing and diffusion of $^{229}ThF_4$ coatings on VUV transparent substrates should be tested. Ref. [228] provides useful information in this direction.

ThF_4 single crystals can be grown using ^{232}Th [255]. The observation of nuclear excitation in $^{229}ThF_4$ thin films rekindles the interest in ^{229}Th-doped $^{232}ThF_4$ crystals, in which ^{229}Th does not cause defects or microstrain (see Chap. 5). This may offer reduced inhomogeneous broadening at high ^{229}Th density as well as full control of the crystal electric field gradient (EFG) quantization axis, enabling unique applications.

Chapter 4

Direct VUV comb spectroscopy of the nuclear clock transition in a CaF_2 host crystal

While the ^{229m}Th has been directly excited by FWM pulsed lasers [27, 74, 76], this alone is not yet enough for building a nuclear clock. In this chapter, we describe the direct VUV comb spectroscopy experiment performed on ^{229}Th hosted in a CaF_2 crystal, following Ref. [24].

In addition to reducing the line center uncertainty by six orders of magnitude, our comb-based measurement demonstrates two key pieces of technology for building a nuclear clock. With a frequency comb, we directly measure the frequency of the nuclear transition, as opposed to previous measurements based on wavemeter measurements [27, 74].[1] Moreover, with the narrow comb lines, we resolve the quantum states whose degeneracy is lifted due to the intrinsic electric field gradient (EFG) in the crystal. This serves as a starting point for us in characterizing the systematic shifts of the nuclear clock in a state-dependent way.

4.1 Crystalline host for ^{229m}Th

To perform spectroscopy of ^{229m}Th using our comb, another key ingredient is a sample that contains a high density of ^{229}Th and with good VUV transmission at 148 nm. The early proposals [11, 12] mentioned the possibility of observing ^{229m}Th in solid-state hosts. However, with the improved values of the nuclear transition energy measurement in Refs. [42, 43], it becomes clear that a large bandgap material is needed to suppress the internal conversion decay channel

[1] "Never measure anything but frequency!" says Arthur Schawlow [256]. The highest accuracy measurements of physical quantities are performed in the frequency domain using atomic clocks.

for observation of radiative ^{229m}Th decay. Estimates of nuclear clock performance based on ^{229}Th doped in VUV-transparent crystalline hosts are presented first in [67, 68].

In 2023, the first observation of nuclear radiative decay is presented in Ref. [25], which uses accelerator-produced short-lived isotopes implanted into host crystals to populate the ^{229m}Th states. In a follow-up work [73], it is confirmed that radiative decay can be observed in $LiSrAlF_6$, CaF_2, and MgF_2 crystals, while AlN and amorphous SiO_2 hosts induce quenching and do not present an observable radiative decay signal. X-ray pumping for populating ^{229m}Th through the second excited state in the ^{229}Th nucleus at 29 keV is also demonstrated [65, 66], further confirming the feasibility of IC suppression and radiative photon detection in crystals.

Inspired by Ref. [25], we started building a spectroscopy setup searching for radiative decay of ^{229m}Th after our VUV comb irradiation.[2] For the sample, we choose to use ^{229}Th-doped CaF_2 crystals grown and characterized by our collaborators at TU Wien [257, 258]. These crystals have the highest ^{229}Th doping concentrations of up to $5 \times 10^{18}/\text{cm}^3$, allowing us to irradiate a large number of ^{229}Th atoms in parallel and maximize our signal rate.

4.2 Spectroscopy experiment setup

The crystal used in this work is named "X2" [228], with a ^{229}Th doping concentration of 4×10^{18} cm^{-3}. This X2 crystal is first grown to be 3.2 mm diameter, 10 mm length. The crystal is then cut into small pieces, used both for the first laser excitation experiment at PTB [27] and for the X-ray pumping experiment at Spring-8 [66]. The excited state ^{229m}Th lifetime of $\sim$ 640 s in CaF_2 is already known when we received a piece of the X2 crystal at JILA.

We choose to perform the experiment in a similar way as Refs. [27, 28], i.e. by performing laser excitation and then fluorescence detection. Using the theory presented in Sect. 3.1 and experimental excitation rate estimations from Refs. [27, 28], the absorption of the laser by the ^{229}Th transition is estimated to be $\sim 10^7$ photons per second, smaller than the total photon flux of our laser beam

[2] Prof. Peter Thirolf gave a fantastic presentation of this work at the International Conference on Laser Spectroscopy 2023. Following the talk and inspiring discussions, we decided to build a setup searching for radiative decay photons.

(consisting of all comb modes) at $\sim 10^{14}$ photons per second.[3] It is easy to see that there is no chance for us to observe the direct absorption signal of the transition in the forward direction of the laser irradiation, where the photon shot noise of 10^7 per second is already similar to the expected signal. Our intensity noise of the VUV comb is likely much higher than its shot noise limit, due to the conversion of phase noise to intensity noise in the fsEC and also the upscaling of intensity noise in the extremely nonlinear HHG process [17].

Instead, in the fluorescence measurement, we are performing a background-free measurement with in principle infinite fundamental signal-to-noise ratio. The noise in the measurement, practically, comes from the technical limitation of the crystal itself. Due to the radioactivity of ^{229}Th, the crystal fluoresces in the VUV and UV constantly [259, 257], giving us a background count rate. The (Poissonian) fluctuation of the background count rate gives us the noise floor of our spectroscopy measurement. There are a few ways to reduce this noise compared to the signal:

- Spectral filtering. Since the noise is broadband in wavelength [259, 257] while signal fluorescent photons are narrow-band, using a narrow-linewidth bandpass filter can efficiently increase the signal-to-noise ratio.

- Time gating. Since the noise comes from the radioactive decay process, it is reasonable that they may have different correlation properties compared to the $^{229\mathrm{m}}$Th radiative decay signal. It is reported in Refs. [228, 260, 66] that a correlation between UV and VUV noise photons can be leveraged to "veto" the background counts and reduce the background count rate by a factor $\sim 10^3$. However, we have not observed this large veto fraction yet and we do not use this method in our work.

- Higher collection efficiency. The signal and background scales up linearly with the collection efficiency. But the noise only increases as the square root (shot noise) of the background counts (thus the collection efficiency). Therefore, a higher collection efficiency and longer averaging mean an increased signal-to-noise ratio.

[3] Considering a single comb line, the expected absorption can already reach the $\sim 1\%$ level. If a continuous-wave laser was available, one could easily perform frequency-modulated absorption spectroscopy on it!

- Smaller crystal. With our laser excitation rate far away from saturating the transition, focusing down the laser beam increases the excitation fraction while decreasing the total number of irradiated atoms, keeping the total number of excited nuclei (thus the signal) the same. However, decreasing the crystal size reduces the amount of radioactive ^{229}Th, thus cutting down the noise.

Following these considerations, we implemented the detection setup shown in Fig. 4.1. Using a small crystal of $1.8\times0.7\times1.4$ mm size (Fig. 4.1a), we minimize the radioactivity and thus the background fluorescence count rate. The laser illuminates through the crystal with a ~ 0.2 mm beam diameter along the 1.4 mm crystal length direction. The crystal is polished and fluorinated [258] right before shipment to JILA, with the optical transmission coefficient of 45% measured at TU Wien. The crystal is glued to a larger piece of MgF_2 using an ultra-high vacuum (UHV) compatible glue (EpoTek H77) for ease of handling and mounting.

We first ensure that the laser passes through the ^{229}Th-doped CaF_2 crystal by monitoring the photoluminescence of the crystal [259, 228] itself as well as the fluorescent light on a Ce:YAG fluorescent screen mounted behind the crystal. A photo of the setup is shown in Fig. 4.1b. As a small fraction of the 3rd and 5th harmonic also propagates to the crystal, causing weak white-blue fluorescence on the CaF_2 crystal similar to the effect of the 7th harmonic. To verify that the 7th harmonic is aligned properly, we deliberately injected ~ 1 torr of air into the vacuum chamber. The 7th harmonic in the VUV gets fully absorbed by the air, while the 3rd and 5th harmonics pass through. By comparing the in-vacuum and in-air fluorescence, we are able to verify that the 7th harmonic beam is indeed aligned to the X2 crystal.

A parabolic mirror [261, 262] (provided by Prof. Thirolf, LMU) with a VUV-enhanced aluminum coating is used to collect the emitted fluorescent photons over a large solid angle; see Fig. 4.1b and c. To align the crystal with the focus of the parabolic mirror, we first use a camera to image objects at infinity ($\sim$ a few meters) distance. Then, combining the camera imaging system and the parabolic mirror, we image the crystal onto the camera when the crystal is in focus [22]. For

fine adjustments, the UV fluorescence of the crystal collected by the parabolic mirror is directed to a photomultiplier tube (PMT). This is done simply by replacing the dichroic mirrors shown in Fig. 4.1 with UV-enhanced aluminum mirrors. We adjust the parabolic mirror position to optimize the UV fluorescence counts obtained on the PMT. Because most of the collection optics are reflective, we anticipate that this also gives us the highest collection efficiency for the VUV fluorescence photons.

Three band reflection filters (150±10 nm) made at Layertech are used to direct signal photons at 148.3 nm while reducing broadband noise photons. The mounts for the mirrors are fixed using precision position pins; thus it is easy to replace them with aluminum mirrors of the same size for diagnostics. We choose to use reflective geometry limited by VUV filter fabrication technology. Although there are narrower transmissive filters, they have typical transmission coefficients of only $\sim 20\%$ compared to $\sim 90\%$ reflectivity of the Layertech coatings and therefore are undesirable. We use three of the filters to achieve higher suppression of the noise photons with a minimal footprint in the experiment setup.

We use a VUV PMT for photon detection because of its high quantum efficiency ($> 10\%$), low intrinsic background noise (< 10 counts per second, cps) and large active area ($\varnothing = 23$ mm). A side-mounted PMT (Hamamatsu R10454) is initially considered because of its higher quantum efficiency. However, the side mounting, as well as the smaller active area, creates more difficulty for alignment. In the end, we used a head-on PMT (Hamamatsu R6835) instead because of its larger active area, better vacuum compatibility, and easier geometry for mounting. The overall signal collection efficiency is estimated to be about 0.3 %. A background count rate of ~ 430 cps is observed, dominated by crystal radioluminescence.

In Ref. [27], the ^{229}Th is irradiated for 120 s and the fluorescence signal is collected for 150 s. In Ref. [28], the ^{229}Th is irradiated for 1200 s and the fluorescence is collected for 1800 s. In our setup, what irradiation and collection times T_{i} and T_{c} are optimal for our signal-to-noise ratio given a reasonable total scanning time? Several considerations are made:

- What is the optimal ratio between the irradiation time and the collection time? In the

Figure 4.1: Detection chamber design. a, Microscope image of the glued X2 crystal. b, Photo of the detection chamber, with parts labeled. c, Illustration of the detection chamber setup.

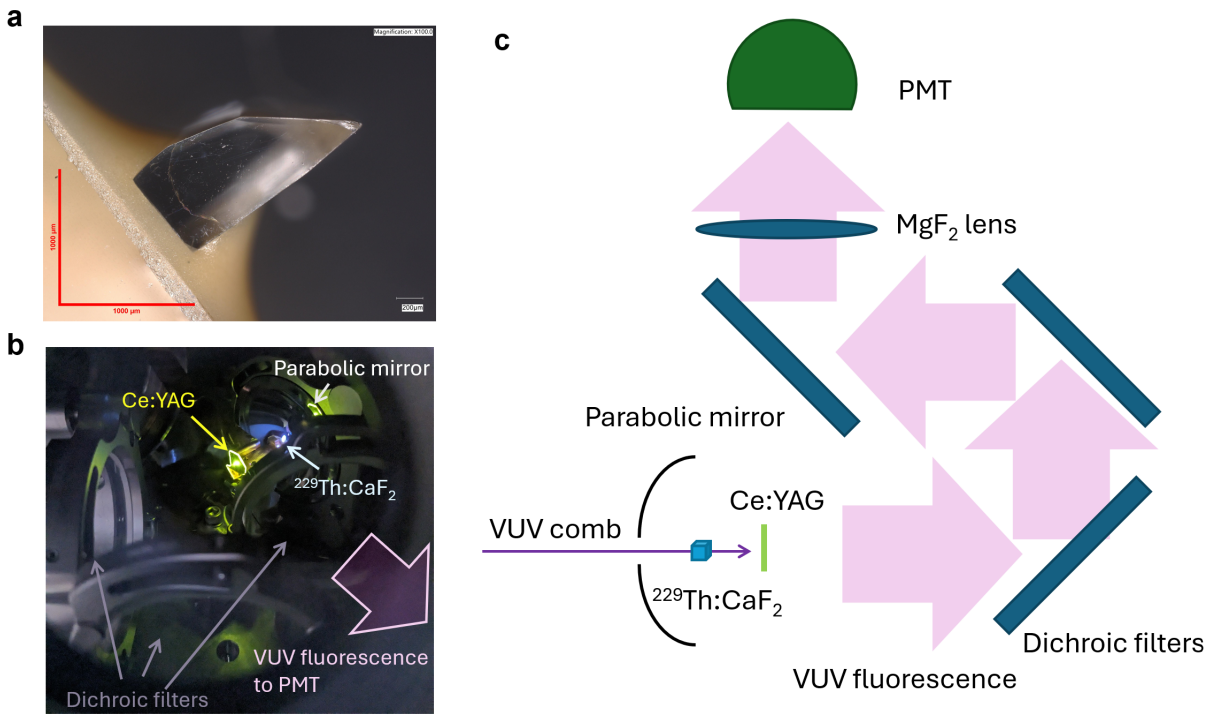

limit of $T_\mathrm{i} \ll \tau$, where $\tau \sim 640$ s [27] is the lifetime of the excited state, the signal increases linearly with both T_i and T_c, while the noise (dominated by the radioactive background) increases as $\sqrt{T_\mathrm{c}}$. We therefore choose the optimal ratio of $T_\mathrm{i}/T_\mathrm{c} = 2:1$ for the best signal-to-noise ratio, given a limited scanning time per step.

- What is the optimal total time spent on one frequency? At short irradiation times $T \ll \tau$, we see that the SNR increases as $T^2/\sqrt{T} \sim T^{3/2}$, faster than a simple averaging of $\sqrt{T}$. If we spend too much time $T \gg \tau$ on a single data point, we know that the excited state population reaches equilibrium and the SNR does not improve further, while we are just wasting time. A quick numerical simulation shows that an irradiation time similar to the lifetime gives us the best SNR. To simplify the experimental operation, we take $T = 600$ as the total irradiation time and $T_\mathrm{i} = 400$ s, $T_\mathrm{c} = 200$ s.

- What is the optimal step size? If the step size $\Delta\nu$ is chosen to be much greater than the decoherence rate γ, we see that using a smaller step size (and a larger total scanning time $f_\mathrm{rep}/\Delta\nu$) allows us to increase the SNR proportional to the total scanning time, which is favorable over simple averaging. With $\Delta\nu \sim \gamma$, a further reduction in the step size does not increase the SNR per unit time. Although when we started the experiment, the decoherence rate γ between $^{229\mathrm{m}}$Th and light is unclear, it is estimated to be $\sim$ 10-100 kHz dominated by our laser linewidth. However, a smaller step size requires a longer total scanning time. Balancing the SNR and the total scanning time, we choose a step size of $\Delta\nu = 240$ kHz. With our comb spacing $f_\mathrm{rep} = 75$ MHz and using $T = 600$ s per step, this leads to an acceptable total scanning time of 50 hours.

With the above consideration, we finalize the timing sequence of the experiment, shown in Fig. 4.2. During the irradiation cycle, the PMT is switched off using a high-voltage relay to avoid saturation and damage caused by excess photons. During the detection cycle, the IR laser is turned off using an AOM to avoid scattered VUV photons contributing to the noise.

Figure 4.2: Timing diagram of the experiment.

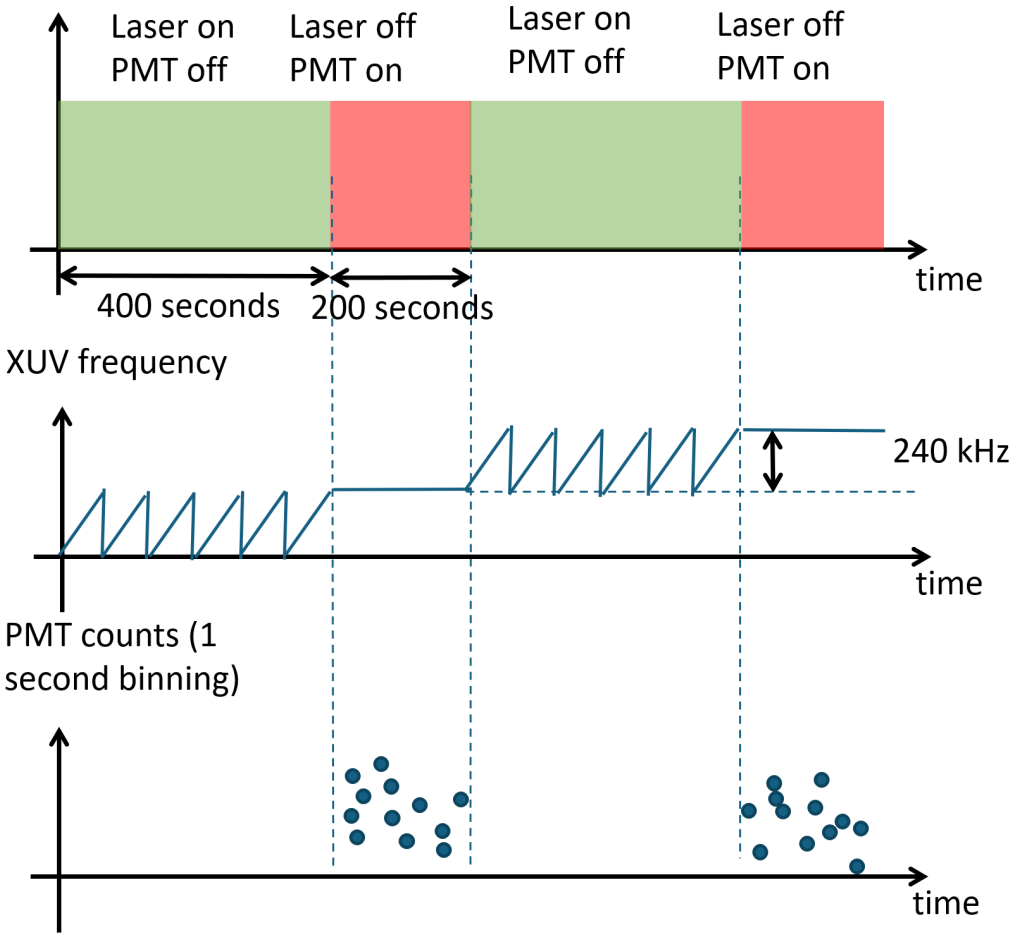

4.3 Quantum-state resolved nuclear spectroscopy with absolute frequency reference

We use the cavity-enhanced HHG process to establish a direct frequency link between the ^{229}Th nuclear transition and the ^{87}Sr optical clock [5], illustrated in Fig. 4.3. The IR frequency comb is locked to the JILA ^{87}Sr clock laser [171], which inherits the stability of the ^{87}Sr clock [5] in the long term. In the short term, we actually rely on the JILA Si cavity [176] to serve as a "flywheel" to keep track of the laser frequency. Even relying on the Si cavity with a stability demonstrated better than 10^{-17} is good enough for our first spectroscopy demonstration. The frequency stability is faithfully transferred to the VUV using the cavity-enhanced 7th harmonic generation process (Chap. 2). One single mode of the VUV comb is then used to excite the ^{229m}Th isomer state. The experimental realization of the locking scheme is described in Chap. 2.

Figure 4.3: Frequency link between ^{87}Sr clock and ^{229}Th nuclear transition. Figure taken from Ref. [24]

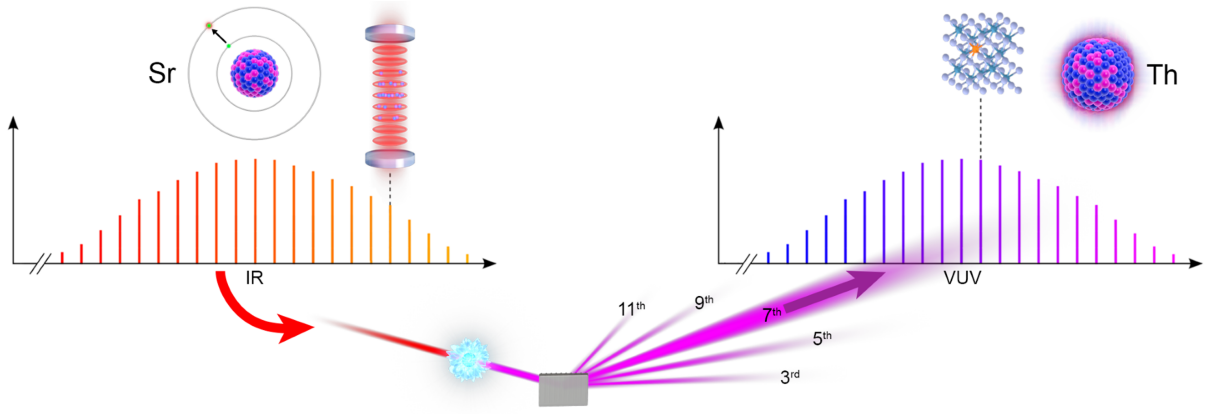

With the fundamental comb f_{ceo} stabilized to a radiofrequency standard at effectively -8 MHz and one of the comb mode stabilized to the ^{87}Sr clock laser, the comb f_{rep} is first measured with a frequency counter to extract the integer mode number that satisfies the frequency comb equation

$$\nu_1 = f_{\text{ceo}} + N_1 \times f_{\text{rep}} \tag{4.1}$$

Knowing the integer mode number, a more accurate f_{rep} value is extracted using the known optical

frequency of the ^{87}Sr clock ν_{Sr}. The 7th harmonic comb frequency is then described by

$$\nu_7 = 7 \times f_{\mathrm{ceo}} + N_7 \times f_{\mathrm{rep}} \tag{4.2}$$

Using the known $^{229\mathrm{m}}$Th energy uncertainty [27, 28], we know that the integer mode number is roughly $N \sim 2.7 \times 10^7$. To search for the transition signal, we scan f_{rep} in a range of ~ 2.8 Hz to scan the comb structure underneath the 7th harmonic spectral envelope without changing the envelope itself. This scan range is multiplied by the comb mode number N to give the scan range in the VUV domain. The corresponding scan range of ~ 75 MHz allows us to ensure that the comb mode numbered N at the end of the scan overlaps the starting point for the $N + 1$ comb mode frequency; see Fig. 4.4 top panel. Thus, we fully cover the spectrum under the approximately 1 nm wide comb spectral envelope.

In the middle panel of Fig. 4.4, the average photon count rate over the 200 s detection window at each frequency setting f_{rep} is plotted. The background photon count rate of ~ 415 cps comes from the intrinsic radioactivity of the ^{229}Th:CaF_2 crystal [257]. On top of the background, six clear spectroscopic features are observed. Four of them are highlighted in green, and their absolute frequencies are determined. Two of them are highlighted in blue. We did not perform absolute frequency determinations of them due to the relatively low SNR. They may originate from different electronic environments in the crystal and will be subject to future studies. In the bottom panel, we plot the measured count rate as a function of time after binning f_{rep} to ~ 15 mHz bins (corresponding to ~ 400 kHz bin size in VUV) to observe the time dependence. We clearly see that the fluorescence of each spectroscopy feature persists beyond the 200 s detection window, consistent with the long lifetime [27, 66] of $^{229\mathrm{m}}$Th in CaF_2 reported in previous measurements.

We then explore the line shape and the lifetime of the $^{229\mathrm{m}}$Th state. We place one comb line on resonance and irradiate the crystal for 1200 s to accumulate a higher $^{229\mathrm{m}}$Th population. We monitor the fluorescence count rate afterwards for ~ 90 min. The trace in Fig. 4.5a is fit to an exponential decay with a time constant $\tau = 641(4)$ s, consistent with the lifetime measured in Refs. [27, 66].

Figure 4.4: A full-range comb scan. The VUV comb repetition rate is scanned by precisely tuning f_{rep} to shift all the comb lines in parallel. The optical frequency gap between adjacent comb lines is fully covered when the Nth comb mode overtakes the original frequency position of the $(N+1)$th comb mode (top panel). Experimentally, the precise f_{rep} control is achieved by fixing f_{ceo}, then digitally changing the phase lock offset frequency between the ^{87}Sr clock laser and its nearest comb line. The average fluorescence photon count rate per second (cps) in the 200 s detection window is plotted against the comb repetition rate. Six distinct spectroscopic features are observed and highlighted in blue and green (middle panel). Four dominant peaks (green), which we later assign to electric quadrupole splittings of the nuclear transition, will be used for absolute frequency determination. The count rate as a function of time (color bar; units in cps) at each frequency bin is plotted in the bottom panel, highlighting a nuclear excited-state lifetime that is significantly longer than the detection window.Figure taken from Ref. [24].

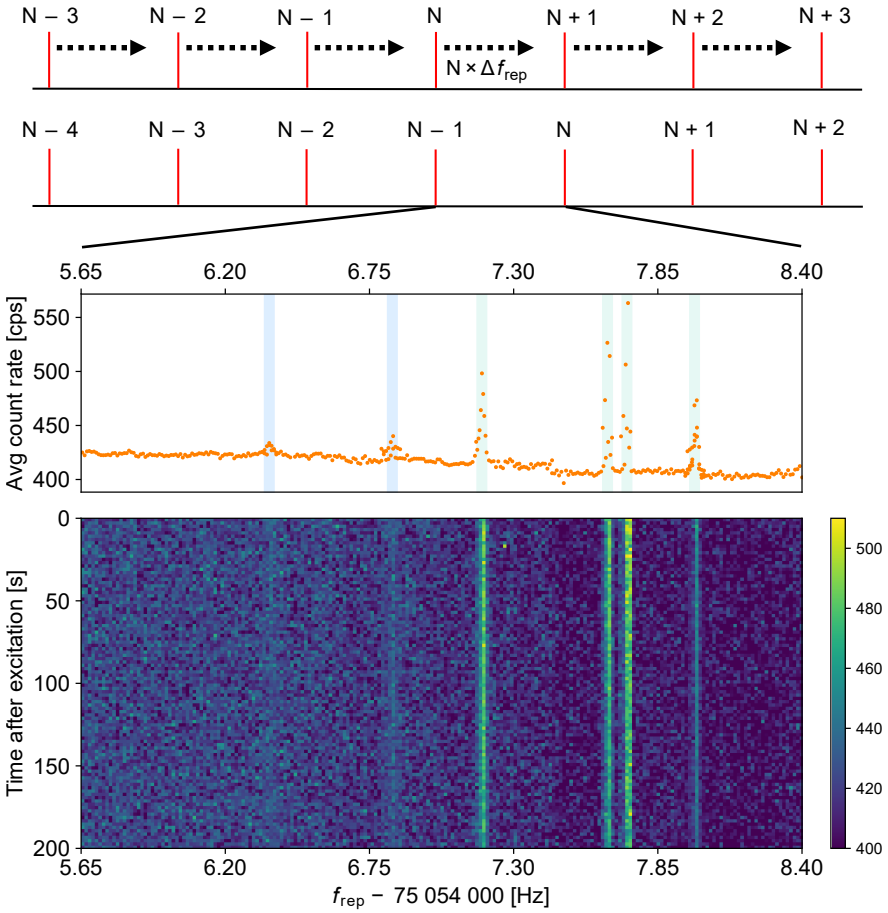

Using our 400 s irradiation and 200 s detection cycle, the long lifetime of ^{229m}Th causes a line shape asymmetry due to the memory effect. The ^{229m}Th population excited from the previous data point does not fully decay before the next measurement starts. To avoid a systematic shift of the center frequency caused by this asymmetry, we performed two measurements. First, we use the same irradiation time of 400 s, but wait for 1800 s ($\sim 3\tau$) between adjacent frequency steps. This allows most of the ^{229m}Th to decay to the ground state. We also kept the excitation frequency fixed (instead of sweeping over the 240 kHz range). Fig. 4.5b shows a measurement using this technique. A symmetric line shape is observed and fit to a Gaussian with a full width at half-maximum (FWHM) of 0.0116(5) Hz in f_{rep}, corresponding to a linewidth of 310(10) kHz in VUV.

However, it is clear that such measurements take extremely long (almost a day for Fig. 4.5). In order to use the measurement time efficiently, we performed bidirectional scans for subsequent measurements. Here, we use the same 400 s on/200 s off experiment cycle but scan the line shape once by increasing f_{rep} and another time by decreasing f_{rep}. The scan range for each step is set to 100 kHz in the VUV. The two scans are each fit to Gaussian line shapes, and the line center is determined by averaging the fit parameters from the two scans; see Fig. 4.5. Both line shapes have slightly asymmetries due to the short detection window, but the systematic center frequency offsets from the two measurements cancel each other out when they are averaged together. Line center uncertainties of $\sim$ 4 kHz and FWHM of $\sim$ 300 kHz are obtained. We used this method for the absolute frequency determination reported in Ref. [24], see below.

Although the crystal is illuminated with all comb modes in parallel, each spectroscopic feature corresponds to nuclear excitation by a unique single comb mode. We use the technique previously demonstrated in Ref. [161] to determine the comb mode number that is exciting the transition, therefore determining the absolute optical frequency of a given peak. To achieve this, we scan the same transition line with three different comb mode numbers N_i (i denotes the scan number) using different f_{rep}, as shown in Fig. 4.6a. These three distinct comb modes correspond to $\sim$ 100 kHz jumps in f_{rep}. Jump step sizes are chosen such that they are much larger than the absolute frequency

Figure 4.5: a Lifetime measurement of the excited clock state 229mTh ($m_g = \pm 5/2$ to $m_{is} = \pm 3/2$ transition, Fig. 4.8, line b). The fluorescence photon count rate is monitored over time after laser excitation of 1200 s. A portion of the data around 2000 s is absent owing to technical reasons. The experimental data is fit with a single exponential decay, leaving no structure in the fit residual. The extracted lifetime of the nuclear excited state is 641(4) s in the CaF_2 host crystal. b, Fine scan showing the line shape (Fig. 4.8, line a) for one of the main clock transitions. We wait 1800 s in between each data point to avoid line-shape asymmetry that could arise from residual excited population from previous scan steps. The fitted Gaussian full-width at half-maximum (FWHM) is 0.0116(5) Hz in f_{rep}, corresponding to 310(10) kHz in absolute frequency. c, Bidirectional scan (Fig. 4.8, line b). To accelerate the experimental cycle in line center determination for the four selected peaks, we use fast (400 s laser on and 200 s laser off) laser scan cycles. We perform scans by stepping f_{rep} in both positive and negative directions, and their results, after proper intensity normalization, are averaged to eliminate systematic shifts caused by potential line-shape asymmetries.Figure taken from Ref. [24].

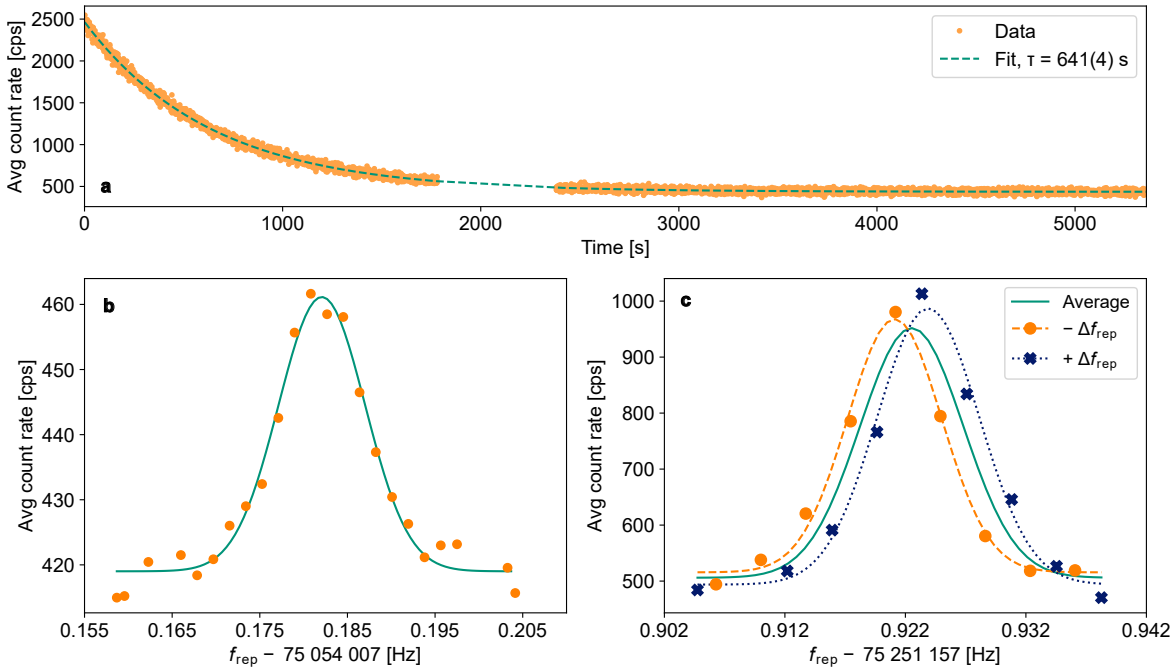

uncertainty in the fitted line centers ($\sim$ 4 kHz)[161]. At each f_{rep} step, the new f_{rep} position of each peak is estimated based on previous knowledge of the transition frequency. Thus, only a small spectral region needs to be scanned to find the exact position of the peak. In combination with the bounds on the transition frequency set by Refs. [27, 28], we determine the integer comb mode number resonant with the nuclear transition at each f_{rep}, and thus the absolute frequency of the transition unambiguously.

The uncertainty range of the nuclear transition at 2020408(3) GHz (given by the weighted average of Refs. [27, 28] corresponds to approximately 80 possible comb mode numbers $N_1 \approx$ 26848820 to 26848900 for f_{rep_1}, shown on the horizontal axis of Fig. 4.6b. We use these mode numbers to compute initial guesses of the absolute frequency ν_{Th}. We use the fitted line centers at f_{rep_2} and f_{rep_3} to assign the integer comb mode N_2 and N_3 closest to the initial guess ν_{Th}. Using the comb equation Eqn. 4.2, we can write down a set of equations for the $^{229\mathrm{m}}$Th transition frequency as

$$\nu_{\mathrm{Th}_i} = N_i f_{\mathrm{rep_i}} + 7 f_{\mathrm{ceo}}. \tag{4.3}$$

For the correct assignment of the comb mode number, the three ν_{Th_i} obtained from f_{rep_i} ($i = 1, 2, 3$) should agree closely within the uncertainties propagated from the center uncertainty of the fitted line. We quantify this average frequency discrepancy as

$$\frac{1}{3}\sum_{i=1}^{3} \left|\nu_{\mathrm{Th}_i} - \nu_{\mathrm{Th}_{\mathrm{avg}}}\right| \tag{4.4}$$

where $\nu_{\mathrm{Th}_{\mathrm{avg}}}$ is the weighted average of the three ν_{Th_i}. We show in Fig. 4.6b that the optimal assignment of comb mode produces the lowest frequency discrepancy of $\sim$ 10 kHz, within the $3-\sigma$ uncertainty region calculated from the center uncertainty of the center of the fitted line. A mistake in the assignment of the comb mode numbers by ± 1 increases the average frequency discrepancy by an order of magnitude.

This optimal comb mode number assignment can also be visualized by using a linear fit based on a rearranged version of Eqn. 4.2:

Figure 4.6: a, Illustration for absolute frequency determination. We precisely scan the same transition line by using three different values of f_{rep}. When these f_{rep} values are sufficiently different from each other and are yet precisely known, the exact mode number associated with each f_{rep} can be unambiguously determined [161]. b, Previous measurements [27, 28] of the nuclear transition energy provides an initial guess range of about 80 possible comb mode numbers. Integer trial values of comb mode number N_1 in the first scan are picked and the transition frequencies are calculated accordingly. We force the comb mode number for the subsequent two measurements to the closest integer according to f_{rep} and calculate the transition frequency from them. The averaged frequency discrepancy between the measurements quantifies the comb mode assignment error. The lowest value of the discrepancy corresponds to the experimentally determined comb mode number assignment. The disagreement jumps by a factor of 10 when the comb mode is misassigned by ± 1. The indicated $1-\sigma$ line and $3-\sigma$ region corresponds to the statistical uncertainty of the fitted Gaussian line center. c, Another method for comb mode determination is to perform a linear fit between the mode number and the inverse value of f_{rep}. With an expanded view in the inset, we plot our measurement data for the two f_{rep} jumps, with the corresponding $1-\sigma$ error bars. The solid dark blue line corresponds to the comb mode number assignment N from b, in agreement with the measurement. Dashed green lines correspond to comb mode $N \pm 1$, in clear disagreement with our measurements. d, With the determination of the mode numbers, three scanned line shapes of a specific nuclear transition, corresponding to three different values of f_{rep} are plotted together against their absolute optical frequencies, confirming their consistency (a.u., arbitrary units. Figure taken from Ref. [24].

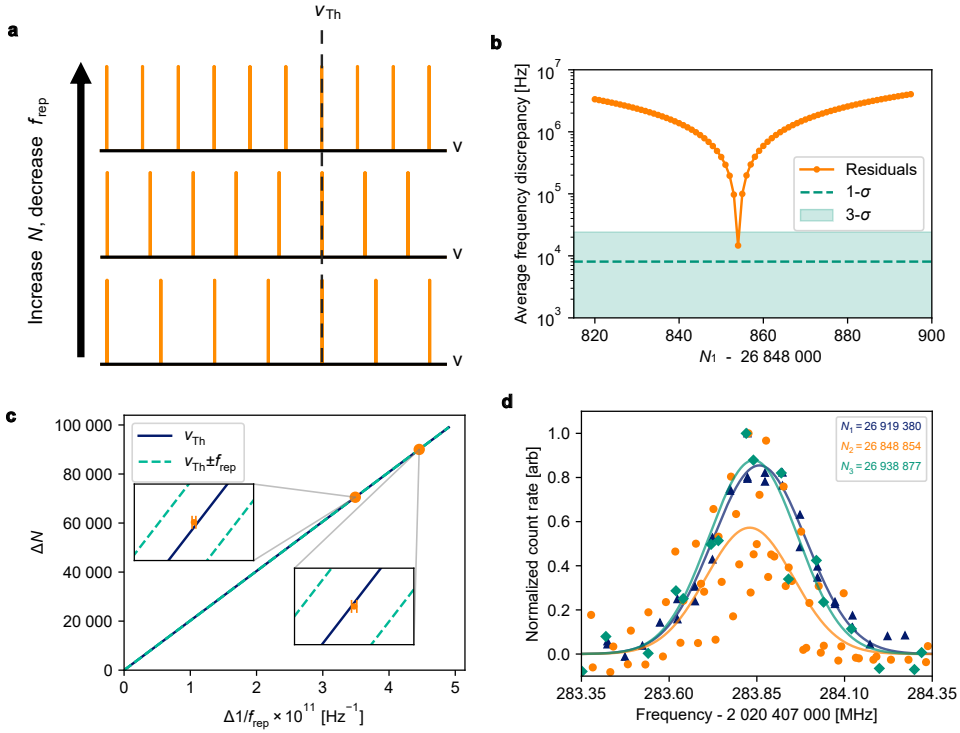

$$\Delta N = (\nu_{\mathrm{Th}} - 7f_{\mathrm{ceo}})\Delta\frac{1}{f_{\mathrm{rep}}} \tag{4.5}$$

where ΔN and $\Delta\frac{1}{f_{\mathrm{rep}}}$ describe the change in the comb mode number and the inverse fitted peak center f_{rep} from one of the measurements, here taken as f_{rep_3}. We then obtain two data points corresponding to f_{rep_1} and f_{rep_2} with error bars calculated from the fitted line center uncertainties, see Fig. 4.6. The insets provide an expanded view. The solid dark blue line passing through the origin with a slope of $\nu_{\mathrm{Th}_{\mathrm{avg}}} - 7f_{\mathrm{ceo}}$ corresponds to the optimal comb mode number assigned in Fig. 4.6. The dashed green lines correspond to comb mode number assignments off by ± 1, in clear disagreement with our measured data. The two analyses in Fig. 4.6 confirm each other and demonstrate that we have assigned the mode number N_i with complete confidence.

With the comb mode numbers N_i for the three measurements uniquely determined, we use Eqn. 4.3 to convert f_{rep} to absolute optical frequency in the VUV. Fig. 4.6d shows the three scans of the same peak (individually normalized) and their Gaussian fits plotted against the absolute frequency, in which the legend displays the determined comb mode number. We see that the three scans overlap perfectly with each other, confirming the correct determination of the absolute frequency. The absolute frequency is then calculated as the weighted average between the three scans.

This procedure is repeated for the four high SNR peaks in Fig. 4.4 (highlighted in green). The four chosen lines are attributed to the nuclear electric quadrupole structure; see Fig. 4.7. As the ^{229}Th nuclei are embedded in a CaF_2 host crystal, they experience a strong electric field gradient originating from the surrounding lattice ions, F^- interstitials and electron configuration [263]. The interaction between the electric quadrupole moment Q of the ^{229}Th nucleus and this electric field gradient gives rise to an electric quadrupole splitting (Fig. 4.7a), predicted to be on the order of hundreds of MHz [67, 68], which matches our observations. The splittings can be extracted from

diagonalizing the Hamiltonian [263, 264]:[4]

$$H_{\mathrm{E2}} = \frac{QV_{zz}}{4I(2I-1)}\left[3I_z^2 - \boldsymbol{I}^2 + \eta(I_x^2 - I_y^2)\right] \tag{4.6}$$

where Q is the spectroscopic nuclear electric quadrupole moment [63, 26] in the ground (Q_{g}) or isomeric (Q_{is}) state, and $\boldsymbol{I}$ is the nuclear angular momentum vector. The principal axis is chosen so that the electric field gradient matrix V_{ij} is diagonal with components V_{xx}, V_{yy}, and V_{zz}. Since the E-field gradient matrix is traceless, we replace V_{yy}, and V_{zz} with a single asymmetry parameter

$$\eta = (V_{xx} - V_{yy})/V_{zz}. \tag{4.7}$$

The ground state of ^{229}Th has a nuclear spin $I_{\mathrm{g}} = 5/2$, while the excited isomer state $^{229\mathrm{m}}$Th has $I_{\mathrm{is}} = 3/2$. Transitions with $\Delta m = 0, \pm 1$ are allowed by selection rules.[5] The expected level diagram is shown in Fig. 4.7b, with five allowed transition lines denoted as lines a-e.

Lines a-d are uniquely assigned to the electric quadrupole structure that fits Eqn. 4.6. In the initial full-range scan shown in Fig. 4.4, we did not observe the line e in the quadrupole structure that corresponds to $m_{\mathrm{g}} = \pm 1/2$ to $m_{\mathrm{is}} = \pm 3/2$. From the Clebsch-Gordon coefficients, this line is predicted to have only approximately one-tenth of the strength of the strongest line. Based on three of the known frequencies, we determine the expected absolute frequency of this fifth line by using the "sum rule":[6]

$$\nu_{\mathrm{e}} = \nu_{\mathrm{c}} + \nu_{\mathrm{d}} - \nu_{\mathrm{a}} = 2,020,407,693.966(7)\ \mathrm{MHz}. \tag{4.8}$$

We then repeat the scan over the corresponding f_{rep} with our comb, and indeed we observe a weak line whose frequency is measured to be $2,020,407,693.98(2)$ MHz, in agreement with the prediction. This frequency is determined using only a single scan by using the expected comb mode number calculated from the expected line center from Eq. 4.8.

[4] For $I = 3/2$ and $I = 5/2$, analytical solutions can be found in Refs. [265, 266].

[5] A large asymmetry of the E-field gradient described by η leads to state mixing and, therefore, additional weak transitions. However, they are not observed in this work and do not correspond to the two weak peaks highlighted in blue in Fig. 4.4. For more details, see Ref. [30].

[6] Imagine starting from $m_{\mathrm{g}} = \pm 1/2$, we change the nuclear state energy by adding $n\nu_{\mathrm{e}}$ to $m_{\mathrm{is}} = \pm 3/2$, subtracting $n\nu_{\mathrm{d}}$ to $m_{\mathrm{g}} = \pm 3/2$, adding $n\nu_{\mathrm{a}}$ to $m_{\mathrm{is}} = \pm 1/2$, and finally subtracting $n\nu_{\mathrm{c}}$ to arrive back at starting state of $m_{\mathrm{g}} = \pm 1/2$. One easily sees that Eqn. 4.8 is true by forming this loop.

Figure 4.7: Illustration of the electric quadrupole splitting. a, Illustration of the lattice structure (Ref. [263]) near a ^{229}Th-doped site in CaF_2showing the Ca^+ (blue), F^- (yellow) of the original CaF_2 lattice, as well as the $^{229}Th^{3+}$ dopant (red) and F^- interstitials (green) for charge compensation. The ion configuration in the crystal may lead to a gradient of electric field $\vec{E}$ (EFG) that interacts with the nuclear quadrupole moment Q. The direction of the largest EFG component V_{zz} sets the quantization axis z. b, Expected electric quadrupole splitting and allowed transition lines. I_g and I_{is} denotes the ground and excited (isomeric) state nuclear spin, with m being the quantum number along z axis.

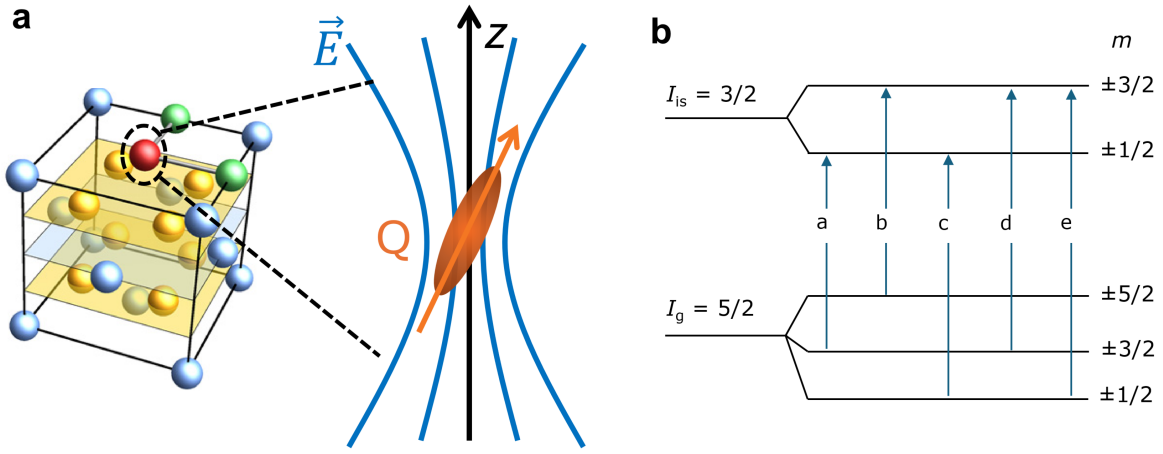

The absolute frequencies of the five lines are tabulated in Table. 4.1. Fig. 4.8 shows the data for the five peaks (labeled a-e according to Fig. 4.7) in absolute frequency, with their peak intensities individually normalized.[7] The center frequency of each line is determined to be of 4 kHz uncertainty (1σ) for lines a-d and 20 kHz for line e. The observed splittings are on the order of hundreds of MHz, in agreement with expectations [67, 68].

Line	m_{g}	m_{is}	ν_{Th} [MHz]
a	3/2	1/2	2 020 407 283.847(4)
b	5/2	3/2	2 020 407 298.727(4)
c	1/2	1/2	2 020 407 446.895(4)
d	3/2	3/2	2 020 407 530.918(4)
e	1/2	3/2	2 020 407 693.98(2)

Table 4.1: Quadrupole-split nuclear transition frequencies. The lines are assigned to the quadrupole splitting structure shown in Fig. 4.7b using their absolute frequencies according to Eqn. 4.6. Data taken from Ref. [24]

We observe that the line splitting caused by the nuclear electric quadrupole moment (Eqn. 4.6) does not shift the center-of-mass of the lines.[8] That is,

$$E_{\mathrm{g,ave}} = [E_{\mathrm{g}}(m_{\mathrm{g}} = \pm 1/2) + E_{\mathrm{g}}(m_{\mathrm{g}} = \pm 3/2) + E_{\mathrm{g}}(m_{\mathrm{g}} = \pm 5/2)]/3 \tag{4.9}$$

$$E_{\mathrm{is,ave}} = [E_{\mathrm{is}}(m_{\mathrm{is}} = \pm 1/2) + E_{\mathrm{is}}(m_{\mathrm{is}} = \pm 3/2)]/2, \tag{4.10}$$

$E_{\mathrm{g,is}}(m)$ represents the energy of the ground or excited isomeric state with particular m quantum numbers, and $E_{\mathrm{g,ave}}$ and $E_{\mathrm{is,ave}}$ are the average energies of the ground and excited state without the quadrupole splitting. This relation can be verified using the analytic solutions of the eigenvalues of Eqn. 4.6 presented in Refs. [265, 266].

Using this relationship, we see that the unsplit transition frequency can be written as

$$\begin{aligned} \nu_{\mathrm{Th}} &= \frac{1}{3}(\nu_{\mathrm{b}} + \nu_{\mathrm{d}} + \nu_{\mathrm{e}}) - \frac{1}{2}(\nu_{\mathrm{d}} - \nu_{\mathrm{a}}) \\ &= \frac{1}{6}(\nu_{\mathrm{a}} + 2\nu_{\mathrm{b}} + 2\nu_{\mathrm{c}} + \nu_{\mathrm{d}}) \\ &= 2,020,407,384,335(2)\ \mathrm{kHz}, \end{aligned} \tag{4.11}$$

[7] The line strength qualitatively matches with the expected value from the Clebsch-Gordan coefficients (averaged over different polarizations). The theoretically expected values can be found in Ref. [30].

[8] This is generally true for the hyperfine structure in atoms as well.

Figure 4.8: The quadrupole line structure when ^{229}Th is subject to an electric field gradient inside the CaF_2 crystal. The assignment of the lines to the corresponding energy levels are shown in Fig. 4.7b. With the absolute frequencies of lines a, b, c and d determined by the direct comb spectroscopy technique, their corresponding quantum numbers are uniquely assigned. An enlarged view shows the measurement data for each line, with their relative intensity normalized to unity. The frequency of line e, which is a factor of 10 weaker in line strength, was calculated first by using the relationship $\nu_e = \nu_c + \nu_d - \nu_a$, and then confirmed with a comb scan using a single comb mode. Absolute frequencies of the five transition lines are listed in Table 4.1. Figure taken from Ref. [24].

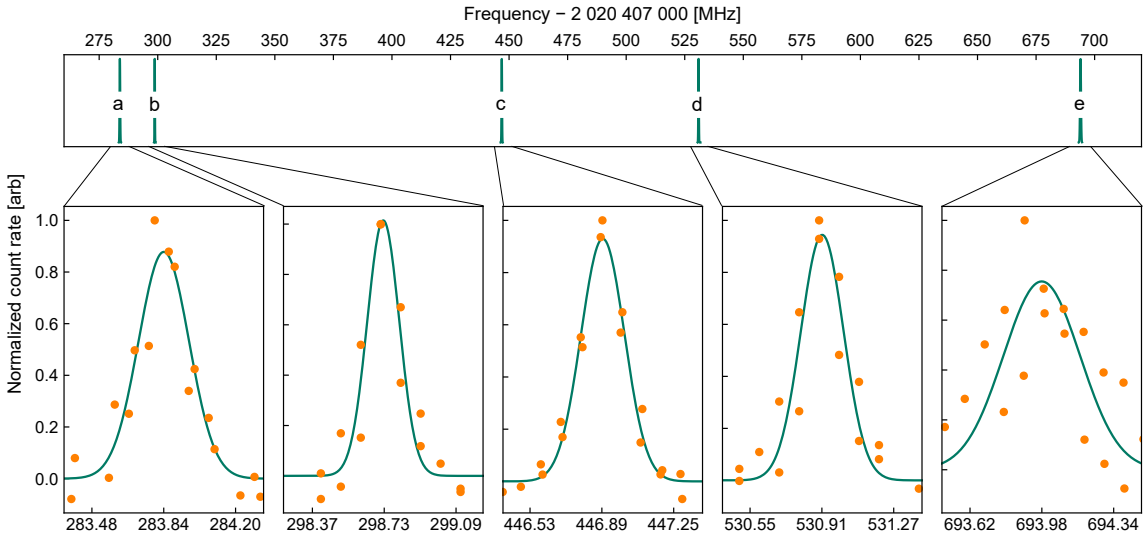

corresponding to a frequency ratio between the ^{229}Th nuclear clock transition and the ^{87}Sr atomic clock transition as

$$\frac{\nu_{\mathrm{Th}}}{\nu_{\mathrm{Sr}}} = 4.707,072,615,078(5) \tag{4.12}$$

for ^{229}Th nuclei embedded in a CaF_2 host crystal at 150(1) K. Characterizing the systematic uncertainty of this frequency ratio is an ongoing research project, with a dominant systematic effect, the temperature of the crystal, characterized in Ref. [77].

4.4 Fundamental physics implications

In addition to being a good clock, we see that ^{229}Th, which is a system very different from existing atomic clocks, may offer a high sensitivity to new physics [30, 267, 268, 269]. Using Eqn. 4.6, we fit the measured line centers to the predicted quadrupole structure using η, $Q_{\mathrm{g}}V_{zz}$ and $Q_{\mathrm{is}}V_{zz}$ as the fitting parameters. This procedure yields

$$\eta = 0.59163(5) \tag{4.13}$$

$$Q_{\mathrm{g}}V_{zz} = 339.258(7) \text{ eb V Å}^{-2} \tag{4.14}$$

$$Q_{\mathrm{is}}V_{zz} = = 193.387(5) \text{ eb V Å}^{-2} \tag{4.15}$$

where 1 eb = 1.6022×10^{-47} C m^2 denotes one electron-barn. The extracted uncertainties are purely statistical (using a Monte-Carlo procedure).

Independent of the crystal environment, the ratio of the quadrupole moment extracted from this fitting procedure is

$$Q_{\mathrm{is}}/Q_{\mathrm{g}} = 0.57003(1), \tag{4.16}$$

consistent with previously reported ratios from laser spectroscopy of the electronic hyperfine structure [63, 44] but with improved uncertainty.[9] This result will be used below to evaluate the

[9] The uncertainties extracted from a Monte-Carlo procedure. Direct division of $Q_{\mathrm{is}}V_{zz}$ and $Q_{\mathrm{g}}V_{zz}$ yields a larger error bar due to correlations. A full analysis of the error propagation is presented in the supplementary material of Ref. [30].

nuclear clock's sensitivity to temporal variation of fundamental constants. Taking the previously published [31] value of $Q_{\mathrm{g}} = 3.11(2)$ eb, the local electric field gradient in the ^{229}Th doped site of CaF_2 is measured to be

$$V_{zz} = 109.1(7)\text{V Å}^{-2}. \tag{4.17}$$

This value serves as a useful probe to understand the defect configuration in the crystal [263].

We focus on the nuclear quadrupole moment in this section and follow Ref. [30] to extract the sensitivity of the nuclear clock transition to variation of the fine-structure constant α. To understand the nuclear shape, we first convert the measured spectroscopic quadrupole moment in the lab frame Q_{lab} to the intrinsic quadrupole moment Q_0 via the relation [30]

$$Q_0 = \frac{Q_{\mathrm{lab}}}{q_{\mathrm{e}} Z} \frac{(2I+3)(I+1)}{3k^2 - I(I+1)}, \tag{4.18}$$

where $Z = 90$ is the number of the thorium nucleus, q_{e} is the elementary charge, and k is the projection of the nuclear spin on the deformation axis.[10] For the spectroscopic quadrupole moment, we follow the definition of Refs. [271, 27, 26] with unit in electron-barn. For the intrinsic quadrupole moment, we remove $q_{\mathrm{e}}Z$ dependence as in Ref. [272] to obtain a quantity purely dependent on the nuclear shape with unit in fm^2 for the following geometric considerations. Combining Eqn. 4.16 and Eqn. 4.18, we obtain the ratio of intrinsic quadrupole moment between the isomeric and ground state of ^{229}Th as

$$Q_0^{\mathrm{is}}/Q_0^{\mathrm{g}} = 1.01791(2). \tag{4.19}$$

We model the nucleus as a prolate spheroid with uniform volume charge density as described in Refs. [273, 272]. From purely the geometrical relations, the mean-square radius $\langle r^2 \rangle$ and the intrinsic quadrupole moment Q_0 are then expressed using the semi-minor and semi-major axes a and c as

$$\langle r^2 \rangle = \frac{1}{5}(2a^2 + c^2), \tag{4.20}$$

$$Q_0 = \frac{2}{5}(c^2 - a^2). \tag{4.21}$$

[10] It is assumed that the nuclear deformation is axially symmetric, see, for example, Ref. [270], Vol. 2, Eqn. (4-69).

This set of equations allows us to express a and c using $\langle r^2 \rangle$ and Q_0. We use the Coulomb energy of the nucleus given by Eqn. (5.11) in Ref. [274] as

$$E_{\mathrm{C}} = \frac{3q_e^2 Z^2}{5R_0} \frac{(1-e^2)^{-1/3}}{2e} \ln \frac{1+e}{1-e}, \tag{4.22}$$

$$e = \sqrt{1 - a^2/c^2} \tag{4.23}$$

$$R_0^3 = a^2 c \tag{4.24}$$

where e is the eccentricity and R_0 is the radius of a sphere containing the same volume.[11] We then compute the Coulomb energy difference between the isomer excited state and the ground state as

$$\Delta E_{\mathrm{C}} = \frac{\partial E_{\mathrm{C}}}{\partial \langle r^2 \rangle} \Delta \langle r^2 \rangle + \frac{\partial E_{\mathrm{C}}}{\partial Q_0} \Delta Q_0. \tag{4.25}$$

To perform this calculation, we used $\langle r^2 \rangle = 5.756(14)$ fm^2 from Ref. [276], $\Delta \langle r^2 \rangle = 0.0105(13)$ fm^2 from Ref. [277], spectroscopic electric quadrupole moment of the ground state $Q_{\mathrm{g}} = 3.11(2)$ eb in Ref. [31], and the newly determined ratio of intrinsic quadrupole moments (Eqn. 4.19). We obtain the Coulomb energy difference between the nuclear isomeric and ground state as [30]

$$\Delta E_{\mathrm{C}} = -0.154(19) \text{ MeV} + 0.203(4) \text{ MeV} \tag{4.26}$$

$$= 0.049(19) \text{ MeV}. \tag{4.27}$$

Using this Coulomb energy difference, we find that the ^{229}Th nuclear transition has a highly enhanced sensitivity to the temporal variation of the fine structure constant α [278, 272, 30]. Imagine a small variation of $\Delta\alpha$ over time, which would lead to a variation of the nuclear transition frequency by changing the Coulomb energy in the nucleus (proportional to α) while keeping other energy terms the same in the nucleus. The fractional change of the clock transition energy is then expressed as

$$\frac{\Delta \nu_{\mathrm{Th}}}{\nu_{\mathrm{Th}}} = \frac{\Delta E_{\mathrm{c}}}{h \nu_{\mathrm{Th}}} \frac{\Delta \alpha}{\alpha}. \tag{4.28}$$

We define the enhancement factor K as

$$K = \frac{\Delta E_{\mathrm{C}}}{h \nu_{\mathrm{Th}}} = 5900(2300). \tag{4.29}$$

[11] This equation assumes a uniform charge density liquid droplet model of a prolate nucleus, see Ref. [275] for more details.

Optical atomic clocks have sensitivity enhancement factors on the order of 1. Thus, a variation of the frequency ratio between the nuclear clock and an atomic clock would indicate the discovery of new physics through the variation of fundamental constants such as α.

The above analysis assumes that the changes in the octupole and higher-order deformation between the ground and excited state of ^{229}Th are small. Although this is likely true, direct measurements of higher-order multipole moments [279] would help determine the enhancement factor in a model-independent way.

Chapter 5

Frequency characterization of a solid-state nuclear clock

To operate the ^{229}Th spectroscopy experiment as a clock, we need to characterize and understand its frequency stability and reproducibility. The systematic shifts of the ^{229}Th transition frequency with respect to environmental variables need to be characterized, which limits the accuracy (systematic frequency uncertainty) of the clock. We would like to understand its stability, i.e. what is the statistical uncertainty dependent on the measurement time? This dictates how much measurement time we need to average the signal in order to reach the systematic frequency uncertainty limit. A good clock should have both high precision and high stability such that the statistical uncertainty can reach the precision within reasonable averaging times [2].

On the other hand, systems with unique advantages in either precision or stability are still desired, as one can combine several systems and harness the best parts of their performance using spectral tailoring [172]. Viewing from the frequency domain, we use phase lock loops (PLLs) with a tailored bandwidth to take the low phase noise portion of each system [178]. Viewing from the time domain, at short times we rely on high-stability sources[1] while performing corrections using high-accuracy sources[2] for long time scales.

For obtaining a good clock stability, the desired system should have a high operating frequency, large atom numbers, and long coherent probe times (narrow linewidths). Detailed discussions on this can be found in Refs. [2, 4]. ^{229}Th offers an operational frequency around 2 PHz, higher than any other existing clock platform. By scaling from single trapped ions [51] to quantum

[1] Say, hydrogen maser for microwave oscillators, or cryogenic Si-cavity [57] for an optical oscillator.
[2] For example, Cs microwave clocks, or Sr optical clock [5].

gas systems with $10^4 \sim 10^6$ atoms [5] to solid-state systems with 10^{12} atoms [67, 68, 76] or beyond in a small volume, we gain orders of magnitude in the number of atoms that can be probed together. The intrinsic coherence time of ^{229}Th limited by its excited-state lifetime [25, 44] also exceeds the best optical clocks used today [3, 5]. However, controlling the decoherence in ^{229}Th systems and reaching a long coherent probing time requires creative solutions in the future, as the currently demonstrated coherence time is only $\sim$ µs (inverse of $\sim$ 100 kHz linewidth) [24].

To understand the accuracy of the clock, systematic shifts should be carefully evaluated. The small nuclear electromagnetic moments of ^{229}Th, together with the shielding effects of the external electronic shell, promise a high accuracy. However, in trapped-ion platforms, suitable electronic states must be chosen to achieve good clock performance [52]. In solid-state ^{229}Th systems, the systematic uncertainty of 10^{-16} is expected due to temperature-induced frequency shifts [67, 68]. We show that by probing several quantum-state resolved lines, the temperature of the crystal can be precisely measured and temperature-induced frequency shift completely eliminated; see Sect. 5.2 for the co-thermometry proposal. Other systematic shifts could potentially be reduced using similar co-sensor ideas.

5.1 Line shift and broadening mechanisms in Mössbauer spectroscopy

To understand the clock stability and accuracy, we briefly summarize the line shift and splitting mechanisms in Mössbauer spectroscopy; see Fig. 5.1. Inhomogeneity of the crystal lattice may lead to site-dependent line shifts, and thus to an inhomogeneous broadening effect.

The isomer shift mechanism shown in Fig. 5.1 comes from the electric monopole interaction between the nucleus and the local electron density. This is also referred to as the "chemical shift" in some Mössbauer spectroscopy literature [33, 281, 264]. The finite charge radius interacts with the local electron charge density, creating a shift to the nuclear energy level that is dependent on the electron configuration in the solid. As the ^{229}Th nuclear ground and excited state have slightly different mean charge radii, this leads to a shift in the observed nuclear transition frequency. Although it is typically assumed that the primary contribution to this isomer shift comes from

Figure 5.1: Line shift and splitting mechanisms in Mössbauer spectroscopy. The electric monopole interaction leads to an overall shift of the transition, while electric quadrupole and magnetic dipole interactions lift the degeneracy of the quantum states and lead to line splittings. Figure adapted from Ref. [280].

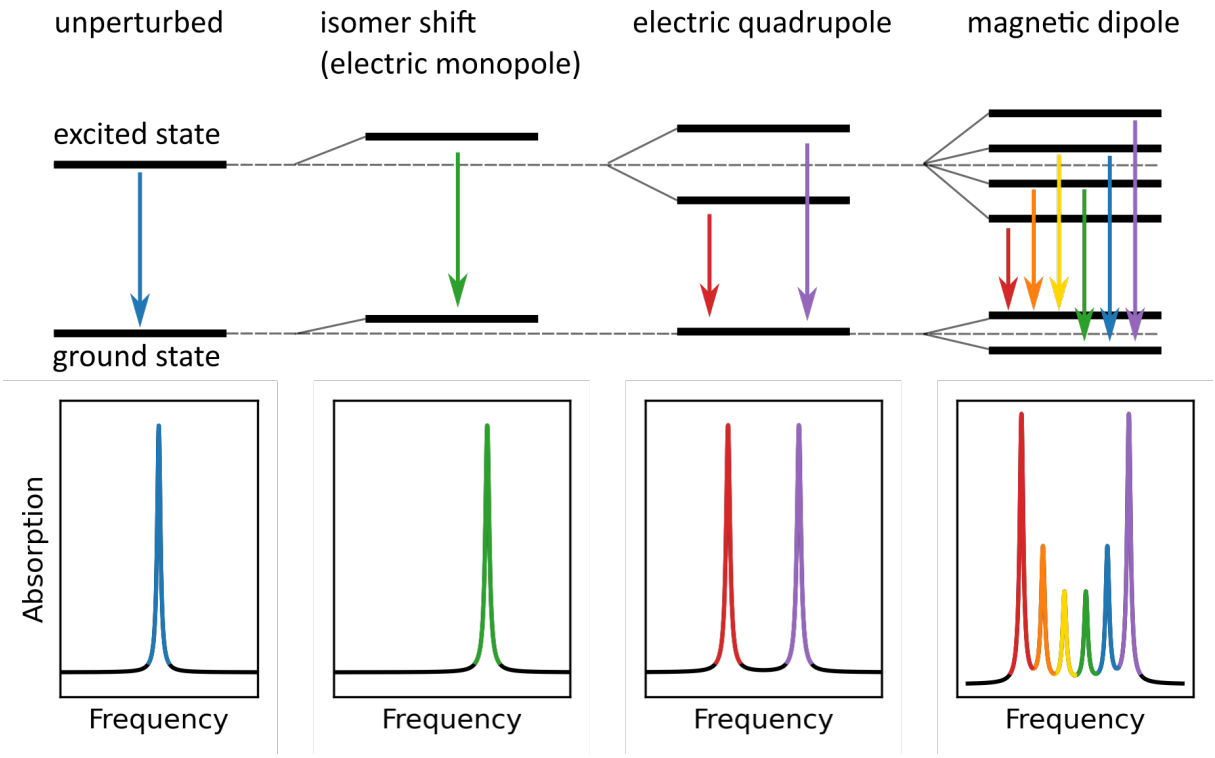

s electrons that have a large overlap with the nucleus, p, d, f electrons can contribute through screening effects [281]. The same effect is expected in trapped-ion nuclear clocks [282].

While the absolute magnitude of the isomer shift is not an observable in our experiment, the temperature dependent change of the isomer shift due to CaF_2 crystal lattice thermal expansion can be directly measured. We describe the change of the isomer shift versus temperature following Refs. [77, 281] as

$$\delta\nu_{E0} = \left(\frac{4\pi Z e^2 r^2}{5h}\right) S'(Z)[\Delta\psi^2(0)] \left[\frac{\Delta r}{r}\right], \tag{5.1}$$

where $\delta\nu_{E0}$ is the change of the EFG-free transition energy given by Eqn. 4.11, $Z = 90$ is the charge number of thorium, e is the charge of electron, R is the nuclear radius with $\Delta r = r_{\mathrm{is}} - r_{\mathrm{g}}$ being the change of the nuclear mean charge radius from ground to isomeric state, and h is Planck's constant. A relativistic correction is taken into account using the correction factor $S'(Z) = 11.68$ for $Z = 90$, see Ref. [77, 281].[3] $[\Delta\psi^2(0)]$ denotes the change in electron wavefunction density at the nucleus with the unit of inverse volume. We also use the approximation $\frac{\Delta r}{r} \approx \frac{\Delta\langle r^2\rangle}{2\langle r^2\rangle}$, where $\langle r^2\rangle = 5.756(14)$ fm^2 is found from Ref. [276] and $\Delta\langle r^2\rangle = 0.0105(13)$ fm^2 is found from Ref. [277].

The second effect of line shift comes from the electric quadrupole moment of the nucleus interacting with the local electric field gradient (EFG), described in Chap. 4 by Eqn. 4.6. Parameters relevant to ^{229}Th hosted in the CaF_2 crystal can be solved using our state-resolved spectroscopy data [24], see Sect. 4.4.

Finally, the magnetic dipole of the ^{229}Th nucleus interacting with an external magnetic field may further lift the degeneracy of the states. The magnetic dipole interaction can simply be described by

$$\Delta\nu_B = g_I \mu_N m_I B, \tag{5.2}$$

where g_I is the g-factor of the ^{229}Th nucleus, μ_N is the nuclear magneton, m_I the nuclear spin and B the magnetic field. The nuclear magnetic moments for both the ground state and the

[3] Ref. [281] Sect. II C contains more details. The first-order perturbation theory gives a factor $S(90) = 16$ listed in Table I of Ref. [281]. Adding the consideration for wavefunction distortion near the origin changes this value slightly, given by another correction factor (Eqn. 10 in Ref. [281]) of $\frac{S'(90)}{S(90)} = 0.73$ listed in the same table.

nuclear isomer are presented in Fig. 1.1. The magnitude of this Zeeman shift is on the order of kHz/Gauss, dependent on the alignment between the magnetic field direction with respect to the EFG quantization axis.

In our experiment with no applied external magnetic field, the Zeeman shift from magnetic dipole interaction can be neglected. However, in the future, the magnetic dipole interactions between ^{229}Th nucleus and nearby randomly oriented fluorine nuclear spins may present a limit to the coherence time of solid-state ^{229}Th nuclear clocks. This broadening due to the magnetic dipole interaction is estimated to be on the order of a few hundred Hz [67, 68, 76]. On the other hand, the coupling between the optically active ^{229}Th nuclear transition with neighboring nuclear spins may also enable optical control of nuclear spin states [283].

Other shift and broadening mechanisms, such as the second-order Doppler effect, are small compared to the discussions presented above [68]. It is well known that phonons also lead to significant decoherence for rare-earth ion qubits hosted in solids at room temperature [284]. However, phonon-induced broadening in ^{229}Th has not been observed in our experiments so far. We can consider phonon-induced line broadening as a frequency modulation process, where the crystal lattice vibration modulates the local electromagnetic field, leading to a modulation of the transition frequency of a two-level system. For the nuclear transition, the modulation amplitude is small ($\sim$ MHz, interaction between the ^{229}Th and the crystal) while the modulation frequency is high ($\sim$ THz, phonon frequencies in the lattice), leading to a small modulation depth and thus negligible broadening [177].

5.2 Investigating the clock accuracy: dependence of center frequency on temperature

So far, temperature-induced frequency shift is predicted to be the dominant systematic effect on a ^{229}Th nuclear clock [67, 68]. Thus, we start by exploring the temperature-induced systematic shifts of the nuclear clock following Ref. [77].

We cool the crystal using a liquid nitrogen (LN2) Dewar connected to the crystal mount; see

Figure 5.2: Schematic of the crystal mount and thermal control. The thorium-doped calcium fluoride crystal is mounted on a baseplate in vacuum, which is connected to an external dewar via a copper thermal link. The temperature is continually monitored using a sensor attached to the mounting plate. The dewar is in contact with a cold trap which condenses molecules to reduce vacuum pressure. The dewar is filled with liquid nitrogen for measurements at 150 K, a methanol/dry ice mixture for measurements at 229 K, and is unfilled for measurements at 293 K. A parabolic mirror collimates fluorescent photons, which are then counted downstream after spectral filtering. Shown in the inset is the crystal structure of calcium fluoride, where one calcium ion is replaced with doped Th^{4+}, and two F^- interstitials are added for charge compensation. Figure taken from Ref. [77].

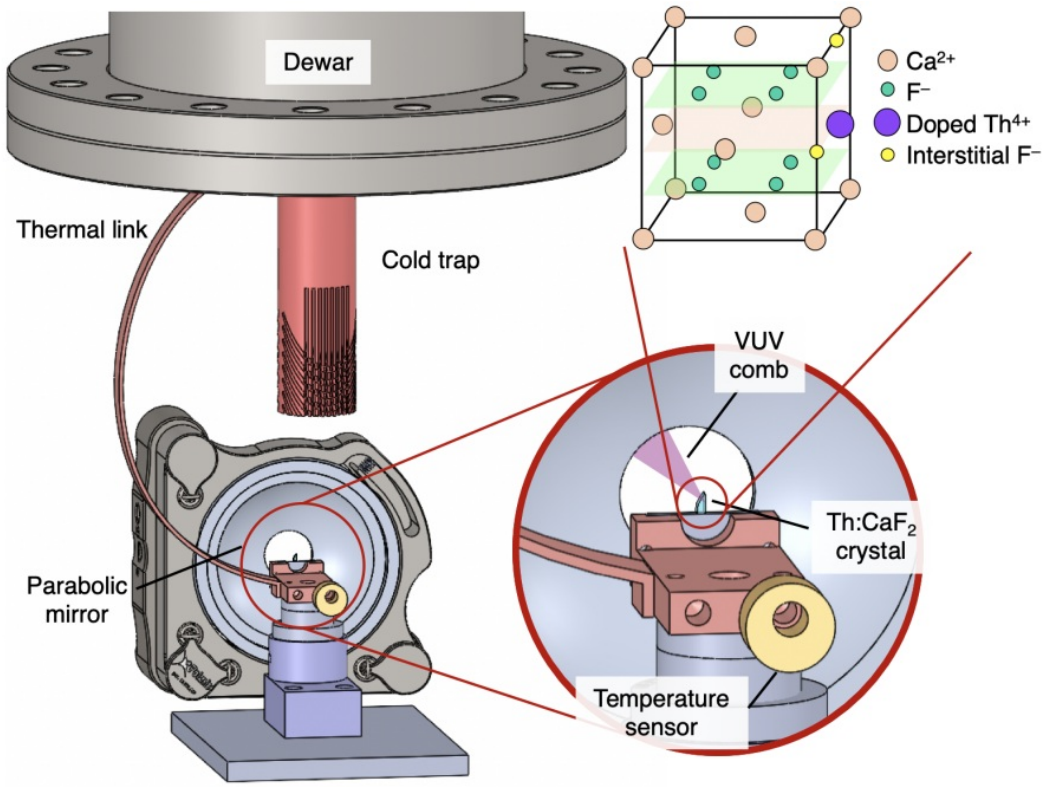

Fig. 5.2. Using different mixtures of the coolant, we sampled a few different temperature points. An optional heater is added close to the crystal for finer temperature control. The temperature reported here is measured using a Si-diode temperature sensor mounted on the same copper structure that holds the crystal. Although the thermal contact between the crystal and the mount may create a temperature gradient and thus a systematic temperature error, we anticipate this systematic effect to be reproducible. As we will see later, the absolute temperature calibration does not pose a problem for the clock accuracy.

First, we check the temperature dependence of the center frequency of the 4 strong lines observed in Ref. [24], shown in Fig. 5.3. The unsplit frequency, as a proper weighted average of the 4 lines by Eqn. 4.11, is also shown as the red line. We interpret the shifts as mainly from the electric monopole and electric quadrupole interaction (Fig. 5.1), both changes due to the thermal expansion of the host crystal. Firstly, as the crystal thermally expands, we anticipate the bond length to be increased and the local electron charge density to be reduced, changing the isomer shift. Secondly, the electric field gradient (EFG) in the crystal reduces as the crystal expands when its temperature is increased. From the Hamiltonian related to this effect, Eqn. 4.6, we see that the splitting between the lines will be reduced at higher temperatures. With the 4 lines measured, we can perform the fitting for quadrupole splitting as described by the Hamiltonian in Eqn. 4.6. The parameters obtained are plotted in Fig. 5.4. As expected, the crystal V_{zz} changes with temperature due to thermal expansion, but the ratio between the ground and excited state parameter QV_{zz}, as an intrinsic nuclear property, remains the same. The change in the η parameter indicates an anisotropic thermal expansion, common in crystals.

We then focus on the temperature dependence of the peak (b) and (c) shown in Fig. 4.8, which corresponds to $m = \pm 5/2 \rightarrow \pm 3/2$ and $m = \pm 1/2 \rightarrow \pm 1/2$, respectively. We measure the line center frequencies as a function of temperature in three different crystals, which are called X2 (^{229}Th concentration: 4×10^{18} cm^{-3}), C13 (^{229}Th concentration: 8×10^{17} cm^{-3}) and C10 (^{229}Th concentration: 3×10^{17} cm^{-3}) [228].

Two observations are made. First, we see that the measurements made in different crystals

Figure 5.3: Temperature shift of nuclear clock transition lines. Top panel shows a Zoom-in view of the bottom panel. The unsplit frequency is the weighted average of the quadrupole split lines using Eqn. 4.11, which is independent of the magnitude of the quadrupole splitting. Figure taken from Ref. [77].

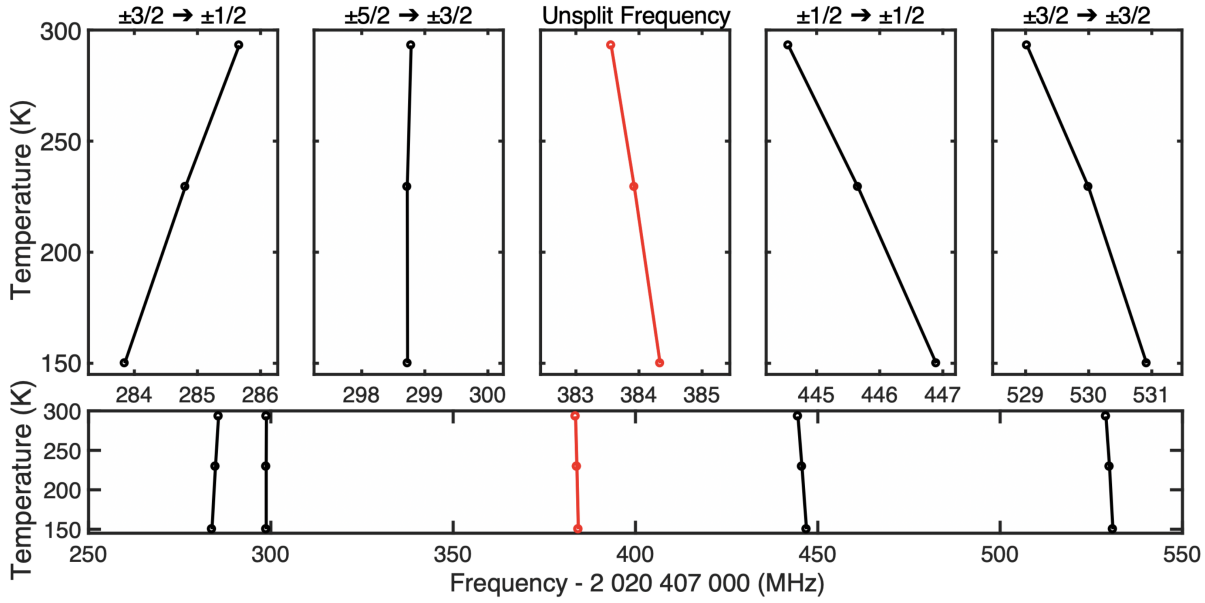

Figure 5.4: Temperature-dependent CaF_2 crystal parameters. a, QV_{zz} as a function of temperature, for both the ground and isomer state. b, Asymmetry parameter η as a function of temperature. Figure taken from Ref. [77].

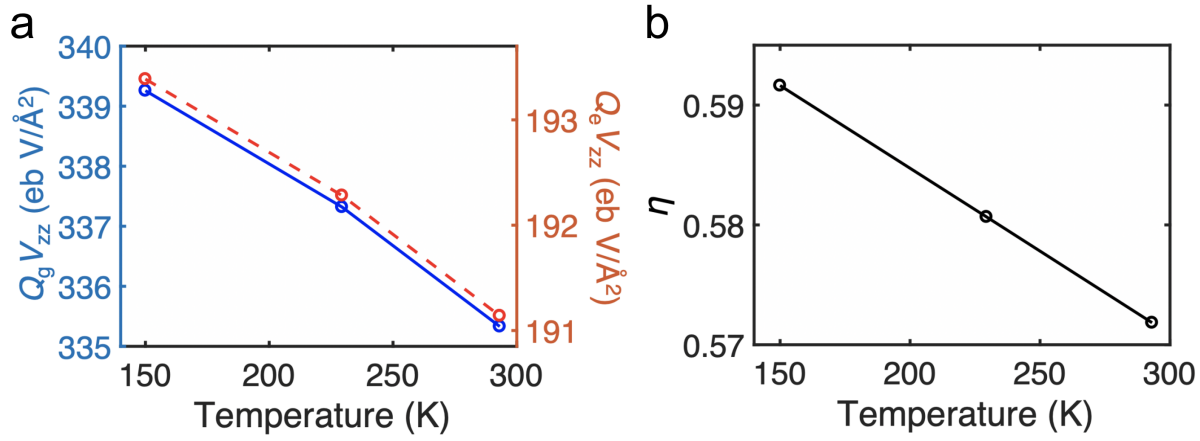

Figure 5.5: Differential temperature sensitivity of two peaks. a, Center frequency of $m = \pm 5/2 \rightarrow \pm 3/2$ (peak b in Fig. 4.8) versus temperature. Data is fit to a second order polynomial. b, Center frequency of $m = \pm 1/2 \rightarrow \pm 1/2$ (peak c in Fig.4.8 as a function of temperature. Both curves are taken with three different crystals, X2 (purple), C13 (green), and C10 (orange). At each temperature, measurements from different days are combined to a single data point by weighted averaging.

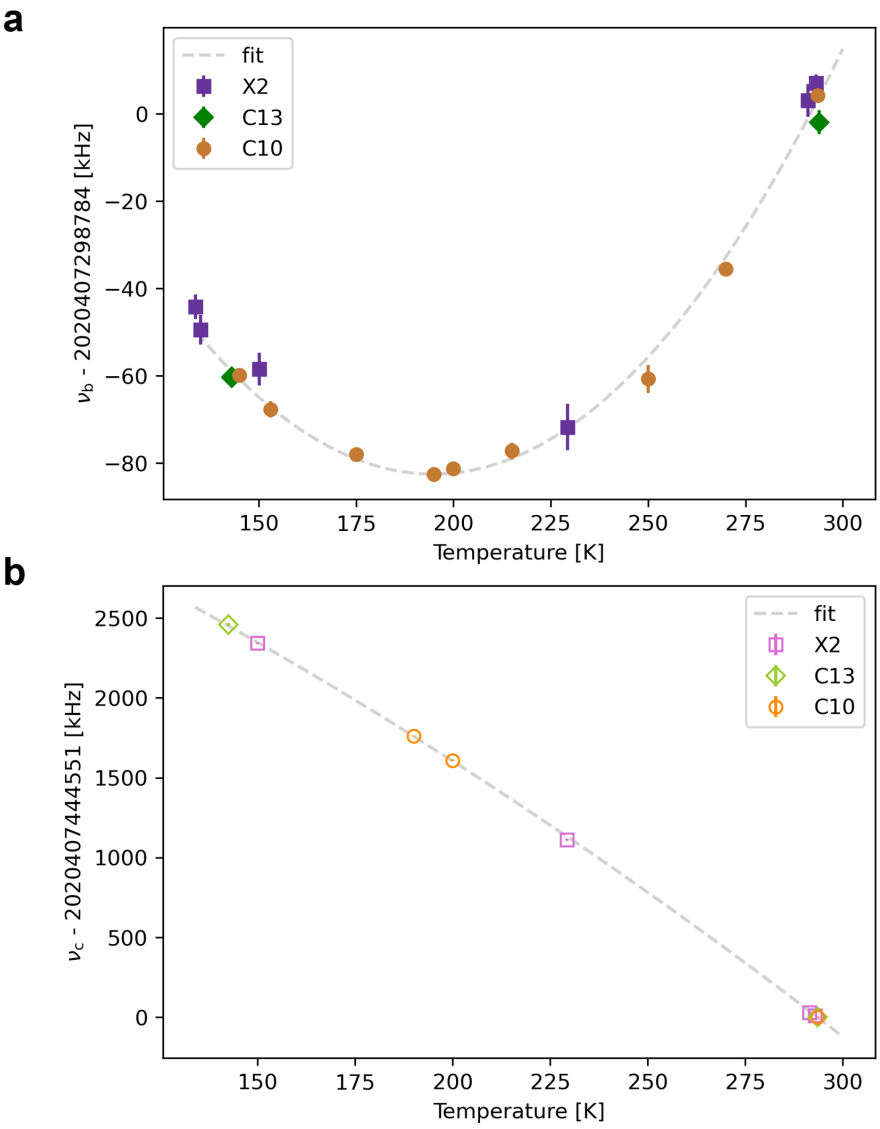

roughly follow the same trend and agree with each other. This is very encouraging: ^{229}Th can indeed be used as an absolute optical frequency reference, as crystals grown in different batches with different doping concentrations yield reproducible absolute optical frequencies.

More importantly, we see that peak b has a much lower temperature sensitivity compared to peak c, see Fig. 5.5. This presents an opportunity to perform co-thermometry using the ^{229}Th nuclear transition in situ. Without rigorous analysis yet, we perform an order-of-magnitude estimation:

The center of the peak c can typically be determined to within $\sim$ 1 kHz uncertainty in our present system. According to Fig. 5.5b, this corresponds to a temperature uncertainty of $\sim$ 0.1 K. From Fig. 5.5a, we see the peak b position has a quadratic turning point at $\sim$ 195 K temperature, and a scaling of roughly

$$\nu_b \sim 9(T - 195)^2 + \text{ Const. (Hz/K)} \tag{5.3}$$

where T is the temperature and ν_b the optical frequency of peak b. A 0.1 K temperature sensitivity thus corresponds to a 0.1 Hz line center uncertainty operating close to the turning point of peak b, giving us an accuracy limit of $\sim 10^{-16}$ from the temperature dependence. Of course, as we improve the center frequency determination for both peaks b and c, it is easy to see that the peak b frequency error due to the temperature shift will always be orders of magnitude smaller than the peak c center frequency uncertainty. By performing co-thermometry, temperature-induced frequency shift will be eliminated from the error budget of a solid-state nuclear clock!

One may ask how good a temperature stability is required to achieve a $\sim 10^{-20}$ accuracy. This corresponds to a line center uncertainty of $\sim$ 0.1 mHz, which can be achieved with a temperature accuracy of 1 mK according to Eqn. 5.3. To facilitate this level of temperature measurement, a $\sim$ 10 Hz line center determination of peak c (Fig. 5.5b) is all we need.

Other factors may also create systematic shifts. Here we take the stress of the crystal as an example. The Young's modulus of CaF_2 [285] is 75.8 GPa while the thermal expansion coefficient is 18.85×10^{-6} /K. Thus, the thermal expansion of 1 mK temperature is on the same order of

magnitude as a 1.4 kPa stress. Care needs to be taken to calibrate the stress on the CaF_2 host crystal, say, by birefringence measurements [286]. Or, the same co-sensor idea may be used to compensate for stress-induced drifts.

5.3 Investigating the clock stability: Dependence of linewidth on ^{229}Th doping concentration

To obtain good clock stability, the coherence time (inverse of the inhomogeneous line broadening) of the nuclear transition should be long. One limitation in solid-state crystalline hosts comes from the interaction between the ^{229}Th nuclear spin with nearby nuclear spins, which is expected to cause an inhomogeneous broadening of $\sim$ hundreds of Hz [67, 68, 76]. Experimentally, we find that the transition linewidths measured are larger at higher doping concentrations. We speculate that microstrain caused by ^{229}Th doping defects in CaF_2 may be the cause of this effect.

It is well known that the crystal lattice near a defect is elastically distorted due to the local microstrain [287]. This elastic distortion decays slowly from the defect, giving rise to observable line broadening [288] and line center shift [289] in high-resolution X-ray and neutron scattering experiments.

Although the lattice distortion due to a defect can be calculated in detail using the method of lattice statics [290], here we ask what the asymptotic behavior is at large distances. An approximate $\xi \sim 1/r^2$ scaling is reported for cubic metals in Ref. [291]. Similar scaling rules are also found in alkali halide crystals [292]. This is perhaps not surprising. If we simply consider adding one atom with a volume of V to a crystal lattice, considering volume conservation, atoms at distance r from the dopant would move roughly by δr satisfying $r^2 \delta r = V$ to conserve the volume. Also, the mean distance r_0 between the defects scales as the inverse of the cubic root of the concentration ρ. Thus, we anticipate the distortion of the lattice structure to be scaling roughly as

$$\delta r \propto 1/r_0^2 \propto \rho^{2/3}. \tag{5.4}$$

How large is this effect in ^{229}Th-doped CaF_2 crystals? For ^{232}Th-doped CaF_2, the mean

lattice parameters (distances) a with two different doping concentrations are measured by X-ray diffraction and reported in Ref. [289]. Here, we do a simple estimation extrapolating the fractional lattice parameter change $\delta a/a$ reported in Ref. [289] to the parameter range used in our experiments, following Eqn. 5.4, see Fig. 5.6. Based on this estimation, it is reasonable to expect that the fractional lattice distance change in our experiment will be of the order of $10^{-4} \sim 10^{-5}$. The exact location and orientation of the defect state will lead to an inhomogeneous broadening of the nuclear clock transition. Returning to Fig. 4.8, we see that the crystal lattice leads to a splitting on the order of a few hundred MHz. The monopole shift is also typically on the GHz level. The expected line broadening effect due to the fractional lattice constant change can therefore be estimated as $10 \sim 100$ kHz, varying depending on the ^{229}Th doping concentration.

Figure 5.6: Lattice constant change with Th-doping concentration. Orange dots are taken from Ref. [289]. Scaling according to Eqn. 5.4 is plotted as a visual guide. For densities used in this thesis work, the fractional lattice distance change is expected to be $10^{-4} \sim 10^{-5}$.

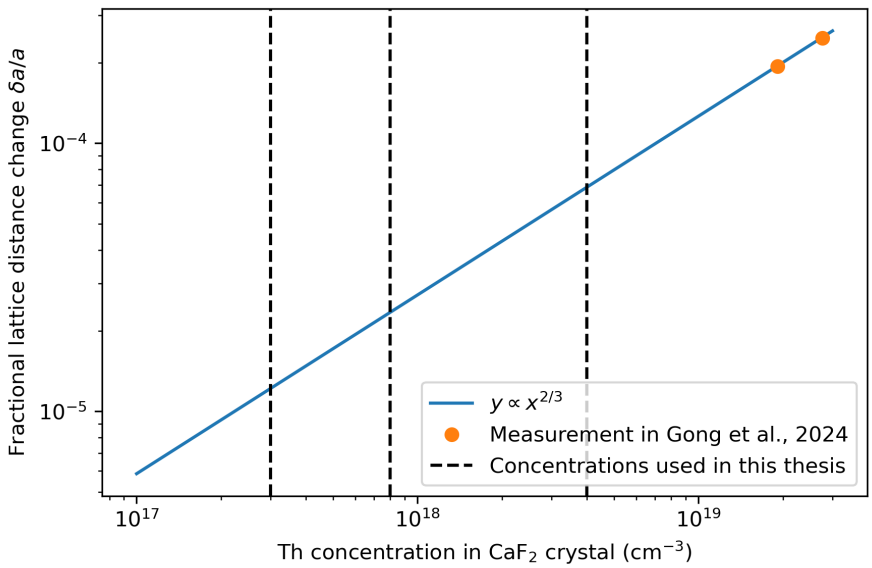

We experimentally verify this using three different crystals with different doping concentrations:

(1) C10, 3×10^{17} cm^{-3} (blue in Fig. 5.7)

(2) C13, 8×10^{17} cm^{-3} (green in Fig. 5.7)

(3) X2, 4×10^{18} cm^{-3} (purple in Fig. 5.7)

Experimentally, different peaks also show different linewidths. The peak b ($m = \pm 5/2 \rightarrow \pm 3/2$, solid markers in Fig. 5.7) appears to always be narrower than the peak c ($m = \pm 1/2 \rightarrow \pm 1/2$, hollow markers in Fig. 5.7). Note that peak b also shows a smaller temperature dependence in Fig. 5.5, resulting from the cancelation between the electric monopole and electric quadrupole shifts. It is possible that the same cancelation makes the peak b less sensitive to crystal lattice distortions caused by microstrain. Although the scaling relation in Eqn. 5.4 does not fully match the experimental observation, we show it as a visual guide in Fig. 5.7. The SNR of the transition observation is significantly reduced going to lower concentrations, limiting our ability to probe the limitation of the linewidth due to other effects.

By the same argument, one may ask if the center frequency of the transition would also change with the doping concentration. However, experimentally, we do not observe differences in the transition frequencies between the different crystals. The dependence of the linewidth on the doping concentration indicates that the ^{229}Th nuclear transition frequency is likely dependent on the mean distance between the ^{229}Th nucleus. The line center independence indicates that the transition frequency cannot be solely dependent on the mean ^{229}Th nuclear distance. Likely, the transition frequency shift also depends on the orientation of the F^- interstitials.

5.4 Reproducibility of the nuclear clock frequency

We keep a record of the frequencies for the peaks b and c over time at room temperature; see Fig. 5.8. The absolute frequencies of the nuclear transition remain within the uncertainty over the half-year data collection time for peak b. For peak c, the larger fluctuations may originate from changes in room temperature. Fig. 5.8 highlights the frequency reproducibility for both clock transition lines across 3 different crystals.

Figure 5.7: ^{229}Th nuclear clock transition linewidth as a function of doping concentration. Two different peaks, b ($m = \pm 5/2 \rightarrow \pm 3/2$, solid markers) and c ($m = \pm 1/2 \rightarrow \pm 1/2$, hollow markers), are studied. Three crystals are used: C10 (orange), C13 (green), and X2 (purple). The dotted line provides a visual guidance for the scaling expected according to Eqn. 5.4.

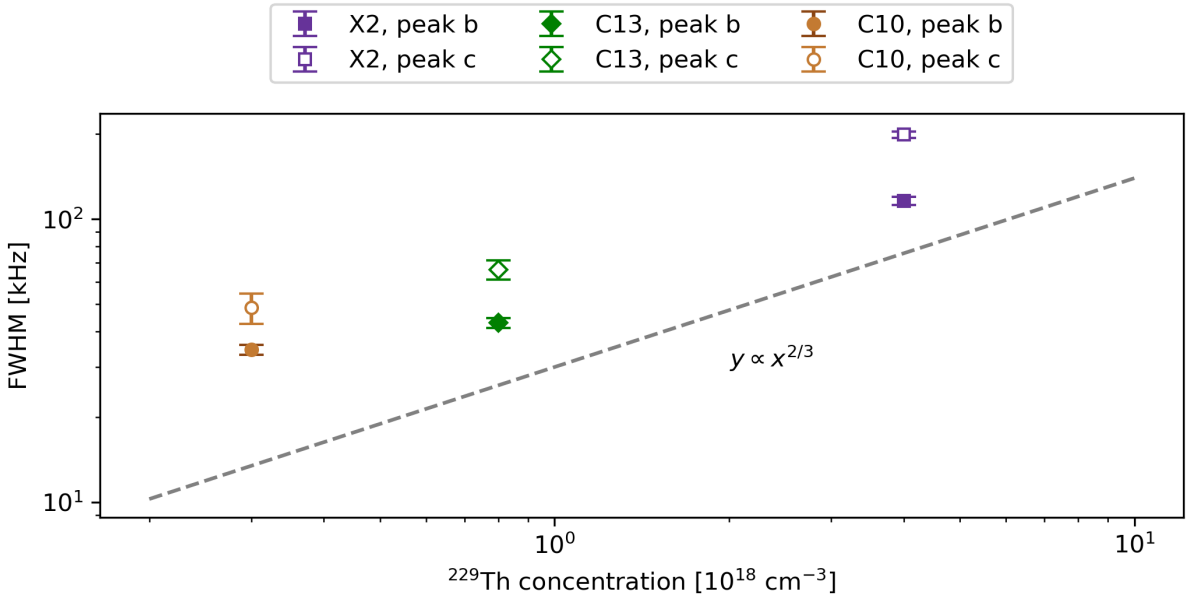

Figure 5.8: Time record of peak b/c frequencies at room temperature. a, the frequencies of peak b at room temperature. The results are reproducible with the uncertainties for peak b. b, Record of peak c frequency at room temperature. The larger fluctuation may come from its higher sensitivity to temperature changes.

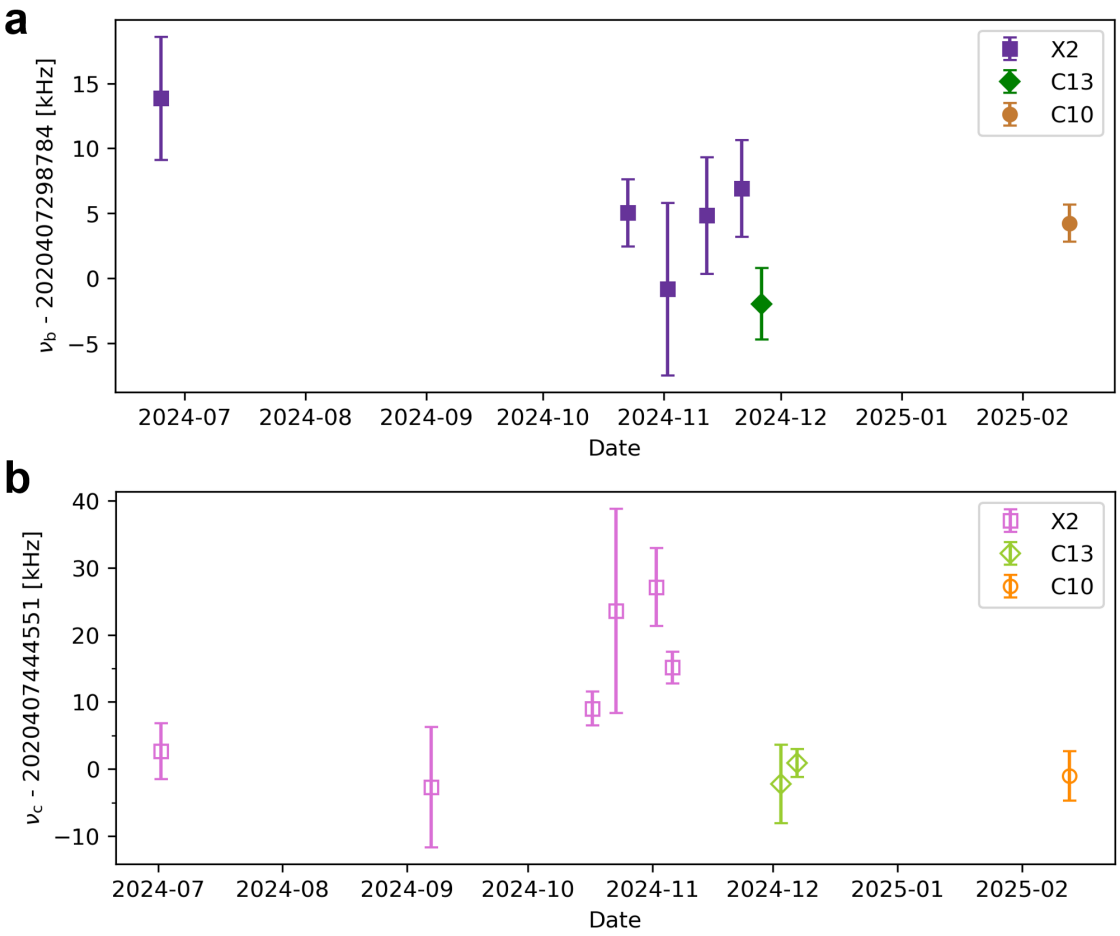

5.5 Projected nuclear clock performance

We perform a simple estimation of the clock stability following Ref. [68], as shown in Fig. 5.9. Two laser frequencies, $\Delta \pm \sigma$, are used to interrogate the nuclear clock transition. After each irradiation subcycle with time θ, a detection window of θ' is used to collect fluorescence photons. After completion of the 4 subcycles, the offset between the laser and the nuclear transition can be calculated using the imbalance between the fluorescence counts in the two detection windows. The laser center frequency is then steered to keep track of the nuclear clock.

In our experiment, the observed nuclear transition line shape can be described by a Gaussian with a peak effective excitation rate of $R_0 \sim 2000$ counts per second (cps); see, for example, Fig. 4.5a. With the narrowest peak b line shape observed being about 100 kHz, we write down the excitation rate as

$$R(\nu) = R_0 \mathrm{e}^{-\ln 2 \cdot \nu^2/\sigma_0^2}, \tag{5.5}$$

where f is the offset from the center frequency, and $\sigma_0 = 50$ kHz is the linewidth (half width at half maximum). Assuming the offset frequency f is small and following the clock sequence shown as in Fig. 5.9, we write down the measured result of f as

$$f = \frac{R(\sigma+f) - R(\sigma-f)}{2\frac{\partial R}{\partial \nu}\big|_{\nu=\sigma}} = \frac{R(\sigma+f) - R(\sigma-f)}{-2\ln 2 \cdot R_0 \sigma/\sigma_0^2 \cdot \mathrm{e}^{-\ln 2 \cdot \sigma^2/\sigma_0^2}} \tag{5.6}$$

where it is assumed that $f \ll \sigma_0$ is a small frequency offset, and we use the fact that $R(\nu)$ is a symmetric function.

We see that the excitation rates can be written as

$$R(f+\sigma) = \frac{N_n - N_{n-1}\mathrm{e}^{-(\theta+\theta')/\tau}}{\tau(1-\mathrm{e}^{-\theta/\tau})(1-\mathrm{e}^{\theta'/\tau})}, \tag{5.7}$$

$$R(f-\sigma) = \frac{N_{n+1} - N_n \mathrm{e}^{-(\theta+\theta')/\tau}}{\tau(1-\mathrm{e}^{-\theta/\tau})(1-\mathrm{e}^{\theta'/\tau})}. \tag{5.8}$$

In equilibrium, the number of counts N accumulated in each bin will be roughly

$$N_i = n_0\theta' + R(\sigma)\tau(1-\mathrm{e}^{-\theta/\tau}) \tag{5.9}$$

Figure 5.9: Illustration of the clock interrogation cycle. Each full cycle contains 4 operations: 1, laser on with a frequency offset σ for time θ. 2, laser off, detection of fluorescence signal for time θ'. 3, laser on with a frequency offset $-\sigma$ for time θ. 4, laser off, detection of fluorescence signal for time θ'. The next cycle begins immediately after the end of the first cycle. Figure taken from Ref. [68].

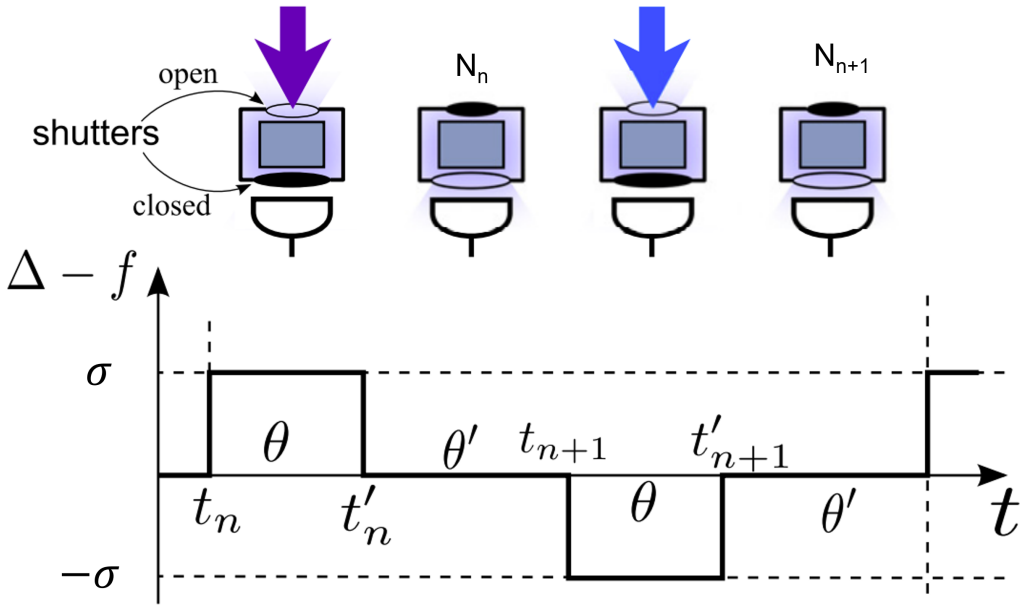

for any i, where $n_0 = 400$ cps is the background count rate. The uncertainty of the count rate measurement comes from the shot noise of the counts that follows a Poisson distribution. We see that the clock stability can be written as

$$\left|\Delta f \cdot \sqrt{2(\theta+\theta')}\right| = \frac{\Delta R(\sigma)\sqrt{\theta+\theta'}}{\ln 2 \cdot R_0\sigma/\sigma_0^2 \cdot \mathrm{e}^{-\ln 2\cdot\sigma^2/\sigma_0^2}}, \tag{5.10}$$

where

$$\Delta R = \frac{\Delta N \cdot \sqrt{1+\mathrm{e}^{-2(\theta+\theta')/\tau}}}{\tau(1-\mathrm{e}^{-\theta/\tau)}(1-\mathrm{e}^{\theta'/\tau})}, \tag{5.11}$$

in which

$$\Delta N = \sqrt{N} = \sqrt{n_0\theta' + R(\sigma)\tau(1-\mathrm{e}^{-\theta/\tau})}. \tag{5.12}$$

We numerically optimize the clock stability $\left|\Delta f \cdot \sqrt{2(\theta+\theta')}\right|$ as a function of the excitation time θ, the detection time θ' and the operation offset σ. Here, we assume that the laser drift during one detection cycle is negligible ($\ll \sigma_0$), which can be achieved by lasers stabilized to state-of-the-art reference cavities [176].

Under these assumptions ($R_0 = 2000$ 1/s, $n_0 = 400$ 1/s, $\sigma_0 = 5\times10^4$ Hz, $\tau = 640$ s), the global optimum for clock stability is found at a step size of $\sigma = 50390$ Hz, with the excitation time of $\theta = 1101$ s and a detection time of $\theta' = 942$ s. The corresponding clock frequency stability is $\left|\Delta f \cdot \sqrt{2(\theta+\theta')}\right| = 7656$ Hz. This corresponds to a fractional clock stability of

$$s_\nu = \left|\Delta f \cdot \sqrt{2(\theta+\theta')}\right|/\nu_0 = 3.8\times10^{-12}/\sqrt{\mathrm{Hz}}, \tag{5.13}$$

where $\nu_0 = 2020.407$ Hz is the nuclear clock transition frequency.

The calculations above are performed for the X2 crystal, which offers the highest signal-to-noise ratio. We can perform the same estimation for the C13 and C10 crystals, with the parameters listed in Table 5.1.

Although this is performance is still far away from the best atomic clocks [5], it is already better than some commercial microwave frequency standards such as rubidium clocks (FS725, Stan-

Parameter	Variable	X2	C10	C13
Excitation rate (cps)	R_0	2000	450	60
Background rate (cps)	n_0	400	1100	300
Linewidth (Hz)	$2\sigma_0$	10^5	4×10^4	3×10^4
Step size (Hz)	σ	50390	17749	13066
Irradiation time (s)	θ	1101	1175	1186
Detection time (s)	θ'	942	631	584
Frequency stability (Hz/$\sqrt{\text{Hz}}$)	$\left\|\Delta f \cdot \sqrt{2(\theta+\theta')}\right\|$	7656	14381	40309
Fractional stability ($1/\sqrt{\text{Hz}}$)	s_ν	3.8×10^{-12}	7.1×10^{-12}	2.0×10^{-11}

Table 5.1: Projected clock stability with 3 different crystals. Top 3 rows contain the assumptions based on experimental measurements. Middle 3 rows contain optimal experimental parameters deduced using Eqn. 5.10. Bottom two rows are the predicted clock stability in terms of both absolute frequency and fractional frequency.

ford Research Systems). Improvements in clock excitation and detection rate, SNR, and coherence time will continue to improve clock performance.

Chapter 6

Conclusions and outlook

In this thesis, we present our journey learning about and building frequency combs in the vacuum ultraviolet [17, 138, 90], using them for spectroscopy of a nuclear state (^{229m}Th) [24], and understanding the spectroscopy results for metrology applications [77] as well as fundamental physics [30]. We also discussed the fabrication of unique thin-film samples to reduce the amount of ^{229}Th consumption, initially intended to build a nuclear clock based on internal conversion [191], but later turned out to work for the radiative decay channel [24].

The highlight of this series of work is the resolution of individual quantum states of ^{229m}Th, split naturally due to the electric field gradient in the host crystal [24], using a frequency comb laser system. Resolving the quantum states allows us to characterize the systematic shifts in a state-dependent way [77] and implement co-sensor ideas to improve the overall uncertainty (see Sect. 5.2). The frequency comb also conveniently allows us to calibrate the frequency of the nuclear transition to the ^{87}Sr atomic clock at JILA [57, 171, 5], facilitating future high-precision clock comparison experiments.

Another attractive application of the ^{229}Th nuclear clock is to miniaturize optical clocks using solid-state systems for applications outside research labs [293]. Although the physical package of ^{229}Th itself can be made small [76], the bulky laser systems used today for nuclear interrogation need to be miniaturized in the future as well.

However, our work represents only the dawn of the nuclear clock research.[1] There are many

[1] This reminds me of a quote from Prof. Jeff Kimble in Ref. [294]. When Prof. Jun Ye, my thesis advisor,

prospects awaiting us, requiring careful characterization of the system, technological innovations, and perhaps some imagination. In the last chapter, we list some of the ideas and directions that we feel are important for the future. We focus on technologies that may improve the clock performance and ease the clock operation and discuss some future prospects of expanding the nuclear clock family to high-energy nuclear transitions.

6.1 Accelerating the readout using new schemes

The readout scheme used in this work and other laser spectroscopy experiments of ^{229}Th [27, 28] is fluorescence counting. We excite the nucleus to the isomer state $^{229\mathrm{m}}$Th, and then wait for it to decay by emitting a photon. Although this scheme gives us enough signal-to-noise ratio to observe the nuclear transition, the long lifetime of the isomer state now becomes a burden that limits the readout speed. In atomic clocks, the clock state population is typically read out through shelving detection, by pumping the excited state population to different states with strong transitions [2]. In ^{229}Th, this is difficult, as the next available state is 29 keV above the ground state [64], where we do not have highly coherent lasers in the foreseeable future. Other detection methods are envisioned to help facilitate a fast state readout.

6.1.1 Double-resonance detection in solid

For trapped ions, a double resonance scheme is proposed [12, 52] where the electronic hyperfine transitions [63, 44] are monitored dependent on the nuclear state. This scheme allows for fast readout of the $^{229\mathrm{m}}$Th population. However, a direct parallel scheme for ^{229}Th in solids is not yet available. In ^{229}Th-doped CaF_2 crystals, ^{229}Th exist as 4+ ions. The exact configuration of the defect state is not fully understood [295, 296]. If there is an optical transition in or near the defect, similar to that in nitrogen-vacancy centers, it may offer a sufficiently narrow linewidth with a sufficiently strong coupling to ^{229}Th to resolve the ^{229}Th quantum states. In this case, one may

observed single atoms trapped in cavities for long times on his last day as a postdoctoral researcher in Jeff's lab, Jeff congratulated him saying "Jun, we have climbed on top of a hill now, and I can see so many flowers lying in the valleys ahead." I am sure people in the lab will continue to enjoy more exciting views ahead after my graduation.

implement a double resonance scheme similar to that proposed for trapped ions [12, 63, 26].

A more realistic proposal is to use the electric quadrupole splitting and perform microwave readout [19, 296] similar to nuclear quadrupole resonance (NQR). Simply, we can use microwave to bridge the gap between the $m_{\rm is} = 1/2$ and $m_{\rm is} = 3/2$ states. Just like in nuclear magnetic resonance spectroscopy (NMR), NQR is routinely performed to characterize materials. Currently, some concerns hinder the implementation of this scheme, but an experiment in the Schumm group in Vienna is actively exploring the possibilities [297]. We list a few open questions in this direction:

- What is the (T_1) lifetime for the mixing between $m_{\rm is} = 1/2$ and $m_{\rm is} = 3/2$ states? It is proposed that one may use the state-resolved laser excitation to populate one of the nuclear excited states, then perform a microwave readout of the population difference between $m_{\rm is} = 1/2$ and $m_{\rm is} = 3/2$. The mixing rate between $m_{\rm is} = 1/2$ and $m_{\rm is} = 3/2$ thus dictates how much time we can use to accumulate the excited state population. If we use the laser pumping to obtain a population difference, and perform a detection based on free-induction decay, a long T_1 would be beneficial. Microwave absorption may also be performed to detect steady-state thermal population differences.

- What is the (T_2) decoherence rate between $m_{\rm is} = 1/2$ and $m_{\rm is} = 3/2$? Although population mixing may be slow (T_1 time), the decoherence between the two states (T_2) may be short, limited by inhomogeneous broadening in the crystal. This could lead to a fast dephasing of the signal and reduces the SNR of a free-induction decay experiment.

- What temperature should we operate at? Detection of small microwave signals is typically limited by thermal noise unless the system is kept at cryogenic temperatures. For $m_{\rm is} = 1/2$ and $m_{\rm is} = 3/2$ with an energy splitting of ~ 250 MHz, $h\nu = k_B T$ gives us a temperature of 12 mK. Although complete suppression of background microwave photons seems impractical, working at cryogenic temperatures still gives us significant reduction of the blackbody microwave background for improved SNR. Of course, thermalization processes take time. It may be possible to prepare the non-equilibrium state and perform the detection before

thermal equilibration.

Of course, with an improved laser excitation rate and atom numbers, the NQR double-resonance scheme should eventually become feasible in terms of SNR.

It is possible to imagine co-doping the CaF_2 crystal (or other hosts) with ^{229}Th and another different species for readout. For example, the crystal microstrain [298] can be leveraged to create favorable co-doped states between ^{229}Th and other dopants. It is also possible to maintain the VUV transparency of the crystals with lanthanide doping [299]. The infused hydrogen atoms in CaF_2 have been characterized by electron spin resonance spectroscopy [300]. It might be possible to use the nuclear-electron spin coupling in such a system to perform the nuclear state readout in the microwave domain. The co-doped impurities may even serve as local strain/temperature/magnetic field sensors for improving the clock accuracy. However, it may be difficult to control the inhomogeneous broadening of the ^{229}Th nuclear transition with co-doped sensors.

6.1.2 Optical-induced quenching

If the SNR of the fluorescence detection is high enough, it could be beneficial to quench the excited state ^{229m}Th after a short detection window. Controlled quenching of ^{229m}Th was first reported using X-rays [66]. Recently, similar quenching effects have been observed using UV lasers [301, 302]. By reducing the readout cycle, the clock stability can be improved.

While the exact photo-quenching mechanism is unclear, it is possible that the photo-quenched state leads to electrons in the conduction band. With a high ^{229m}Th excitation fraction, it is possible to imagine direct detection of the excited state population using photo-induced electrical conductivity like that in typical photodetectors [233].

6.1.3 Internal-conversion decay

As discussed in Ref. [22, 191], for a clock based on internal-conversion decay, the readout is naturally performed much faster. With a 10 µs interrogation cycles and a 10 nm thick $^{229}ThO_2$ film

irradiated using a 10 nW laser power, a clock stability of $\sim 10^{-14}/\sqrt{\text{Hz}}$ may be possible [191]. However, the IC detection scheme needs to first be demonstrated with reasonable detection efficiency. A thin $^{229}ThO_2$ layer is naturally more sensitive to surface effects and inhomogeneous broadening. The feasibility of this scheme will be further investigated in the future.

6.1.4 Direct absorption measurement

If a continuous-wave laser with a narrow linewidth is available, one can even operate the clock by directly performing absorption spectroscopy. Of course, frequency-modulation techniques may be used to generate an error signal for stabilizing the clock laser directly onto the nuclear transition. External cavities, if available, may also help to improve the absorption signal [303, 304]. For enhanced stability (but not absolute frequency accuracy), spectral hole burning in the inhomogeneously broadened sample may prove useful [305].

Assuming a ^{229}Th density of 10^{19} cm^{-3} with a length of 1 cm, and an inhomogeneous linewidth of 100 kHz, the peak absorption would be on the order of 1%. If an external cavity with finesse of $\sim$ 1000 is used, the system can be impedance matched to get full absorption of the input light. Assuming a 1 mm by 1 mm cross section, the saturation intensity of the laser in absorption spectroscopy will be about 1 µW, or $\sim 10^{12}$ photons per second. The shot-noise limited stability can thus reach $10^{-16}/\sqrt{\text{Hz}}$, even approaching the performance of a cryogenic Si cavity [57].

6.2 Accelerating the excitation using new lasers

Another important limitation so far is the low excitation fraction of the ^{229}Th nuclei in the experiment. If lasers with higher spectral power and narrower linewidth are available, coherent manipulation of the ^{229}Th nuclear state will enable numerous experiments such as Ramsey or Rabi spectroscopy for clock readout, etc. Here, we briefly discuss a few existing proposals on how to improve the laser system.

6.2.1 Dispersive wave generation and four-wave mixing in hollow-core fibers

Cavity-enhanced HHG is a great and relatively mature tool for precision spectroscopy in the frequency domain and high repetition rate photoelectron spectroscopy in the time domain [17], especially for high photon energies > 10 eV. For the ^{229}Th nuclear transition at 8.4 eV, we ask if there are other technologies to upconvert a frequency comb there. In fact, intense pulsed VUV light can be generated using gas-filled hollow core fibers [306, 307, 308, 309].[2] While the scheme has only been demonstrated at repetition rates too low to be useful as a frequency comb, it may be possible to scale up the repetition rate and obtain a coherent frequency comb in the VUV in the future.

6.2.2 Continuous wave lasers at 148 nm

Although frequency combs offer the unique combination of high peak power for efficient nonlinear frequency conversion and the narrow linewidth of single comb lines for precision spectroscopy, only one comb mode can be used to interrogate the ^{229}Th nucleus at a time. This presents difficulties not only in power scaling for an increased excitation rate, but also additional problems of quenching [301, 302], crystal damage [228], and potentially light-induced frequency shifts. Direct absorption measurement is also extremely challenging because of intensity noise and shot noise limitations from other comb lines. A continuous wave (CW) laser with a narrow linewidth would be ideal for nuclear clock operation.

Several proposals for building CW lasers at 148 nm wavelength exist. To generate CW lasers using nonlinear optics, we are limited to perturbative processes. Broadly speaking, one typically uses the second or third order nonlinearity, in gas or solid systems, for nonlinear frequency upconversion. The difficulty mainly lies in the limited material choice transparent for VUV light

[2] Prof. Alex Gaeta visited JILA on February 2020. We asked him this question, and he immediately said "Yes!" We then continued to explore the possibility of VUV comb generation in hollow-core fibers together with Alex Gaeta, Yoshitomo Okawachi, Philip Russell, Francesco Tani, Martin Fermann, and Jacob Lampen. Some preliminary tests were performed at IMRA America, Inc., but without successful results. Later in 2024, we had more discussions about this concept with John Travers, Federico Belli, and Jason Jones. In parallel, Henry Kapteyn, Drew Morrill, and Jeremy Thurston showed us their setup in the Kapteyn-Murnane group at JILA based on a similar scheme.

and stringent conditions for achieving phase-matching due to the large material dispersion in the VUV.

Second-order harmonic or sum-frequency generation in crystals are typically very efficient. $KBe_2BO_3F_2$ (KBBF) crystal has been widely used for the generation of CW lasers in vacuum ultraviolet. Although its transmission cuts off at 147 nm [310], the efficiency of sum frequency generation drops drastically below 150 nm [311]. Since the desired wavelength is very close to the cutoff wavelength of KBBF, it could be of interest to investigate growth methods and operating conditions to slightly extend the cutoff wavelength. For example, material bandgaps tend to increase slightly when cooled to cryogenic temperatures. Frequency doubling cannot be phase matched in KBBF to this low wavelength. However, sum frequency generation may work [18].

Another material, $BaMgF_4$ (BMF), is proposed for 148.38 nm CW laser generation in Ref. [18]. Being a ferroelectric crystal, BMF is compatible with quasi phase matching schemes using periodic poling [312, 313, 314] for VUV light generation. A frequency doubling scheme using periodically poled BMF is currently under investigation at the Johannes Gutenberg University of Mainz [315]. It is proposed [316] that one can even dope ^{229}Th directly into a BMF crystal, building a system that performs both the nonlinear frequency upconversion as well as ^{229}Th spectroscopy in situ, eliminating the need for vacuum systems for the operation of a nuclear clock in vacuum ultraviolet.

Another possible route to generate continuous-wave VUV light is using resonance-enhanced four-wave mixing in metal gas vapors [317] as described in detail in Ref. [318]. By tuning the laser frequencies close to resonances in the metal vapor, the nonlinear susceptibility can be drastically enhanced, making four-wave mixing generation of VUV light possible even with CW lasers. A CW laser at the hydrogen Lyman-α line of 121.56 nm was generated [319] and used for spectroscopy [320]. For the ^{229}Th nuclear transition, a four-wave mixing scheme using cadmium vapor is proposed in Ref. [321]. With realistic parameters, the generation of $> 10\,\mu W$ of VUV power at 148.38 nm wavelength seems possible. Metal vapors hosted in hollow-core hybrid fibers [322] have been used to enable four-wave mixing at extremely low light power [323]. Guiding of VUV light can also be achieved using hollow core fibers [324]. Therefore, it might be possible to enhance the FWM

efficiency using hybrid hollow core fibers filled with metal vapor [322].

VUV light can also be generated by anti-Stokes scattering using hydrogen gas [325, 326], sulfur, and selenium [327]. For hydrogen, the anti-Stokes scattering process provides a fixed frequency shift ($\sim$ 127 THz). Thus, to reach 148.38 nm, a $\sim$ 158 nm wavelength laser needs to be built first. Using a hollow core fiber and pulsed pump lasers with $\sim$ kW peak power, anti-Stokes shifting of light in the VUV has been demonstrated with $\sim$ 60% conversion efficiency [328]. This process works like a frequency modulator and does not require high power in the VUV. Even single photons can be used as the seed for the anti-Stokes process and are efficiently frequency shifted using the (pulsed) Raman process [329]. However, it is difficult to achieve the same high efficiency using CW lasers, due to the comparatively low peak power [330].

Similar to resonant VUV generation in gas, resonant nanostructures (metamaterials) have also been used for the generation of VUV light, although with a low conversion efficiency demonstrated [331, 332, 333]. It would be interesting to explore the limitations of nanophotonics for VUV generation and enhanced interaction with ^{229}Th.

Besides generation via nonlinear optics methods, direct lasing with gain medium is also possible in the VUV. The limitation is that VUV lasers typically require huge pumping power to reach population inversion, due to short excited-state lifetimes. Excimer lasers, for this reason, typically operate in pulsed mode. However, it might be possible to build continuously tunable VUV lasers with lanthanide doped in crystals [334] with long excited state lives.

6.3 Ease the constrain on laser technology by new excitation pathways

The couplings of the nuclear state to its electronic states, which is the mechanism behind the IC decay channel, may be used to our advantage to obtain a more efficient population of the ^{229m}Th isomer. A process under investigation is the electron bridge excitation mechanism. Two (or more) lasers can be used whose frequencies add to the nuclear transition frequency, allowing one to use more standard UV/visible lasers. Schemes have been proposed using either $^{229}Th^{+}$ [335], $^{229}Th^{2+}$ [336], $^{229}Th^{3+}$ [337, 338], highly charged thorium ions [339], ^{229}Th doped in

CaF_2 crystals [295], etc. A similar process of nuclear excitation via two-photon electronic transition is discussed in Ref. [340]. In a ^{229}Th doped CaF_2 crystal, two-photon excitation through the modulation of crystal lattice field is also discussed in Ref. [341]. If the ^{229}Th doping site is non-centrosymmetric, one may imagine an enhanced degenerate two-photon transition rate. Excitation of the ^{229m}Th state using electrons has also been considered [342], though this process would not be useful as a frequency discriminator for optical clocks.

6.4 Improving the ^{229}Th coherence in solids

As discussed in Sect. 5.3, currently the linewidth of the ^{229}Th nuclear transition depends on the doping concentration, likely due to microstrain caused by defects. ^{229}Th doped in $^{232}ThF_4$ will not create defect states, thus may eliminate this density-dependent line broadening. Although $^{229}ThF_4$ thin films grown in Ref. [76] are likely amorphous, crystalline $^{232}ThF_4$ can be grown using mature crystal growing technologies [255].

The next-order limitation of the coherence may come from a random internal magnetic field created by the fluorine nuclear spins. It would be interesting to explore new crystals with low spin density, yet still transparent in the VUV. While amorphous SiO_2 is opaque at 148 nm, crystalline quartz is actually transparent at the nuclear transition wavelength [343]. Alternatively, a frozen noble gas like Argon may offer a convenient solid-state host with zero nuclear spins near the ^{229}Th site. In addition to solid-state hosts, liquid hosts may offer additional advantages in that inhomogeneity may be averaged due to rapid fluctuations [344].

Nuclear magnetic resonance spectroscopy is common in F nuclear spin. With a magnetic field on the order of a few Tesla, the F nuclear spin precession frequency can reach ~ 100 MHz. Obviously, it is still difficult to freeze out the nuclear spins of F. However, dynamical decoupling [345] schemes may be used to average out the F nuclear spin interaction in our observation time scales. One may even consider using the interaction between the ^{229}Th isomer and the F nuclear spin to control and align the F nuclear spin state [283].

6.5 Studying ^{229m}Th in the quantum regime

In addition to being a tool for the precision metrology of time, the long coherence of ^{229}Th offers a promising candidate for the development of quantum technology. Here, we briefly discuss the possibilities and technical challenges of using ^{229}Th together with quantum optics and quantum information processing.

6.5.1 Nuclear superradiance

Novel quantum optical effects can be expected when we have high-density quantum emitters with low inhomogeneous broadening. Specifically with nuclear transitions in X-ray [346], one can observe quantum-optical effects such as collective Lamb shift [250], electromagnetically induced transparency [347], storage of nuclear excitation through magnetic switching [348], etc.

For thorium specifically, it has been proposed that coherence effects may enhance the detection of the ^{229}Th nuclear clock transition [349, 350]. The proposed directional emission with an enhanced emission rate is similar to the effect of nuclear forward scattering [351], and can potentially be probed with existing broadband pulsed laser systems [27, 28] to reveal the coherence of the ^{229}Th sample. Single-photon superradiance [352] with a ^{229}Th nuclear sample may even provide a competitive check of gravitational and general relativistic time dilation [353] in small length scales.[3] Note that effects similar to the proposed superradiance deflection in gravitational field in Ref. [353] may be observable with slow or stopped light [354] and with a magnetic field instead of gravity [355]. The storage of light, whether using EIT or superradiance, may be useful in resolving gravitational effects using photons [356].

6.5.2 Nuclear qubits

^{229}Th is not the only optically active quantum emitter in solids. Color centers [357] and rare earth ions [358] embedded in solids have been spectroscopically characterized and are used

[3] In Table 1 of Ref. [353], coherence times τ_{coh} of different nuclear isomers are listed. However, for some nuclear transitions, T_1 time is quoted (especially for long lifetime ones), while for ^{229}Th the quoted τ_{coh} is an estimated T_2 coherence time.

for applications such as quantum information processing [359], quantum sensing [360, 361], study of quantum many-body physics [362, 363], precision laser metrology [305] and searches for beyond standard model physics [364]. These platforms bear obvious similarities to the ^{229}Th embedded in crystals. It is possible to imagine using ^{229}Th as a complementary approach in some of the applications. The obvious advantage of ^{229}Th is that one can obtain long T_1 lifetime of > 600 s and decent ($> 1\,\mu$s) T_2 coherence times at room temperature[24]. Of course, with more research on nuclear clocks and nuclear qubits, the coherence time T_2 is expected to improve significantly. A reasonable estimate of ~ 1 ms comes from Refs. [67, 68]. Although the operation of a vacuum ultraviolet laser may limit the viability of quantum network applications, transduction between VUV and infrared photons, or even dedicated networks for entanglement distribution, may circumvent some of the technical difficulties [365].

6.6 Nuclear clocks in the extreme ultraviolet and X-ray

While ^{229}Th is currently the only accessible candidate to build a nuclear clock, other narrow-linewidth transitions in atomic nuclei may be used with future technology breakthroughs. Even in 1960, a narrow transition with 9.4 µs lifetime at 93 keV in ^{67}Zn was considered for "the possibility of the most precise nuclear clock available." [10]. In ^{235}U, there exists a 76 eV nuclear isomer with a lifetime longer than the age of the universe. Novel schemes using electron-nuclear coupling may reduce the requirements of laser power to interrogate this state [13]. In ^{45}Sc, a clock state with a lifetime of 0.45 s is recently excited using a high-brightness X-ray free-electron laser (FEL). The energy of the clock transition is determined to be $12389.59 \pm 0.15_{\mathrm{stat}} \pm 0.12_{\mathrm{syst}}$ eV [14].

While high-energy nuclear excitations and even some forms of coherent manipulation [366] can be performed with existing X-rays sources, reading out their absolute frequency has not been achieved. It is proposed that X-ray combs may be generated via pulse-shaping methods [367], coherent laser-electron scattering [368], seeding of free-electron lasers using HHG sources'[369] or directly using an X-ray cavity-based [370] oscillator [369]. Another possibility is to use a phase-based measurement akin to Ramsey spectroscopy. Using HHG sources, pairs of XUV pulses can be

generated and used for spectroscopy. By taking the pair of fundamental pulses from a frequency comb, precise scans of the pulse delay with extremely long delay times can be achieved, promising a resolution similar to that achievable with frequency combs; see Refs. [371, 372] for demonstration of the "Ramsey-comb" spectroscopy. Extending this scheme to the X-ray via phase-synchronized X-ray FEL pulses seems promising. Although X-ray FEL exists as large billion-dollar facilities today, compact designs using inverse Compton scattering may significantly reduce the cost of them [356, 373, 374, 375]. Laser-based electron accelerators offer another promising route for more compact X-ray laser sources [376], even potentially to the chip scale [377, 378]. We may have more nuclear clocks in the future!

Bibliography

[1] Alan V Oppenheim and George C Verghese. Signals, systems & inference. Pearson London, 2017.

[2] Andrew D Ludlow, Martin M Boyd, Jun Ye, Ekkehard Peik, and Piet O Schmidt. Optical atomic clocks. Reviews of Modern Physics, 87(2):637–701, 2015.

[3] Tobias Bothwell, Colin J Kennedy, Alexander Aeppli, Dhruv Kedar, John M Robinson, Eric Oelker, Alexander Staron, and Jun Ye. Resolving the gravitational redshift across a millimetre-scale atomic sample. Nature, 602(7897):420–424, 2022.

[4] Fritz Riehle. Frequency standards: basics and applications. John Wiley & Sons, 2006.

[5] Alexander Aeppli, Kyungtae Kim, William Warfield, Marianna S Safronova, and Jun Ye. Clock with 8×10^{-19} systematic uncertainty. Physical Review Letters, 133(2):023401, 2024.

[6] Colin J Kennedy, Eric Oelker, John M Robinson, Tobias Bothwell, Dhruv Kedar, William R Milner, G Edward Marti, Andrei Derevianko, and Jun Ye. Precision metrology meets cosmology: improved constraints on ultralight dark matter from atom-cavity frequency comparisons. Physical Review Letters, 125(20):201302, 2020.

[7] Ross B Hutson, William R Milner, Lingfeng Yan, Jun Ye, and Christian Sanner. Observation of millihertz-level cooperative *lamb* shifts in an optical atomic clock. Science, 383(6681):384–387, 2024.

[8] Edwin Pedrozo-Peñafiel, Simone Colombo, Chi Shu, Albert F Adiyatullin, Zeyang Li, Enrique Mendez, Boris Braverman, Akio Kawasaki, Daisuke Akamatsu, Yanhong Xiao, et al. Entanglement on an optical atomic-clock transition. Nature, 588(7838):414–418, 2020.

[9] John M Robinson, Maya Miklos, Yee Ming Tso, Colin J Kennedy, Tobias Bothwell, Dhruv Kedar, James K Thompson, and Jun Ye. Direct comparison of two spin-squeezed optical clock ensembles at the 10^{-17} level. Nature Physics, 20(2):208–213, 2024.

[10] DE Nagle, PP Craig, and WE Keller. Ultra-high resolution γ-ray resonance in zinc-67. Nature, 186(4726):707–708, 1960.

[11] EV Tkalya, VO Varlamov, VV Lomonosov, and SA Nikulin. Processes of the nuclear isomer ^{229m}Th ($3/2^+$, 3.5±1.0 eV) resonant excitation by optical photons. Physica Scripta, 53(3):296, 1996.

[12] E Peik and Chr Tamm. Nuclear laser spectroscopy of the 3.5 eV transition in Th-229. Europhysics Letters, 61(2):181, 2003.

[13] JC Berengut. Resonant electronic-bridge excitation of the ^{235}U nuclear transition in ions with chaotic spectra. Physical Review Letters, 121(25):253002, 2018.

[14] Yuri Shvyd'ko, Ralf Röhlsberger, Olga Kocharovskaya, Jörg Evers, Gianluca Aldo Geloni, Peifan Liu, Deming Shu, Antonino Miceli, Brandon Stone, Willi Hippler, et al. Resonant X-ray excitation of the nuclear clock isomer ^{45}Sc. Nature, 622(7983):471–475, 2023.

[15] R Jason Jones, Kevin D Moll, Michael J Thorpe, and Jun Ye. Phase-coherent frequency combs in the vacuum ultraviolet via high-harmonic generation inside a femtosecond enhancement cavity. Physical Review Letters, 94(19):193201, 2005.

[16] Christoph Gohle, Thomas Udem, Maximilian Herrmann, Jens Rauschenberger, Ronald Holzwarth, Hans A Schuessler, Ferenc Krausz, and Theodor W Hänsch. A frequency comb in the extreme ultraviolet. Nature, 436(7048):234–237, 2005.

[17] Ioachim Pupeza, Chuankun Zhang, Maximilian Högner, and Jun Ye. Extreme-ultraviolet frequency combs for precision metrology and attosecond science. Nature Photonics, 15(3):175–186, 2021.

[18] Lars von der Wense and Benedict Seiferle. The ^{229}Th isomer: prospects for a nuclear optical clock. The European Physical Journal A, 56(11):277, 2020.

[19] Ekkehard Peik, Thorsten Schumm, MS Safronova, Adriana Palffy, Johannes Weitenberg, and Peter G Thirolf. Nuclear clocks for testing fundamental physics. Quantum Science and Technology, 6(3):034002, 2021.

[20] Kjeld Beeks, Tomas Sikorsky, Thorsten Schumm, Johannes Thielking, Maxim V Okhapkin, and Ekkehard Peik. The thorium-229 low-energy isomer and the nuclear clock. Nature Reviews Physics, 3(4):238–248, 2021.

[21] Peter G Thirolf, Sandro Kraemer, Daniel Moritz, and Kevin Scharl. The thorium isomer ^{229m}Th: review of status and perspectives after more than 50 years of research. The European Physical Journal Special Topics, pages 1–19, 2024.

[22] Lars Von der Wense. On the direct detection of ^{229m}Th. Springer, 2017.

[23] Sven Gösta Nilsson. Binding states of individual nucleons in strongly deformed nuclei. Dan. Mat. Fys. Medd., 29(CERN-55-30):1–69, 1955.

[24] Chuankun Zhang, Tian Ooi, Jacob S Higgins, Jack F Doyle, Lars von der Wense, Kjeld Beeks, Adrian Leitner, Georgy A Kazakov, Peng Li, Peter G Thirolf, et al. Frequency ratio of the ^{229m}Th nuclear isomeric transition and the ^{87}Sr atomic clock. Nature, 633(8028):63–70, 2024.

[25] Sandro Kraemer, Janni Moens, Michail Athanasakis-Kaklamanakis, Silvia Bara, Kjeld Beeks, Premaditya Chhetri, Katerina Chrysalidis, Arno Claessens, Thomas E Cocolios, João GM Correia, et al. Observation of the radiative decay of the ^{229}Th nuclear clock isomer. Nature, 617(7962):706–710, 2023.

[26] Atsushi Yamaguchi, Yudai Shigekawa, Hiromitsu Haba, Hidetoshi Kikunaga, Kenji Shirasaki, Michiharu Wada, and Hidetoshi Katori. Laser spectroscopy of triply charged ^{229}Th isomer for a nuclear clock. Nature, pages 1–5, 2024.

[27] J Tiedau, MV Okhapkin, K Zhang, J Thielking, G Zitzer, E Peik, F Schaden, T Pronebner, I Morawetz, L Toscani De Col, et al. Laser excitation of the Th-229 nucleus. Physical Review Letters, 132(18):182501, 2024.

[28] R Elwell, Christian Schneider, Justin Jeet, JES Terhune, HWT Morgan, AN Alexandrova, HB Tran Tan, Andrei Derevianko, and Eric R Hudson. Laser excitation of the ^{229}th nuclear isomeric transition in a solid-state host. Physical Review Letters, 133(1):013201, 2024.

[29] Benedict Seiferle, Lars Von Der Wense, and Peter G Thirolf. Lifetime measurement of the ^{229}Th nuclear isomer. Physical Review Letters, 118(4):042501, 2017.

[30] Kjeld Beeks, Georgy A Kazakov, Fabian Schaden, Ira Morawetz, Luca Toscani de Col, Thomas Riebner, Michael Bartokos, Tomas Sikorsky, Thorsten Schumm, Chuankun Zhang, et al. Fine-structure constant sensitivity of the Th-229 nuclear clock transition. arXiv preprint arXiv:2407.17300, 2024.

[31] SG Porsev, MS Safronova, and MG Kozlov. Precision calculation of hyperfine constants for extracting nuclear moments of ^{229}Th. Physical Review Letters, 127(25):253001, 2021.

[32] Harry J Lipkin. Quantum mechanics: new approaches to selected topics. Courier Corporation, 2014.

[33] Norman Neill Greenwood. Mössbauer spectroscopy. Springer Science & Business Media, 2012.

[34] Robert V Pound and Glen A Rebka Jr. Apparent weight of photons. Physical Review Letters, 4(7):337, 1960.

[35] Robert V Pound and GA Rebka Jr. Resonant absorption of the 14.4-kev γ ray from 0.10-μsec Fe^{57}. Physical Review Letters, 3(12):554, 1959.

[36] Hofstadter Robert. Means for detecting ionizing radiations, February 12 1952. US Patent 2,585,551.

[37] DV Freck and J Wakefield. Gamma-ray spectrum obtained with a lithium-drifted p–i–n junction in germanium. Nature, 193(4816):669–669, 1962.

[38] LA Kroger and CW Reich. Features of the low-energy level scheme of ^{229}Th as observed in the α-decay of ^{233}U. Nuclear Physics A, 259(1):29–60, 1976.

[39] C. W. Reich and R. G. Helmer. The level at a few eV of excitation in ^{229}Th. In Akunuri V. Ramayya, editor, Proceedings of the International Symposium on Nuclear Physics of Our Times, page 474, Singapore, 1993. World Scientific.

[40] RG Helmer and CW Reich. An excited state of ^{229}Th at 3.5 eV. Physical Review C, 49(4):1845, 1994.

[41] Zwinglio de Oliveira Guimarães-Filho and O Helene. Energy of the $3/2^+$ state of ^{229}Th reexamined. Physical Review C, 71(4):044303, 2005.

[42] BR Beck, JA Becker, P Beiersdorfer, GV Brown, Kenton J Moody, Jerry B Wilhelmy, FS Porter, CA Kilbourne, and RL Kelley. Energy splitting of the ground-state doublet in the nucleus ^{229}Th. Physical Review Letters, 98(14):142501, 2007.

[43] BR Beck, C Wu, P Beiersdorfer, GV Brown, JA Becker, KJ Moody, JB Wilhelmy, FS Porter, CA Kilbourne, and RL Kelley. Improved value for the energy splitting of the ground-state doublet in the nucleus ^{229m}Th. Technical report, Lawrence Livermore National Lab.(LLNL), Livermore, CA (United States), 2009.

[44] A Yamaguchi, H Muramatsu, T Hayashi, N Yuasa, K Nakamura, M Takimoto, H Haba, K Konashi, M Watanabe, H Kikunaga, et al. Energy of the ^{229}Th nuclear clock isomer determined by absolute γ-ray energy difference. Physical Review Letters, 123(22):222501, 2019.

[45] Tomas Sikorsky, Jeschua Geist, Daniel Hengstler, Sebastian Kempf, Loredana Gastaldo, Christian Enss, Christoph Mokry, Jörg Runke, Christoph E Düllmann, Peter Wobrauschek, et al. Measurement of the ^{229}Th isomer energy with a magnetic microcalorimeter. Physical Review Letters, 125(14):142503, 2020.

[46] AM Dykhne and EV Tkalya. Matrix element of the anomalously low-energy (3.5±0.5 eV) transition in ^{229}Th and the isomer lifetime. Journal of Experimental and Theoretical Physics Letters, 67:251–256, 1998.

[47] Eugene V Tkalya, Alexander N Zherikhin, and Valerii I Zhudov. Decay of the low-energy nuclear isomer ^{229}Th^{m} ($3/2^{+}$, 3.5±1.0 eV) in solids (dielectrics and metals): A new scheme of experimental research. Physical Review C, 61(6):064308, 2000.

[48] Hans Dehmelt. Experiments with an isolated subatomic particle at rest. Reviews of Modern Physics, 62(3):525, 1990.

[49] Dietrich Leibfried, Rainer Blatt, Christopher Monroe, and David Wineland. Quantum dynamics of single trapped ions. Reviews of Modern Physics, 75(1):281, 2003.

[50] Juan I Cirac and Peter Zoller. Quantum computations with cold trapped ions. Physical Review Letters, 74(20):4091, 1995.

[51] Samuel M Brewer, J-S Chen, Aaron M Hankin, Ethan R Clements, Chin-wen Chou, David J Wineland, David B Hume, and David R Leibrandt. $^{27}Al^{+}$ quantum-logic clock with a systematic uncertainty below 10^{-18}. Physical Review Letters, 123(3):033201, 2019.

[52] Corey J Campbell, Alexander G Radnaev, A Kuzmich, Vladimir A Dzuba, Victor V Flambaum, and Andrei Derevianko. Single-ion nuclear clock for metrology at the 19th decimal place. Physical Review Letters, 108(12):120802, 2012.

[53] CJ Campbell, AV Steele, LR Churchill, MV DePalatis, DE Naylor, DN Matsukevich, A Kuzmich, and MS Chapman. Multiply charged thorium crystals for nuclear laser spectroscopy. Physical Review Letters, 102(23):233004, 2009.

[54] CJ Campbell, AG Radnaev, and A Kuzmich. Wigner crystals of ^{229}Th for optical excitation of the nuclear isomer. Physical Review Letters, 106(22):223001, 2011.

[55] Kevin Scharl, Shiqian Ding, Georg Holthoff, Mahmood Irtiza Hussain, Sandro Kraemer, Lilli Löbell, Daniel Moritz, Tamila Rozibakieva, Benedict Seiferle, Florian Zacherl, et al. Setup for the ionic lifetime measurement of the $^{229m}Th^{3+}$ nuclear clock isomer. Atoms, 11(7):108, 2023.

[56] G Zitzer, J Tiedau, MV Okhapkin, K Zhang, C Mokry, J Runke, Ch E Düllmann, and E Peik. Sympathetic cooling of trapped Th^{3+} alpha-recoil ions for laser spectroscopy. Physical Review A, 109(3):033116, 2024.

[57] DG Matei, T Legero, S Häfner, Ch Grebing, R Weyrich, W Zhang, L Sonderhouse, JM Robinson, J Ye, F Riehle, et al. 1.5 μm lasers with sub-10 mhz linewidth. Physical Review Letters, 118(26):263202, 2017.

[58] V Barci, G Ardisson, G Barci-Funel, B Weiss, O El Samad, and RK Sheline. Nuclear structure of ^{229}Th from γ-ray spectroscopy study of ^{233}U α-particle decay. Physical Review C, 68(3):034329, 2003.

[59] Lars Von Der Wense, Benedict Seiferle, Mustapha Laatiaoui, Jürgen B Neumayr, Hans-Jörg Maier, Hans-Friedrich Wirth, Christoph Mokry, Jörg Runke, Klaus Eberhardt, Christoph E Düllmann, et al. Direct detection of the ^{229}Th nuclear clock transition. Nature, 533(7601):47–51, 2016.

[60] FF Karpeshin and MB Trzhaskovskaya. Impact of the electron environment on the lifetime of the $^{229}Th^{m}$ low-lying isomer. Physical Review C, 76(5):054313, 2007.

[61] EV Tkalya, Christian Schneider, Justin Jeet, and Eric R Hudson. Radiative lifetime and energy of the low-energy isomeric level in ^{229}Th. Physical Review C, 92(5):054324, 2015.

[62] Benedict Seiferle, Lars von der Wense, Pavlo V Bilous, Ines Amersdorffer, Christoph Lemell, Florian Libisch, Simon Stellmer, Thorsten Schumm, Christoph E Düllmann, Adriana Pálffy, et al. Energy of the ^{229}Th nuclear clock transition. Nature, 573(7773):243–246, 2019.

[63] Johannes Thielking, Maxim V Okhapkin, Przemysław Głowacki, David M Meier, Lars von der Wense, Benedict Seiferle, Christoph E Düllmann, Peter G Thirolf, and Ekkehard Peik. Laser spectroscopic characterization of the nuclear-clock isomer ^{229m}Th. Nature, 556(7701):321–325, 2018.

[64] Takahiko Masuda, Akihiro Yoshimi, Akira Fujieda, Hiroyuki Fujimoto, Hiromitsu Haba, Hideaki Hara, Takahiro Hiraki, Hiroyuki Kaino, Yoshitaka Kasamatsu, Shinji Kitao, et al. X-ray pumping of the ^{229}Th nuclear clock isomer. Nature, 573(7773):238–242, 2019.

[65] Koichi Okai, Kjeld Beeks, Hiroyuki Fujimoto, Yuta Fukunaga, Ming Guan, Hiromitsu Haba, Takahiro Hiraki, Yoshitaka Kasamatsu, Shinji Kitao, Kenji Konashi, et al. The observation of the VUV signal from the isomeric state of ^{229}thorium nuclei toward realizing the atomic clock. In APS Meeting Abstracts, pages E02–003, 2023.

[66] Takahiro Hiraki, Koichi Okai, Michael Bartokos, Kjeld Beeks, Hiroyuki Fujimoto, Yuta Fukunaga, Hiromitsu Haba, Yoshitaka Kasamatsu, Shinji Kitao, Adrian Leitner, et al. Controlling ^{229}Th isomeric state population in a VUV transparent crystal. Nature communications, 15(1):5536, 2024.

[67] Wade G Rellergert, D DeMille, Richard R Greco, Markus Peter Hehlen, JR Torgerson, and Eric R Hudson. Constraining the evolution of the fundamental constants with a solid-state optical frequency reference based on the ^{229}Th nucleus. Physical Review Letters, 104(20):200802, 2010.

[68] GA Kazakov, AN Litvinov, VI Romanenko, LP Yatsenko, AV Romanenko, Matthias Schreitl, Georg Winkler, and Thorsten Schumm. Performance of a ^{229}Thorium solid-state nuclear clock. New Journal of Physics, 14(8):083019, 2012.

[69] Justin Jeet, Christian Schneider, Scott T Sullivan, Wade G Rellergert, Saed Mirzadeh, A Cassanho, HP Jenssen, Eugene V Tkalya, and Eric R Hudson. Results of a direct search using synchrotron radiation for the low-energy ^{229}Th nuclear isomeric transition. Physical Review Letters, 114(25):253001, 2015.

[70] Justin Jeet. Search for the low lying transition in the ^{229}Th nucleus. University of California, Los Angeles, 2018.

[71] Simon Stellmer, Georgy Kazakov, Matthias Schreitl, Hendrik Kaser, Michael Kolbe, and Thorsten Schumm. Attempt to optically excite the nuclear isomer in ^{229}Th. Physical Review A, 97(6):062506, 2018.

[72] M Verlinde, S Kraemer, J Moens, K Chrysalidis, JG Correia, Stefaan Cottenier, H De Witte, DV Fedorov, VN Fedosseev, R Ferrer, et al. Alternative approach to populate and study the ^{229}th nuclear clock isomer. Physical Review C, 100(2):024315, 2019.

[73] SV Pineda, P Chhetri, S Bara, Y Elskens, S Casci, AN Alexandrova, M Au, M Athanasakis-Kaklamanakis, M Bartokos, K Beeks, et al. Radiative decay of the $^{229\mathrm{m}}$Th nuclear clock isomer in different host materials. Physical Review Research, 7(1):013052, 2025.

[74] Richard Elwell. Direct Excitation of the Thorium-229 Nuclear Isomeric Transition and Investigations of Its Behavior in Solid-State Hosts. PhD thesis, University of California, Los Angeles, 2024.

[75] J Thielking, K Zhang, J Tiedau, J Zander, G Zitzer, MV Okhapkin, and E Peik. Vacuum-ultraviolet laser source for spectroscopy of trapped thorium ions. New Journal of Physics, 25(8):083026, 2023.

[76] Chuankun Zhang, Lars von der Wense, Jack F Doyle, Jacob S Higgins, Tian Ooi, Hans U Friebel, Jun Ye, R Elwell, JES Terhune, HWT Morgan, et al. $^{229}ThF_4$ thin films for solid-state nuclear clocks. Nature, 636(8043):603–608, 2024.

[77] Jacob S Higgins, Tian Ooi, Jack F Doyle, Chuankun Zhang, Jun Ye, Kjeld Beeks, Tomas Sikorsky, and Thorsten Schumm. Temperature sensitivity of a thorium-229 solid-state nuclear clock. arXiv preprint arXiv:2409.11590, Phys. Rev. Lett., in press, 2024.

[78] Y.A. Akovali. Nuclear data sheets for A = 229. Nuclear Data Sheets, 58(2):555–588, 1989.

[79] CW Reich and RG Helmer. Energy separation of the doublet of intrinsic states at the ground state of ^{229}Th. Physical Review Letters, 64(3):271, 1990.

[80] Zsolt Varga, Adrian Nicholl, and Klaus Mayer. Determination of the ^{229}Th half-life. Physical Review C, 89(6):064310, 2014.

[81] CW Forsberg and LC Lewis. Uses for uranium-233: what should be kept for future needs. Oak Ridge National Lab, 6952(7), 1999.

[82] National isotope development center. https://www.isotopes.gov/, 2025.

[83] Eckert & ziegler. https://www.ezag.com/, 2025.

[84] Christoph Düllmann and Dennis Renisch. Th-229 material descriptions and radioactive target fabrication techniques. private communication, 2022.

[85] Justin R Griswold, Dmitri G Medvedev, Jonathan W Engle, Roy Copping, JM Fitzsimmons, V Radchenko, JC Cooley, ME Fassbender, DL Denton, KE Murphy, et al. Large scale accelerator production of ^{225}Ac: Effective cross sections for 78–192 MeV protons incident on ^{232}Th targets. Applied Radiation and Isotopes, 118:366–374, 2016.

[86] Oak ridge project supports fight against cancer. https://www.energy.gov/em/articles/oak-ridge-project-supports-fight-against-cancer, 2025.

[87] Saed Mirzadeh and Marc Garland. Production of thorium-229 from thorium-230, May 19 2005. US Patent App. 10/938,044.

[88] Susan Hogle, Rose Ann Boll, Karen Murphy, David Denton, Allison Owens, Tamara J Haverlock, Marc Garland, and Saed Mirzadeh. Reactor production of Thorium-229. Applied Radiation and Isotopes, 114:19–27, 2016.

[89] Sander De Groot, Klaas Bakker, and Nicola Asquith. Method for producing actinium-225 from a radium-226 target by shielding the target from thermal neutrons in a moderated nuclear reactor, June 20 2023. US Patent 11,682,498.

[90] Chuankun Zhang, Peng Li, Jie Jiang, Lars von der Wense, John F Doyle, Martin E Fermann, and Jun Ye. Tunable VUV frequency comb for ^{229m}Th nuclear spectroscopy. Optics Letters, 47(21):5591–5594, 2022.

[91] James N Eckstein, AI Ferguson, and TW Hänsch. High-resolution two-photon spectroscopy with picosecond light pulses. Physical Review Letters, 40(13):847, 1978.

[92] Herman A Haus. Mode-locking of lasers. IEEE Journal of Selected Topics in Quantum Electronics, 6(6):1173–1185, 2000.

[93] David R Carlson, Daniel D Hickstein, Wei Zhang, Andrew J Metcalf, Franklyn Quinlan, Scott A Diddams, and Scott B Papp. Ultrafast electro-optic light with subcycle control. Science, 361(6409):1358–1363, 2018.

[94] Pascal Del'Haye, Albert Schliesser, Olivier Arcizet, Tom Wilken, Ronald Holzwarth, and Tobias J Kippenberg. Optical frequency comb generation from a monolithic microresonator. Nature, 450(7173):1214–1217, 2007.

[95] Steven T Cundiff and Jun Ye. Colloquium: Femtosecond optical frequency combs. Reviews of Modern Physics, 75(1):325, 2003.

[96] Scott A Diddams, Kerry Vahala, and Thomas Udem. Optical frequency combs: Coherently uniting the electromagnetic spectrum. Science, 369(6501):eaay3676, 2020.

[97] John M Dudley, Goëry Genty, and Stéphane Coen. Supercontinuum generation in photonic crystal fiber. Reviews of Modern Physics, 78(4):1135–1184, 2006.

[98] David J Jones, Scott A Diddams, Jinendra K Ranka, Andrew Stentz, Robert S Windeler, John L Hall, and Steven T Cundiff. Carrier-envelope phase control of femtosecond mode-locked lasers and direct optical frequency synthesis. Science, 288(5466):635–639, 2000.

[99] Nathalie Picqué and Theodor W Hänsch. Frequency comb spectroscopy. Nature Photonics, 13(3):146–157, 2019.

[100] J_J Macklin, JD Kmetec, and CL Gordon III. High-order harmonic generation using intense femtosecond pulses. Physical Review Letters, 70(6):766, 1993.

[101] Paul B Corkum. Plasma perspective on strong field multiphoton ionization. Physical Review Letters, 71(13):1994, 1993.

[102] Maciej Lewenstein, Ph Balcou, M Yu Ivanov, Anne L'huillier, and Paul B Corkum. Theory of high-harmonic generation by low-frequency laser fields. Physical Review A, 49(3):2117, 1994.

[103] Zenghu Chang. Fundamentals of attosecond optics. CRC press, 2016.

[104] Anh-Thu Le, Hui Wei, Cheng Jin, and CD Lin. Strong-field approximation and its extension for high-order harmonic generation with mid-infrared lasers. Journal of Physics B: Atomic, Molecular and Optical Physics, 49(5):053001, 2016.

[105] Stephen Bradley Schoun. Attosecond high-harmonic spectroscopy of atoms and molecules using mid-infrared sources. The Ohio State University, 2015.

[106] Dylan Yost. Development of an extreme ultraviolet frequency comb for precision spectroscopy. PhD thesis, University of Colorado at Boulder, 2011.

[107] Craig Benko. Extreme ultraviolet frequency combs for precision measurement and strong-field physics. PhD thesis, University of Colorado at Boulder, 2016.

[108] R Jason Jones and Jun Ye. Femtosecond pulse amplification by coherent addition in a passive optical cavity. Optics Letters, 27(20):1848–1850, 2002.

[109] R Jason Jones and Jun Ye. High-repetition-rate coherent femtosecond pulse amplification with an external passive optical cavity. Optics Letters, 29(23):2812–2814, 2004.

[110] Anthony E Siegman. Lasers. University science books, 1986.

[111] Ronald WP Drever, John L Hall, Frank V Kowalski, James Hough, GM Ford, AJ Munley, and Hywel Ward. Laser phase and frequency stabilization using an optical resonator. Applied Physics B, 31:97–105, 1983.

[112] Michael J Thorpe, R Jason Jones, KD Moll, Jun Ye, and Ramin Lalezari. Precise measurements of optical cavity dispersion and mirror coating properties via femtosecond combs. Optics Express, 13(3):882–888, 2005.

[113] I Hartl, TR Schibli, A Marcinkevicius, DC Yost, DD Hudson, ME Fermann, and Jun Ye. Cavity-enhanced similariton Yb-fiber laser frequency comb: 3×10^{14} W/cm^2 peak intensity at 136 MHz. Optics Letters, 32(19):2870–2872, 2007.

[114] Axel Ruehl, Andrius Marcinkevicius, Martin E Fermann, and Ingmar Hartl. 80 W, 120 fs Yb-fiber frequency comb. Optics Letters, 35(18):3015–3017, 2010.

[115] Nicolai Lilienfein, Christina Hofer, Simon Holzberger, C Matzer, P Zimmermann, M Trubetskov, V Pervak, and Ioachim Pupeza. Enhancement cavities for few-cycle pulses. Optics Letters, 42(2):271–274, 2017.

[116] Jan Schulte, Thomas Sartorius, Johannes Weitenberg, Andreas Vernaleken, and Peter Russbueldt. Nonlinear pulse compression in a multi-pass cell. Optics Letters, 41(19):4511–4514, 2016.

[117] Kilian Fritsch, Markus Poetzlberger, Vladimir Pervak, Jonathan Brons, and Oleg Pronin. All-solid-state multipass spectral broadening to sub-20 fs. Optics Letters, 43(19):4643–4646, 2018.

[118] Fabian Schmid, Jorge Moreno, Johannes Weitenberg, Peter Russbüldt, Theodor W Hänsch, Thomas Udem, and Akira Ozawa. An ultra-stable high-power optical frequency comb. APL Photonics, 9(2), 2024.

[119] G. et al. Scoles. Atomic and Molecular Beam Methods Vol. I. Oxford Univ. Press, 1988.

[120] KD Moll, R Jason Jones, and Jun Ye. Nonlinear dynamics inside femtosecond enhancement cavities. Optics Express, 13(5):1672–1678, 2005.

[121] TK Allison, A Cingöz, DC Yost, and J Ye. Extreme nonlinear optics in a femtosecond enhancement cavity. Physical Review Letters, 107(18):183903, 2011.

[122] Gil Porat, Christoph M Heyl, Stephen B Schoun, Craig Benko, Nadine Dörre, Kristan L Corwin, and Jun Ye. Phase-matched extreme-ultraviolet frequency-comb generation. Nature Photonics, 12(7):387–391, 2018.

[123] Tobias Saule, Stephan Heinrich, Johannes Schötz, Nicolai Lilienfein, Maximilian Högner, O DeVries, M Plötner, Johannes Weitenberg, D Esser, J Schulte, et al. High-flux ultrafast extreme-ultraviolet photoemission spectroscopy at 18.4 MHz pulse repetition rate. Nature communications, 10(1):458, 2019.

[124] Simon Holzberger, Nicolai Lilienfein, Henning Carstens, Tobias Saule, Maximilian Högner, F Lücking, M Trubetskov, V Pervak, T Eidam, Jens Limpert, et al. Femtosecond enhancement cavities in the nonlinear regime. Physical Review Letters, 115(2):023902, 2015.

[125] Kevin D Moll, R Jason Jones, and Jun Ye. Output coupling methods for cavity-based high-harmonic generation. Optics Express, 14(18):8189–8197, 2006.

[126] DC Yost, A Cingöz, TK Allison, A Ruehl, ME Fermann, I Hartl, and J Ye. Power optimization of xuv frequency combs for spectroscopy applications. Optics Express, 19(23):23483–23493, 2011.

[127] Christopher Corder, Peng Zhao, Jin Bakalis, Xinlong Li, Matthew D Kershis, Amanda R Muraca, Michael G White, and Thomas K Allison. Ultrafast extreme ultraviolet photoemission without space charge. Structural Dynamics, 5(5), 2018.

[128] Kentaro Wakui, Kazuhiro Hayasaka, and Tetsuya Ido. Generation of vacuum ultraviolet radiation by intracavity high-harmonic generation toward state detection of single trapped ions. Applied Physics B, 117:957–967, 2014.

[129] Akira Ozawa, Zhigang Zhao, Makoto Kuwata-Gonokami, and Yohei Kobayashi. High average power coherent vuv generation at 10 MHz repetition frequency by intracavity high harmonic generation. Optics Express, 23(12):15107–15118, 2015.

[130] Edward D Palik. Handbook of optical constants of solids, volume 3. Academic press, 1998.

[131] Haig A Atikian, Neil Sinclair, Pawel Latawiec, Xiao Xiong, Srujan Meesala, Scarlett Gauthier, Daniel Wintz, Joseph Randi, David Bernot, Sage DeFrances, et al. Diamond mirrors for high-power continuous-wave lasers. Nature communications, 13(1):2610, 2022.

[132] DC Yost, TR Schibli, and Jun Ye. Efficient output coupling of intracavity high-harmonic generation. Optics Letters, 33(10):1099–1101, 2008.

[133] Oleg Pronin, Vladimir Pervak, Ernst Fill, Jens Rauschenberger, Ferenc Krausz, and Alexander Apolonski. Ultrabroadband efficient intracavity XUV output coupler. Optics Express, 19(11):10232–10240, 2011.

[134] Julian Fischer, Jakub Drs, François Labaye, Norbert Modsching, Michael Müller, Valentin J Wittwer, and Thomas Südmeyer. Efficient xuv-light out-coupling of intra-cavity high harmonics by a coated grazing-incidence plate. Optics Express, 30(17):30969–30979, 2022.

[135] Ioachim Pupeza, Simon Holzberger, T Eidam, Henning Carstens, D Esser, J Weitenberg, P Rußbüldt, Jens Rauschenberger, J Limpert, Th Udem, et al. Compact high-repetition-rate source of coherent 100 eV radiation. Nature Photonics, 7(8):608–612, 2013.

[136] Ioachim Pupeza, M Högner, Johannes Weitenberg, Simon Holzberger, Dominik Esser, Tino Eidam, Jens Limpert, Andreas Tünnermann, Ernst Fill, and Vladislav S Yakovlev. Cavity-enhanced high-harmonic generation with spatially tailored driving fields. Physical Review Letters, 112(10):103902, 2014.

[137] Maximilian Högner, Tobias Saule, Stephan Heinrich, Nikolai Lilienfein, Dominik Esser, Michael Trubetskov, Volodymyr Pervak, and Ioachim Pupeza. Cavity-enhanced noncollinear high-harmonic generation. Optics Express, 27(14):19675–19691, 2019.

[138] Chuankun Zhang, Stephen B Schoun, Christoph M Heyl, Gil Porat, Mette B Gaarde, and Jun Ye. Noncollinear enhancement cavity for record-high out-coupling efficiency of an extreme-uv frequency comb. Physical Review Letters, 125(9):093902, 2020.

[139] Jian Wu and Heping Zeng. Cavity-enhanced noncollinear high-harmonic generation for extreme ultraviolet frequency combs. Optics Letters, 32(22):3315–3317, 2007.

[140] Akira Ozawa, Andreas Vernaleken, Waldemar Schneider, Igor Gotlibovych, Th Udem, and Th W Hänsch. Non-collinear high harmonic generation: a promising outcoupling method for cavity-assisted XUV generation. Optics Express, 16(9):6233–6239, 2008.

[141] Aleksey Vladimirovich Birulin, Viktor T Platonenko, and Vasilii Vyacheslavovich Strelkov. High-order harmonic generation in colliding beams. Quantum Electronics, 26(5):377, 1996.

[142] SV Fomichev, P Breger, B Carre, P Agostini, and DF Zaretsky. Non-collinear high-harmonic generation. Laser Physics, 12(2):383–388, 2002.

[143] Daniel D Hickstein, Franklin J Dollar, Patrik Grychtol, Jennifer L Ellis, Ronny Knut, Carlos Hernández-García, Dmitriy Zusin, Christian Gentry, Justin M Shaw, Tingting Fan, et al. Non-collinear generation of angularly isolated circularly polarized high harmonics. Nature Photonics, 9(11):743–750, 2015.

[144] Pei-Chi Huang, Carlos Hernández-García, Jen-Ting Huang, Po-Yao Huang, Chih-Hsuan Lu, Laura Rego, Daniel D Hickstein, Jennifer L Ellis, Agnieszka Jaron-Becker, Andreas Becker, et al. Polarization control of isolated high-harmonic pulses. Nature Photonics, 12(6):349–354, 2018.

[145] CM Heyl, SN Bengtsson, Stefanos Carlström, Johan Mauritsson, CL Arnold, and A L'Huillier. Noncollinear optical gating. New Journal of Physics, 16(5):052001, 2014.

[146] Maité Louisy, CL Arnold, Miguel Miranda, Esben Witting Larsen, Samuel N Bengtsson, David Kroon, Marija Kotur, Diego Guénot, Linnea Rading, Piotr Rudawski, et al. Gating attosecond pulses in a noncollinear geometry. Optica, 2(6):563–566, 2015.

[147] CM Heyl, Piotr Rudawski, Fernando Brizuela, SN Bengtsson, Johan Mauritsson, and Anne L'Huillier. Macroscopic effects in noncollinear high-order harmonic generation. Physical Review Letters, 112(14):143902, 2014.

[148] Jennifer L Ellis, Kevin M Dorney, Charles G Durfee, Carlos Hernández-García, Franklin Dollar, Christopher A Mancuso, Tingting Fan, Dmitriy Zusin, Christian Gentry, Patrik Grychtol, et al. Phase matching of noncollinear sum and difference frequency high harmonic generation above and below the critical ionization level. Optics Express, 25(9):10126–10144, 2017.

[149] JB Bertrand, Hans Jakob Wörner, H-C Bandulet, É Bisson, M Spanner, J-C Kieffer, DM Villeneuve, and Paul Bruce Corkum. Ultrahigh-order wave mixing in noncollinear high harmonic generation. Physical Review Letters, 106(2):023001, 2011.

[150] M Negro, M Devetta, Davide Facciala, Anna Gabriella Ciriolo, F Calegari, F Frassetto, L Poletto, V Tosa, C Vozzi, and Salvatore Stagira. Non-collinear high-order harmonic generation by three interfering laser beams. Optics Express, 22(24):29778–29786, 2014.

[151] CM Heyl, SB Schoun, G Porat, H Green, and J Ye. A nozzle for high-density supersonic gas jets at elevated temperatures. Review of Scientific Instruments, 89(11), 2018.

[152] LR CANFIELD, N SWANSON, GA URIANO, and CE KUYATT. NBS measurement services: for ultraviolet detector standards. National Bureau of Standards Special Publication, (250-2), 1987.

[153] CM Heyl, Cord L Arnold, Arnaud Couairon, and Anne L'Huillier. Introduction to macroscopic power scaling principles for high-order harmonic generation. Journal of Physics B: Atomic, Molecular and Optical Physics, 50(1):013001, 2016.

[154] M Bellini, C Lyngå, A Tozzi, MB Gaarde, TW Hänsch, Anne L'Huillier, and C-G Wahlström. Temporal coherence of ultrashort high-order harmonic pulses. Physical Review Letters, 81(2):297, 1998.

[155] Philippe Balcou, Pascal Salieres, Anne L'Huillier, and Maciej Lewenstein. Generalized phase-matching conditions for high harmonics: The role of field-gradient forces. Physical Review A, 55(4):3204, 1997.

[156] Kenneth J Schafer and Kenneth C Kulander. High harmonic generation from ultrafast pump lasers. Physical Review Letters, 78(4):638, 1997.

[157] Philippe Balcou, Anne S Dederichs, Mette B Gaarde, and Anne L'Huillier. Quantum-path analysis and phase matching of high-order harmonic generation and high-order frequency mixing processes in strong laser fields. Journal of Physics B: Atomic, Molecular and Optical Physics, 32(12):2973, 1999.

[158] Dylan C Yost, Thomas R Schibli, Jun Ye, Jennifer L Tate, James Hostetter, Mette B Gaarde, and Kenneth J Schafer. Vacuum-ultraviolet frequency combs from below-threshold harmonics. Nature Physics, 5(11):815–820, 2009.

[159] James A Hostetter, Jennifer L Tate, Kenneth J Schafer, and Mette B Gaarde. Semiclassical approaches to below-threshold harmonics. Physical Review A, 82(2):023401, 2010.

[160] James AR Samson. Techniques of vacuum ultraviolet spectroscopy. Pied Publications, Lincoln, Nebraska, 1967.

[161] Arman Cingöz, Dylan C Yost, Thomas K Allison, Axel Ruehl, Martin E Fermann, Ingmar Hartl, and Jun Ye. Direct frequency comb spectroscopy in the extreme ultraviolet. Nature, 482(7383):68–71, 2012.

[162] Maximilian Högner, V Tosa, and Ioachim Pupeza. Generation of isolated attosecond pulses with enhancement cavities—a theoretical study. New Journal of Physics, 19(3):033040, 2017.

[163] Jorge Moreno, Fabian Schmid, Johannes Weitenberg, Savely G Karshenboim, Theodor W Hänsch, Thomas Udem, and Akira Ozawa. Toward XUV frequency comb spectroscopy of the 1 S–2 S transition in He^+. The European Physical Journal D, 77(4):67, 2023.

[164] Johannes Weitenberg. A monolithic noncollinear femtosecond enhancement cavity. private communication, 2023.

[165] Anne L'Huillier, XF Li, and LA Lompré. Propagation effects in high-order harmonic generation in rare gases. Journal of the Optical Society of America B, 7(4):527–536, 1990.

[166] Surya P Tewari and GS Agarwal. Control of phase matching and nonlinear generation in dense media by resonant fields. Physical Review Letters, 56(17):1811, 1986.

[167] GS Agarwal and Surya P Tewari. Large enhancements in nonlinear generation by external electromagnetic fields. Physical Review Letters, 70(10):1417, 1993.

[168] Yihan Li, Naoya Kuse, Antoine Rolland, Yuriy Stepanenko, Czesław Radzewicz, and Martin E Fermann. Low noise, self-referenced all polarization maintaining ytterbium fiber laser frequency comb. Optics Express, 25(15):18017–18023, 2017.

[169] Martin E Fermann, VI Kruglov, BC Thomsen, John M Dudley, and John D Harvey. Self-similar propagation and amplification of parabolic pulses in optical fibers. Physical Review Letters, 84(26):6010, 2000.

[170] Laura C Sinclair, J-D Deschênes, Lindsay Sonderhouse, William C Swann, Isaac H Khader, Esther Baumann, Nathan R Newbury, and Ian Coddington. Invited article: A compact optically coherent fiber frequency comb. Review of scientific instruments, 86(8), 2015.

[171] E Oelker, RB Hutson, CJ Kennedy, L Sonderhouse, T Bothwell, A Goban, D Kedar, C Sanner, JM Robinson, GE Marti, et al. Demonstration of 4.8×10^{-17} stability at 1 s for two independent optical clocks. Nature Photonics, 13(10):714–719, 2019.

[172] Lingfeng Yan, Stefan Lannig, William R Milner, Max N Frankel, Ben Lewis, Dahyeon Lee, Kyungtae Kim, and Jun Ye. A high-power clock laser spectrally tailored for high-fidelity quantum state engineering. arXiv preprint arXiv:2501.09343, 2025.

[173] Gene F Franklin, J David Powell, Abbas Emami-Naeini, and J David Powell. Feedback control of dynamic systems, volume 4. Prentice hall Upper Saddle River, 2002.

[174] Floyd M Gardner. Phaselock techniques. John Wiley & Sons, 2005.

[175] Paul Horowitz, Winfield Hill, and Ian Robinson. The art of electronics, volume 2. Cambridge university press Cambridge, 1989.

[176] William R Milner, John M Robinson, Colin J Kennedy, Tobias Bothwell, Dhruv Kedar, Dan G Matei, Thomas Legero, Uwe Sterr, Fritz Riehle, Holly Leopardi, et al. Demonstration of a timescale based on a stable optical carrier. Physical Review Letters, 123(17):173201, 2019.

[177] John Hall and M. Zhu. An introduction to phase-stable optical sources, volume CXVIII. North-Holland, 1993. JILA Pub. 4738.

[178] David Owen. Good practice guide to phase noise measurement. Technical report, National Physical Laboratory, 2004.

[179] Enrico Rubiola. Enrico rubiola home page. https://rubiola.org/, 2025.

[180] Craig Benko, Thomas K Allison, Arman Cingöz, Linqiang Hua, François Labaye, Dylan C Yost, and Jun Ye. Extreme ultraviolet radiation with coherence time greater than 1 s. Nature Photonics, 8(7):530–536, 2014.

[181] Long-Sheng Ma, Peter Jungner, Jun Ye, and John L Hall. Delivering the same optical frequency at two places: accurate cancellation of phase noise introduced by an optical fiber or other time-varying path. Optics Letters, 19(21):1777–1779, 1994.

[182] J-H Oelmann, L Guth, T Heldt, N Griesbach, R Hector, N Lackmann, J Nauta, T Pfeifer, and JR Crespo López-Urrutia. Closed-cycle noble gas recycling system for high-repetition rate high-harmonic generation. Review of Scientific Instruments, 95(3), 2024.

[183] National Institute of Standards and Technology (NIST). Oxygen, NIST chemistry webbook, SRD 69, 2025. Accessed: 2025-02-07.

[184] Gerald T Brower and George Thodos. Vapor pressures of liquid oxygen between the triple point and critical point. Journal of Chemical & Engineering Data, 13(2):262–264, 1968.

[185] David Hanson and Konrad Mauersberger. The vapor pressures of solid and liquid ozone. The Journal of chemical physics, 85(8):4669–4672, 1986.

[186] V.A. Rabinovich and T.B. Selover. Thermophysical Properties of Neon, Argon, Krypton, and Xenon. National Standard Reference Data Service of the USSR. Hemisphere Publishing Corporation, 1988.

[187] W.M. Haynes. CRC Handbook of Chemistry and Physics. CRC Press, 2014.

[188] National Institute of Standards and Technology (NIST). Xenon, NIST chemistry webbook, SRD 69. Accessed: 2025-02-07.

[189] RE Stevens, C-W Hsiao, Linh Le, NJ Curro, BJ Monton, B-Y Chang, C-Y Kung, C Kittrell, and JL Kinsey. A partial pressure monitor and controller for stable ozone flow from a silica gel trap. Review of scientific instruments, 69(6):2504–2509, 1998.

[190] Lars von der Wense, Benedict Seiferle, Simon Stellmer, Johannes Weitenberg, Georgy Kazakov, Adriana Pálffy, and Peter G Thirolf. A laser excitation scheme for ^{229m}Th. Physical Review Letters, 119(13):132503, 2017.

[191] Lars von der Wense and Chuankun Zhang. Concepts for direct frequency-comb spectroscopy of ^{229m}Th and an internal-conversion-based solid-state nuclear clock. The European Physical Journal D, 74:1–17, 2020.

[192] RM Sternheimer. Shielding and antishielding effects for various ions and atomic systems. Physical Review, 146(1):140, 1966.

[193] Christopher J Foot. Atomic physics, volume 7. Oxford university press, 2005.

[194] Heung-Ryoul Noh and Wonho Jhe. Analytic solutions of the optical Bloch equations. Optics Communications, 283(11):2353–2355, 2010.

[195] HC Torrey. Transient nutations in nuclear magnetic resonance. Physical Review, 76(8):1059, 1949.

[196] Lars von der Wense, Pavlo V Bilous, Benedict Seiferle, Simon Stellmer, Johannes Weitenberg, Peter G Thirolf, Adriana Pálffy, and Georgy Kazakov. The theory of direct laser excitation of nuclear transitions. The European Physical Journal A, 56:1–22, 2020.

[197] Robert C Hilborn. Einstein coefficients, cross sections, f values, dipole moments, and all that. arXiv preprint physics/0202029, 2002.

[198] A Anders. Recombination of a xenon plasma jet. Beiträge aus der Plasmaphysik, 27(5):373–398, 1987.

[199] Robert Gillis. Determining the extreme ultraviolet constants of thoria by spectral ellipsometry, 2007.

[200] David H Dowell and John F Schmerge. Quantum efficiency and thermal emittance of metal photocathodes. Physical Review Special Topics—Accelerators and Beams, 12(7):074201, 2009.

[201] R Haas, S Lohse, Ch E Düllmann, K Eberhardt, C Mokry, and J Runke. Development and characterization of a drop-on-demand inkjet printing system for nuclear target fabrication. Nuclear Instruments and Methods in Physics Research Section A: Accelerators, Spectrometers, Detectors and Associated Equipment, 874:43–49, 2017.

[202] Ursula EA Fittschen, Nicolas H Bings, Stephan Hauschild, Stephan Förster, Arne F Kiera, Ezer Karavani, Andreas Frömsdorf, Julian Thiele, and Gerald Falkenberg. Characteristics of picoliter droplet dried residues as standards for direct analysis techniques. Analytical chemistry, 80(6):1967–1977, 2008.

[203] Microdrop Technologies. Picoliter dispensing. https://www.microdrop.de/ad-md-series.html, 2025.

[204] W Streule, T Lindemann, G Birkle, R Zengerle, and P Koltay. Pipejet: a simple disposable dispenser for the nano-and microliter range. SLAS Technology, 9(5):300–306, 2004.

[205] Safwat A Mahmoud. Characterization of thorium dioxide thin films prepared by the spray pyrolysis technique. Solid State Sciences, 4(2):221–228, 2002.

[206] A Jaworek. Electrospray droplet sources for thin film deposition. Journal of Materials Science, 42:266–297, 2007.

[207] PV Borisyuk, OS Vasilyev, AV Krasavin, Yu Yu Lebedinskii, VI Troyan, EV Chubunova, and SP Derevyashkin. Formation of local thorium silicate compound by electrochemical deposition from an acetone solution of thorium nitrate. Journal of Sol-Gel Science and Technology, 81:313–320, 2017.

[208] Larry Jassin and Lars von der Wense. Th-229 electroplating procedure. private communication, 2021.

[209] Jill Chastain and Roger C King Jr. Handbook of X-ray photoelectron spectroscopy. Perkin-Elmer Corporation, 40:221, 1992.

[210] JAMES C Warf, WD Cline, and Ruth D Tevebaugh. Pyrohydrolysis in determination of fluoride and other halides. Analytical Chemistry, 26(2):342–346, 1954.

[211] Dong Xiaoyu, Zheng Xiaobei, Song Yulong, Liu Yuxia, and Zhang Lan. Pyrohydrolysis of uranium tetrafluoride and thorium tetrafluoride. Journal of Nuclear and Radiochemistry, 36, 2014.

[212] PW Baumeister. Properties of multilayer filters. Technical report, Institute of Optics, Univ. Rochester, 1973.

[213] AJ Darnell, WA McCollum, and TA Milne. Vapor pressure of thorium. The Journal of Physical Chemistry, 64(3):341–346, 1960.

[214] Edward Shapiro. Vapor pressure of thorium oxide from 2050 to 2250°K. Journal of the American Chemical Society, 74(20):5233–5235, 1952.

[215] AJ Darnell and FJ Keneshea. Vapor presure of thorium–thorium tetrafluoride. The Journal of Physical Chemistry, 62(9):1143–1145, 1958.

[216] Geirr Sletten. Preparation of targets of alpha-radioactive isotopes. Nuclear Instruments and Methods, 102(3):465–468, 1972.

[217] HL Adair. Preparation and characterization of radioactive samples for various areas of research. Nuclear Instruments and Methods, 167(1):45–53, 1979.

[218] KM Glover, L Bint, DB Gayther, M King, B Whittaker, and RAP Wiltshire. The preparation of stable and actinide nuclide targets for nuclear measurements. IEEE Transactions on Nuclear Science, 28(2):1593–1596, 1981.

[219] HJ Maier. Preparation of nuclear accelerator targets by vacuum evaporation. IEEE Transactions on Nuclear Science, 28(2):1575–1583, 1981.

[220] HJ Maier, R Grossmann, and HU Friebel. Radioactive targets for nuclear accelerator experiments. Nuclear Instruments and Methods in Physics Research Section B: Beam Interactions with Materials and Atoms, 56:926–932, 1991.

[221] John P Greene, Irshad Ahmad, and George E Thomas. Radioactive targets and source development at Argonne National Laboratory. Nuclear Instruments and Methods in Physics Research Section A: Accelerators, Spectrometers, Detectors and Associated Equipment, 334(1):101–110, 1993.

[222] Alexander T Chemey, Ashley Pica, Walter D Loveland, and Matt Silveira. Preparation of actinide targets at Oregon State University. Journal of Radioanalytical and Nuclear Chemistry, 331(12):5101–5106, 2022.

[223] Anubhav Jain, Shyue Ping Ong, Geoffroy Hautier, Wei Chen, William Davidson Richards, Stephen Dacek, Shreyas Cholia, Dan Gunter, David Skinner, Gerbrand Ceder, et al. Commentary: The materials project: A materials genome approach to accelerating materials innovation. APL materials, 1(1), 2013.

[224] Jason K Ellis, Xiao-Dong Wen, and Richard L Martin. Investigation of thorium salts as candidate materials for direct observation of the ^{229m}Th nuclear transition. Inorganic Chemistry, 53(13):6769–6774, 2014.

[225] T Gouder, R Eloirdi, RL Martin, M Osipenko, M Giovannini, and R Caciuffo. Measurements of the band gap of ThF_4 by electron spectroscopy techniques. Physical Review Research, 1(3):033005, 2019.

[226] Marion Mallweger. Deuteriumlamp as a calibration source for a superconducting nanowire. Master's thesis, TU Wien, 2020.

[227] Julian A Steele, Eduardo Solano, David Hardy, Damara Dayton, Dylan Ladd, Keith White, Peng Chen, Jingwei Hou, Haowei Huang, Rafikul Ali Saha, et al. How to GIWAXS: Grazing incidence wide angle X-ray scattering applied to metal halide perovskite thin films. Advanced Energy Materials, 13(27):2300760, 2023.

[228] Kjeld Beeks. The nuclear excitation of thorium-229 in the CaF_2 environment: development of a crystalline nuclear clock. PhD thesis, Technische Universität Wien, 2022.

[229] Zemax LLC. Zemax opticstudio, 2012. Zemax v12.2.

[230] M Bagge-Hansen, RA Outlaw, K Seo, and DM Manos. Morphology and crystallization of ThO_2 thin films on polycrystalline Ir. Thin solid films, 520(13):4249–4253, 2012.

[231] WE Danforth. Thorium oxide and electronics. In Advances in Electronics and Electron Physics, volume 5, pages 169–211. Elsevier, 1953.

[232] JL Bates and RR Schemmel. Electrical conductivity of thorium dioxide. Technical report, Battelle Pacific Northwest Labs., Richland, Wash., 1972.

[233] Wei Zheng, Richeng Lin, Junxue Ran, Zhaojun Zhang, Xu Ji, and Feng Huang. Vacuum-ultraviolet photovoltaic detector. Acs Nano, 12(1):425–431, 2018.

[234] Siwapon Srisonphan, Myungji Kim, and Hong Koo Kim. Space charge neutralization by electron-transparent suspended graphene. Scientific reports, 4(1):3764, 2014.

[235] G Hassink, R Wanke, I Rastegar, W Braun, C Stephanos, P Herlinger, JH Smet, and J Mannhart. Transparency of graphene for low-energy electrons measured in a vacuum-triode setup. APL Materials, 3(7), 2015.

[236] Satoru Suzuki, Yuichi Haruyama, Akinobu Yamaguchi, Tomoki Yamamoto, Takuya Yoshizumi, Ayaka Fujii, Seiji Nakashima, Yakumo Fuchiwaki, Hironori Fujisawa, Takuo Ohkochi, et al. X-ray absorption and photoemission spectroscopy of bulk insulating materials using graphene. Journal of Applied Physics, 128(1), 2020.

[237] Jürgen Kraus, Robert Reichelt, Sebastian Günther, Luca Gregoratti, Matteo Amati, Maya Kiskinova, Alexander Yulaev, Ivan Vlassiouk, and Andrei Kolmakov. Photoelectron spectroscopy of wet and gaseous samples through graphene membranes. Nanoscale, 6(23):14394–14403, 2014.

[238] Fangze Liu, Lei Guo, Jeffrey DeFazio, Vitaly Pavlenko, Masahiro Yamamoto, Nathan A Moody, and Hisato Yamaguchi. Photoemission from bialkali photocathodes through an atomically thin protection layer. ACS Applied Materials & Interfaces, 14(1):1710–1717, 2021.

[239] Jason Paul Allmaras. Modeling and development of superconducting nanowire single-photon detectors. California Institute of Technology, 2020.

[240] Galen OŃeil, Kjeld Beeks, Eric Hudson, Justin Jeet, David Leibrandt, Marion Mallweger, Sae Woo Nam, Sayan Patra, Gil Porat, Dileep Reddy, Thorsten Schumm, Stephen Schoun, Benedict Seiferle, Christian Schneider, Lars von der Wense, Peter Thirolf, Varun Verma, Jun Ye, and Chuankun Zhang. Direct detection of the $\sim$ 8.4 eV internal conversion energy of ^{229m}th embedded in a superconducting nanowire. in preparation, 2025.

[241] Mikhail Osipenko, Carlos de Almeida Carrapico, Dmytro Burdeinyi, Roberto Caciuffo, Rachel Eloirdi, Mauro Giovannini, Alban Kellerbauer, Rikard Malmbeck, Marco Ripani, and Mauro Taiuti. Measurement of photo-and radio-luminescence of thin ThF_4 films. Nuclear Instruments and Methods in Physics Research Section A: Accelerators, Spectrometers, Detectors and Associated Equipment, 1068:169744, 2024.

[242] Edward M Purcell, Henry Cutler Torrey, and Robert V Pound. Resonance absorption by nuclear magnetic moments in a solid. Physical Review, 69(1-2):37, 1946.

[243] G Nienhuis and C Th J Alkemade. Atomic radiative transition probabilities in a continuous medium. Physica B+C, 81(1):181–188, 1976.

[244] GLJA Rikken and YARR Kessener. Local field effects and electric and magnetic dipole transitions in dielectrics. Physical Review Letters, 74(6):880, 1995.

[245] EV Tkalya. Spontaneous emission probability for M1 transition in a dielectric medium: $^{229}\mathrm{Th}^{\mathrm{m}}$ ($3/2^{+}$, 3.5±1.0 eV) decay. Journal of Experimental and Theoretical Physics Letters, 71:311–313, 2000.

[246] HP Urbach and GLJA Rikken. Spontaneous emission from a dielectric slab. Physical Review A, 57(5):3913, 1998.

[247] Walter Lukosz and RE Kunz. Light emission by magnetic and electric dipoles close to a plane interface. I. Total radiated power. JOSA, 67(12):1607–1615, 1977.

[248] W Lukosz and RE Kunz. Light emission by magnetic and electric dipoles close to a plane dielectric interface. II. Radiation patterns of perpendicular oriented dipoles. JOSA, 67(12):1615–1619, 1977.

[249] W Lukosz. Light emission by magnetic and electric dipoles close to a plane dielectric interface. III. Radiation patterns of dipoles with arbitrary orientation. JOSA, 69(11):1495–1503, 1979.

[250] Ralf Röhlsberger, Kai Schlage, Balaram Sahoo, Sebastien Couet, and Rudolf Rüffer. Collective Lamb shift in single-photon superradiance. Science, 328(5983):1248–1251, 2010.

[251] U Van Bürck, DP Siddons, JB Hastings, U Bergmann, and R Hollatz. Nuclear forward scattering of synchrotron radiation. Physical Review B, 46(10):6207, 1992.

[252] PP Craig, DE Nagle, and DRF Cochran. Zeeman effect in the recoilless γ-ray resonance of ^{67}Zn. Physical Review Letters, 4(11):561, 1960.

[253] VA Dornow, J Binder, A Heidemann, GM Kalvius, and G Wortmann. Preparation of narrow-line sources for the 6.2 keV Mössbauer resonance of ^{181}Ta. Nuclear Instruments and Methods, 163(2-3):491–497, 1979.

[254] YR Uhm, JJ Kim, SM Choi, and KJ Son. Thermal diffusion of ^{57}Co into rh foil for preparing Mössbauer source. Archives of Metallurgy and Materials, 2017.

[255] RC Pastor and K Arita. Preparation and crystal growth of $^{229}\mathrm{ThF}_4$. Materials Research Bulletin, 9(5):579–583, 1974.

[256] Theodor W Hänsch. Nobel lecture: passion for precision. Reviews of Modern Physics, 78(4):1297–1309, 2006.

[257] Kjeld Beeks, Tomas Sikorsky, Veronika Rosecker, Martin Pressler, Fabian Schaden, David Werban, Niyusha Hosseini, Lukas Rudischer, Felix Schneider, Patrick Berwian, et al. Growth and characterization of thorium-doped calcium fluoride single crystals. Scientific Reports, 13(1):3897, 2023.

[258] Kjeld Beeks, Tomas Sikorsky, Fabian Schaden, Martin Pressler, Felix Schneider, Björn N Koch, Thomas Pronebner, David Werban, Niyusha Hosseini, Georgy Kazakov, et al. Optical transmission enhancement of ionic crystals via superionic fluoride transfer: Growing VUV-transparent radioactive crystals. Physical Review B, 109(9):094111, 2024.

[259] Simon Stellmer, Matthias Schreitl, and Thorsten Schumm. Radioluminescence and photoluminescence of Th:CaF_2 crystals. Scientific Reports, 5(1):15580, 2015.

[260] Takahiro Hiraki. Experimental apparatus for detection of radiative decay of ^{229}Th isomer from Th-doped CaF_2. Interactions, 245(1):14, 2024.

[261] PG Thirolf, D Kalb, Mustapha Laatiaoui, et al. Towards an all-optical access to the lowest nuclear excitation in ^{229m}Th. Acta Physica Polonica B, 44(3):391–394, 2013.

[262] Benedict Seiferle, Lars von der Wense, Mustapha Laatiaoui, and Peter G Thirolf. A VUV detection system for the direct photonic identification of the first excited isomeric state of ^{229}Th. The European Physical Journal D, 70:1–12, 2016.

[263] P Dessovic, P Mohn, RA Jackson, G Winkler, M Schreitl, G Kazakov, and T Schumm. ^{229}Thorium-doped calcium fluoride for nuclear laser spectroscopy. Journal of Physics: Condensed Matter, 26(10):105402, 2014.

[264] B.D. Dunlap and G.M. Kalvius. Mössbauer spectroscopy on actinides and their compounds. In Handbook on the Physics and Chemistry of the Actinides, volume II, pages 331–434. Elsevier Science Pub. Co., 1985.

[265] Peter Zory. Nuclear electric-field gradient determination utilizing the Mössbauer effect (Fe^{57}). Physical Review, 140(4A):A1401, 1965.

[266] E Gerdau, J Wolf, H Winkler, and J Braunsfurth. Quadrupole interaction of 181ta in hf compounds. Proceedings of the Royal Society of London. A. Mathematical and Physical Sciences, 311(1504):197–206, 1969.

[267] Elina Fuchs, Fiona Kirk, Eric Madge, Chaitanya Paranjape, Ekkehard Peik, Gilad Perez, Wolfram Ratzinger, and Johannes Tiedau. Implications of the laser excitation of the Th-229 nucleus for dark matter searches. arXiv preprint arXiv:2407.15924, 2024.

[268] Andrea Caputo, Doron Gazit, Hans-Werner Hammer, Joachim Kopp, Gil Paz, Gilad Perez, and Konstantin Springmann. On the sensitivity of nuclear clocks to new physics. arXiv preprint arXiv:2407.17526, 2024.

[269] VA Dzuba and VV Flambaum. Using the Th III ion for a nuclear clock and searches for new physics. arXiv preprint arXiv:2412.18308, 2024.

[270] Aage Niels Bohr and Ben R Mottelson. Nuclear Structure (in 2 volumes). World Scientific Publishing Company, 1998.

[271] R Neugart and G Neyens. Nuclear moments. The Euroschool Lectures on Physics with Exotic Beams, Vol. II, pages 135–189, 2006.

[272] Pavel Fadeev, Julian C Berengut, and Victor V Flambaum. Sensitivity of ^{229}Th nuclear clock transition to variation of the fine-structure constant. Physical Review A, 102(5):052833, 2020.

[273] Julian C Berengut, Vladimir A Dzuba, Victor V Flambaum, and Sergey G Porsev. Proposed experimental method to determine α sensitivity of splitting between ground and 7.6 ev isomeric states in ^{229}Th. Physical Review Letters, 102(21):210801, 2009.

[274] Rainer W Hasse and William D Myers. Geometrical relationships of macroscopic nuclear physics. Springer Science & Business Media, 2012.

[275] Robert Beringer and WJ Knox. Liquid-drop nuclear model with high angular momentum. Physical Review, 121(4):1195, 1961.

[276] István Angeli and Krassimira Petrova Marinova. Table of experimental nuclear ground state charge radii: An update. Atomic Data and Nuclear Data Tables, 99(1):69–95, 2013.

[277] MS Safronova, SG Porsev, MG Kozlov, J Thielking, MV Okhapkin, P Głowacki, DM Meier, and E Peik. Nuclear charge radii of ^{229}Th from isotope and isomer shifts. Physical Review Letters, 121(21):213001, 2018.

[278] VV Flambaum. Enhanced effect of temporal variation of the fine structure constant and the strong interaction in ^{229}Th. Physical Review Letters, 97(9):092502, 2006.

[279] CE Bemis, FK McGowan, JLC Ford Jr, WT Milner, RL Robinson, PH Stelson, GA Leander, and CW Reich. Coulomb excitation of states in ^{229}Th. Physica Scripta, 38(5):657, 1988.

[280] Catherine A McCammon. Insights into phase transformations from Mössbauer spectroscopy. Reviews in Mineralogy and Geochemistry, 39(1):241–264, 2000.

[281] DA Shirley. Application and interpretation of isomer shifts. Reviews of Modern Physics, 36(1):339, 1964.

[282] VA Dzuba and VV Flambaum. Effects of electrons on nuclear clock transition frequency in ^{229}Th ions. Physical Review Letters, 131(26):263002, 2023.

[283] Andrei Ruskuc, Chun-Ju Wu, Jake Rochman, Joonhee Choi, and Andrei Faraon. Nuclear spin-wave quantum register for a solid-state qubit. Nature, 602(7897):408–413, 2022.

[284] GH Larson and CD Jeffries. Spin-lattice relaxation in some rare-earth salts. I. Temperature dependence. Physical Review, 141(1):461, 1966.

[285] Calcium fluoride. https://www.crystran.com/optical-materials/calcium-fluoride-caf2, 2025.

[286] JP Szczesniak, D Cuddeback, and JC Corelli. Stress-induced birefringence of solids transparent to 1-to 12-μm light. Journal of Applied Physics, 47(12):5356–5359, 1976.

[287] Simone Dolabella, Aurelio Borzì, Alex Dommann, and Antonia Neels. Lattice strain and defects analysis in nanostructured semiconductor materials and devices by high-resolution X-ray diffraction: Theoretical and practical aspects. Small Methods, 6(2):2100932, 2022.

[288] Mikhail A Krivoglaz. X-ray and neutron diffraction in nonideal crystals. Springer Berlin, Heidelberg, 1996.

[289] Qiaorui Gong, Siliang Tao, Chengchun Zhao, Yin Hang, Shining Zhu, and Longsheng Ma. Structures and properties of high-concentration doped Th:CaF_2 single crystals for solid-state nuclear clock materials. Inorganic Chemistry, 63(8):3807–3814, 2024.

[290] H Kanzaki. Point defects in face-centred cubic lattice—I distortion around defects. Journal of Physics and Chemistry of Solids, 2(1):24–36, 1957.

[291] John W Flocken and John R Hardy. Asymptotic lattice displacements about point defects in cubic metals. Physical Review B, 1(6):2447, 1970.

[292] John R Hardy. The lattice dynamics and statics of alkali halide crystals. Springer Science & Business Media, 2012.

[293] Jonathan D Roslund, Arman Cingöz, William D Lunden, Guthrie B Partridge, Abijith S Kowligy, Frank Roller, Daniel B Sheredy, Gunnar E Skulason, Joe P Song, Jamil R Abo-Shaeer, et al. Optical clocks at sea. Nature, 628(8009):736–740, 2024.

[294] Jun Ye. How did i come to know jeff kimble. https://iqim.caltech.edu/2012/12/19/how-did-i-come-to-know-jeff-kimble/, 2012.

[295] Brenden S Nickerson, Martin Pimon, Pavlo V Bilous, Johannes Gugler, Kjeld Beeks, Tomas Sikorsky, Peter Mohn, Thorsten Schumm, and Adriana Pálffy. Nuclear excitation of the ^{229}Th isomer via defect states in doped crystals. Physical Review Letters, 125(3):032501, 2020.

[296] Brenden S Nickerson, Martin Pimon, Pavlo V Bilous, Johannes Gugler, Georgy A Kazakov, Tomas Sikorsky, Kjeld Beeks, Andreas Grüneis, Thorsten Schumm, and Adriana Pálffy. Driven electronic bridge processes via defect states in ^{229}Th-doped crystals. Physical Review A, 103(5):053120, 2021.

[297] Crystalclock: readout scheme for solid-state nuclear clock. https://www.tuwien.at/en/phy/ati/quantum-metrology/research/crystalclock, 2025.

[298] Arnold M Karo and John R Hardy. Calculation of point-defect energies and displacements in alkali halides using the lattice-statics method. Physical Review B, 3(10):3418, 1971.

[299] VX Quang, NN Dat, VP Tuyen, NM Khaidukov, VN Makhov, LD Thanh, NX Ca, NT Thanh, PTT Nga, and PV Do. VUV spectroscopy of lanthanide doped fluoride crystals K_2YF_5. Optical Materials, 107:110049, 2020.

[300] JL Hall and RT Schumacher. Electron spin resonance of hydrogen atoms in CaF_2. Physical Review, 127(6):1892, 1962.

[301] JES Terhune, R Elwell, HB Tan, UC Perera, HWT Morgan, AN Alexandrova, Andrei Derevianko, and Eric R Hudson. Photo-induced quenching of the ^{229}Th isomer in a solid-state host. arXiv preprint arXiv:2412.08998, 2024.

[302] F Schaden, T Riebner, I Morawetz, L Toscani De Col, GA Kazakov, K Beeks, T Sikorsky, T Schumm, K Zhang, V Lal, et al. Laser-induced quenching of the Th-229 nuclear clock isomer in calcium fluoride. arXiv preprint arXiv:2412.12339, 2024.

[303] Bjarke TR Christensen, Martin R Henriksen, Stefan A Schäffer, Philip G Westergaard, David Tieri, Jun Ye, Murray J Holland, and Jan W Thomsen. Nonlinear spectroscopy of sr atoms in an optical cavity for laser stabilization. Physical Review A, 92(5):053820, 2015.

[304] SA Schäffer, BTR Christensen, SM Rathmann, MH Appel, MR Henriksen, and JW Thomsen. Towards passive and active laser stabilization using cavity-enhanced atomic interaction. In Journal of Physics: Conference Series, volume 810, page 012002. IOP Publishing, 2017.

[305] Shon Cook, Till Rosenband, and David R Leibrandt. Laser-frequency stabilization based on steady-state spectral-hole burning in $Eu^{3+} : Y_2SiO_5$. Physical Review Letters, 114(25):253902, 2015.

[306] Ka Fai Mak, John C Travers, Philipp Hölzer, Nicolas Y Joly, and Philip St J Russell. Tunable vacuum-UV to visible ultrafast pulse source based on gas-filled Kagome-PCF. Optics Express, 21(9):10942–10953, 2013.

[307] Alexey Ermolov, Ka Fai Mak, Michael H Frosz, John C Travers, and P St J Russell. Supercontinuum generation in the vacuum ultraviolet through dispersive-wave and soliton-plasma interaction in a noble-gas-filled hollow-core photonic crystal fiber. Physical Review A, 92(3):033821, 2015.

[308] John C Travers, Teodora F Grigorova, Christian Brahms, and Federico Belli. High-energy pulse self-compression and ultraviolet generation through soliton dynamics in hollow capillary fibres. Nature Photonics, 13(8):547–554, 2019.

[309] Md Selim Habib, Christos Markos, JE Antonio-Lopez, and Rodrigo Amezcua-Correa. Extreme UV light generation through dispersive wave trapping in a tapered gas-filled hollow fiber. IEEE Photonics Technology Letters, 31(10):795–798, 2019.

[310] CT Chen, GL Wang, XY Wang, and ZY Xu. Deep-UV nonlinear optical crystal $KBe_2BO_3F_2$—discovery, growth, optical properties and applications. Applied Physics B, 97:9–25, 2009.

[311] Tomoharu Nakazato, Isao Ito, Yohei Kobayashi, Xiaoyang Wang, Chuangtian Chen, and Shuntaro Watanabe. Phase-matched frequency conversion below 150 nm in $KBe_2BO_3F_2$. Optics Express, 24(15):17149–17158, 2016.

[312] Simon J Herr, Hiroki Tanaka, Ingo Breunig, Matthias Bickermann, and Frank Kühnemann. Fanout periodic poling of $BaMgF_4$ crystals. Optical Materials Express, 13(8):2158–2164, 2023.

[313] Encarnacion G Villora, Kiyoshi Shimamura, Keiji Sumiya, and Hiroyuki Ishibashi. Birefringent-and quasi phase-matching with $BaMgF_4$ for vacuum-UV/UV and mid-IR all solid-state lasers. Optics Express, 17(15):12362–12378, 2009.

[314] Luis Mateos, Mariola O Ramírez, Irene Carrasco, Pablo Molina, Juan F Galisteo-López, Encarnación G Víllora, Carmen de las Heras, Kiyoshi Shimamura, Cefe Lopez, and Luisa E Bausá. $BaMgF_4$: An ultra-transparent two-dimensional nonlinear photonic crystal with strong χ (3) response in the UV spectral region. Advanced Functional Materials, 24(11):1509–1518, 2014.

[315] Keerthan Subramanian, Nutan Kumari Sah, Srinivasa Pradeep Arasada, Florian Zacherl, and Lars von der Wense. Towards the development of a CW laser at 148.38 nm for driving the ^{229}Th nuclear clock transition. in The 54th Winter Colloquium on the PHYSICS of QUANTUM ELECTRONICS Abstract Book, 2025.

[316] HWT Morgan, R Elwell, JES Terhune, HB Tan, UC Perera, A Derevianko, AN Alexandrova, and ER Hudson. ^{229}Th-doped nonlinear optical crystals for compact solid-state clocks. arXiv preprint arXiv:2410.23364, 2024.

[317] RR Freeman, GC Bjorklund, NP Economou, PF Liao, and JE Bjorkholm. Generation of cw VUV coherent radiation by four-wave sum frequency mixing in Sr vapor. Applied Physics Letters, 33(8):739–742, 1978.

[318] J Nolting, H Kunze, I Schütz, and R Wallenstein. CW coherent VUV radiation generated by resonant sum-frequency mixing in metal vapors. Applied Physics B, 50:331–344, 1990.

[319] KSE Eikema, J Walz, and TW Hänsch. Continuous wave coherent Lyman-α radiation. Physical Review Letters, 83(19):3828, 1999.

[320] Kjeld SE Eikema, J Walz, and TW Hänsch. Continuous coherent Lyman-α excitation of atomic hydrogen. Physical Review Letters, 86(25):5679, 2001.

[321] Qi Xiao, Gleb Penyazkov, Ruihan Yu, Beichen Huang, Jiatong Li, Juanlang Shi, Yanmei Yu, Yuxiang Mo, and Shiqian Ding. Proposal for the generation of continuous-wave vacuum ultraviolet laser light for Th-229 isomer precision spectroscopy. arXiv preprint arXiv:2406.16841, 2024.

[322] Christos Markos, John C Travers, Amir Abdolvand, Benjamin J Eggleton, and Ole Bang. Hybrid photonic-crystal fiber. Reviews of Modern Physics, 89(4):045003, 2017.

[323] Pablo Londero, Vivek Venkataraman, Amar R Bhagwat, Aaron D Slepkov, and Alexander L Gaeta. Ultralow-power four-wave mixing with Rb in a hollow-core photonic band-gap fiber. Physical Review Letters, 103(4):043602, 2009.

[324] Destry Dewitt, Dmitry Vorobiev, Thomas Livingston, Brian Fleming, Emily Farr, Tim A Birks, Bartlomiej Winter, Kerrianne Harrington, and William Wadsworth. Transmission and bend loss in far ultraviolet hollow-core fibers for compact fiber-fed, multi-object spectrographs and reflectometers. In UV, X-Ray, and Gamma-Ray Space Instrumentation for Astronomy XXIII, volume 12678, pages 241–249. SPIE, 2023.

[325] Federico Belli, Amir Abdolvand, Wonkeun Chang, John C Travers, and Philip St J Russell. Vacuum-ultraviolet to infrared supercontinuum in hydrogen-filled photonic crystal fiber. Optica, 2(4):292–300, 2015.

[326] Rinat Tyumenev, Philip St J Russell, and David Novoa. Narrowband vacuum ultraviolet light via cooperative Raman scattering in dual-pumped gas-filled photonic crystal fiber. ACS Photonics, 7(8):1989–1993, 2020.

[327] K Ludewigt, R Dierking, W Pfingsten, and B Wellegehausen. Vacuum ultraviolet anti-Stokes Raman lasers. IEEE journal of quantum electronics, 22(10):1967–1974, 1986.

[328] Manoj K Mridha, David Novoa, Pooria Hosseini, and Philip St J Russell. Thresholdless deep and vacuum ultraviolet raman frequency conversion in hydrogen-filled photonic crystal fiber. Optica, 6(6):731–734, 2019.

[329] Rinat Tyumenev, Jonas Hammer, NY Joly, P St J Russell, and David Novoa. Tunable and state-preserving frequency conversion of single photons in hydrogen. Science, 376(6593):621–624, 2022.

[330] Anica Hamer, Frank Vewinger, Michael H Frosz, and Simon Stellmer. Frequency conversion in a hydrogen-filled hollow-core fiber: power scaling, background, and bandwidth. arXiv preprint arXiv:2501.04049, 2025.

[331] Michael Semmlinger, Ming Lun Tseng, Jian Yang, Ming Zhang, Chao Zhang, Wei-Yi Tsai, Din Ping Tsai, Peter Nordlander, and Naomi J Halas. Vacuum ultraviolet light-generating metasurface. Nano letters, 18(9):5738–5743, 2018.

[332] Michael Semmlinger, Ming Zhang, Ming Lun Tseng, Tzu-Ting Huang, Jian Yang, Din Ping Tsai, Peter Nordlander, and Naomi J Halas. Generating third harmonic vacuum ultraviolet light with a TiO_2 metasurface. Nano letters, 19(12):8972–8978, 2019.

[333] Arash Ahmadivand and Burak Gerislioglu. Deep- and vacuum-ultraviolet metaphotonic light sources. Materials Today, 51:208–221, 2021.

[334] Ronald W Waynant and Philipp H Klein. Vacuum ultraviolet laser emission from Nd^{+3}: LaF_3. Applied physics letters, 46(1):14–16, 1985.

[335] SG Porsev, VV Flambaum, E Peik, and Chr Tamm. Excitation of the isomeric ^{229m}Th nuclear state via an electronic bridge process in $^{229}Th^{+}$. Physical Review Letters, 105(18):182501, 2010.

[336] VA Dzuba and VV Flambaum. Resonance nuclear excitation of the ^{229}Th nucleus via electronic bridge process in Th II. arXiv preprint arXiv:2502.12028, 2025.

[337] Robert A Müller, Andrey V Volotka, S Fritzsche, and A Surzhykov. Theoretical analysis of the electron bridge process in $^{229}Th^{3+}$. Nuclear Instruments and Methods in Physics Research Section B: Beam Interactions with Materials and Atoms, 408:84–88, 2017.

[338] Wu Wang, Fen Zou, Stephan Fritzsche, and Yong Li. Isomeric population transfer of the ^{229}Th nucleus via hyperfine electronic bridge. Physical Review Letters, 133(22):223001, 2024.

[339] Pavlo V Bilous, Hendrik Bekker, Julian C Berengut, Benedict Seiferle, Lars von der Wense, Peter G Thirolf, Thomas Pfeifer, José R Crespo López-Urrutia, and Adriana Pálffy. Electronic bridge excitation in highly charged ^{229}Th ions. Physical Review Letters, 124(19):192502, 2020.

[340] Robert A Müller, Andrey V Volotka, and Andrey Surzhykov. Excitation of the ^{229}Th nucleus via a two-photon electronic transition. Physical Review A, 99(4):042517, 2019.

[341] Haowei Xu, Hao Tang, Guoqing Wang, Changhao Li, Boning Li, Paola Cappellaro, and Ju Li. Solid-state ^{229}Th nuclear laser with two-photon pumping. Physical Review A, 108(2):L021502, 2023.

[342] EV Tkalya. Excitation of ^{229m}Th at inelastic scattering of low energy electrons. Physical Review Letters, 124(24):242501, 2020.

[343] G Hass and WR Hunter. Transmittance of cultured crystalline quartz in the vacuum ultraviolet before and after electron irradiation. Applied Optics, 17(15):2310–2315, 1978.

[344] RH Dicke. The effect of collisions upon the doppler width of spectral lines. Physical Review, 89(2):472, 1953.

[345] Lorenza Viola, Emanuel Knill, and Seth Lloyd. Dynamical decoupling of open quantum systems. Physical Review Letters, 82(12):2417, 1999.

[346] Bernhard W Adams, Christian Buth, Stefano M Cavaletto, Jörg Evers, Zoltán Harman, Christoph H Keitel, Adriana Pálffy, Antonio Picón, Ralf Röhlsberger, Yuri Rostovtsev, et al. X-ray quantum optics. Journal of modern optics, 60(1):2–21, 2013.

[347] Ralf Röhlsberger, Hans-Christian Wille, Kai Schlage, and Balaram Sahoo. Electromagnetically induced transparency with resonant nuclei in a cavity. Nature, 482(7384):199–203, 2012.

[348] Yu V Shvyd'Ko, T Hertrich, U Van Bürck, E Gerdau, O Leupold, J Metge, HD Rüter, S Schwendy, GV Smirnov, W Potzel, et al. Storage of nuclear excitation energy through magnetic switching. Physical Review Letters, 77(15):3232, 1996.

[349] Wen-Te Liao, Sumanta Das, Christoph H Keitel, and Adriana Pálffy. Coherence-enhanced optical determination of the ^{229}Th isomeric transition. Physical Review Letters, 109(26):262502, 2012.

[350] Brenden S Nickerson, Wen-Te Liao, and Adriana Pálffy. Collective effects in ^{229}Th-doped crystals. Physical Review A, 98(6):062520, 2018.

[351] GV Smirnov. Nuclear resonant scattering of synchrotron radiation. Hyperfine Interactions, 97(1):551–588, 1996.

[352] Marlan O Scully and Anatoly A Svidzinsky. The super of superradiance. Science, 325(5947):1510–1511, 2009.

[353] Wen-Te Liao and Sven Ahrens. Gravitational and relativistic deflection of X-ray superradiance. Nature Photonics, 9(3):169–173, 2015.

[354] Georg Heinze, Christian Hubrich, and Thomas Halfmann. Stopped light and image storage by electromagnetically induced transparency up to the regime of one minute. Physical Review Letters, 111(3):033601, 2013.

[355] Leon Karpa and Martin Weitz. A Stern–Gerlach experiment for slow light. Nature Physics, 2(5):332–335, 2006.

[356] JB Rosenzweig, N Majernik, RR Robles, Gerard Andonian, O Camacho, A Fukasawa, A Kogar, G Lawler, Jianwei Miao, P Musumeci, et al. An ultra-compact X-ray free-electron laser. New Journal of Physics, 22(9):093067, 2020.

[357] Marcus W Doherty, Neil B Manson, Paul Delaney, Fedor Jelezko, Jörg Wrachtrup, and Lloyd CL Hollenberg. The nitrogen-vacancy colour centre in diamond. Physics Reports, 528(1):1–45, 2013.

[358] Guokui Liu and Bernard Jacquier. Spectroscopic properties of rare earths in optical materials, volume 83. Springer Science & Business Media, 2006.

[359] Zong-Quan Zhou, Chao Liu, Chuan-Feng Li, Guang-Can Guo, Daniel Oblak, Mi Lei, Andrei Faraon, Margherita Mazzera, and Hugues de Riedmatten. Photonic integrated quantum memory in rare-earth doped solids. Laser & Photonics Reviews, 17(10):2300257, 2023.

[360] Romana Schirhagl, Kevin Chang, Michael Loretz, and Christian L Degen. Nitrogen-vacancy centers in diamond: nanoscale sensors for physics and biology. Annual Review of Physical Chemistry, 65(1):83–105, 2014.

[361] John F Barry, Jennifer M Schloss, Erik Bauch, Matthew J Turner, Connor A Hart, Linh M Pham, and Ronald L Walsworth. Sensitivity optimization for NV-diamond magnetometry. Reviews of Modern Physics, 92(1):015004, 2020.

[362] Mi Lei, Rikuto Fukumori, Jake Rochman, Bihui Zhu, Manuel Endres, Joonhee Choi, and Andrei Faraon. Many-body cavity quantum electrodynamics with driven inhomogeneous emitters. Nature, 617(7960):271–276, 2023.

[363] Mi Lei, Rikuto Fukumori, Chun-Ju Wu, Edwin Barnes, Sophia Economou, Joonhee Choi, and Andrei Faraon. Quantum thermalization and Floquet engineering in a spin ensemble with a clock transition. arXiv preprint arXiv:2408.00252, 2024.

[364] Mingyu Fan, Bassam Nima, Aleksandar Radak, Gonzalo Alonso-Álvarez, and Amar Vutha. First results from a search for axionlike dark matter using octupole-deformed nuclei in a crystal. arXiv preprint arXiv:2410.02218, 2024.

[365] Yuexun Huang, Francisco Salces-Carcoba, Rana X Adhikari, Amir H Safavi-Naeini, and Liang Jiang. Vacuum beam guide for large scale quantum networks. Physical Review Letters, 133(2):020801, 2024.

[366] Kilian P Heeg, Andreas Kaldun, Cornelius Strohm, Christian Ott, Rajagopalan Subramanian, Dominik Lentrodt, Johann Haber, Hans-Christian Wille, Stephan Goerttler, Rudolf Rüffer, et al. Coherent X-ray-optical control of nuclear excitons. Nature, 590(7846):401–404, 2021.

[367] Stefano M Cavaletto, Zoltán Harman, Christian Ott, Christian Buth, Thomas Pfeifer, and Christoph H Keitel. Broadband high-resolution X-ray frequency combs. Nature Photonics, 8(7):520–523, 2014.

[368] Michael J Quin, Antonino Di Piazza, and Matteo Tamburini. Coherent frequency combs from electrons colliding with a laser pulse. arXiv preprint arXiv:2412.08554, 2024.

[369] Bernhard Adams, Gabriel Aeppli, Thomas Allison, Alfred QR Baron, Phillip Bucksbaum, Aleksandr I Chumakov, Christopher Corder, Stephen P Cramer, Serena DeBeer, Yuntao Ding, et al. Scientific opportunities with an X-ray free-electron laser oscillator. arXiv preprint arXiv:1903.09317, 2019.

[370] Rachel Margraf, River Robles, Alex Halavanau, Jacek Kryzywinski, Kenan Li, James MacArthur, Taito Osaka, Anne Sakdinawat, Takahiro Sato, Yanwen Sun, et al. Low-loss stable storage of 1.2 Å X-ray pulses in a 14 m Bragg cavity. Nature Photonics, 17(10):878–882, 2023.

[371] Dominik Z Kandula, Christoph Gohle, Tjeerd J Pinkert, Wim Ubachs, and Kjeld SE Eikema. Extreme ultraviolet frequency comb metrology. Physical Review Letters, 105(6):063001, 2010.

[372] LS Dreissen, C Roth, EL Gründeman, JJ Krauth, M Favier, and KSE Eikema. High-precision Ramsey-comb spectroscopy based on high-harmonic generation. Physical Review Letters, 123(14):143001, 2019.

[373] Gerardo D'Auria, E Adli, M Aicheler, AVNİ Aksoy, D Alesini, R Apsimon, J Arnsberg, R Auchettl, A Bainbridge, K Balazs, et al. The CompactLight design study. The European Physical Journal Special Topics, pages 1–208, 2024.

[374] WS Graves, SLY Chang, D Dwyer, P Fromme, M Holl, BDA Levin, LE Malin, JL Vincent, JCH Spence, EA Nanni, et al. Nanopatterned electron beams for temporal coherence and deterministic phase control of x-ray free-electron lasers. arXiv preprint arXiv:1906.01525, 2019.

[375] W Graves. The CXFEL project at Arizona State University. In Proceedings of the 67th ICFA Adv. Beam Dyn. Workshop Future Light Sources, Luzern, Switzerland, pages 54–57, 2023.

[376] Wentao Wang, Ke Feng, Lintong Ke, Changhai Yu, Yi Xu, Rong Qi, Yu Chen, Zhiyong Qin, Zhijun Zhang, Ming Fang, et al. Free-electron lasing at 27 nanometres based on a laser wakefield accelerator. Nature, 595(7868):516–520, 2021.

[377] Neil V Sapra, Ki Youl Yang, Dries Vercruysse, Kenneth J Leedle, Dylan S Black, R Joel England, Logan Su, Rahul Trivedi, Yu Miao, Olav Solgaard, et al. On-chip integrated laser-driven particle accelerator. Science, 367(6473):79–83, 2020.

[378] Tomáš Chlouba, Roy Shiloh, Stefanie Kraus, Leon Brückner, Julian Litzel, and Peter Hommelhoff. Coherent nanophotonic electron accelerator. Nature, 622(7983):476–480, 2023.

[379] Lev Albertovich Wainstein and VD Zubakov. Extraction of signals from noise. Prentice-Hall, 1962.

[380] Glenn Ierley and Alex Kostinski. Extraction of unknown signals in arbitrary noise. Physical Review E, 103(2):022130, 2021.

Appendix A

$^{229}ThO_2$ thin film spectroscopy data

Data collected during IC thin film scans are shown in Fig. A.1. The top panel of each subplot is the raw signal counts collected during one bin. Colored dots with open circles represent valid data points, whereas the filled red dots correspond to when the laser was unlocked, and thus are discarded. The change in marker color indicates the start of a new scan file, where the data count rate may show a discontinuity due to technical issues. Some variations of the count rate come from a change of VUV comb power caused by GIP outcoupler degradation and us changing to new spots on the GIP.

The black trace in each subplot is a smoothed version of the raw data by convolution with a Gaussian function (FWHM 10 kHz). The trace shown in the bottom panel shows the smoothed data, further normalized by a low-pass filtered version of itself (2 MHz corner frequency). The anomaly at the end of the scan range comes from the numerical instability of this normalization process. Other smoothing bin sizes and data processing techniques such as matched filters have also been tested, but are not shown here [379]. Although in our case it is reasonable to assume that a convolution with a Gaussian waveform that matches the shape of the transition line is the best way to extract the signal [379], it could be interesting to consider more advanced data processing techniques [380].

Points deviating from the white noise, especially showing correlations in different scan data traces, are identified and scanned again. Unfortunately, among all scans performed with $^{229}ThO_2$ thin films, we find no repeatable signal.

Figure A.1: $^{229}ThO_2$ thin film scan data. a, b, c, d, e, and f are taken with ^{229}Th#10, a 100 µm diameter, ∼ 30 nm thickness, 19.5 Bq $^{229}ThO_2$ target as produced. g, h, and i taken with ^{229}Th#15, a 100 µm diameter, ∼ 60 nm thickness, 18 Bq $^{229}ThO_2$ target annealed at 700 °C for 60 hours. j and k are taken with ^{229}Th#20, a 100 µm, 19 Bq $^{229}ThO_2$ target fabricated on a Ce:YAG substrate. Before $^{229}ThF_4$ deposition, the Ce:YAG was first coated with 5 nm Ti then 10 nm Au to ensure the surface is conductive while still transparent. After $^{229}ThF_4$ deposition and pyrohydrolysis, the sample is coated with a monolayer graphene to improve electrical conductivity on the surface.

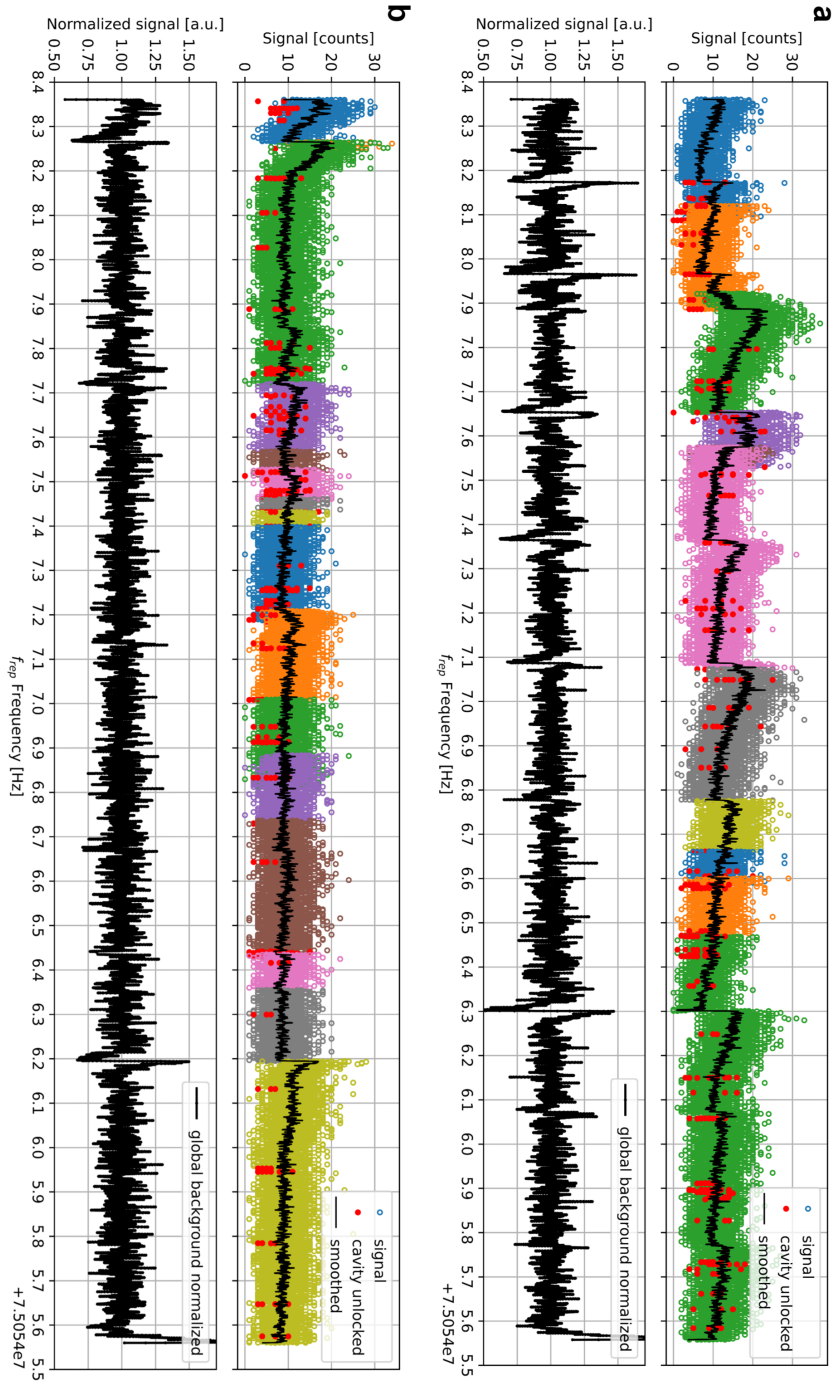

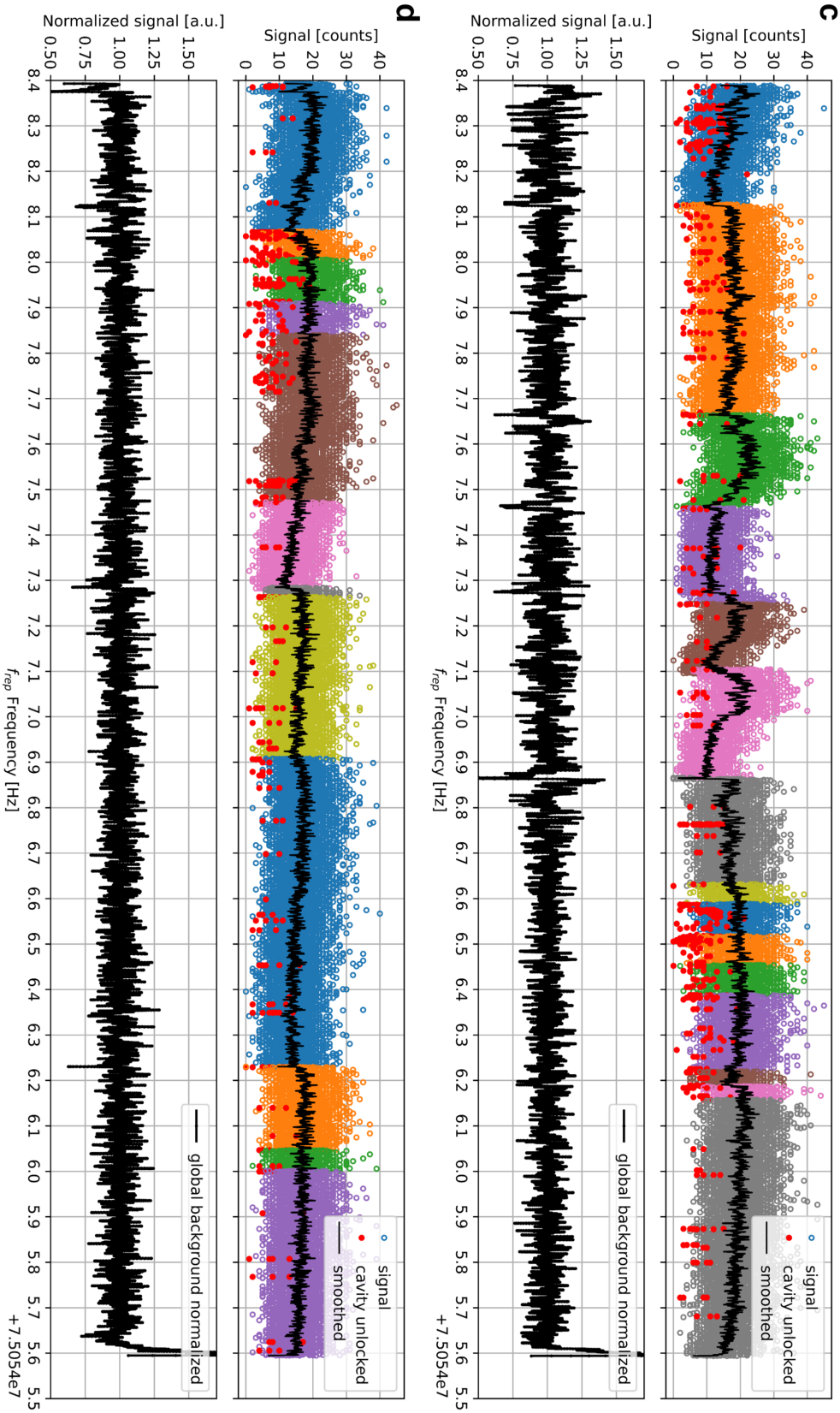
c
Signal [counts]
signal
cavity unlocked
smoothed
Normalized signal [a.u.]
global background normalized
f_{rep} Frequency [Hz]
+7.5054e7
d
Signal [counts]
signal
cavity unlocked
smoothed
Normalized signal [a.u.]
global background normalized
f_{rep} Frequency [Hz]
+7.5054e7

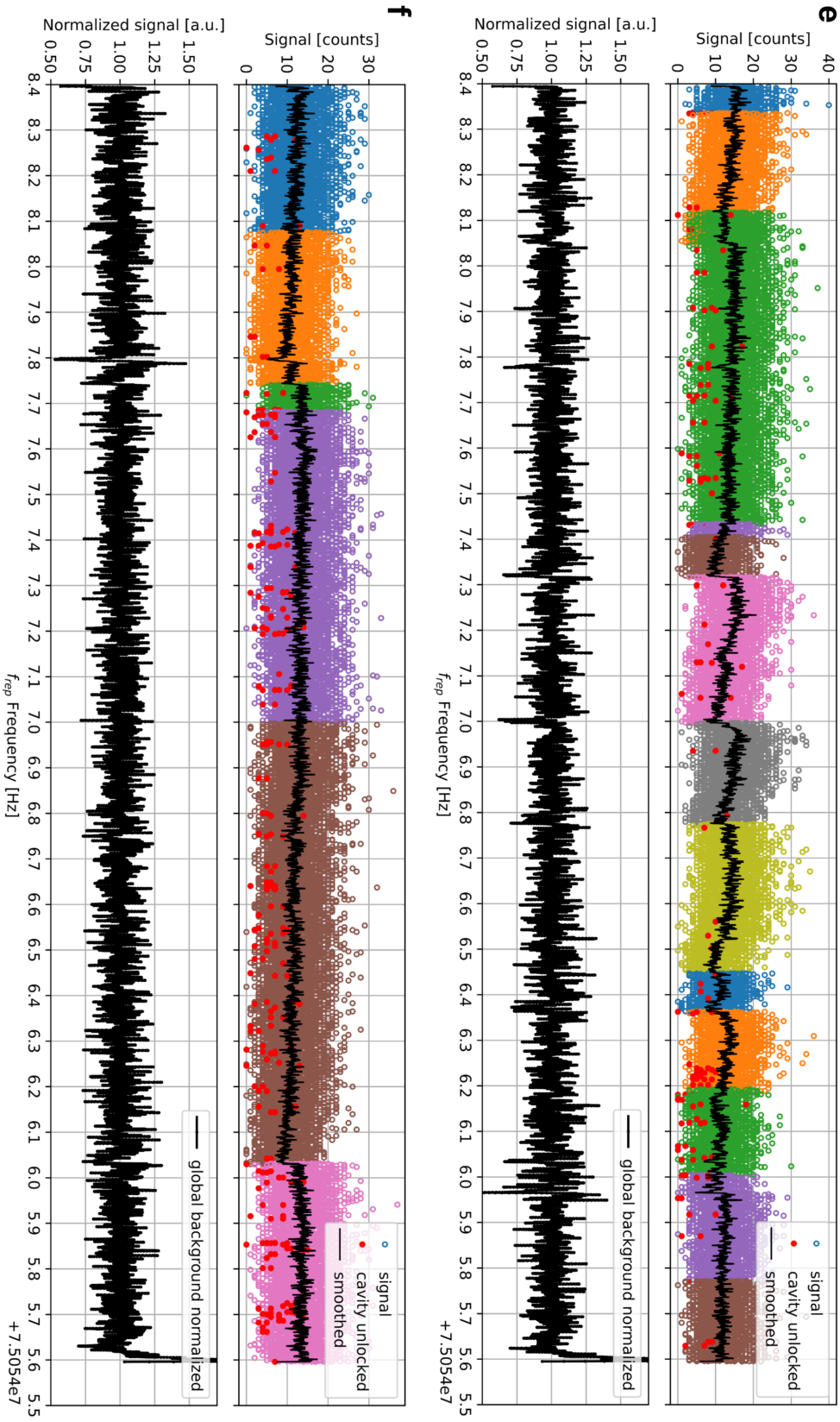
e
Signal [counts]
signal
cavity unlocked
smoothed
Normalized signal [a.u.]
global background normalized
f_{rep} Frequency [Hz]
+7.5054e7
f
Signal [counts]
signal
cavity unlocked
smoothed
Normalized signal [a.u.]
global background normalized
f_{rep} Frequency [Hz]
+7.5054e7

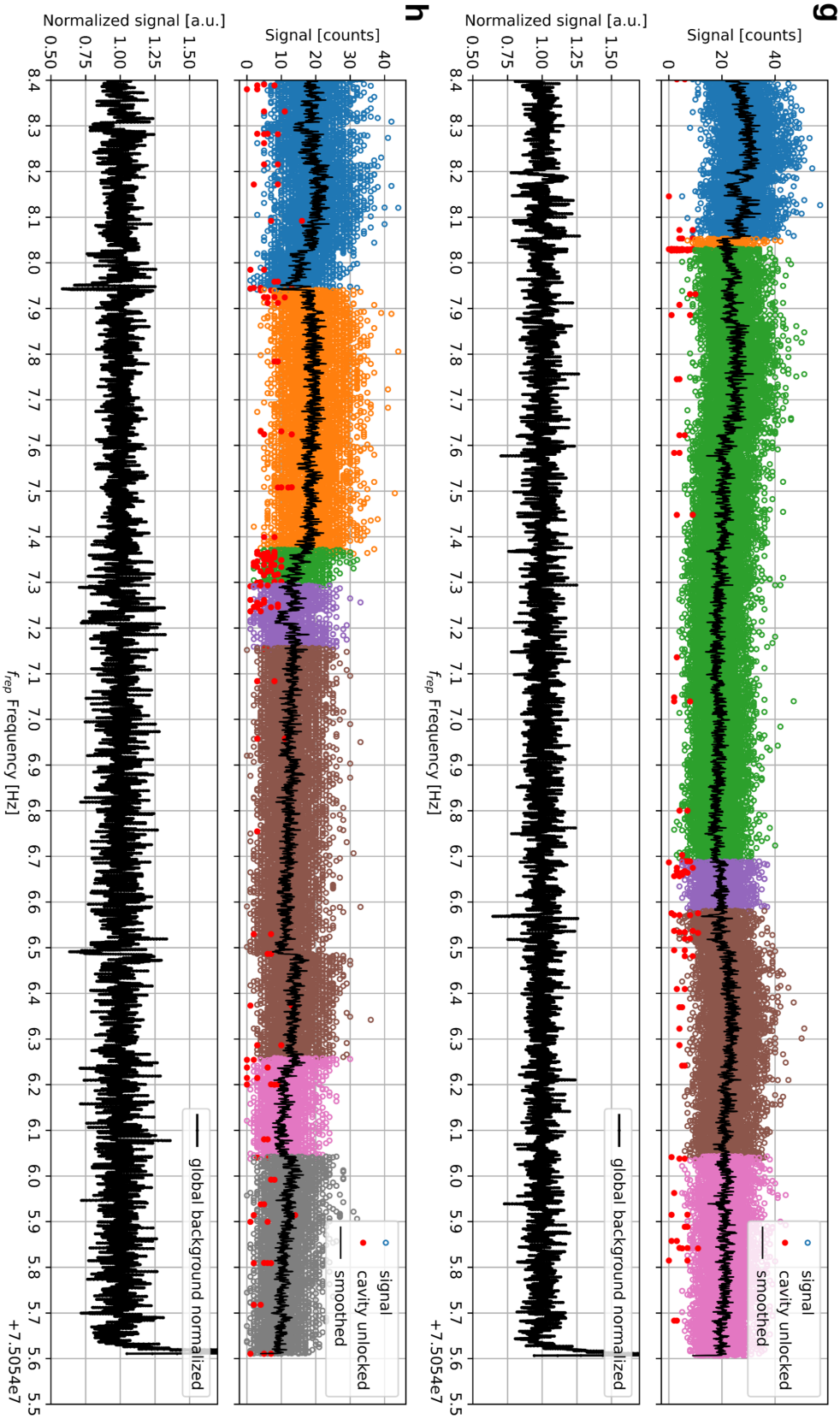
g
Signal [counts]
signal
cavity unlocked
smoothed
Normalized signal [a.u.]
global background normalized
f_{rep} Frequency [Hz]
+7.5054e7
h
Signal [counts]
signal
cavity unlocked
smoothed
Normalized signal [a.u.]
global background normalized
f_{rep} Frequency [Hz]
+7.5054e7

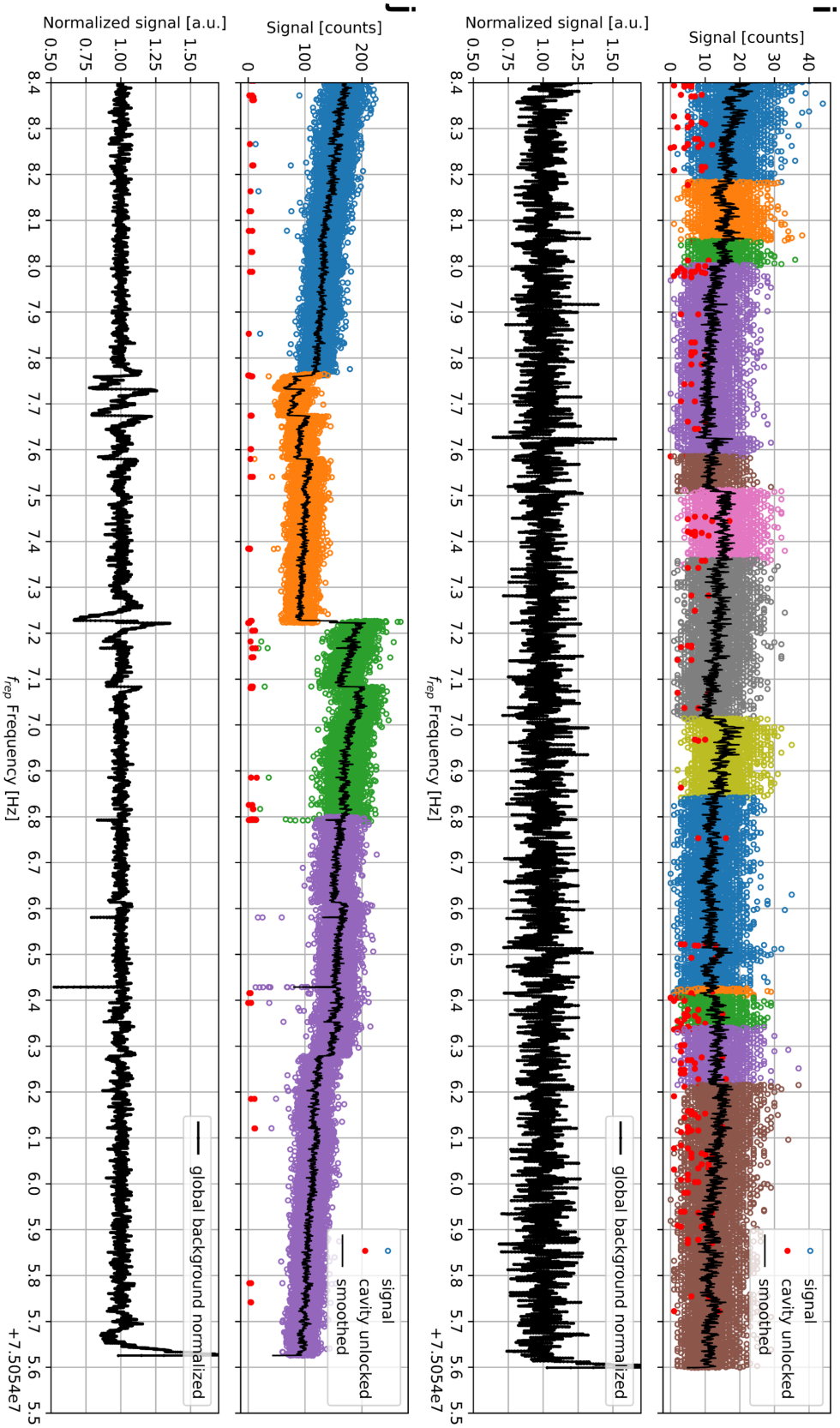
i
Signal [counts]
signal
cavity unlocked
smoothed
Normalized signal [a.u.]
global background normalized
f_{rep} Frequency [Hz]
+7.5054e7
j
Signal [counts]
signal
cavity unlocked
smoothed
Normalized signal [a.u.]
global background normalized
f_{rep} Frequency [Hz]
+7.5054e7

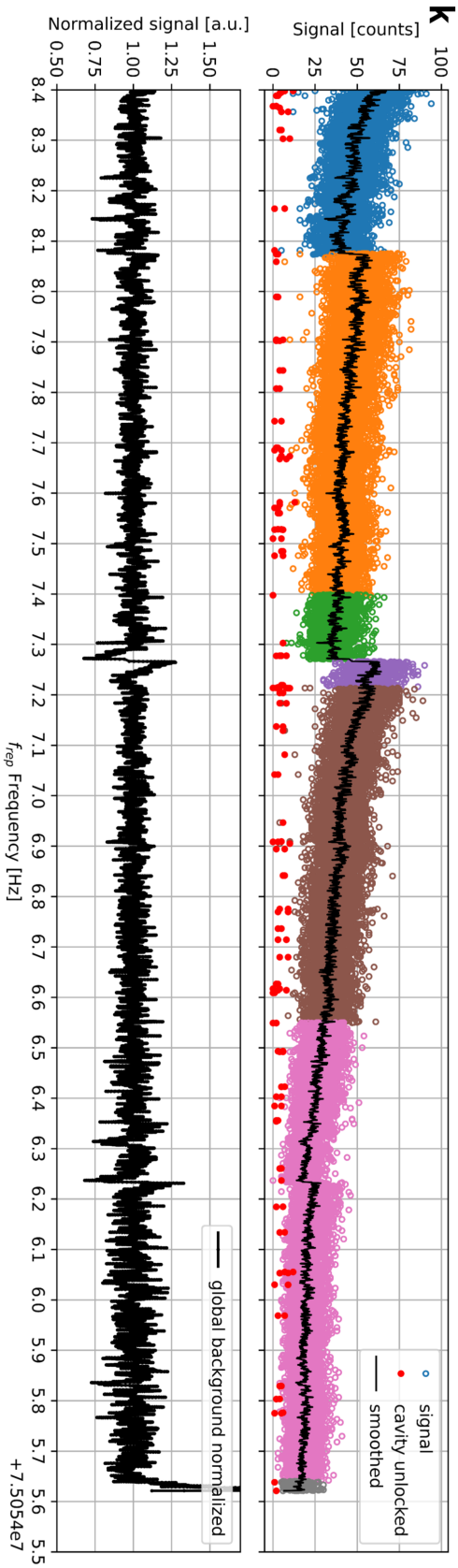
K
Signal [counts]
signal
cavity unlocked
smoothed
Normalized signal [a.u.]
global background normalized
f_{rep} Frequency [Hz]
+7.5054e7